Biomimetic photonic nanocavity arrays

Bincy Jose M.Sc.

Thesis submitted for the degree of
Doctor of Philosophy

Supervisors

Prof. Tia E. Keyes
Prof. Robert J. Forster

School of Chemical Sciences
Dublin City University
December 2010

I hereby certify that this material, which I now submit for assessment on the programme of study leading to the award of Doctor of Philosophy is entirely my own work, that I have exercised reasonable care to ensure that the work is original, and does not to the best of my knowledge breach any law of copyright, and has not been taken from the work of others save and to the extent that such work has been cited and acknowledged within the text of my work.

Signed: _____ (Candidate)   ID No.: 57100012

Date: _____

Acknowledgements

Biomimetic photonic nanocavity arrays

Bincy Jose

Abstract

Plasmonics is currently one of the hottest fields in photonics and potential applications of plasmonic substrates range from biosensors to optical computing. Surface enhanced Raman spectroscopy (SERS) is an important plasmonic effect but the main obstacle to its wide use in analytical science is the high cost of exerting control and reproducibility over metal surface nanostructures. With the advent of nanosphere lithographic methods in recent years, the preparation of homogeneous nanoscale metal topography across macroscopic length scales is now within easy reach and the power of such materials to enhance for example Raman spectroscopic signatures has been demonstrated by a number of groups. This thesis exploits the surface modification of spherical nanocavity arrays as (a) as a means of exploring issues around plasmonic enhancement of Raman and luminescent signal from gold nanocavity arrays. (b) a means of fabricating biomimetic lipid films to provide an electrochemically addressable environment in which proteins can be incorporated into lipid membranes which have aqueous interface at both sides of the membrane.

The opening chapter describes some of the theory behind this work. Background to plasmonic substrates and the impact of such materials on luminescence and Raman signals from species aligned on or near to their surfaces is described as well as the current state of the art regarding supported lipid membrane fabrication. Chapter 2 describes the fabrication of 820 nm diameter gold and cobalt nanocavity arrays on fluorine-doped tin-oxide (FDTO) substrates using nanosphere lithography followed by electrochemical deposition of the metal. The thickness of the film (600 nm) was controlled by monitoring charge passed through the cell during electrodeposition. Fluid filling properties of the gold nanocavity arrays were investigated using a surface-active luminophore $[Ru(bpy)_2(Qbpy)]^{2+}$ complex, where bpy is 2,2'-bipyridyl and Qbpy is 2,2':4,4":4,4"-quarterpyridyl, dissolved in water and methanol. Critically, it was found that complete filling of dried arrays even with solvent to which the solvent was high wettable required sonication. The impact of the gold nanocavity arrays on the photophysics of solutions of $[Ru(bpy)_2(Qbpy)]^{2+}$ and fullerene (C_{60}) which has an extremely low fluorescence quantum yield, encapsulated within the cavities was explored. $[Ru(bpy)_2(Qbpy)]^{2+}$ filled 820 nm diameter gold nanocavity arrays show approximately an order of magnitude enhancement in emission intensity compared to bulk solution or emission from filled cobalt nanocavity arrays.

Chapter 3 describes a novel method for selective surface modification of gold nanocavity arrays which exploits the nanosphere template as a mask for surface adsorption. This approach permitted assembly of two different surface-active species across the array. One was selectively assembled at the top surface of the array and the second at the cavity surfaces using a two-step adsorption process. The Raman signal intensity of

$[Ru(bpy)_2(Qbpy)]^{2+}$ adsorbed only at the top surface of the arrays and separately only at the cavity interior walls was compared as a function of Raman excitation wavelength. The signal intensity from each region was referenced to that from a single monolayer of the same dye on a planar gold surface of roughness factor of 1.3. A systematic study in the enhancement of Raman signal intensity from the selectively modified gold nanocavity arrays reveals that the top surface of the arrays provide two orders of magnitude enhancement in Raman signal intensity compared to the interior walls of the array. In the second part of this chapter enhancement in emission intensity is also observed for molecules adsorbed at the top surface of the nanocavity arrays reveals the effective coupling of molecular resonance of $[Ru(bpy)_2(Qbpy)]^{2+}$ dye with localized surface plasmon resonance at the top surface.

Chapter 4 presents an investigation into the thermal stability of the gold nanocavity arrays. The gold arrays were annealed at 100, 300 and 500 ºC and then surface modified with $[Ru(bpy)_2(Qbpy)]^{2+}$. The Raman and emission intensities recorded from the $[Ru(bpy)_2(Qbpy)]^{2+}$ monolayers adsorbed on those arrays and substantial increases to emission signals demonstrated at higher annealing temperatures. These signal intensities were then correlated with topographical changes to the arrays which were studied by SEM and AFM as a function of annealing temperature. The implications of these changes for application of such arrays in sensing were discussed.

Finally, Chapter 5 describes the preparation of suspended lipid bilayers Dimyristoylphosphatidylcholine (DMPC) across the gold nanocavity arrays. The objective of this chapter was to create a biomimetic environment for studying the ion-channel forming properties of transmembrane protein, Gramicidin D. The main advantage of spanning lipid bilayer on top of cavity is the proximity of both sides of the membrane to aqueous environments, which is a crucial requirement to maintain the fluidity of the lipid bilayers. Moreover, the composition of solution inside and outside the membrane can be varied by choosing appropriate solutions to fill the nanocavity arrays. The mobility of the lipids bilayers formed on top of dried and prefilled arrays was compared using fluorescence recovery after photobleaching (FRAP) technique. FRAP measurements reveal that the mobility of lipid bilayers assembled on dried arrays were approximately an order of magnitude less than that formed on prefilled arrays. The diffusion coefficient for spanned lipid bilayers on the gold nanocavity arrays was approximately 10.9 ± 0.7 $\mu m^2.s^{-1}$ and for lipid bilayers assembled on dried gold nanocavity arrays was approximately 0.04 ± 0.01 $\mu m^2.s^{-1}$. The interaction of molecules between inside the cavity and the top surface of the prefilled array in the bilayer was studied using Fluorescence resonance energy transfer (FRET) measurements. Finally, the ion channel formation on the spanned lipid bilayers were studied using an ion-channel forming protein, gramicidin.

In conclusion, gold nanocavity arrays fabricated using nanosphere lithography technique are capable of enhancing spectroscopic signals from molecules adsorbed or close to the surface. Annealing of the gold nanocavity arrays increases the emission intensity from molecules adsorbed on the surface therefore, these arrays can be useful for the study of hybridization assays. In addition, suspended lipid bilayers were prepared across gold nanocavity arrays, which can be useful for the investigation of the properties of proteins in cell-environment.

Table of contents

3   Selective Surface Modification of gold Nanocavity Arrays: Insights into regions of plasmonic enhancement

`4   Thermal stability of gold nanocavity arrays

5   Formation of spanning lipid membrane on top of dried and prefilled gold nanocavity arrays

Glossary of Acronyms

Acronym	-	Explanation
AFM	-	Atomic force microscopy
BLM	-	Black lipid membrane
c	-	Speed of light ($3x10^8$ m/s)
D	-	Diameter
DAF	-	5-dodecanoyl aminofluorescein
DMPC	-	Dimyristoylphosphatidylcholine
DNA	-	Deoxyribonucleic acid
FDTO	-	Fluorine-doped Tin-oxide
FLIM	-	Fluorescence lifetime imaging microscopy
FRAP	-	Fluorescence recovery after photobleaching
IC	-	Internal conversion
ISC	-	Inter-system crossing
k_{nr}	-	Non-radiative decay rate
k_{ph}	-	Wave-vector of photons
k_r	-	Radiative decay rate
k_{sp}	-	Wave-vector of surface plasmons
NSL	-	Nanosphere Lithography
LSPR	-	Localized surface plasmon resonance
PBS	-	Phosphate buffered saline
PSPR	-	Propagating surface plasmon resonance
r	-	Radius
R_0	-	Förster distance
SAMs	-	Self-assembled monolayers
SEFS	-	Surface enhanced fluorescence spectroscopy
SEM	-	Scanning electron microscope
SERRS	-	Surface enhanced resonance Raman spectroscopy
SERS	-	Surface enhanced Raman spectroscopy
SPP	-	Surface plasmon polaritons

THF	-	Tetrahydrofuran
α	-	Polarizability
γ	-	Surface tension
ε	-	Dielectric constant
λ	-	Wavelength
μ	-	Dipole moment
τ	-	Lifetime
φ	-	Quantum yield
ω	-	Optical excitation frequency

Publications and presentations

Jose, B., Steffen, R., Neugebauer, U., Sheridan, E., Marthi, R., Forster, R. J., Keyes, T. E. 'Emission Enhancement within Gold Spherical Nanocavity Arrays', *Physical Chemistry Chemical Physics,* (2009), **11**, 10923.

Mallon, C. T., Jose B., Forster, R. J., Keyes T. E., 'Protein Nanopatterning and Release from Gold Nanocavity Arrays', *Chemical Communications*, (2010), **46**,106.

Lordan, F., Rice, J. H., Jose, B., Forster, R. J., Keyes T. E., 'Surface enhanced resonance Raman and luminescence on plasmon active nanostructured cavities', *Applied Physics Letters*, (2010), **97**, 153110.

Photonics Ireland – 2009, Ireland, *Oral presentation:* 'Emission enhancement within gold spherical nanocavity arrays'.

International Conference on Advanced Materials (ICAM) - 2008, India, *Oral presentation*: 'Use of Surface Active Luminophore: $[Ru(bpy)_2(Qbpy)]^{2+}$ to Interogate Gold Nanocavity Arrays'.

3rd International conference on Nanomaterials and Nanomanufacturing - 2007, Ireland, *Poster presentation*: 'Use of Surface Active Luminophore: $[Ru(bpy)_2(Qbpy)]^{2+}$ to Interrogate Gold Nanocavity Arrays'.

Chapter 1

Literature survey

1.1 Introduction

Model platforms of cell membranes are an area of intense interest due to their applications in the investigation of dynamic properties of biosystems and as test-beds for transmembrane protein-drug interactions.[1,2] The immobilization of trans-membrane proteins on solid supported bilayers can lead to their denaturation through loss of secondary structure. Therefore, it is critical to provide a cell-like environment to support both proteins and lipid bilayers. In recent years, a small number of groups have applied porous substrates to support lipid bilayers in order to provide water at both interfaces of the membrane.[3,4] However, the observations of conformational changes of proteins on these platforms requires high protein concentrations which makes the measurements expensive. Therefore, one possibility is to exploit plasmons at the underlying platform to aid detection of structural changes in biomaterials at these interfaces using, for example luminescence and Raman spectroscopy. The most appropriate model of cell membrane requires an aqueous environment at both interfaces of the membrane. Absence of water at both interfaces can destroy the fluidity of the membrane which can affect the activity and mobility of any associated protein. A number of groups, most notably, Bartlett and co-workers have reported that gold nanocavity arrays made by nanosphere lithography can provide excellent and highly reproducible surface enhanced Raman spectra.[5,6] Nanocavity arrays fabricated using polymer nanosphere lithography, followed by electrochemical deposition of gold is one of the cheapest and most reproducible ways to fabricate metal surfaces with nanoscale features. This method offers easy control over the diameter and thickness of the nanocavity arrays.

The work presented in this thesis is a part of a broader project aimed at fabricating a biomimetic platform by spanning lipid bilayers across gold nanocavity arrays for studying transmembrane proteins. It is expected to use the voids in gold nanocavity arrays as an aqueous well for both lipid bilayers and associated proteins. This thesis

addresses some of the issues in that project including fluid filling of the array, location of enhancement, selective modification and preliminary attempts at suspending lipid bilayers across the arrays. For the future applications of this platform, it is essential to have enough volume inside the cavity in order to provide a cytoplasmic-like fluid for the cytoplasmic tail of the transmembrane proteins such as an integrin. In order to provide required volume for the proteins inside the void, it is essential to control the thickness and diameter of the cavity to avoid the direct contact of protein with the bottom of the voids. Here, in gold nanocavity arrays, the metal was deposited up to 80 % of the sphere in order to provide enough volume for the cytoplasmic tail of the transmembrane proteins.
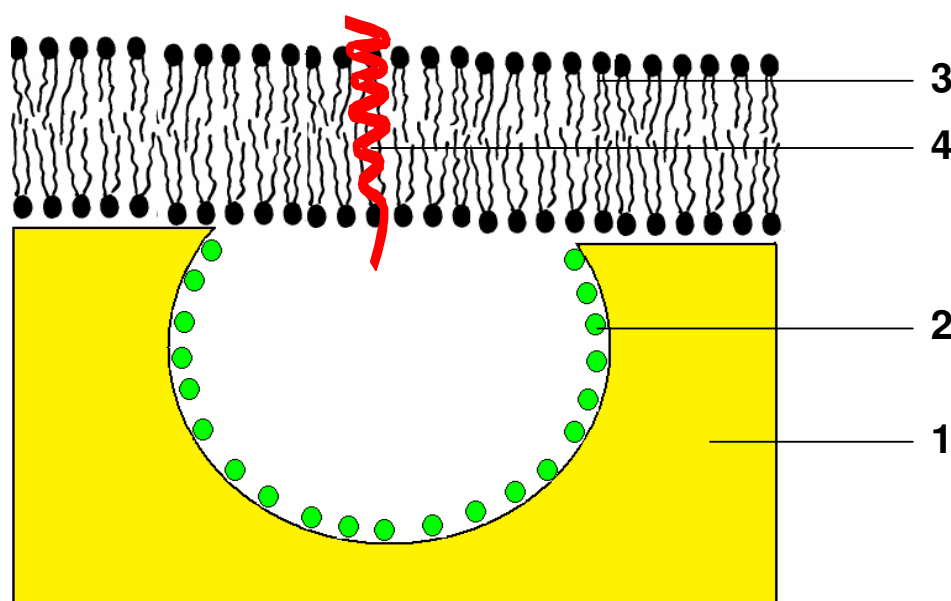
Scheme 1.1: Schematic representation of biomimetic platform for the study transmembrane proteins. (1) Gold nanocavity as a surface enhanced spectroscopic platform. (2) Agonist layer selectively adsorbed at the interior walls of the cavity. (3) Spanned lipid bilayers across the gold cavity to mimic cellular membrane (4) Dye labelled transmembrane protein.

Scheme 1.1 shows a schematic representation of a potential biomimetic platform designed to study transmembrane protein. As shown in Scheme 1.1 (1) gold nanocavity arrays fabricated on a gold surface are intended to use as a substrate for surface enhanced spectroscopic studies. A key objective of this design is to selectively adsorb a protein activator at the interior walls of the cavity and electrochemically release the activator from the wall after spanning lipid bilayers incorporating transmembrane protein on the top surface of the array.[7] Scheme 1.1 (2)

shows the selectively adsorbed activator on the interior walls of the cavity. In order to optimize the sensitivity of detection of spectroscopic signals from this platform, it is crucial to identify the region of enhancement in the array. The enhancement could be either from the interior walls of the array or from the top surface therefore, the main issue here is to identify the region of enhancement. Scheme 1.1 (3) shows the spanning of lipid bilayers across the cavity to create a natural environment for the transmembrane protein. The dye labelled transmembrane protein is shown in Scheme 1.1 (4).

This thesis describes work underlying the development of this biomimetic platform model by addressing issues such as fluid filling, selective modification, thermal stability and bilayer modification of gold nanocavity arrays.
.

1.2 Nanostructured metal surfaces

Recently, nanostructured metal surfaces got significant attention due to their ability to support localized surface plasmons which can be useful for the amplification of both Raman and luminescence signal intensity.[8,9] This section reviews the fabrication, characterisation and advantages of varieties of surface enhanced spectroscopic substrates. A wide range of nanostructured metal surfaces has been reported such as roughened electrodes,[8] metal grating structures,[9] colloidal particle array [10] and nanostructured surfaces.[5] Electrochemically roughened electrodes have played a key role in the development of surface enhanced spectroscopies, especially surface enhanced Raman spectroscopy (SERS). In 1974, Fleischmann and co-workers first observed a million fold enhancement in Raman signal intensity from pyridine adsorbed on an electrochemically roughened silver surface.[11] Fleischmann's idea was to roughen the electrode to increase its surface area and hence increase the number of adsorbing molecules, but the signal intensity was dramatically exceeded that anticipated based on surface coverage alone. Jeanmaire and Van Duyne [12] and Albrecht and Creighton[13] recognized independently that the roughness could only account for 10-fold enhancement and attributed the true origin of this enhancement to the strength of the local electromagnetic field. The enhancement factor achieved using electrochemical roughening can be as high as 10^4-10^6.[14] The fabrication of SERS substrates by electrochemical roughening of electrodes is still widely used because of their simplicity and low cost. However, the main problem with these substrates is the lack of reproducibility due to the random surface structures formed by nanoparticles, which is a crucial requirement for analytical applications of SERS.

Another class of widely studied SERS substrate is colloidal metal nanoparticles.[15,16] Colloidal nanoparticles dried on planar substrates have also shown significant enhancement in Raman signal intensity from adsorbate compared to molecule on a glass substrate. For example, the enhancement of Raman signal intensity from rhodamine 6G molecules adsorbed on silver colloidal nanoparticles was approximately 10^{14}-10^{15} compared to rhodamine adsorbed on a glass substrate in absence of silver.[15] However, the major problems with these substrates are poor uniformity and reproducibility, which make them inappropriate for analytical applications. Recently efforts have increasingly focussed on preparation of

4

reproducible nanostructured surfaces and the preparation methods of highly ordered nanostructures include Langmuir-Blodgett (LB),[17] nanosphere lithography[5] and imprint methods.[18] There are now a variety of surface enhanced spectroscopic surfaces available with nanoscale structures, including, metal nanotriangles,[19] metal film over nanosphere[20] and nanodot structures.[21] Figure 1.1 shows examples of such positive curvature surfaces, which have been shown to support localized surface plasmons. Figure 1.1 (A) and (B) show AFM images of silver triangles and silver film over nanosphere prepared using nanosphere lithography followed by vapour deposition of the metal. These surfaces have been shown to enhance the Raman signal intensity as high as 10^7 due to the presence of localized electric field on the metal surface. Compared to previously discussed platforms such as electrochemically roughened electrodes and colloidal nanoparticles, these platforms show significant reproducibility.[19]
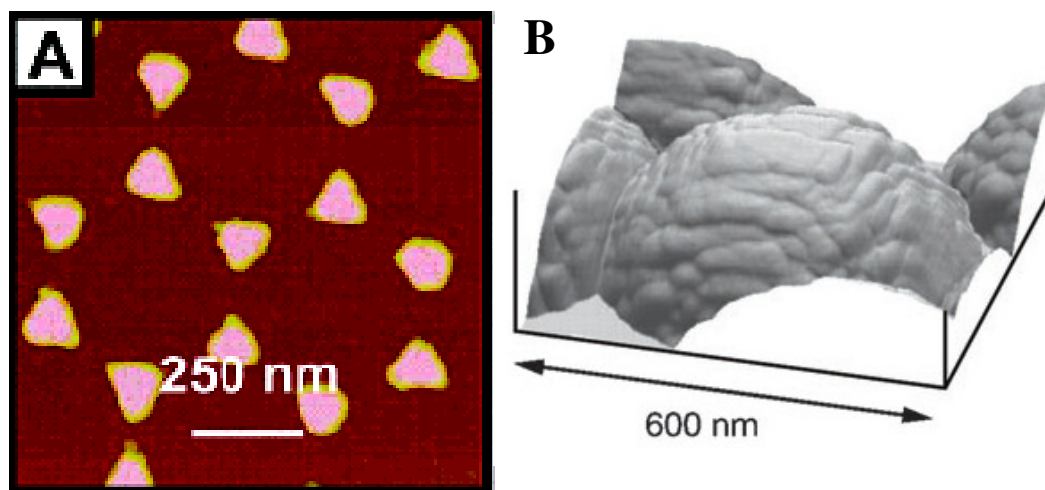
Fig.1.1: Examples of ordered nanostructured metal surfaces (A) Tapping mode AFM image of silver nanoparticles array with 50 nm height. The templated sphere diameter was 400 nm. (B) AFM image of film over nanosphere (FON) substrate fabricated using nanosphere lithography followed by vapour deposition. *Taken from Van Duyne et al., J. Phys. Chem. B, 2004, 108, 109.*[19]

Surfaces with negative curvature such as nanocavities[5] and nanoholes[22] are becoming increasingly popular due to the presence of localized surface plasmons analogous to metal nanoparticles. Highly ordered, negative curvature surfaces with high degree of control over the geometry can be fabricated using lithographic techniques such as

nanosphere lithography,[5] electron-beam lithography,[21] and focused ion beam milling.[22] For example, Brolo et al. fabricated gold nanohole arrays using focused ion beam (FIB) milling.[22] Figure 1.2 (A) and (B) show scanning electron microscopy (SEM) images of nanoholes at different magnifications. The array was patterned on a 100 nm gold film with 200 nm diameter on a glass substrate. They have shown that the sub-wavelength holes on silver or gold films can be reproducibly fabricated with different periodicities using this technique. The techniques such as electron-beam lithography or focused ion beam milling are highly effective as described however, it requires highly specialized equipments.
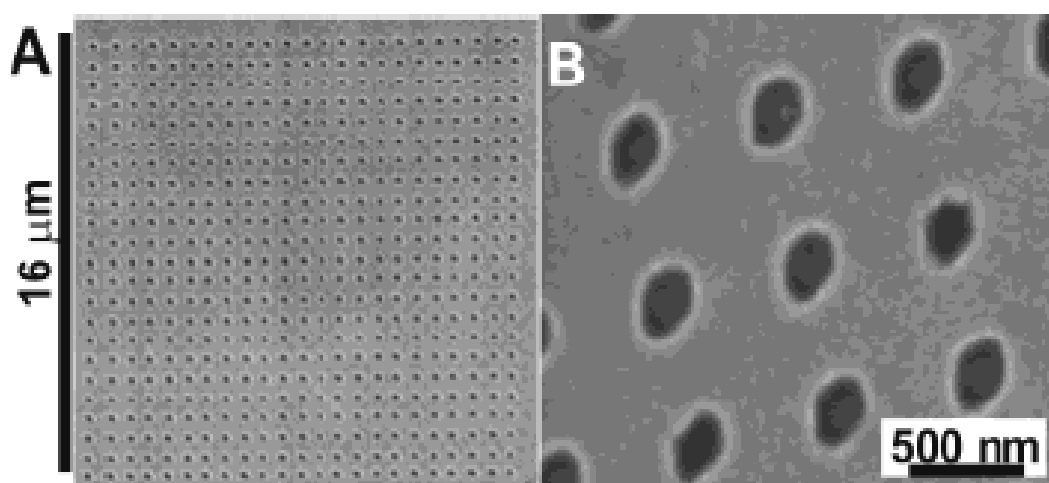
Fig. 1.2: Scanning electron microscopy images of sub-wavelength holes at different magnifications. The array was patterned on a 100 nm thick gold film with 200 nm diameter using ion beam milling. *Taken from Brolo et al., Langmuir, 2004, 20, 4813.*[22]

Nanosphere lithography is an attractive alternative approach to prepare highly ordered nanoporous assemblies on different substrates such as glass or metals.[19] The key advantages of this technique is its simplicity and cost effectiveness compared to other lithographic methods.[23,24] In addition, features such as diameter and thickness of the desired platform can be controlled easily and reproducibly through template-based lithography.[25] A key step in templated metal deposition is the assembly of spheres at the surface of substrates. Figure 1.3 (A) shows a SEM image of self-assembled polystyrene spheres, with a diameter 820 nm, formed by direct evaporation method on a fluorine-doped tin-oxide (FDTO) surface. The "evaporation induced" assembly of colloidal nanosphere takes place near the meniscus of evaporating liquid films and

this technique exploits the strong capillary force, which forms at the meniscus between the substrate and colloidal suspension.[26] The capillary force results from pressure differences and surface tension effects arise when the spheres interrupt the shape of the vapour-liquid phase boundary. According to the Laplace equation, the pressure inside the curved surface is less than the atmospheric pressure by approximately $2\gamma / r$, where r is the radius of the capillary tube and γ is the surface tension of liquid. Denkov et al. demonstrated that when a suspension of spheres is brought into contact with a substrate, a pressure difference draws spheres to the air-water boundary and across the meniscus surface towards the substrate.[26] The total force acting on a single sphere in the direction normal to a flat substrate when a liquid film is lower than the radius of the sphere is described by Denkov et al. This is given by the sum of the capillary adhesion due to the pressure difference across the free surface and the surface tension forces acting tangentially to the interface along the contact line. Tull and co-workers also supported the idea that the assembly of colloidal spheres with diameters less than 1 µm mainly occurs due to such capillary interactions.[27]
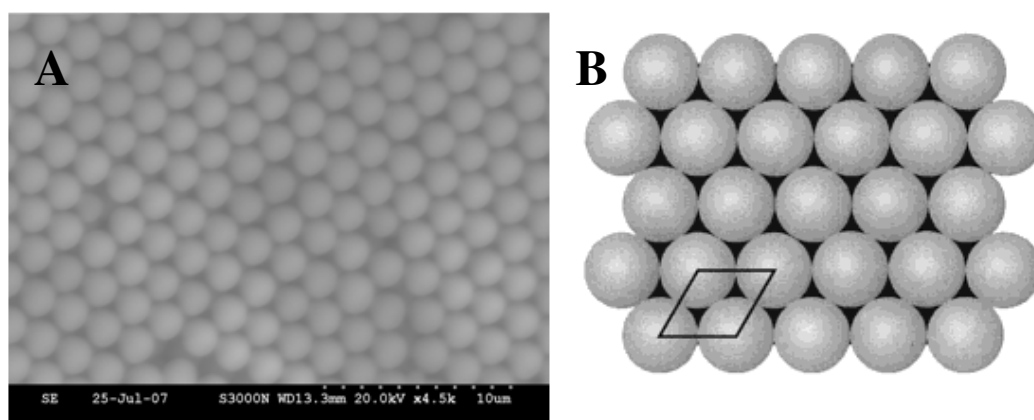
Fig. 1.3: (A) SEM image of self-assembled polystyrene spheres on FDTO substrate. The diameter of the sphere was 820 nm. (B) Schematic of polystyrene spheres and the dark region represents the interstitial voids of the template. *Taken from Van Duyne et al., J. Phys. Chem. B, 2001, 105, 5599.*[28]

Figure 1.3 (B) shows a schematic representation of the interstitial voids formed after the self-assembly of polystyrene spheres. Several different routes have been reported to deposit the desired metal through these interstitial voids which includes sol-gel chemistry,[29] chemical vapour deposition,[30] electroless deposition or precipitation from saturated solution.[31] These different methods to deposit metal through the voids of the template are discussed below. In 1999, Velev et al. reported the first

fabrication of metallic nanostructures on colloidal crystal templates of polystyrene spheres. [32]   They prepared gold nanostructures by depositing 15-25 nm gold nanoparticles through the voids of the template by filtration.   Highly ordered nanostructured surfaces were created after the removal of polystyrene sphere template by calcination or dissolving the spheres in trichloromethane after deposition of metal nanoparticles.   The main problem with this method was that the deposition of nanoparticle through the template created porosity due to incomplete filling around the spheres. Vapour deposition is another useful approach to deposit metals through the templates. For instance, Jenson and co-workers have reported the preparation of silver triangles using vapour deposition of metal through the polystyrene sphere template. [33]   The templates for deposition were prepared using nanosphere lithography. After the vapour deposition of the metal through the voids, the samples were sonicated in methylene chloride to remove the spheres. Depending on the metal deposition time they prepared silver triangles or silver film over spheres. The AFM images of the resulting ordered nanostructured silver surfaces are shown in Figure 1.1. This method is extensively used to fabricate highly ordered nanostructured surfaces on non-conducting substrates.   Another deposition method for the fabrication of nanostructured metal surfaces is chemical reduction. For example, Yan et al. have reported the fabrication of nanoporous NiO and metallic Ni film by template precipitation followed by chemical reduction.[34] Colloidal polystyrene spheres were used as the template for the fabrication of macroporous structures. In this method, incomplete filling of metal created highly porous nanostructured arrays.

Braun et al. first introduced electrochemical deposition as a means of metal deposition through the colloidal template.[35] They prepared ordered microporous films of cadmium selenide and cadmium sulphide. Electrochemical deposition offers many advantages over the other methods such as deposition of nanoparticles or vapour deposition methods, which can create microporosity around the spheres, or it, can result in incomplete filling. Electrochemical deposition can provide a greater density of the deposited material around the surface of the spheres, ensuring fine control over the thickness of the resulting film.   Nanoporous arrays can be electrochemically prepared using any conducting materials such as conducting polymers, alloys, and metals. Several groups reported the templated electrochemical deposition of metal to fabricate nanostructured surfaces and the relevant articles are

discussed below. For example, Wijnhoven and co-workers have prepared nanoporous gold films on indium tin oxide (ITO) slides using silica particles as the template.[36] The deposition of gold was carried out after suspending the slide in 0.1 M HAuCl$_4$ solution with a pH of 6. They deposited gold on the ITO substrate at a potential of - 0.5 V vs. scanning calomel electrode (SCE). They used silica templates and which they removed by etching in HF after metal deposition. Xu et al. have reported the fabrication of three-dimensional ordered arrays of nickel and gold meshes using electrochemical deposition.[37] They electrodeposited the metals through multilayer templates of silica sphere arrays. The electrochemical deposition of metals was carried out by a constant current method over 36 hours with a low current density (0.50 mA.cm^{-2}). Then, the spheres were removed by soaking it in HF for 24 hours. The multilayer of gold and nickel structures were characterised using SEM after dissolving the spheres. In this experimental method, the deposition required a long time, which makes the process inconvenient.
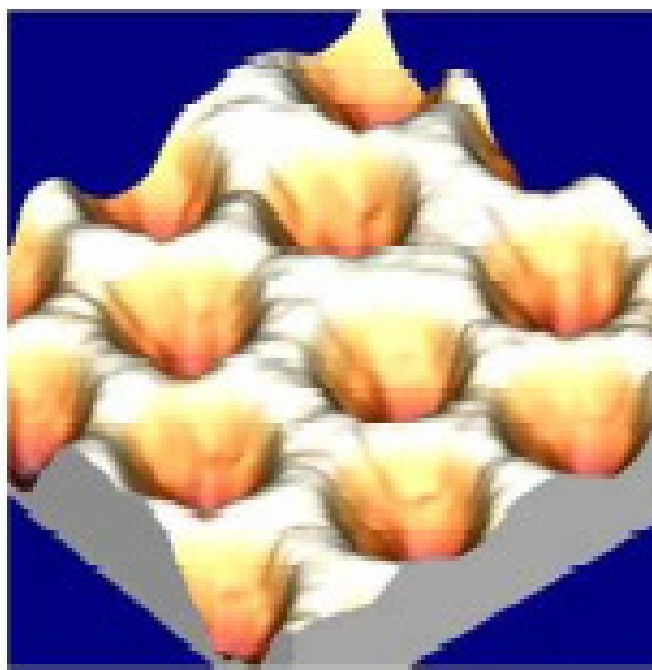
Fig.1.4: Three-dimensional image of 600 nm diameter gold nanocavity array taken with near-field optical microscopy in topography mode. *Taken from Lacharmoise et al., Phys. Rev. B, 2008, 78, 125410.*[38]

Bartlett and co-workers have reported the fabrication of nanocavity arrays using a number of metals by an electrochemical deposition method.[39] Highly ordered macroporous films of platinum, palladium and cobalt were prepared by

electrodeposition of these metals through templates of polystyrene spheres on gold surfaces. The nanoporous arrays on gold substrates were characterised using scanning electron microscope (SEM). Figure 1.4 shows a three dimensional image of gold nanocavity array (600 nm diameter) taken using near-field optical microscopy in topography mode.[38] Bartlett, Cole and Baumberg have probably carried out the most extensive and systematic study of the properties of such electrodeposited arrays in the literature.[38,39] Their work has demonstrated the influence of cavity size, aperture and thickness on both the plasmon energy and distribution of the plasmon modes in these arrays.[40,41] They have also demonstrated that the resonance energies of spherical nanocavities are tuneable from ultraviolet to near infrared by controlling the diameter and height. The theoretical studies by Baumberg et al. on gold nanocavity arrays revealed that the localized surface plasmons[42] can effectively couples to incident light. They have studied the optical properties of the gold nanocavity arrays by varying the film thickness and they have systematically studied the enhancement in Raman signal intensity from benzenethiol adsorbed on these arrays.[43] Previous reports have shown that the negative curvature substrate such as gold nanocavity arrays, prepared using nanosphere lithography followed by electrochemical deposition exhibit greater reproducibility with greater enhancement in Raman signal intensity.[44] One of the reports reveals that the enhancement in resonance Raman signal intensity (SERRS) from this platform can be as high as 10^9 which can provide highly sensitive detection.[44] The enhancement in signal intensity is attributed to the coupling of localized surface plasmons present at the surface with the incident light. In this thesis, gold nanocavity arrays prepared using nanosphere lithography followed by electrochemical deposition are used as a surface enhanced spectroscopic substrate in order to create a cell-membrane like environment for transmembrane proteins.

1.3 Surface plasmons

The origin of spectroscopic signal enhancement from nanostructured metal surfaces arises due to the presence of localized surface plasmons on the metal surface. This section describes different types of surface plasmons present on a planar metal surface and nanostructured metal surfaces. Recently, there has been significant interest in the design and fabrication of metallic nanostructures due to their fascinating optical and electronic properties. [45,46] The physical origin of these properties arises due to the presence of free electrons in the metal. It is well known that the presence of free conduction electrons in metals results in greater heat or electrical conductivity. In 1956, Pines described the characteristic energy losses experienced by electrons travelling through metals. He attributed those losses to collective oscillations of free electrons in the metal. [47] He introduced the term 'plasmons' for these collective charge density oscillations due to the resemblance to the electronic plasma oscillations in gaseous discharges. When incident photons couple with this free electron plasma, it creates an electromagnetic wave in the metal called a plasmon polariton. In 1957, Ritchie performed a study on electron energy losses in thin metal films, in which he showed that plasmon modes can exist near the surface of metals. That means, the charge density waves or surface plasmons can propagate at the metal/dielectric interface.[48] Cunningham et al. introduced the term Surface plasmon-polaritons (SPP) to describe the interaction of these surface charge density waves with electromagnetic waves (photon).

Generally, there are two types of surface plasmon polaritons present on metal surfaces (i) propagating surface plasmon polaritons (PSPP) and (ii) localized surface plasmon polaritons (LSPR). Propagating surface plasmon polaritons are mainly present on planar metal surfaces; they propagate through the metal surfaces and their amplitude falls off exponentially with distance into the dielectric from the interface. In contrast, localized surface plasmons are non-propagating and present on nanostructured metal surfaces or on nanoparticles. Figure 1.5 illustrates the difference between the propagating and localized surface plasmons.[49] Figure 1.5 (a) shows propagating surface plasmons which are electromagnetic waves that propagate in the x-y plane and decay exponentially in the z-direction.
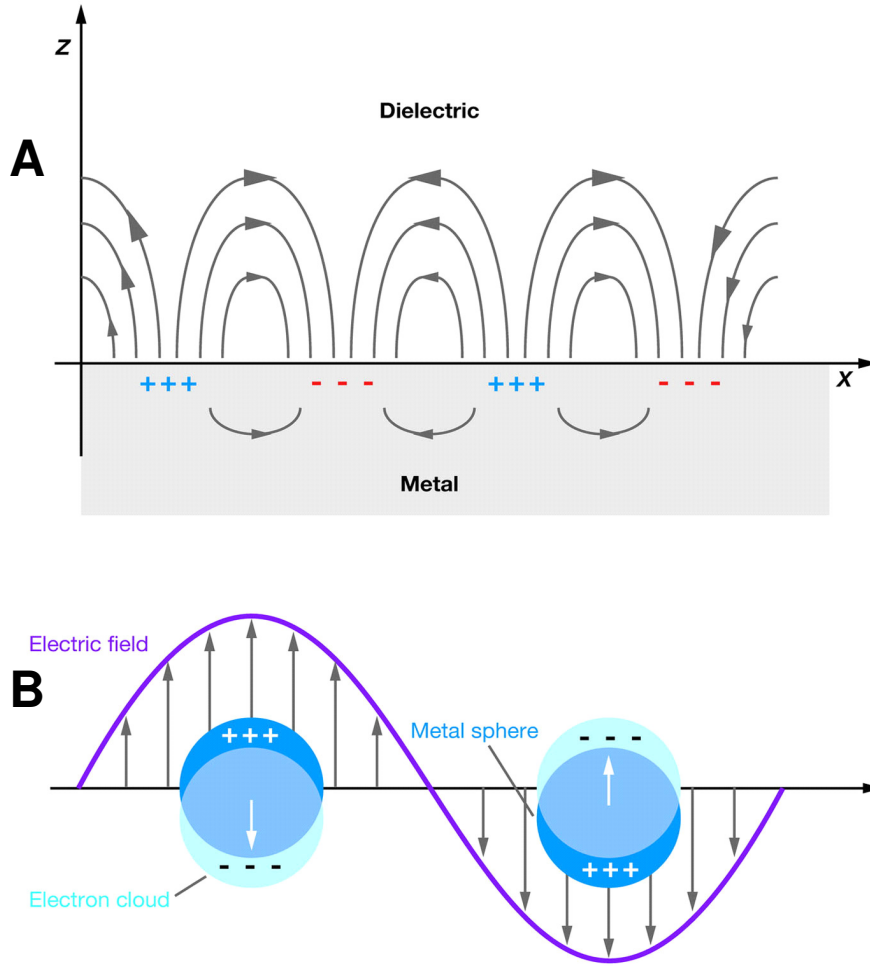
Fig. 1.5: Schematic representation of (A) propagating plasmon resonance, which is present on the flat metal surfaces and (B) localized surface plasmon resonance, which is present at the metal nanoparticles or nanostructured metal surfaces. *Taken from Duyne et al., Science, 2004, 306, 985.*[49]

1.3.1 Propagating Surface Plasmon Resonance (PSPR)

Planar metal surfaces have charge density oscillations at the surface, which cannot be directly excited optically due to the requirements of momentum conservation. The plasmon excitation by incident light takes place only when the energy and the momentum of these particles are conserved. This condition is met when the wave vector of the surface plasmons, k_{sp}, and incident photons, k_{ph}, are equal in magnitude and direction for the same frequency waves, where k_{sp} and k_{ph} are described by Equation 1.1 and 1.2.

$$k_{ph} = \omega/c \sqrt{\varepsilon_d} \qquad\qquad 1.1$$

$$k_{SP} = \omega/c \sqrt{\frac{\varepsilon_m . \varepsilon_d}{(\varepsilon_m + \varepsilon_d)}} \qquad\qquad 1.2$$

where, ω is the optical excitation frequency, c is speed of the light, ε_m and ε_d are the dielectric constants for metal and contact medium respectively typically either air or water. Surface plasmon excitation becomes possible if the momentum of the incident photon is modified to match that of the plasmon. This can be achieved for a flat metal by passing the light through a prism or grating on the surface. In 1968, Otto as well as Kretschmann and Raether developed such methods for the optical excitation of plasmons on the metal films and this method is widely exploited in analytical surface plasmon resonance.[50,51]

Propagating surface plasmon resonance (PSPR) occurs when plane polarized light is incident on a metal film under total internal reflection conditions as shown in Figure 1.6. When the wave vector of the incident light coincides with the electron oscillation frequency at the metal surface, the electron density couples with the incident light, and an electron resonance is created.[52] A decrease in the reflected light intensity can be observed at surface plasmon resonance condition as shown in Figure 1.6 (B). At the resonance condition, the electric field of an evanescent wave can penetrate through the interface and decays exponentially with distance. It can propagate through the metal surface on the order of 10-100 µm with an associated electric field that decays evanescently in the Z direction on the order of 200 nm.[53,54,55] The propagation length of the surface plasmon mode at an interface depends on the materials refractive index, therefore, this technique is usually used to detect refractive index changes at an interface.[56] Small refractive index changes caused by the binding of low molecular weight analytes shifts the surface plasmon resonance condition, which can be measured as the intensity, wavelength, or angle shift of surface plasmon resonance. Liedbergh et al. first demonstrated the use of PSPR in biosensing.[57] He could sense immunoglobulin antibodies by observing the changes in the critical angle when the antibodies bound selectively to a gold film. These days it has become an effective tool for analysing biomolecular interactions. PSPR sensors have been used

13

as a refractive index based sensors to detect analyte binding on the metal surface and have been widely used to monitor a broad range of analyte-surface binding interactions including the adsorption of small molecules,[58] ligand-receptor binding,[59] and antibody-antigen binding.[60,61]
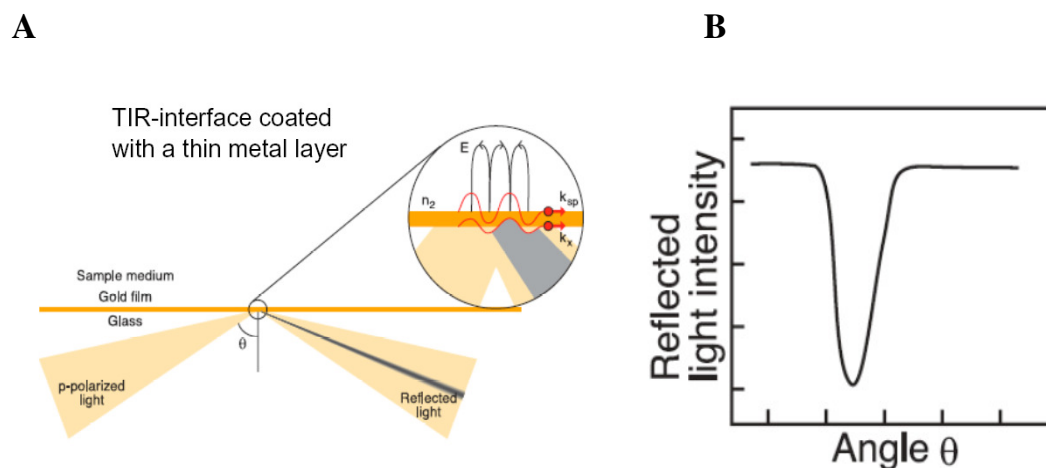
Fig. 1.6: Schematic representation of (A) setup for the coupling of propagating surface plasmon with light. (B) Decrease in the reflected light intensity at a specific angle of incidence. *Taken from reference 62.*

1.3.2 Localized Surface Plasmon Resonance (LSPR)

Localized surface plasmons are the collective oscillation of surface charge confined to sub-wavelength regions, which can be excited around nanostructured metal surfaces or on the surface of metal nanoparticles. In this case, the electromagnetic fields are concentrated in nanoscopic regions at the surface which results in a large localized electric field intensity. In spherical metal nanoparticles, with a diameter smaller than the wavelength of the light, conduction electrons on the metal surfaces move in phase with plane-wave excitation but the positively charged nuclei will remain static as shown in Figure.1.5. This leads to the formation of polarization charges on the surface of NPs and the coulombic attraction between the electrons and the metal cations act as a restoring force for the electrons when they are off-equilibrium.[63,64] A resonantly enhanced field builds up inside the metal particle and a dipolar field is produced outside. This results in strong light scattering and enhancement of the near-field on the metal surface. When incident light, with a electromagnetic field vector E_0 pointing along the z-axis, hits on a spherical metal

particle, embedded in some medium of dielectric constant ε_0, then the field outside the sphere $\mathbf{E}_{out}$, is written as,

$$\mathbf{E}_{out} = E_0 z - \alpha E_0 [z/r^3 - 3z/r^5 (z\mathbf{z} + x\mathbf{x} + y\mathbf{y})] \qquad 1.3$$

where α is the metal polarizability, x, y, z are the Cartesian coordinates, r is the radial distance and $\mathbf{x, y, z}$ are the unit vectors. E_0 is the magnitude of $\mathbf{E_0}$. The first term is the applied field of the light and the second is the induced dipole of the polarized sphere. Assume that the sphere has a dielectric constant of ε_i, and radius of a, then the polarizability, α, is:

$$\alpha = g\, \alpha^3 \qquad 1.4$$

with $\qquad g = \varepsilon_i - \varepsilon_0 / \varepsilon_i + 2\varepsilon_0 \qquad 1.5$

where ε_i and ε_0 are the dielectric constants for the sphere and the medium respectively. When the real part of ε_i is $-2\varepsilon_0$ and the imaginary part is small, α becomes large, making the induced field large. This implies that the dielectric of the particle must be large and negative for plasmons and SERS to take place.[67] For larger metallic nanoparticles (d > 30 nm) a reduction in the depolarisation field is observed at the particle centre because all of the conduction electrons do not move in phase with the excitation field. This results in a decrease in the total enhancement of the spectroscopic response of the adsorbed species.[65,66] The increased field intensity provides the basis for a set of enhanced spectroscopic methods including Surface enhanced Raman scattering (SERS),[67,68] Surface enhanced resonance Raman scattering (SERRS) and Surface enhanced Fluorescence spectroscopy (SEFS).[69,70] Metal nanoparticles such as gold, silver, copper, aluminium can exhibit surface plasmon resonance in the UV-visible wavelength range.[71] Silver and gold are the most widely used metals for surface enhanced spectroscopic studies due to the matching of electron oscillation frequency with the incident frequency of light in the visible range. The LSPRs are sensitive to the size and shape of the nanoparticles or nanostructured metal surfaces. Therefore, LSPR can be tailored by changing the size and shape of the nanoparticles. It is even possible to tune the surface plasmon resonance from UV to near infrared region.

1.3.3 Comparison between PSPR and LSPR

➢ For PSPR, both wave vector and frequency of the plasmon has to match with the incident laser while for LSPR only frequency conservation is required. The conservation of wave vector requires more complex experimental setup such as ATR configuration.

➢ In LSPR based sensors, it is possible to tune the sensing capability by changing the size and shape of the nanoparticles.[72]

➢ In LSPR, the electromagnetic decay length, l_d is approximately 5-15 nm depending on the size, shape, and composition of the nanoparticles and in PSPR, l_d is approximately 200-300 nm.[73]

As discussed earlier, the potential applications of LSPRs on metal nanoparticles or on nanostructured metal surfaces include enhancement of Raman and emission spectroscopic signals from molecules near to or adsorbed to the substrates. The enhancement mechanisms of both emission and Raman intensity are discussed in the following section.

1.4 Luminescence and its enhancement by metal substrates

Metal-induced luminescence enhancement is a plasmonic phenomenon and is thought to arise mainly from an increased rate of radiative decay of the luminophore leading to decreased lifetimes of the fluorophore. [74] Luminescence is the radiative deactivation of molecules from an electronically excited state to ground state. The photophysical processes of an electronically excited molecule can undergo different transitions, which can be represented on a Jablonski diagram as shown in Figure 1.7. When a luminophore absorbs photons with sufficient energy, it is usually excited to higher electronic excited levels (S_1 or S_2) from S_0 ground state. From here, the excited molecules relax to the lowest vibrational levels of the S_1 state by vibrational relaxation and internal conversion (IC). Internal conversion is a rapid, iso-energetic, non-radiative transition (10^{-13} -10^{-11} s), which occurs between different electronic states of the same spin multiplicity. Molecules in the S_1 state can then decay either by radiative or by non-radiative pathways. The spin-allowed radiative transition is called fluorescence and this typically occurs within 10^{-9} s. Molecules in the S_1 state can also undergo spin conversion to the triplet state (T) and this "forbidden" conversion of singlet state to triplet state is called inter system crossing (ISC). Molecules in the
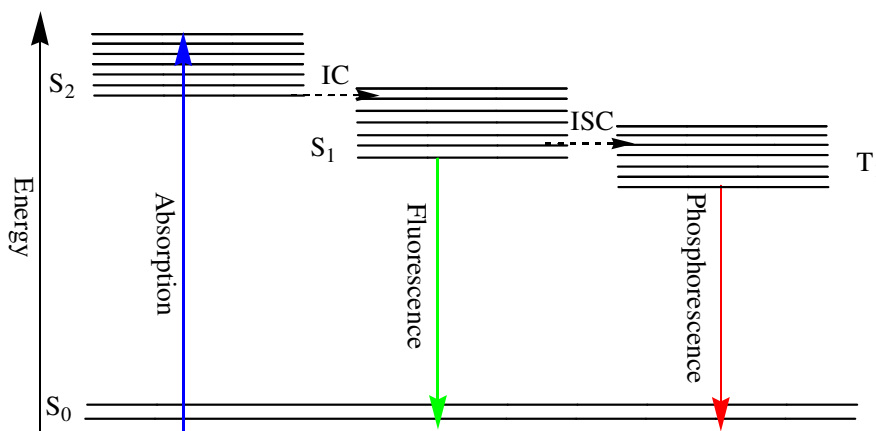
Fig. 1.7: Energy level diagram (Jablonski diagram) represents the mechanism of fluorescence and phosphorescence. IC represents internal conversion that occurs between different electronic states with same spin multiplicity and ISC represents inter system crossing which also occurs between different electronic states but with different multiplicity.

triplet state can return to the ground state through a radiative transition termed as phosphorescence. Transition from T_1 to the singlet ground state is forbidden, and, as a result, the emission occurs several orders of magnitude more slowly (10^3-10^0 s^{-1}) than the fluorescence.

Metals are well known for quenching fluorescence of the fluorophore but recent studies reveal that the distance dependent quenching and enhancement of fluorescence can be balanced.[75] In general, it is thought that metallic surfaces may quench the fluorescence when the distance is <5 nm. However, at longer distances ranging from 5 to 200 nm useful coupling occurs between the fluorophore and the surface plasmons can result in an enhanced fluorescence from the fluorophore.[76] Metal enhanced fluorescence is a relatively new sensing technology in diagnostics and biotechnology and it can be used to increase the sensitivity and the detection limits of fluorescence signalling.[75] The detection of fluorescence from a fluorophore is limited by its quantum yield and photostability. Recently, several reports have shown that with the aid of metal surfaces, the emission intensity of the fluorophore can be increased at least by an order of magnitude.[77,78] The control of the interaction between the metal and the fluorophore is termed radiative decay engineering.[79]

The mechanism of metal enhanced fluorescence can be explained in two ways: (1) the localized electric field at the metal surface can excite the fluorophore (2) the emission from the fluorophore can excite the electron density at the metal surface. In former case, the incident light excites the electrons at the metal surface and the resulting electric field created by the metal surface plasmons in effect increases the absorbance cross section of the fluorophore resulting in more efficient excitation. In the latter case, the fluorophore in the excited state acts as an oscillatory dipole and the oscillations in the excited state of the fluorophore can induce vibrations in the electron density of the metal. These vibrations of the surface plasmons create an electric field and this field can interact with the fluorophore. This interaction of the electric field can change the radiative decay rate and the lifetimes of the fluorophore. The metal enhanced fluorescence pathways can be included in a Jablonski diagram as shown in Figure 1.8.[80] The quantum yield (Φ_o) and lifetime (τ_0) of the fluorophore in the absence of metal surface is given by,

$$\Phi_o = k_r / (k_r + k_{nr}) \qquad\qquad 1.6$$

$$\tau_0 = (k_r + k_{nr})^{-1} \qquad\qquad 1.7$$

where k_r is the radiative rate of the fluorophore and k_{nr} is the rate of non-radiative decay. In the presence of a plasmonic metal surface, the quantum yield (Φ_m) and the lifetime (τ_m) of the fluorophore is given by,

$$\Phi_m = (k_r + k_{r\,m}) / (k_r + k_{r\,m} + k_{nr}) \qquad\qquad 1.8$$

$$\tau_m = (k_r + k_{rm} + k_{nr})^{-1} \qquad\qquad 1.9$$

where k_{rm} is the radiative decay rate of the fluorophore in the presence of metal. The extent of enhancement of fluorescence depends on the quantum yield of the fluorophore; the enhancement is typically largest for low quantum yield fluorophores compared to high quantum yield dyes because there is less remaining capacity for the
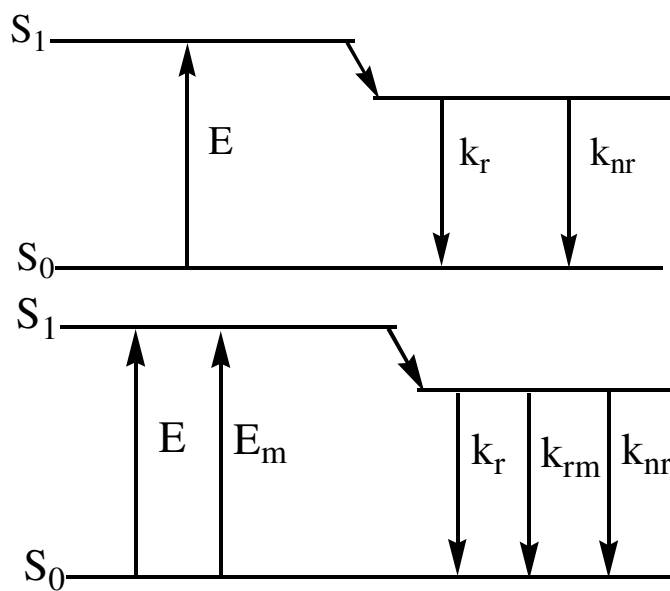
Fig. 1.8: Jablonski diagram for a fluorophore (bottom) with and (top) without the presence of metal. Scheme represents the excitation (E) of an electron from the ground state to excited state followed by emission by radiative (k_r) and non-radiative (k_r) pathways. E_m is the enhanced excitation of molecules in presence of metal.

enhancement of Φ as the maximum enhancement achievable is Φ of 1. For very high quantum yield dyes, the enhancement in fluorescence is typically best approached through an increased rate of absorption.

Theoretical interpretations of metal enhanced fluorescence have been developing and recently, a radiating plasmon model has been proposed.[81] In this model, the non-radiative decay occurs from the excited state of the fluorophore to the surface plasmons. These surface plasmon electrons radiate to the surroundings with the photophysical characteristics of the coupling fluorophore. A key potential application of the metal enhanced fluorescence is mainly in the field of biotechnology including the detection of labeled proteins.[81]
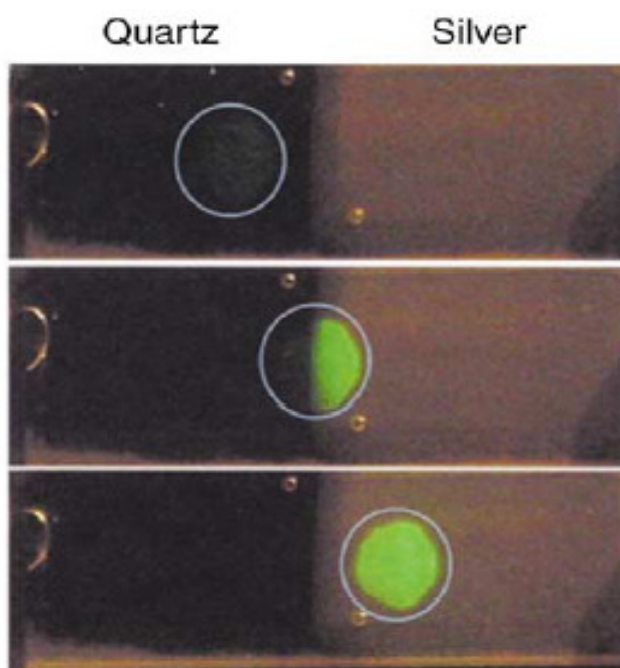
Fig. 1.9: Fluorescence enhancement from Fluorescein isothiocyanate (FITC) -labeled human serum albumin on quartz and silver films. The green colour shows the metal enhanced emission from labelled protein on the metal surface. *Taken from Aslan et al., Curr. Opin. Biotechnol., 2005, 16, 55.*[81]

For example, Aslan et al. has demonstrated metal enhanced fluorescence from fluorescein isothiocyanate labeled human serum albumin (FITC-labeled HSA) using silver films.[81] FITC-labelled HSA (250 μl, 10 μM) in 0.1 M PBS was deposited on each quartz slide and placed in a humid chamber at 5 °C overnight. Then, the slides were washed with 0.1 M buffer before the measurement. The amount of bound HSA on quartz substrate was estimated using absorption spectra. The size of the silver

nanoparticles was between 30-40 nm. The enhancement in fluorescence signal intensity was 17 times larger from the fluorescein labeled serum albumin in the presence of silver films compared to the protein on glass alone. The difference in intensity of labeled serum albumin on the silver films and on quartz is shown in Figure 1.9. As fluorescein is prone to self-quenching, which arises from Förster resonance energy transfer between adjacent fluorescein molecules, the origin of the large enhancement was attributed to the decrease in self-quenching of the fluorophore due to the increased rate of radiative decay.

Most metal enhanced fluorescence studies have focussed on roughened nanoparticulate surfaces although very recently studies have been undertaken on cavity structures. For example, Sugawara and co-workers have reported the coupling of localized surface plasmons and organic excitons in metal nanocavities.[82] They demonstrated an enhancement in fluorescence intensity from solid deposits of an organic dye (Figure 1.10 (A)), which forms a J-aggregate, on 600 nm diameter gold nanocavities at different thicknesses (t = 0.29 and t = 1.00).
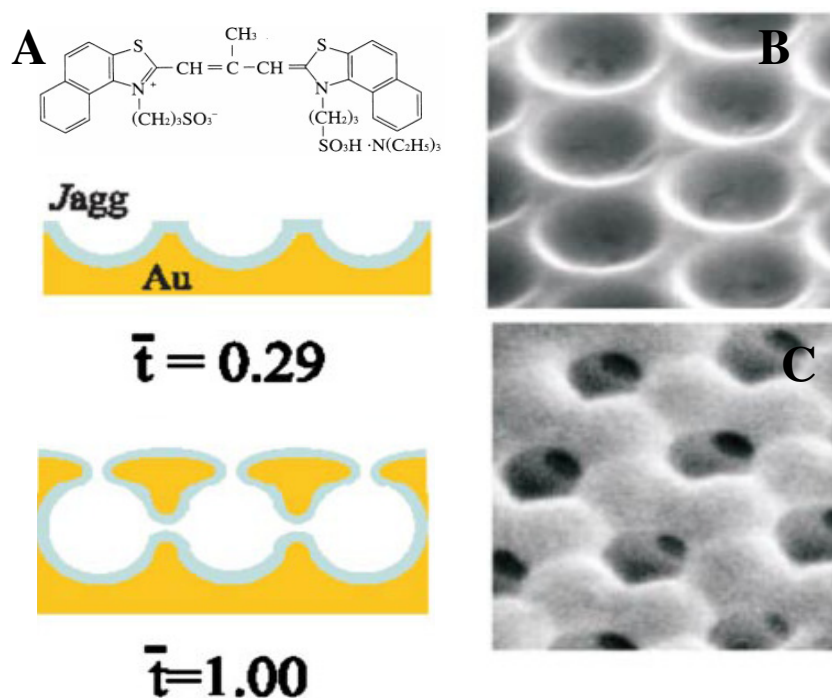
Fig. 1.10: (A) Chemical structure of an organic dye, which forms J-aggregate. (B) and (C) show SEM images of 600 nm diameter gold nanocavity array at different thickness, t =0.29 and t = 1.00 respectively. *Taken from Sugawara et al., Phys. Rev. Lett., 2006, 97, 266808.* [82]

Figure 1.10 (B) and (C) show the SEM images of 600 nm diameter gold nanocavity arrays at t = 0.29 and t = 1.00 respectively. The report revealed that both Mie and Bragg plasmons inside the gold cavity can couple with J-aggregate excitons but the enhancement of the Bragg modes was roughly 10 times greater than the Mie modes. The origin of this enhancement was attributed to the plasmon-coupled emission, which occurs due to the creation of excited localized surface plasmons, by excited fluorophore. Furthermore, angle dependent fluorescence studies were carried out using the gold nanocavities and they reported that the Mie Plasmon modes were not affected by angle. In the context of this thesis, the enhancement in emission intensity from molecules adsorbed on gold nanocavity arrays is important in order to create a sensitive biomimetic platform for the study of labeled proteins.

Ruthenium polypyridyl complexes

Most of the research on metal enhanced fluorescence is focussed on fluorescent dyes predominantly organic molecules as they have been widely used to label biomolecules. However, recently long-lived luminescent dyes showed great promise in labelling biomolecules due to their large Stoke shift and its interesting photophysical properties.[83,84]
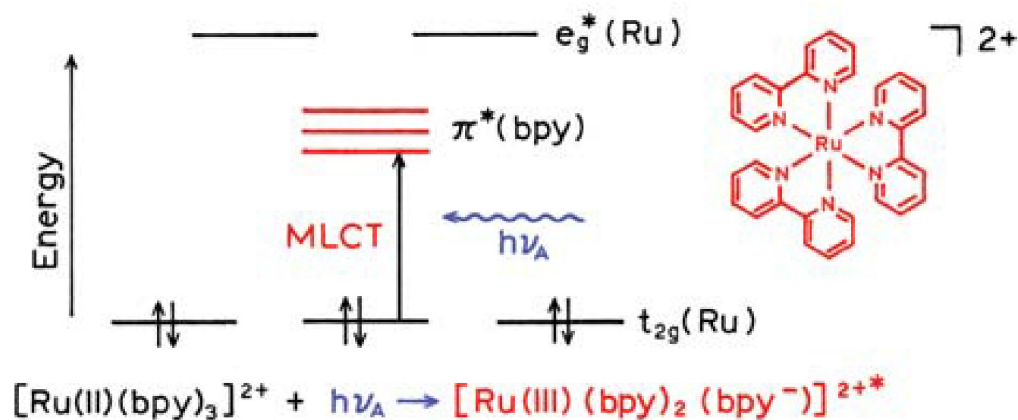
Fig.1.11: Metal-to-ligand charge transfer transition (MLCT) in $[Ru(bpy)_3]^{2+}$ complex. The chemical structure of $[Ru(bpy)_3]^{2+}$ complex is shown in right hand side. The presence of ligands splits metal d-orbital energy levels into two energy levels (three t_{2g} and two e_g levels). Upon absorption of light an electron promoted from lower t_{2g} level of the metal to π^* orbital of the ligand. The equation shows the oxidized state of the metal and reduced state of the ligand after MLCT. *Taken from Lakowicz et al.*[74]

In particular, ruthenium polypyridyl complexes are interesting because of their potential applications such as solar energy conversion, [85 , 86] luminescent and electroluminescent sensors.[87] The photophysical properties of ruthenium polypyridyl compounds can be summarized using a Jablonski diagram as shown in Figure 1.11.[88] When $[Ru(bpy)_3]^{2+}$ is excited into its MLCT (Metal to ligand charge transition, approximately 450 nm), an electron is promoted from the metal based ground state to a π*-orbital of the 2,2'-bipyridyl legend. Following absorption, fast and efficient intersystem crossing occurs from the singlet-excited MLCT state to the triplet MLCT state. Several deactivation processes can occur from this triplet state, via either radiative or non-radiative pathways.
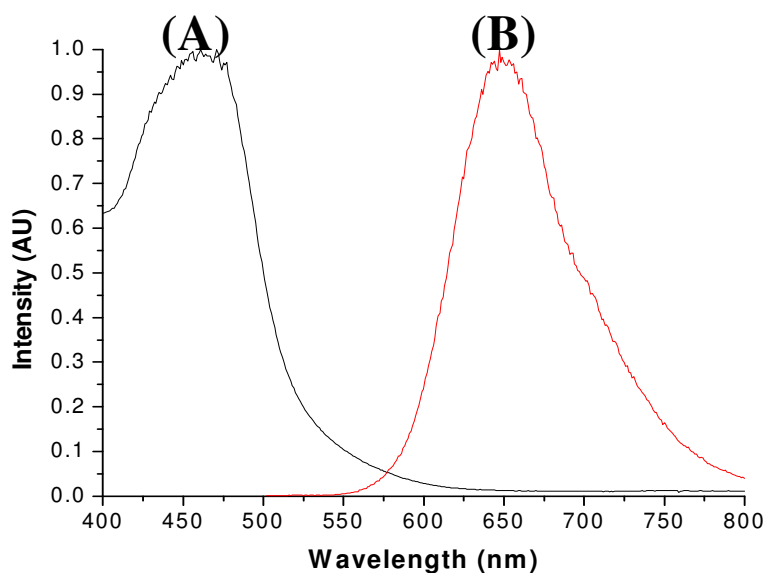
Fig. 1.12: (a) Absorption and (b) emission spectra of $[Ru(bpy)_2(Qbpy)]^{2+}$ in methanol (100 μM). The excitation wavelength for emission spectrum was 450 nm and the slit width was 5 nm. Both spectra were normalized to its maximum intensity value.

The optical properties of Ru (II) polypyridyl complexes can be altered by using different ligands and it is possible to tune the excited energy levels with different substituents on the ligand.[89] The ruthenium polypyridyl complex containing the quarterpyridyl ligand, $[Ru(bpy)_2(Qbpy)]^{2+}$ where bpy is 2,2'-bipyridyl and Qbpy is 2,2':4,4":4,4"-quarterpyridyl, is surface active. Its solution behaviour is similar to that of $[Ru(bpy)_3]^{2+}$ where it exhibits a metal to ligand charge transfer (MLCT) transition centred at 460 nm and a triplet MLCT emission centred at 650 nm, with a quantum yield of 0.078 and lifetime of 1418 ns in deaerated acetonitrile.[90] The UV-

visible absorption and emission spectra of $[Ru(bpy)_2(Qbpy)]^{2+}$ complex in 100 μM methanol is shown in Figure 1.12. In aerated methanol, the lifetime was recorded as 300 ns. This complex forms a stable self-assembled monolayer on gold or platinum over 48-hour assemblies from alcohol solutions. On a smooth gold surface, the luminescence of a monolayer of $[Ru(bpy)_2(Qbpy)]^{2+}$ was surprisingly, not significantly quenched by the metal and a biexponential lifetimes of 1.2 μs and 6 μs were recorded for the complex with broadening of the emission band, consistent with its incorporation into a rigid film[90] In this thesis, because of these properties $[Ru(bpy)_2(Qbpy)]^{2+}$ complex is used as a probe molecule in order to study the affect of gold nanocavity arrays on the photophysical properties of long-lived luminescent dyes.

1.5 Surface Enhanced Raman Spectroscopy (SERS)

Fluorescence spectroscopy can provide information about the dynamics of labelled molecules such as protein in cell membrane. In addition, metal enhanced fluorescence can increase the sensitivity of detection. However, information about the structural changes of the molecule is even difficult with the aid of metal enhanced fluorescence. Raman spectroscopy is a powerful tool for the identification and characterisation of molecules however, lack of sensitivity remains as one of the key limitations. Therefore, a special kind of enhancement effect should be required to boost the signal intensity such as resonance Raman, Surface enhanced Raman spectroscopy (SERS) or surface enhanced resonance Raman spectroscopy (SERRS).

When a light wave, which is considered as a propagating oscillating dipole, is incident on a molecule, it interacts with the electron clouds around the nuclei. That means, the incident light induces a polarization in the molecule and the energy is transferred from incident light to the molecule. This results in formation of a high energy form of the molecule with different electron geometry. The actual shape of the distorted electron geometry depends on the amount of light transferred to the molecule and therefore it depends on the frequency of the laser used. This high energy state is not stable and this energy is released as a form of scattered radiation. If the scattered photons have same energy as the incident light then the collision is called elastic scattering. In elastic scattering, the electron cloud relaxes without any nuclear movement. The inelastically scattered photons are lower or higher in energy than the incident photon, which are called Stokes scattering, and anti-Stokes scattering, respectively. A schematic representation of Rayleigh and Raman scattering is shown in Figure 1.13. The difference in energy of the inelastically scattered photons arises from different vibrational energy levels of the molecule before excitation. The energy difference between the initial and the final vibrational levels, $\Delta\upsilon$, is described by Equation 1.10

$$\Delta\upsilon \ = 1 \ / \ \lambda_{incident} - 1 \ / \ \lambda_{scattered} \qquad\qquad 1.10$$

where $\lambda_{incident}$ and $\lambda_{scattered}$ are the wavelength of the incident and inelastically or Raman scattered photons respectively.
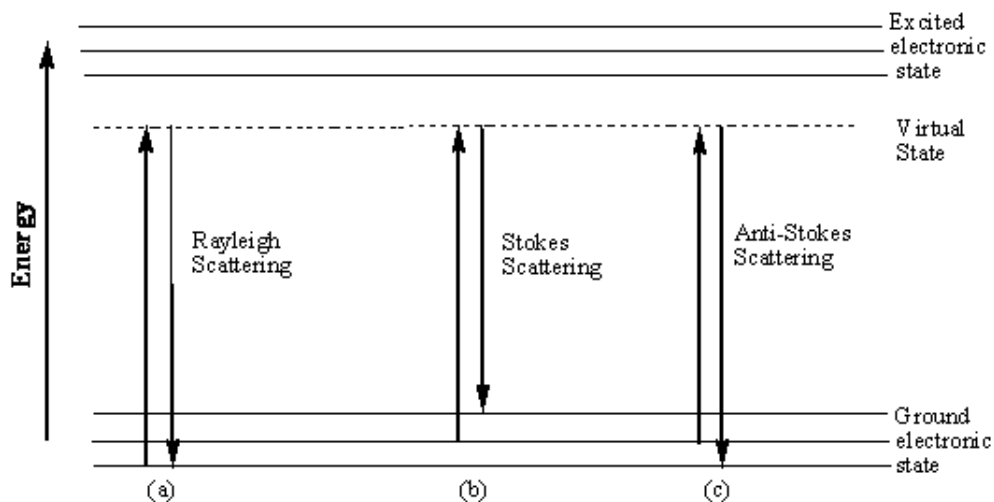
Fig. 1.13: Energy level diagram for Raman scattering: Incident light is scattered by molecules in different ways. (a) Rayleigh scattering, in which the wavelength of the scattered light is same as the incident light. (b) Stokes (c) anti-stokes Raman scattering - energy is lower and higher than the incident light.

In the scattering process, most of the photons are elastically scattered typically through Rayleigh scattering but a small fraction of photons (approximately 1 in 10^6 photons) are scattered inelastically. Therefore, as mentioned Raman is inherently a weak phenomenon.[91] To compensate this problem an intense laser source should be used for Raman measurements. However, bleaching of the sample can be a major issue at high incident laser power. In Raman microscopy, the light is focussed at the sample through an objective with high numerical aperture and the scattered light is collected by the same optical pathway. Then, the elastically scattered light is filtered out and then focussed through a pinhole to the CCD (charge-coupled devices) detector. There are a number of important ways to improve the sensitivity of the Raman measurement such as resonance Raman, surface enhanced Raman scattering (SERS), and surface enhanced resonance Raman scattering (SERRS). Both SERS and SERRS are applied to this thesis.

Resonance Raman occurs when the wavelength of the exciting laser is resonant with that of an electronic transition of a molecule, wherein the molecule is excited to one

of its excited electronic levels rather than virtual energy states in conventional Raman. Important advantages of the resonance Raman include enhanced sensitivity and selectivity. The selectivity arises because the vibrational modes associated with the chromophoric unit undergoing the electronic transition are selectively enhanced in resonance Raman. This selective enhancement of scattering from chromophoric vibrational modes also provides a useful means of identifying the location of the chromophores in complex systems.[92] For example, resonance Raman spectroscopy has found particular application in the study of biological macromolecules such as heme protein because only vibrations localized within the chromophoric group are enhanced when the exciting frequency approaches that of the relevant chromophore.[92] Sensitivity arises because resonance Raman gives several orders of magnitude in signal intensity compared to Raman spectroscopy.

SERS can help to increase the sensitivity of detection. Surface enhanced Raman scattering exploits localized field enhancement present at the metal surfaces for the amplification of the weak Raman signal. Several groups have fabricated SERS active substrates which can provide ultra-sensitive detection limits, including single molecule sensitivity.[93,94] SERS shows a great promise in over-coming the low sensitivity problems in Raman spectroscopy and the enhancement in Raman signal intensity has been regularly observed in the range of 10^4-10^6, and can be as high[95] as 10^8-10^{14}. However, a key issue in analytical applications is the reproducibility in the signal intensity both between substrates and across a single substrate.

Two types of mechanisms are generally accepted to give rise to SERS; chemical enhancement (CT) and electromagnetic enhancement (EM).[96] Electromagnetic enhancement is attributed to the coupling of the incident light and the re-emitted Raman field with the local plasmonic field on the metal surface as discussed earlier. The electric field of the surface plasmons must lie perpendicular to the surface in order to be scattering. Therefore, SERS is strongly dependent on the surface morphology and the shape of the roughness features at the metal surface. When incident light falls on a Raman-active molecule adsorbed at a roughened metal surface, the electromagnetic field induces a dipole within the molecule resulting in an enhanced Raman signal intensity. A theoretical study reported that the local electric field experienced by the molecule in the presence of nanostructured metal surfaces

can be enhanced by incident light by as much as 10^5 and the emission intensity radiated by a dipole can be high as 10^5. Therefore, theoretically the electromagnetic enhancement[73] contribution can be as high as 10^{10}.

Chemical enhancement can arise when the molecule is chemisorbed at a metal surface. Chemical enhancement applies to only species which have formed a chemical bond with the metal surfaces.[97] The chemical enhancement mechanism arises from changes to the polarizability of the molecule due to the formation of its surface complexes with the metal. The metal can act as a charge-transfer donor or acceptor, when the Fermi level of the metal fall within the HOMO and LUMO levels of adsorbate molecules. Chemical enhancement cannot explain the observed signal enhancement in all cases, but EM theory can explain the enhancement even from physisorbed species. Earlier studies have shown that the chemical enhancement can provide only one or two orders of magnitude while the EM enhancement is the primary contributor to the SERS.[97] In contrast, recently, Fromm et al. illustrated that the SERS signal intensity can be as high as 10^7 due to the chemical enhancement.[98] This enhancement is observed from p-mercaptoaniline (pMA) adsorbed on a single bowtie nanostructure and the enhancement was attributed to the charge transfer between the gold surface and the molecule. They reported that this chemical enhancement occurs due to the increased wave function mixing between π-orbitals in the benzene ring and Au when a pMA molecule lies down at the surface.

Several varieties of metal nanostructured surfaces have been studied as SERS platforms including nanoholes[99] and nanocavity arrays.[5] In this section of the thesis the enhancement in Raman signal intensity reported from different nanostructured surfaces is surveyed, focussing particularly on surface architectures.

Sackmann and co-workers reported an order of magnitude enhancement in Raman signal intensity from crystal violet (CV) molecules adsorbed on nanodot gold surfaces.[21] The nanodots were prepared on a silicon surface using electron beam lithography. Figure 1.14 (A) shows SEM image of the substrate and the inset shows the structure of crystal violet. Figure 1.14 (B) shows SERS from CV adsorbed on the nanostructured surface. The enhancement in Raman signal intensity was lower compared to electrochemically roughened electrodes. This decrease in enhancement

factor was attributed to the absence of surface roughness on nanodot structures. As discussed earlier, highly reproducible SERS substrates can be fabricated using electron-beam lithographic techniques, however, this is an expensive technique.
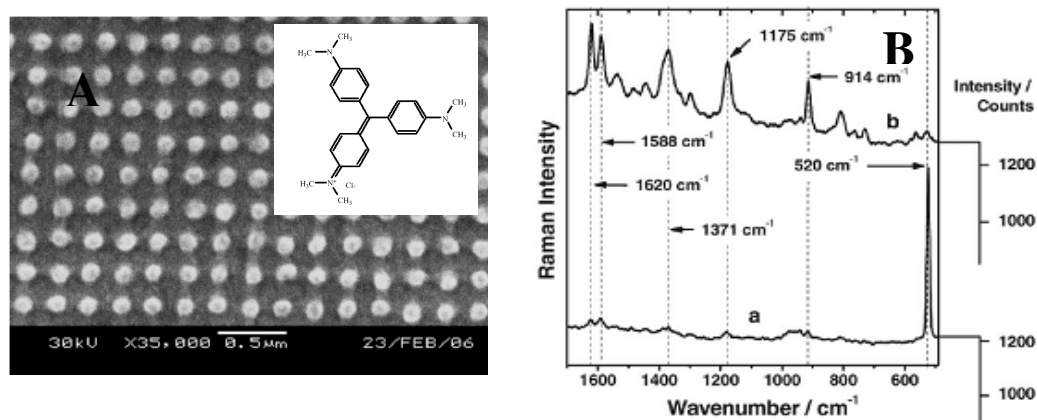
Fig. 1.14: (A) SEM image of the gold nanostructure produced by electron beam lithography. The distance between two nanodots is 240±5 nm, diameter is 125± 5 nm and the height is approximately 25 nm. The inset shows the structure of crystal violet. (B) Raman spectra of crystal violet on (a) pure silicon surface (b) gold nanostructures. *Taken from Sackmann et al., J. Raman Spectrosc., 2007, 38, 277.*[21]

Brolo et al. reported surface enhanced Raman scattering from oxazine 720 dye adsorbed on nanohole arrays.[99] The nanohole arrays were fabricated using focussed ion beam milling and the SEM images of the arrays are shown in Figure 1.2. The structure of the dye is shown in inset of Figure 1.15. They reported an enhancement factor of approximately 2 x 10^5 for the oxazine molecules adsorbed at gold nanohole arrays. The observed enhancement was attributed to the combination of surface plasmon resonance from the nanoholes and the internal electronic resonances from the adsorbed molecules. The Raman signal intensity observed from rhodamine 6G and pyridine molecules adsorbed on the same nanohole arrays, the signal intensity in each case was very weak indicating that internal electronic resonance, as in the resonance Raman, is required to get a strong Raman signal from these nanoholes. Therefore, only some molecules can be studied using this array after tuning the surface plasmon resonance into their molecular electronic bands.
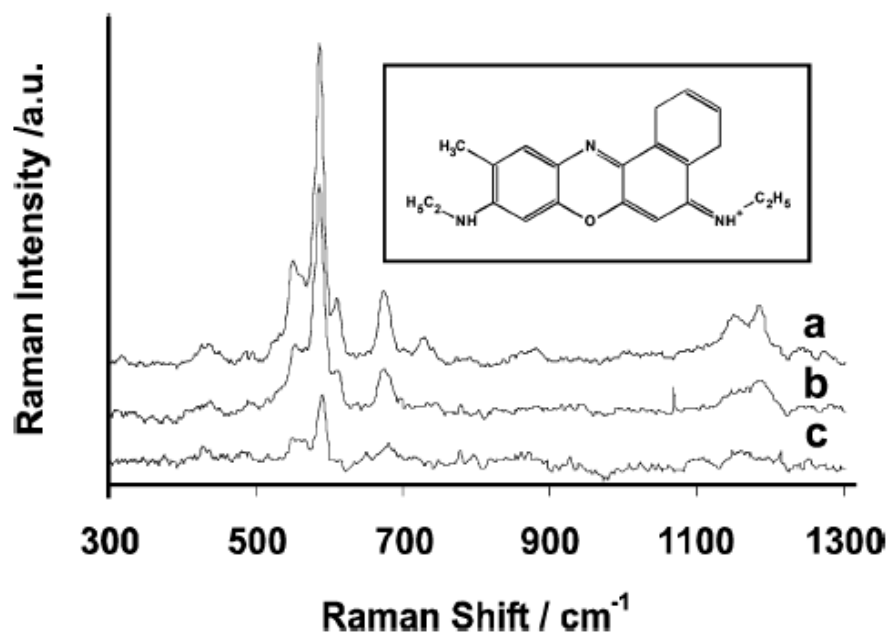
Fig. 1.15: Enhanced Raman scattering from oxazine adsorbed on nanohole array with different periodicities (a) 560 nm (b) 590 nm (c) 620 nm. The inset shows the structure of the oxazine molecule. *Taken from Brolo et al., Nano Lett., 2004, 4, 2015.*[99]

Mahajan and co-workers reported SERS from benzenethiol adsorbed on spherical nanovoid structures.[100] The gold nanocavity arrays were fabricated by electrodeposition of gold through the interstitial voids of self-assembled polystyrene spheres. They fabricated the arrays with different diameters and thicknesses using this technique. The SEM images of 900 nm diameter arrays with different thicknesses ((a) 0.25 D; (b) 0.45 D; (c) 0.7 D and (d) 0.9 D) are shown in Figure 1.16 (A). The thickness of the arrays was monitored by the charge passed through the electrochemical cell during deposition. The arrays with different diameters were prepared by retracting the electrode from the plating solution using a micrometer stage. The arrays were treated with benzene thiol solution for 24 h. to form monolayers on the arrays. Figure 1.16 (B) shows the SERS observed from the benzene thiol adsorbed on 900 nm diameter arrays under 1064 nm excitation. Systematic analysis of the height dependence of SERS enhancement on 900 nm diameter arrays showed that the greatest enhancement was obtained for the film with
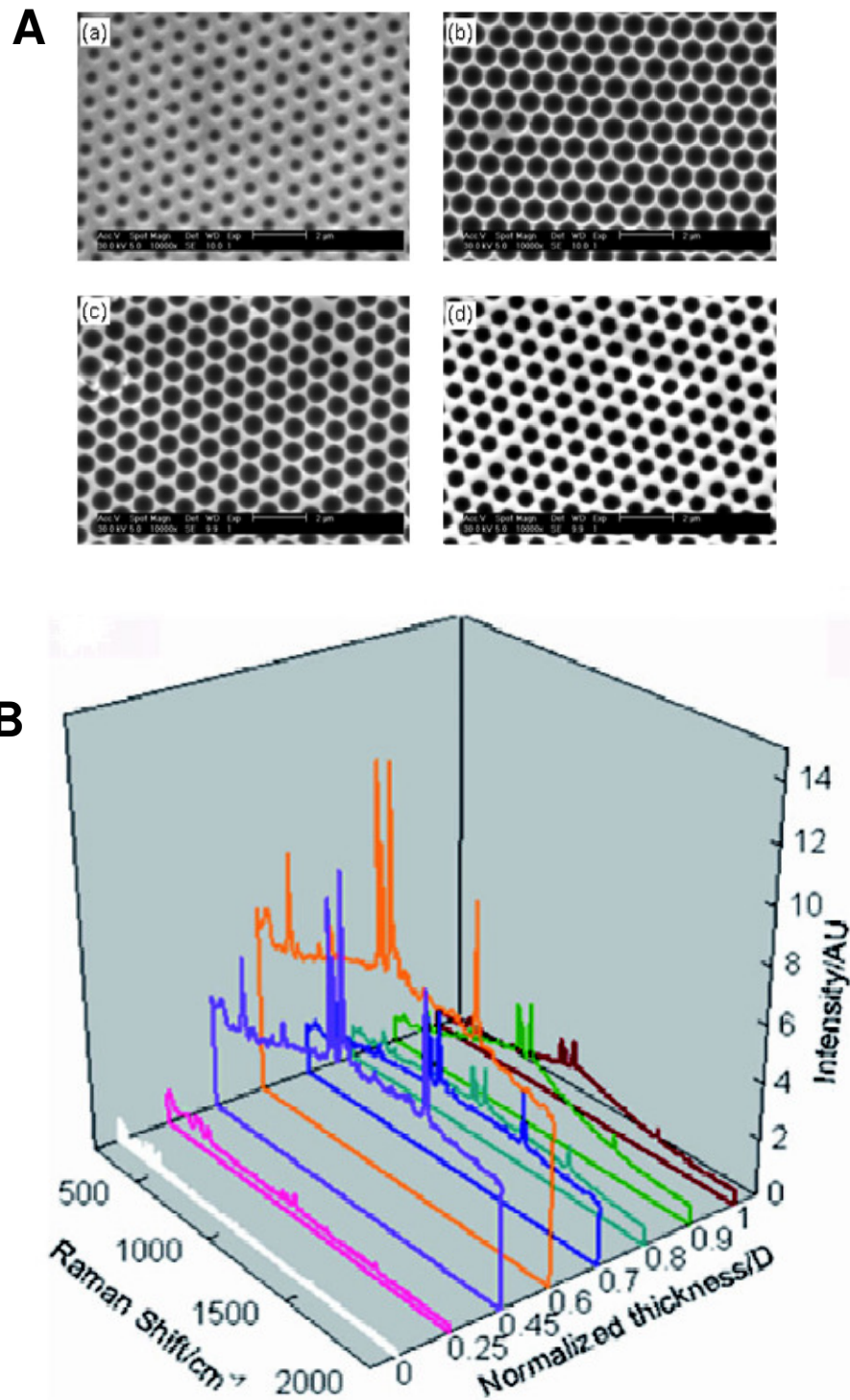
Fig. 1.16: (A) SEM image of gold film fabricated using 900 nm diameter sphere templates recorded at various film thickness of (a) 0.25 D; (b) 0.45 D; (c) 0.7 D and (d) 0.9 D. (B) Raman spectra of benzene thiol adsorbed on 900 nm sphere templated gold films. *Taken from Mahajan et al., Phys. Chem. Chem. Phys., 2007, 9, 104.*[100]

a thickness ~ 0.6 D. The enhancement factor reported was approximately 3×10^6 from a monolayer of benzenethiol adsorbed on the gold nanocavity arrays. It was found that the maximum enhancement occurs when both the ingoing (incident laser) and outcoming radiation (scattered radiation) resonates with the surface plasmons on the substrate.

Cintra et al. also reported a systematic study on the diameter and thickness dependence of enhancement in Raman signal intensity from the gold cavity array using benzene thiol.[101] The greatest SERS intensity was observed for gold nanocavity arrays prepared using 350 nm diameter spheres grown to a thickness of 140 nm as shown in Figure 1.17. The excitation wavelength was 633 nm. It is interesting to note that the greater enhancement in Raman signal intensity from benzene thiol adsorbed on gold nanocavity arrays arises when the film is grown to a thickness in between 0.4-0.6 D. They attributed the enhancement in Raman signal intensity to the localized surface plasmons present at the metal surface.

Kelf and co-workers have also investigated the presence of different surface plasmon modes on the gold nanocavity arrays with different thickness.[102] These detailed studies on surface plasmon modes revealed the presence of both delocalized and localized surface plasmon modes, Bragg and Mie plasmons respectively, on the gold nanocavity arrays. For thinner gold nanocavity arrays the Bragg plasmons are proposed to couple with Mie modes to create new mixed states. As the thickness increases over hemispherical voids, the rim of the cavity breaks into triangles that prevent the propagation of plasmon modes. As a result, the thicker gold nanocavity arrays are thought to support mainly the localized Mie plasmons at the metal surface.
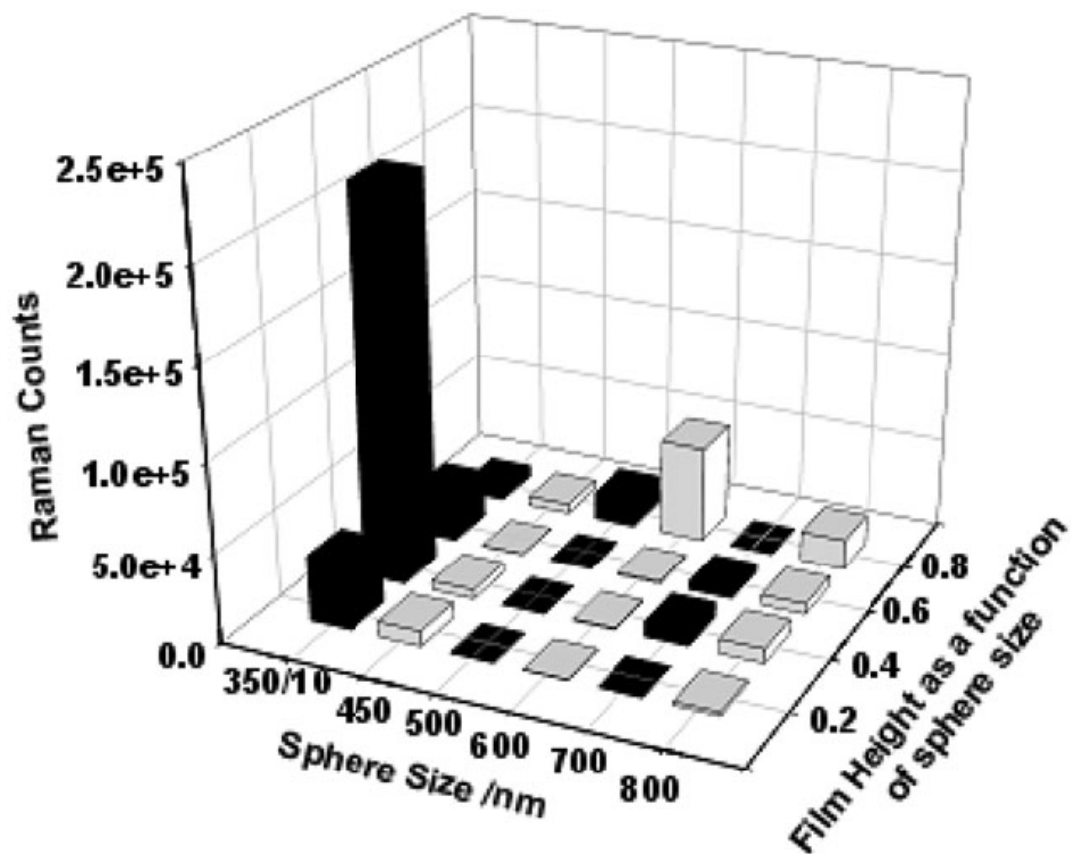
Fig. 1.17: SERS intensity (1571 cm^{-1} band) spectrum of thiol adsorbed on gold nanocavity as a function of film thickness and sphere diameter. *Taken from Cintra et al., Faraday Discuss., 2006, 132, 191.*[101]

1.6 Surface Enhanced Resonance Raman Spectroscopy (SERRS)

SERRS is a powerful analytical tool as it combines the effect of both surface enhancement (SERS) and molecular resonance enhancement. SERRS has been shown to enhance Raman signal intensity as high as 10^{14}, which makes the Raman spectroscopy technique more sensitive up to single molecule detection.[95] The signals obtained from SERRS resemble those of resonance Raman but with a huge increase in intensity.[44] In this thesis, SERRS from gold nanocavity arrays are investigated using a surface-active luminophore ruthenium dye. Recently, Mahajan and co-workers have reported SERRS from gold nanocavity arrays using an organic fluorophore.[44] They recorded SERRS from Cy5 molecules immobilized on 600 nm diameter gold nanocavity arrays. The excitation wavelength used was 633 nm, therefore, only Cy5 was resonant to the excitation laser line and SERS was expected from Cy3 (λ_{exc}~549 nm). SERRS from Cy5 and SERS from Cy3 recorded from gold nanocavity arrays are shown in Figure 1.18. The spectra are shown without background subtraction but both spectra were normalized for laser power and collection time. An enhancement factor of 1.6×10^{8} for Cy5 was reported after comparing to conventional Raman of Cy3 molecules. This huge enhancement in resonance Raman signal intensity from the gold nanocavity arrays has wide potential in highly sensitive measurements particularly for studying labelled biomolecules. The study of labelled biomolecules on biomimetic platform is a part of the long-term objective of the project.
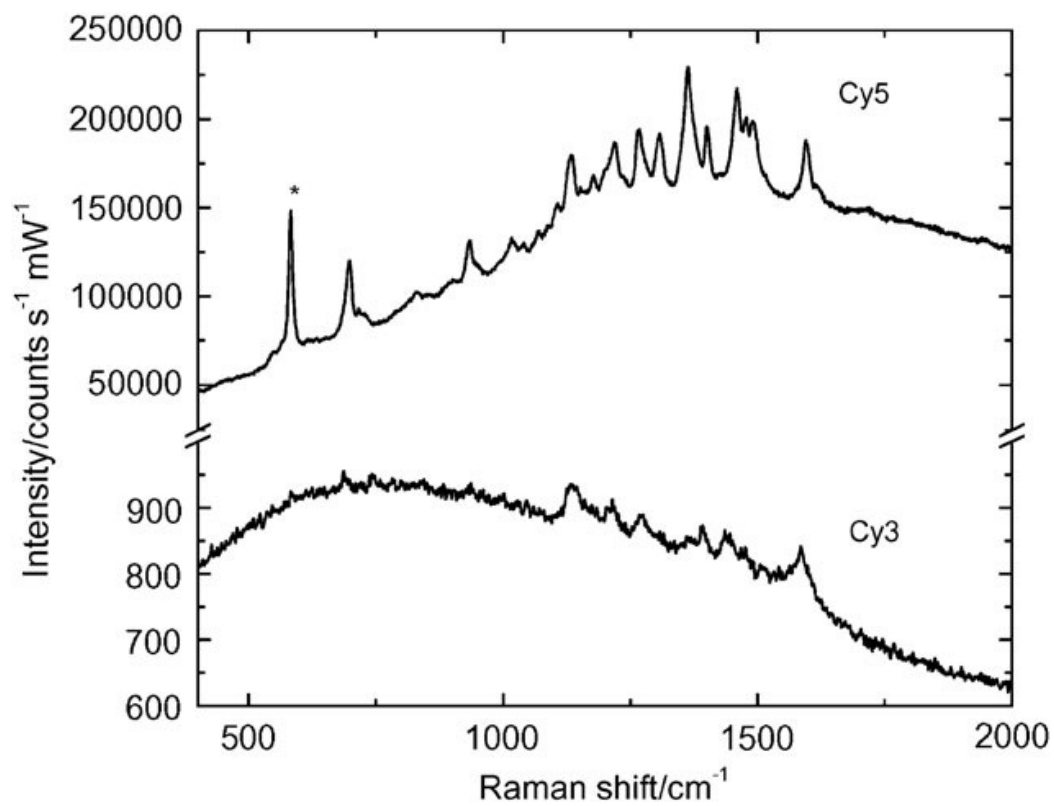
Fig. 1.18: SERRS spectrum of Cy5 and SERS spectrum of Cy3 recorded from 600 nm diameter gold nanocavity arrays. The excitation wavelength was 633 nm. *Taken from Mahajan et al., Phys. Chem. Chem. Phys., 2007, 9, 6016.*[44]

1.7 Locating the Region of optimal plasmonic enhancement

Several groups have reported enhancement of both Raman and fluorescence signal intensity from a variety of nanostructured metal surfaces.[11,80,99] The enhancement in signal intensity is not homogeneous across the various surface morphologies. Typically, there are some regions that can contribute greater enhancement in signal intensity due to the localization of electric field on the nanostructured surfaces. These localized regions with intense plasmonic fields referred to as "hot spots". In order to achieve the optimum enhancement from the nanostructured metal surfaces, it is crucial to identify the location of the electric field and significant theoretical and experimental effort has been invested in assessing this hot spots.[103,104] For example, the distribution of electric field around a metal nanoparticle calculated using computational electrodynamics method is shown in Figure 1.19.[103] It can be seen that the electric field around the sphere is not uniform. In addition, it has been predicted and demonstrated that the field distribution around the metal nanoparticle depends on the size and shape of the particle.[103]
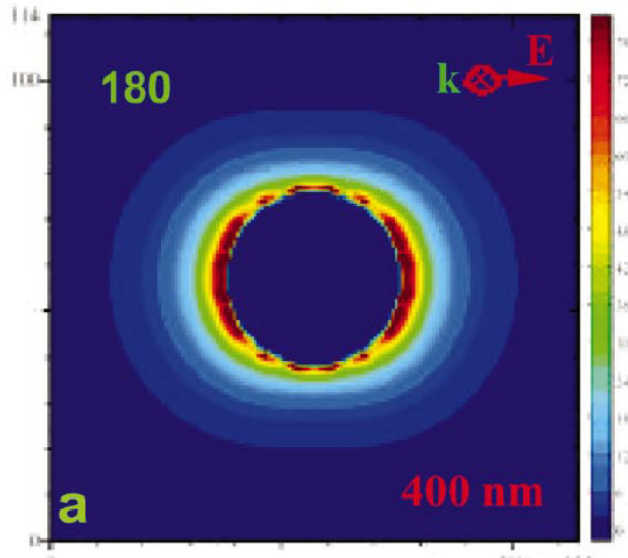
Fig. 1.19: Electric field enhancement on spherical silver nanoparticle (radii = 19 nm) calculated using computational electrodynamics methods. *Taken from Hao et al., J. Fluoresc., 2004, 14, 331.*[103]

Hot spots are believed to form at the junction between plasmonically coupled metal particles or at fractal island films. Van Duyne et al. have fabricated silver nanotriangles using nanosphere lithography followed by thermal evaporation of

metal.[105] They demonstrated that most of the surface on the triangle exhibits a small induced electric field but the edges of the triangle shows approximately 12000 times greater field than the incident light. In fact, the enhancement in Raman signal intensity seems mainly to arise from these spots at the sharp tip of the triangles.

Moerner and co-workers have conducted significant investigations into hot spots at triangles and they found that the enhancement of both Raman and fluorescence signals from molecules in the gap between gold bowtie nanostructures.[106] They fabricated bowtie structures using electron beam lithography with ≤ 20 nm gaps between the triangles. The structure and the calculated local electric field intensity are shown in Figure 1.20. SERS from these bowtie structures were studied using a monolayer of p-mercaptoaniline (pMA). As discussed earlier, they observed an enhancement of $>10^7$ from pMA molecule on the single bowtie nanoantennas which they attributed to chemical enhancement. Fluorescence enhancement from these structures was also studied using a TPQDI dye (N,N'-bis(2,6-diisopropylphenyl)-1,6,11,16-tetra-[4-(1,1,3,3-tetramethylbutyl)phenoxy]quaterrylene- 3,4:13,14-bis(dicarboximide)) as luminophore. The molecular structure of TPQDI dye is shown in Figure 1.20 (B). The enhancement in fluorescence signal was studied as a function of gap size between the triangles.
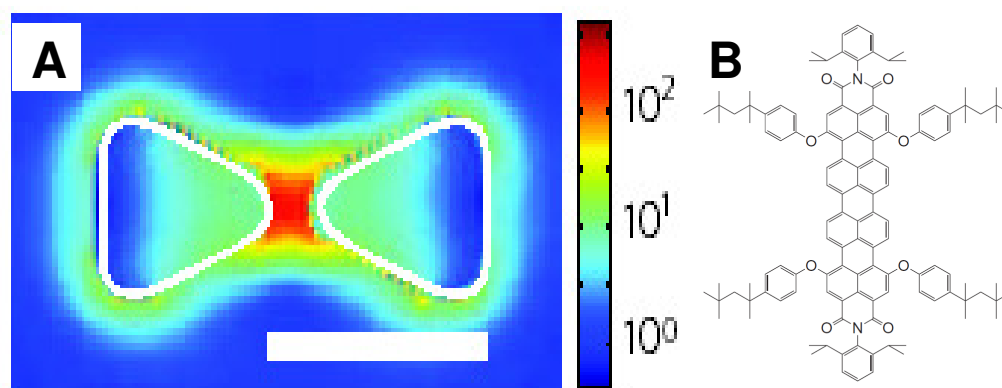
Fig.1.20: (A) Finite-difference time-domain calculation of local intensity enhancement from bowtie structures. Scale bar is 100 nm. (B) Molecular structure of TPQDI dye (N,N'-bis(2,6-diisopropylphenyl)- 1,6,11,16-tetra-[4-(1,1,3,3-tetramethylbutyl) phenoxy]quaterrylene- 3,4:13,14-bis(dicarboximide)). *Taken from Moerner et al., J. Chem. Phys., 2006, 124, 061101.*[98]

The study revealed that the bowtie structures with smallest gaps provide the greatest enhancement, which indicates the presence of stronger local field strength at the smallest gaps (~10 nm) compared to larger gaps between the nanotriangles. Moerner et al. reported enhancement in fluorescence signal up to 1340 times from a single molecule on these bowtie nanoantennas. Theoretical calculations reveal that the enhancement in fluorescence signal intensity is due to both greatly enhanced absorption and increased radiative rate. In order to elucidate the location of plasmonic enhancement and extent of coupling of so-called Mie-Bragg plasmons, Cole and co-workers were prepared gold–nickel hybrid structures using templated electrochemical deposition.[107,108] These hybrid structures allowed the rim plasmon and void plasmon modes to be separately identified. The results showed that the gold nanocavity with a nickel rim show very weak Raman signal intensity, whereas the nickel cavity with gold rim and gold only cavity show greatest enhancement in Raman signal intensity. In summary, they reported that the rim of the gold nanocavity arrays shows strongest enhancement in Raman signal intensity than the void modes.

Dreier and co-workers reported the electric field distribution around gold nanocavities with different packing densities.[109] The fabrication of gold nanocavity arrays was achieved using a number of methods including colloidal lithography, template stripping process and plasma etching. The SEM images of the gold nanocavities made using this technique are shown in Figure 1.21. The SEM images show the difference in packing density of 100 nm diameter gold cavity arrays. The gold nanocavity arrays were 40 nm thick and the calculated field distribution in the arrays are shown in Figure 1.21 E. A theoretical study revealed that in gold nanocavity arrays, the electric field is concentrated at the rim of the array which is consistent with Bartlett's experimental results obtained using hybrid metal structures.[108] In this thesis, the location of enhancement from the gold nanocavity arrays was carried out using a selective modification method by exploiting interfacial self-assembly.
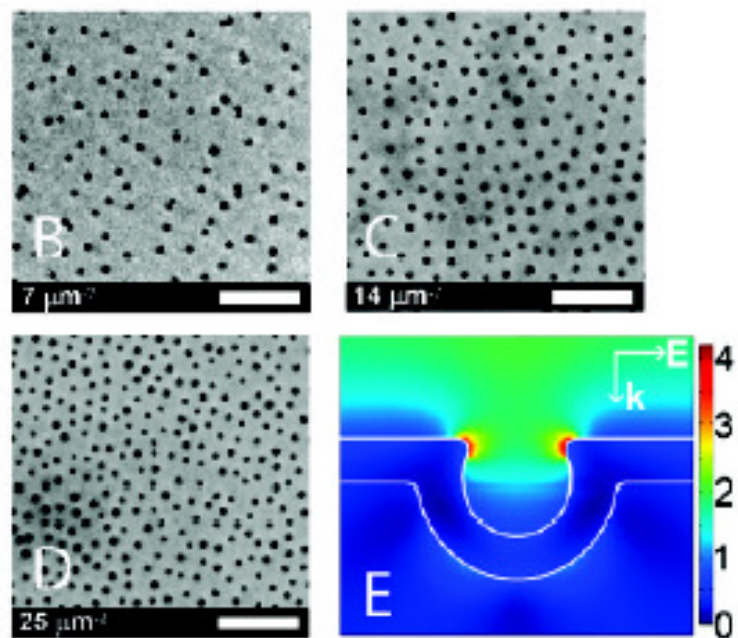
Fig. 1.21: SEM images of gold nanocavity arrays with different packing density. (E) Simulation of electric field distribution in a cross section through the spherical cavity with an inner diameter of 100 nm imprinted in a gold film with 40 nm thickness. The color bar shows the enhancement factor of the electric field. *Taken from Dreier et al., Phys. Chem. Lett., 2010, 1, 260.*[109]

1.8 Interfacial Self-assembly

In this thesis, interfacial self-assembly is a key tool exploited to create selectively modified arrays and to study plasmonic enhancement on luminescence and Raman signal. Furthermore, self-assembly of polystyrene spheres play a vital role in fabricating ordered gold nanocavity arrays. The self-assembly of molecules such as thiol or pyridine is used to investigate the enhancement properties of gold nanocavity arrays. In addition, self-assembly of lipid bilayers at the interface of gold nanocavity arrays play a significant role in the fabrication of biomimetic platform.

Interfacial assemblies can be formed on substrates in number of ways including self-assembly, spontaneous adsorption, spin coating, and dip coating. Well-defined, ordered interfacial assemblies of molecules can be achieved by using spontaneous adsorption and self-assembly.[110] Both self-assembly and spontaneous adsorption create monolayers on substrates with the formation of strong bond between the active group and the substrate. However, in self-assembly stabilizing lateral interactions occurs between adsorbates after the surface bond formation resulting often a highly ordered, close packed array. For example, thiols or pyridine spontaneously forms strong covalent bonds with metals such as gold, platinum, copper and silver. Following this adsorption, the adsorbate reorients to achieve a stable assembly organized through lateral non-covalent bonding interactions. The structure and packing density of the monolayer depend critically on the nature of the substrates. The surface properties such as reactivity and hydrophobicity can be controlled using self-assembly of thiol terminated carboxylic acid and amine esters.[110] The attractive feature of the self-assembly is that it does not require special conditions such as vacuum or anhydrous environment.

Self-assembled monolayers (SAMs) of colloidal particles have also attracted extensive interest due to their wide variety of applications ranging from photonics to sensors.[111,112] Self- assembly of nanospheres occurs when the nanospheres interact with one another through a balance of weak attractive and repulsive interactions. However, in such systems Brownian motion becomes irrelevant and gravity and friction becomes important due to the difference in the mobility of the components. Self-assembly of colloidal nanospheres provides a convenient, flexible and

inexpensive route for the fabrication of three-dimensional photonic crystal architectures. For instance, commercially available polystyrene spheres spontaneously form self-assembled monolayers on different substrates from particle suspension.[5] Nanoparticles have a strong tendency to aggregate due to Van der Waals interactions. Generally, this tendency can be overcome by inducing repulsive forces between the particles to balance attractive force.[113] Generally, two types of stabilization occur, electrostatic stabilization and steric stabilization as shown in Figure 1.22.[114] Electrostatic stabilization involves the creation of an electrical double layer arising from the ions adsorbed on the surface and the associated counter ions that surround the particles. Steric stabilization can be achieved by adsorption of large molecules such as polymer on the surface of nanoparticles, and the length of the polymer chain should be larger than the range over which the attraction forces between the colloidal particles are active.
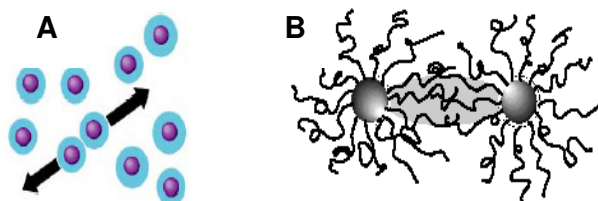
Fig. 1.22: Particles in colloid (A) charged particles repelled each other. (B) Steric stabilization of metal colloid particles by polymers. *Taken from Bossel et al., Mater. Sci. Eng. A, 1995, 204, 107.*[114]

One of the most common surface modification assemblies is the adsorption of alkane thiol on gold. In this thesis, the self-assembly of cysteamine is used to modify the surface properties of a smooth gold substrate, in which the cysteamine is covalently attached to the gold substrate by a strong Au-S bond. Moreover, the self-assembly of alkane thiol is used here for the selective modification of top surface and interior walls of gold nanocavity arrays. Since gold has a particular affinity for sulphur groups, it adsorbs alkane thiols easily and forms ordered assemblies. Bare surfaces of metals and metal oxides tend to adsorb organic materials readily because this adsorbate lowers the free energy of the interface between the metal and the ambient environment.[115] The gold-sulphur bond energy is approximately 45 kcal.mol^{-1} which forms a semi-covalent bond (Bond strength of C-C is 83 kcal.mol^{-1}). The van der Waals forces between the methylene head groups in the alkanethiol causes tilting of

alkanethiol chain in order to minimize the surface energy. Figure 1.23 shows an example for supra-molecular self-assembled monolayers of thiol on gold. SAMs have been used in wide range of area from molecular electronics to biological arrays.[116]
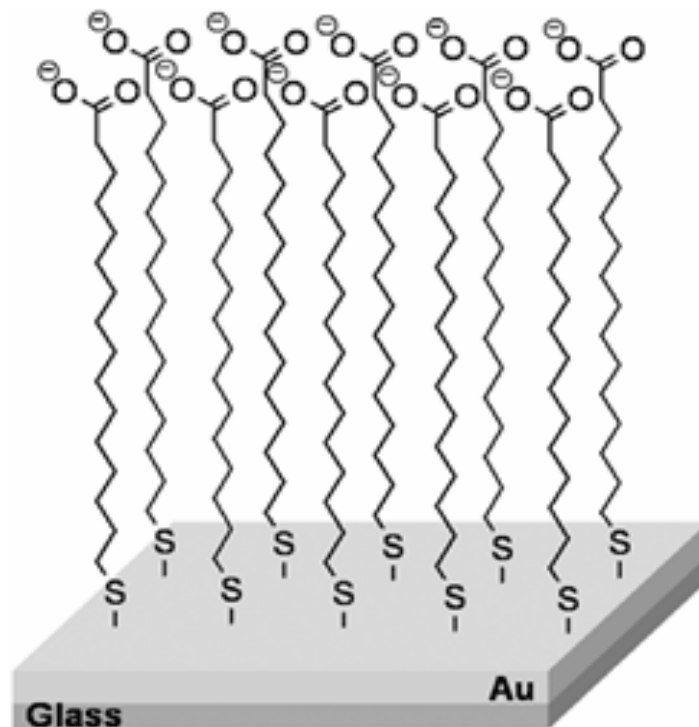
Fig. 1.23: Self-assembled monolayers of thiol formed on a gold substrate.

It is widely accepted that, pyridine forms self-assembled monolayers on several metal surfaces especially on, gold, silver and platinum. For example, the surface enhanced Raman scattering was first reported from self-assembled monolayers of pyridine on an electrochemically roughened silver substrate. Recently, Qbpy (2,2':4,4":4'4" - quarterpyridyl) ligand has been used as a surface binding group and the studies have shown that this ligand strongly binds to metal surfaces through the nitrogen lone pair.[90] The photophysical and electrochemical properties of monolayers of ruthenium and osmium complexes were systematically studied after immobilising the molecules by self-assembly on electrodes.[90] In this thesis, the plasmonic properties of the gold nanocavity arrays were investigated using self-assembled monolayers of $[Ru(bpy)_2(Qbpy)]^{2+}$ in which the free nitrogen on the Qbpy ligand forms a strong covalent bond with gold. In addition, the identification of location of enhancement is achieved using selective self-assembly of dye or thiol on the top surface and interior walls of the arrays.

1.9 Biomembranes

As shown in Scheme 1.1, a key objective of this thesis is to assemble lipid bilayer at the top surface in order to provide a platform for studying the dynamics of transmembrane proteins. Biological membranes play a vital role in cell life.[117] The cell membrane acts as a selective barrier across which transport of species into the cell and the toxic compounds out of the cell occurs. The cell membrane is composed of lipids, proteins and carbohydrates. The lipid components of biological membranes are principally phospholipids.[118,119] The phospholipids have fatty acyl chains, which are esterified to glycerol and possess a charged head group. Phosphatidylcholine (PC) is the most abundant phospholipid found in animal cells.

The fluid mosaic model introduced by Singer and Nicholson remains the most broadly accepted model of the biological membrane.[120] According to this model, the cell membrane mainly consists of lipids and proteins, in which the proteins are inserted into this 2-D solvent made up of lipids as shown in Figure 1.24. The phospholipids are arranged as bilayer with their polar part in contact with water. The thick lines represent the folded polypeptide chains of integral proteins, which are partially or completely embedded in the membrane depending on the size and structure of the molecule. The ionic residues or polar part (+ or -) of the protein protrude from the membrane and the non-polar parts are embedded in the hydrophobic part of the membrane. There are mainly two types of proteins found in membranes: peripheral and integral proteins. Peripheral proteins are dissociated from lipids when the membranes are washed with different concentrations of buffer solution. Whereas, the integral proteins remain associated with the membrane after the removal of the peripheral proteins, which suggests that the integral proteins are associated with the hydrophobic part of the bilayer. The distribution of the membrane proteins in the membrane depends on the orientation of lipids in the bilayer. This model has been used to explain the formation of pores and channels in the membrane and can explain the two-dimensional diffusion of proteins in the lipid bilayer.
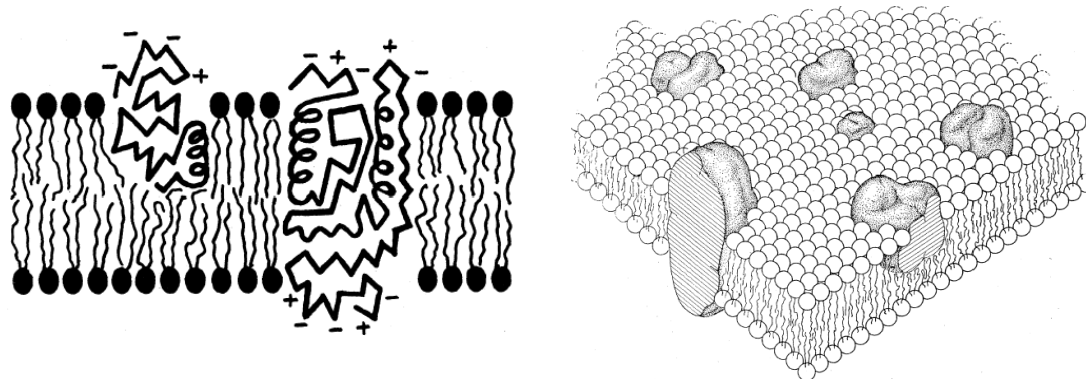
Fig. 1.24: The 'fluid mosaic model' proposed by Singer and Nicholson. Schematic 2-dimensional and 3-dimentional views of biomembrane. The phospholipids are arranged as a bilayer with their polar part in contact with water. The thick lines represent the folded polypeptide chains of integral proteins, which are partially or completely embedded in the membrane depending on the size and structure of the molecule. The ionic residues or polar part (+ or -) of the protein protruding from the membrane and the non-polar part embedded in the hydrophobic part of the membrane. *Taken from Singer et al., Science, 1972, 175, 720.*[120]

The structure of common types of lipids is shown in Figure 1.25. The binding forces behind the bilayer structure of lipids are mainly non-covalent hydrophobic and hydrophilic interactions. The non-polar part of the lipid is sequestered away from the aqueous phase, whereas the charged groups of the phospholipids are oriented so they are in direct contact with water at the exterior surface. In this membrane structure, both hydrophobic and hydrophilic interactions are maximized to attain the lowest free energy state in the aqueous environment. Most lipids exist in a bilayer structure in contact with aqueous solution as explained by Gorter and Grendel due to hydrophobic effects.[121] There has been significant interest in the preparation of planar lipid bilayers, which incorporate with proteins to understand the fundamental function of transmembrane proteins without the complexity of the cell membrane resulting in a variety of membrane models. The earliest bilayer model developed was the black lipid membrane (BLM) which was achieved by painting the lipid onto the support. The name originates from the appearance of the membrane in optical microscopy. In 1962, Mueller et al. developed the first artificial lipid bilayer across a 1 mm hole between two teflon solution chambers.[122] The lipid was dissolved in organic solvent and applied across the aperture using a brush. Generally, the capacitance of a typical biomembrane is in the range of 0.5-1.3 $\mu F/cm^2$.[123] The initial characterisation of the BLM showed a capacitance of 2 $\mu F/cm^2$. Later, Montal and Mueller prepared black

lipid membranes from monolayers of lipid at a water/air interface.[124] They divided a Teflon cup into two compartments by a wall with a hole. The compartments were filled with water and the level of the water kept below the hole before the experiment. Then, the lipids dissolved in chloroform were introduced onto the surface of water in both compartments and the level of the water was increased slowly after the evaporation of chloroform. The main advantage of these black lipid membranes was the presence of an aqueous phase at both interfaces of the membrane. The incorporation of channel formers and receptors improved the ion transport properties of lipid bilayers, which showed properties close to that of biomembranes. However, the stability of these black lipid membranes was poor, and also it was difficult to access the membrane to study using different techniques other than electrochemistry.[125]
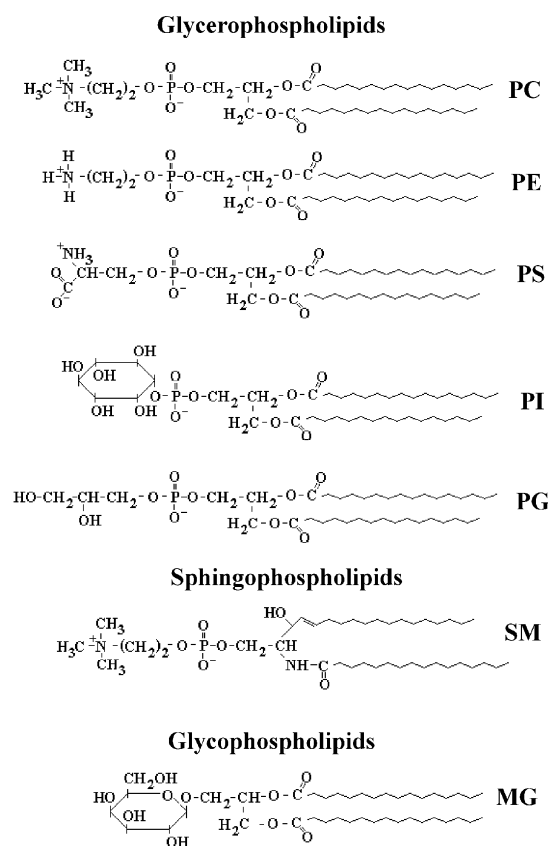
Fig.1.25: Structure of different lipids. PC - Phosphatidylcholine, PE - phosphatidylethanolamine, PS – phosphatidylserine, PI – phosphatidylinositol, PG – phosphatidylglycerol, SM – sphingomyelin, MG – monogalactosyldiglyceride, GC – galactosylceramide. *Taken from Bartlett et al.*[123]

1.10 Solid supported lipid bilayers

BLMs showed great promise in study the ion transport properties of lipid bilayers, however, such platforms are not easily applied for the investigation of the structural and binding properties of transmembrane proteins using advanced optical and spectroscopic techniques. Solid supported lipid bilayers can provide the structural and dynamic features of free bilayers, which enable to use surface specific analytical techniques for lipid bilayers. There are number of ways reported to prepare stable supported bilayer membranes. (1) Lipid bilayers with the inner monolayer attached to the solid substrate (2) Lipid or protein separated from the substrate using a spacer such as ultrathin layers of polymer cushion or an aqueous layer (3) an ultra thin film of polymer such as dextran hydrophobized by coupling of the alkane chain to the polymer backbone.[126] Tien and Salamon first proposed a simple method to prepare solid supported lipid bilayer.[127] They introduced a silver wire into lipid solution in n-decane and then cut the tip of the wire. The thin films of lipids formed at the fresh part of the wire when immersed into the electrolyte. However, the film formed on this rough surface was inhomogeneous and composed of multilayers of lipids. In an alternative approach, Spinke and co-workers introduced polymer supported lipid bilayers on a planar substrate.[128] In this approach, lipid bilayers were separated from solids by ultrathin layers of water or polymer films.[129,130,131,132]

Generally, solid supported lipid bilayers can be formed onto a variety of substrates using different methods. For example, lipids can be self-assembled onto alkane thiol modified gold substrates or lipid bilayers can be assembled onto polymer supported substrates. The advantages and disadvantages of these techniques are discussed below. Covalently attached inner alkyl monolayers were prepared on solid supports using self-assembly. In the case of Si-SiO$_2$ substrates, the inner alkyl monolayer can be formed from alkyl silane solution.[126] A highly stable homogeneous film of lipid bilayers can be prepared on the smooth gold substrate using chemisorbed alkane thiols. In this method, the alkanethiol forms a covalent bond with the gold substrate and the alkane chain creates a hydrophobic surface. In both cases, the second monolayer can be formed by techniques such as Langmuir-Blodgett technique or by dip coating method i.e., dipping the slide in lipid solution. Figure 1.26 shows the schematic representation of lipid bilayers formed with a covalently attached inner

layer. A key advantage of this method is that the packing density of the outer layer can be determined from the packing density of the inner layer. However, the main issue with these solid supported BLMs is that the thickness of the lipid bilayers is very small which leads to direct contact of associated proteins with the underlying substrate. Therefore, it was impossible to study the large integral proteins in the membrane. In addition, the insertion of the protein is difficult due to the packing density of the layers.[133] The lateral mobility of proteins in the membrane was lower on these substrates due to the direct contact of the protein with the substrate. Finally, studies of ion transport properties of protein incorporated biomembranes are limited due to the lack of water in between the lipid bilayer and the gold substrate.
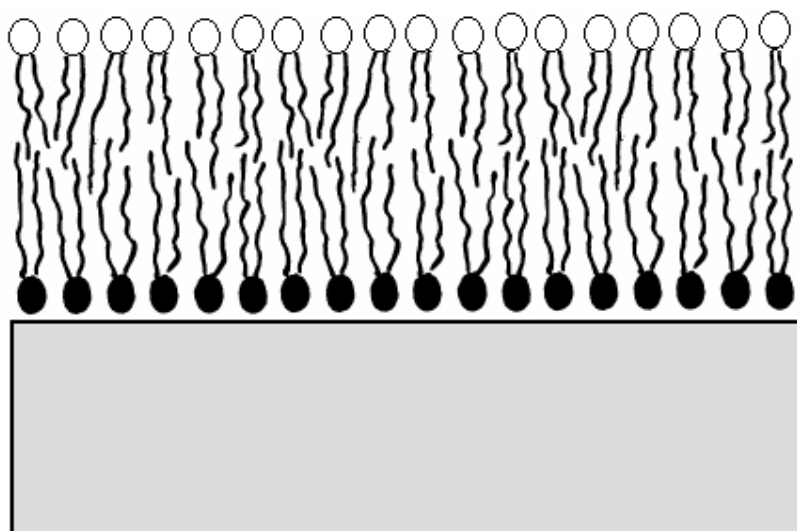
Fig. 1.26: Schematic representation of a lipid bilayer in which the inner layer is covalently attached to a gold substrate. The filled circles show the tethered lipids and the unfilled circles represent the polar part of the lipid.

To minimize undesired interactions between the substrate and the membrane proteins, researchers have made efforts to increase the gap between the bilayer and the substrate using spacers at the surface such as polymer cushions as shown in Figure 1.27. Mainly, there are two types of polymer cushions, polyelectrolytes[129,134,135] and lipopolymer tethers.[128,136] In polyelectrolyte cushions, layers of polymer are formed on the solid substrates by electrostatic interaction. The thickness of the polymer cushion can be controlled through layer-by-layer deposition. For example, polyethylenimine (PEI) deposited on mica or quartz has been used as a solid supported platform for bilayers.[125] The key factors for the selection of the polymer spacer are achieving minimum interaction of the polymer with the lipid membrane

and maximum hydrophilicity of the polymer. In addition, the polymer has to be sufficiently soft to support the diffusion of transmembrane proteins.[126] A number of polymer cushions have been reported as solid supports such as cellulose [137] and dextran.[131] Volker et al. reported the formation of lipid bilayers on top of polyethylene glycol cushion.[138] The lipid bilayers formed on this cushion seemed to show a diffusion coefficient in the range of 0.8-1.2x10^{-8} cm^{2}s^{-1}. However, the majority of the incorporated proteins in the membrane showed very low mobility (10^{-10} cm^{2}s^{-1}) on those substrates. Hillebrandt and co-workers prepared multilayers of cellulose derivatives with substituted alkyl-chain polymer cushion as a support for lipid bilayers on octadecyltrichlorosilane functionalized ITO surface to reduce the interaction between the substrate and the membrane.[137] A membrane capacitance of 0.57 µF/cm^2 (capacitance of biomembrane is approximately 0.9 µF/cm^2) was observed from lipid bilayers on the polymer cushioned ITO substrate. The report revealed that the lipid membrane maintained a high fluidity on the polymer cushioned substrate, which is similar to natural biomembranes.

In lipopolymer tethers (thiol terminated artificial lipids with an extended epoxy chain), a lipopolymer is covalently bonded to the substrate by tethers such as metal-sulphur, epoxy group linkage or silane bonding.[139] For example, Lang and co-workers first prepared a stable lipid bilayer with a hydrophilic spacer between the membrane and the substrate.[140] They synthesised thiol terminated artificial lipids with an extended epoxy chain as a hydrophilic spacer group. This hydrophilic group served as an aqueous phase which decouples the bilayer from the substrate and the thiol can covalently attach to the gold surface to form stable layers. They reported a bilayer capacitance in the range of 0.72-0.93 µF/cm^2 depending on the thiol and the lipid. Naumann and co-workers introduced peptide-tethered lipid bilayers in which the peptide acts as the hydrophilic spacer instead of ethylene glycol. These tethered lipid bilayers were covalently attached to the substrates such as Au-S-, Si-O-, Si-O-Si- and this model provides greater stability for the lipid layers. In summary, the capacitance of the solid supported lipid bilayers were close to the capacitance of biomembranes, however, the investigation of ion transport properties of transmembrane proteins was challenging on these platforms.
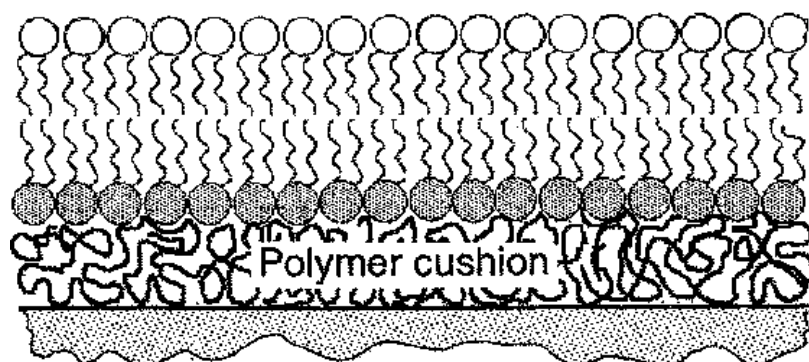
Fig. 1.27 Schematic representation of solid supported lipid bilayers. The lipid bilayer was formed on a polymer cushioned solid support. *Taken from Sackmann et al., Science, 1996, 271, 43.*[126]

1.11 Suspended lipid bilayers

As discussed earlier, Muller et al. first introduced suspended lipid bilayers on small apertures using a painting technique[122] and following this Montal and Muller established a tip-dip technique for the preparation of suspended lipid bilayers.[124] These BLMs permitted the examination of ion transport properties of lipid bilayers using electrochemistry and the solid supported lipid bilayers allowed the exploration of transmembrane protein dynamics using advanced fluorescence techniques. In the most recent efforts to provide a truly biomimetic host environment to proteins, researchers combined elements of both BLM and solid supported bilayers. Cheng and co-workers prepared suspended lipid bilayers across 100 µm circular pores.[141,142] However, the stability of these suspended lipid bilayers was approximately 5 hours. Furthermore, Eisenberg and co-workers prepared lipid bilayers across 250 µm aperture on silicon, again the stability of membrane was low. Vogel and co-workers introduced an alternative method to prepare suspended lipid bilayers across 0.6-7 µm hole on silicon.[143,144] A schematic representation of the platform proposed by Vogel et al. is shown in Figure 1.28.
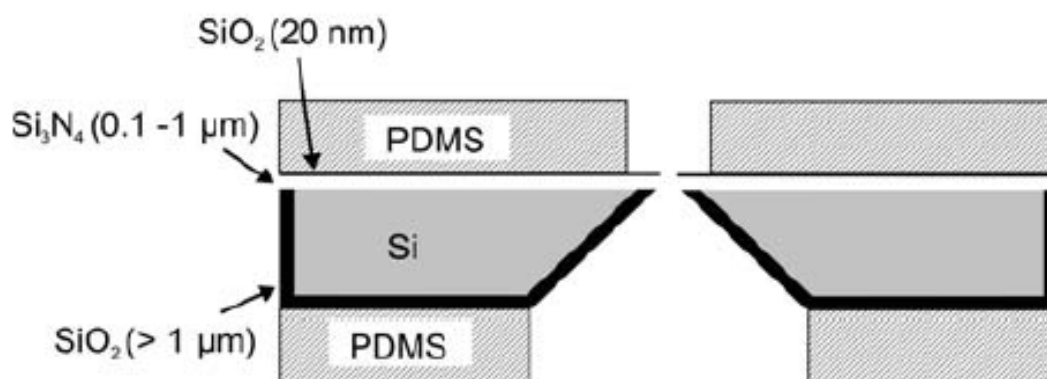
Fig: 1.28: Schematic representation of micro machined aperture in silicon for lipid bilayers described by Vogel et al. *Taken from Janshoff et al., Anal. Bioanal. Chem., 2006, 385,433.*[139]

Further research to increase the stability of suspended bilayers, focussed on suspended bilayers on porous substrates with diameters in the range from µm-mm apertures. Simon et al. suspended bilayers across apertures with hundreds of nanometres diameter on silicon using the Langmuir-Blodgett technique.[145] Steinem et al. have also been developing suspended lipid bilayers on porous alumina and

porous silicon substrates.[146,147] They suspended lipid bilayers across porous material using a vesicle fusion technique. The top surface of the porous substrates was coated with gold and then the gold surface was functionalized using 1,2-dipalmitoyl-sn-glycero-3-phosphothioethanol to make the surface hydrophobic. Diphytanoyl-phosphatidylcholine was then spread on the porous substrate. A schematic representation of the lipid bilayers formed on top of the porous alumina substrate is shown in Figure 1.29. The lipid bilayers suspended on top of porous alumina with 60 and 280 nm diameter were called nano-BLMs and 1 μm pore diameter were called macro-BLMs. Impedance measurements of these suspended lipid bilayers across the pores showed a capacitance that are similar to single lipid bilayers. The stability of spanned lipid bilayers on different platforms including gold nanocavity arrays is an issue, which has to be addressed in future.
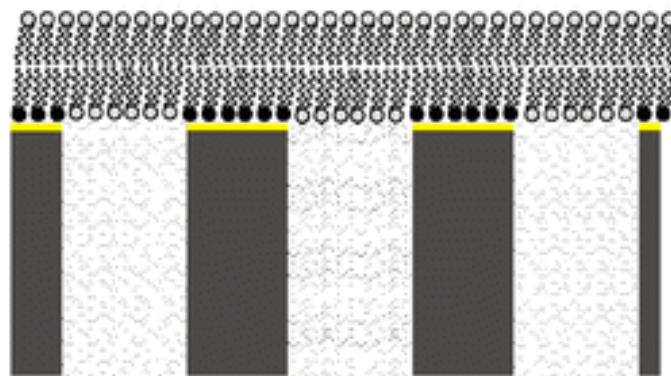
Fig. 1.29: Schematic representation of a suspended lipid bilayer formed across porous alumina. The yellow colour represents the gold on top of the porous alumina and the filled circles show the tethered lipids attached to the gold surface. *Taken from Janshoff et al., Anal. Bioanal. Chem., 2006, 385,433.*[139]

Ion channels are transmembrane proteins which play a vital role in balancing ion concentration across the cell. The study of ion transport properties of the proteins requires an aqueous environment at both interfaces of the membrane. Therefore, Steinem and co-workers have suspended lipid bilayers across a porous alumina and then they studied the ion transport properties using a model peptide, Gramicidin D.[1] They have spanned lipid bilayer across 40 nm diameter alumina pores using vesicle fusion technique after functionalizing the top gold surface with thiol. An increase in conductance for the spanned lipid bilayers incorporated with Gramicidin D was reported which confirmed the formation of pore spanning membrane on top of porous

alumina.   Several groups have been incorporated channel forming transmembrane proteins on the spanned lipid bilayer.[1,4]   However, the systematic studies of the dynamics of receptors such as αllβllla on spanned lipid bilayers are not reported yet. The incorporation of transmembrane proteins such as receptors on the spanned lipid bilayers are important but challenging approach to membrane-based sensing platform.

1.12 Conclusions

This thesis focuses on the fabrication of a novel biomimetic platform which can exploit the plasmonic properties of the underlying substrate in order to investigate the structural and dynamic properties of transmembrane proteins. One of the key issues is the fabrication of nanostructured metal surfaces which can provide reproducible enhancement in both Raman and emission signal intensity across the substrate. Therefore, the first part of the literature survey mainly focuses on the varieties of techniques reported for the fabrication and characterisation of reproducible nanostructured metal surfaces. The spectral reproducibility of both electrochemically roughened electrodes and metallic colloids were poor, however high Raman signal intensity enhancement can be achieved from molecules adsorbed on these substrates. Therefore, these substrates can be useful for qualitative analysis with high sensitivity. In this work, reproducibility of the signal intensity is critical therefore, highly ordered nanostructured arrays preferred over those electrochemically roughened electrodes. Different methods to fabricate reproducible nanostructured surfaces are discussed in detail and the literature survey revealed that lithographic techniques such as electron beam lithography or focussed ion beam lithography requires specialized equipments which are highly expensive. However, nanosphere lithography offers many advantages including reproducibility and simplicity. In addition, it is an inexpensive technique. Therefore, gold nanocavity arrays fabricated using nanosphere lithography followed by electrodeposition. The highlights of gold nanocavity arrays, fabrication and its plasmonic properties are briefly discussed. The systematic study of diameter and thickness dependent SERS from gold nanocavity arrays is also reviewed. The literature survey reveals that these arrays can provide SERRS enhancement on the order of 9 and this huge enhancement in signal intensity can be useful for the study of biomolecules. The enhancement mechanism of both fluorescence and Raman intensity has been described briefly in this literature review.

The second part of the literature survey focuses on the efforts to identify the location of the enhancement on nanostructured substrates. Recent developments in this field revealed that the largest electromagnetic enhancements occur at the corners and the junctions between metallic nanostructures. The relevant articles relating to these hot

spots are discussed in detail and the reports revealed that the greatest enhancement in signal intensity is observed when the gaps between nanotriangles were small 10 nm compared to larger gaps. The literature survey presented here has shown that interfacial self-assembly is an easiest way to control the surface properties of the substrate therefore; this method is used as a key tool in this thesis.

Finally, the literature survey focuses on the structure of the biomembrane and then discusses the recent developments reported for the fabrication of biomimetic platforms. Different methods have been introduced to explore the properties of transmembrane proteins, including black lipid bilayers, solid supported lipid bilayers and suspending lipid bilayers. The advantages and disadvantages of different membrane models have been analysed and discussed in detail. The literature review relating to spanning lipid bilayers has shown that suspending of lipid bilayers on porous substrates is an emerging area of research, which can provide significant insights regarding the function and properties of transmembrane proteins.

1.13 References

[1]   Schmitt, E. K.; Weichbrodt, C.; Steinem, C. *Soft Matter,* **2009**, *5*, 3347.

[2]   Baciu, M.; Sebai, S. C.; Ces, O.; Mulet, X.; Clarke, J. A.; Shearman, G. C.; Law, R. V.; Templer, R. H.; Plisson, C.; Parker, C. A.; Gee, A. *Phil. Trans. R. Soc. A,* **2006**, *364*, 2597.

[3]   Mey, I.; Stephan, M.; Schmitt, E. K.; Muller, M. M.; Ben Amar, M.; Steinem, C.; Janshoff, A. *J. Am. Chem. Soc.,* **2009**, *131*, 7031.

[4]   White, R. J.; Ervin, E. N.; Yang, T.; Chen, X.; Daniel, S.; Cremer, P. S.; White, H. S. *J. Am. Chem. Soc.,* **2007**, *129*, 11766.

[5]   Bartlett, P. N.; Baumberg, J. J.; Birkin, P. R.; Ghanem, M. A.; Netti, M. C. *Chem. Mater.,* **2002**, *14*, 2199.

[6]   Cole, R. M.; Baumberg J. J.; Garcia de Abajo, F.J.; Mahajan, S.; Abdelsalam, M. E.; Bartlett P.N. *Nano Lett.,* **2007***, 7*, 2094.

[7]   Mallon, C.T.; Jose B.; Forster, R.J.; Keyes, T.E. *Chem. Commun.,* **2010**, *46*, 106.

[8]   Tian, Z. Q.; Ren, B.; Wu, D. Y. *J. Phys. Chem. B,* **2002**, *106*, 9463.

[9]   Baltog, I.; Primeau, N.; Reinisch, R.; Coutaz, J. L. *Appl. Phys. Lett.,* **1995**, *66*, 1187.

[10]   Freeman, R. G.; Grabar, K. C.; Allison, K. J.; Bright, R. M.; Davis, J. A.; Guthrie, A. P.; Hommer, M. B.; Jackson, M. A.; Smith, P. C.; Walter, D. G.; Natan, M. J. *Science,* **1995**, *267*, 1629.

[11]   Fleischmann, M.; Hendra, P. J.; McQuillan, A. J. *Chem. Phys. Lett.,* **1974***, 26*, 163.

[12]   Jeanmaire, D. L.; Van Duyne, R. P. *J. Electroanal. Chem.,* **1977***, 84*, 1.

[13]   Albrecht, M. G.; Creighton, J. A. *J. Am. Chem. Soc.,* **1977***, 99*, 5215.

[14]   Xiu-Mei L.; Yan C.; Yan-Hui X.; Bin R.; Zhong-Qun T. *Anal. Bioanal. Chem.,* **2009**, *394*, 1729.

[15]   Nie, S. M.; Emery, S. R. *Science,* **1997**, *275*, 1102.

[16]   Kneipp, K.; Wang, Y.; Kneipp, H.; Perelman, L. T.; Itzkan, I.; Dasari, R.; Feld, M. S. *Phys. Rev. Lett.,* **1997**, *78*, 1667.

[17]   Tao, A. R; Huang, J. X; Yang, P. D. *Acc. Chem. Res.,* **2008,** *41*,1662.

[18] Huebner, U.; Boucher, R.; Schneidewind, H.; Cialla, D.; Popp, J. *Microelectron. Eng.,* **2008,** *85*, 1792.

[19] Willets, K. A.; Van Duyne, R. P. *Annu. Rev. Phys. Chem.,* **2007**, *58*, 267.

[20] Haes, A. J.; Zou, S.; Schatz, G. C.; Van Duyne, R. P. *J. Phys. Chem. B,* **2004***, 108*, 109.

[21] Sackmann, M.; Bom, S.; Balster, T.; Materny A. *J. Raman Spectrosc.,* **2007***, 38*, 277.

[22] Brolo, A. G.; Gordon, R.; Leathem, B.; Kavanagh, K. L. *Langmuir,* **2004**, *20*, 4813.

[23] Deckmann, H. W.; Dunsmuir, J.H. *Appl. Phys. Lett.,* **1982***, 41*, 377.

[24] Burmeister, F.; Schäfle, C.; Keilhofer, B.; Bechinger, C.; Boneberg, J.; Leiderer, P. *Adv. Mater.,* **1998***, 10*, 495.

[25] Peter, M. T.; Velev O. D.; Anand, T. K.; John, F. R.; Abraham, M. L.; Eric, W.K. *J. Am. Chem. Soc.,* **2000***, 122*, 9554.

[26] Denkov, N.; Velev, O.; Kralchevski, P.; Ivanov, I.; Yoshimura, H.; Nagayama, K. *Langmuir,* **1992***, 8*, 3183.

[27] Tull, E. J.; Bartlett, P. N.; Ryan, K. R. *Langmuir,* **2007***, 23*, 7859.

[28] Haynes, C. L.; Van Duyne, R. P. *J. Phys. Chem. B,* **2001***, 105*, 5599.

[29] Imhof, A.; Pine, D. J. *Nature,* **1997**, *389*, 948.

[30] Haes, A. J.; Van Duyne, R. P. *Anal. Bioanal. Chem.,* **2004**, *379*, 920.

[31] Kulinowski, K. M.; Jiang, P.; Vaswani, H.; Colvin, V. L. *Adv. Mater.,* **2000**, *12*, 833.

[32] Velev, O. D.; Tessier, P. M.; Lenhoff, A. M.; Kaler, E. W. *Nature,* **1999**, *401*, 548.

[33] Jensen, T. R.; Duval, M. L.; Kelly, K. L.; Lazarides, A. A.; Schatz, G. C.; Van Duyne, R. P. *J. Phys. Chem. B,* **1999**, *103*, 9846.

[34] Yan, H. W.; Blanford, C. F.; Holland, B. T.; Parent, M.; Smyrl, W. H.; Stein, A. *Adv. Mater.,* **1999**, *11*, 1003.

[35] Braun, P. V.; Wiltzius, P. *Nature,* **1999**, *402*, 603.

[36]   Wijnhoven, J.; Zevenhuizen, S. J. M.; Hendriks, M. A.; Vanmaekelbergh, D.; Kelly, J. J.; Vos, W. L. *Adv. Mater.,* **2000**, *12*, 888.

[37]   Xu, L. B.; Zhou, W. L. L.; Frommen, C.; Baughman, R. H.; Zakhidov, A. A.; Malkinski, L.; Wang, J. Q.; Wiley, J. B. *Chem. Commun.,* **2000**, *12*, 997.

[38]   Lacharmoise, P.D.; Tognalli, N.G.; Goni, A.R.; Alonso, M. I.; Fainstein, A.; Cole, R. M.; Baumberg, J. J.; de Abajo, J. G.; Bartlett, P. N. *Phys. Rev. B*, 78, 12, 125410.

[39]   Bartlett, P. N.; Birkin, P. R.; Ghanem, M. A. *Chem. Commun.,* **2000**, *17*, 1671.

[40]   Kelf, T. A.; Sugawara, Y.; Cole, R. M.; Baumberg J. J.; Abdelsalam, M. E.; Cintra, S.; Mahajan, S.; Russell, A. E.; Bartlett P.N. *Phys. Rev. B,* **2006***, 74*, 245415.

[41]   Abdelsalam, M. E.; Bartlett, P. N.; Baumberg, J. J.; Cintra, S.; Kelf, T. A.; Russell, A. E. *Electrochem. Commun.,* **2005**, *7*, 740.

[42]   Netti, M. C.; Coyle, S.; Baumberg, J. J.; Ghanem, M. A.; Birkin, P. R.; Bartlett, P. N.; Whittaker, D. M. *Adv. Mater.,* **2001**, *13*, 1368.

[43]   Bartlett, P. N.; Baumberg, J. J.; Coyle, S.; Abdelsalam, M. E. *Faraday Discuss.,* **2004**, *125*, 117.

[44]   Mahajan, S.; Baumberg, J. J.; Russell, A. E.; Bartlett, P. N. *Phys. Chem. Chem. Phys.,* **2007**, *9*, 6016.

[45]   Zhang, X.; Whitney, A. V.; Zhao, J.; Hicks, E. M.; Van Duyne, R. P. *J. Nanosci. Nanotechnol.,* **2006**, *6*, 1920.

[46]   Kreibig, U.; Vollmer, M. *Optical properties of metal clusters*, Springer, **1995**.

[47]   Pines, D. *Rev. Mod. Phys.,* **1956***, 28*, 184.

[48]   Ritchie, R. H. *Phys. Rev.,* **1957***, 106*, 874.

[49]   Van Duyne, R. P. *Science,* **2004***, 306*, 985.

[50]   Otto, A. *Z.Phys.,* **1968***, 216,* 398.

[51]   Kretschmann, E.; Raether, H. *Z. Naturforsch. Teil A,* **1968***, 23A*, 2135.

[52]   Stewart, M. E.; Anderton, C. R.; Thompson, L. B.; Maria, J.; Gray, S. K.; Rogers, J. A.; Nuzzo, R. G. *Chem. Rev.,* **2008***, 108*, 494.

[53]   Brockman, J. M.; Nelson, B. P.; Corn, R. M. *Annu. Rev. Phys. Chem.,*

2000, *51*, 41.

[54]   Knoll, W. *Annu. Rev. Phys. Chem.,* **1998***, 49*, 569.

[55]   Knobloch, H.; Brunner, H.; Leitner, A.; Aussenegg, F.; Knoll, W. *J. Chem. Phys.,* **1993***, 98*, 10093.

[56]   Homola, J. *Anal. Bioanal. Chem.,* **2003***, 377*, 528.

[57]   Liedberg, B.; Nylander, C.; Lundstroem, I. *Sens. Actuators,* **1983***, 4*, 299.

[58]   Jung, L. S.; Campbell, C. T. *J. Phys. Chem. B,* **2000***, 104*, 11168.

[59]   Perez-Luna, V. H.; O'Brien, M. J.; Opperman, K. A.; Hampton, P. D.; Lopez, G. P.; Klumb, L. A.; Stayton, P. S. *J. Am. Chem. Soc.,* **1999***, 121*, 6469.

[60]   Berger, C. E. H.; Beumer, T. A. M.; Kooyman, R. P. H.; Greve, J *Anal. Chem.,* **1998***, 70*, 703.

[61]   Mrksich, M.; Grunwell, J. R.; Whitesides, G. M. *J. Am. Chem. Soc.,* **1995***, 117*, 12009.

[62]   http://csacs.mcgill.ca/francais/docs/CHEM634/SPR_Badia.pdf.

[63]   Han, S.; Shi, X.; Zhou, F. *Nano Lett.,* **2002***, 2*, 435.

[64]   Alvarifio, J. M.; Cuadrado, L.; Hernández, M. L.; Laganà, A. *Chem. Phys. Lett.,* **1995***, 241*, 408.

[65]   Kelly, K. L.; Coronado, E.; Zhao, L. L.; Schatz, G. C. *J. Phys. Chem. B,* **2003***, 107*, 668.

[66]   Miller, M. M.; Lazarides, A. A. *J. Phys. Chem. B,* **2005***, 109*, 21556.

[67]   Schwartzberg, A. M.; Zhang, J. Z. *J. Phys. Chem. C,* **2008***, 112*, 10323.

[68]   Katrin, K.; Yang, W.; Harald, K.; Lev, T. P.; Irving, I.; Ramachandra, R. D.; Michael, S. F. *Phys. Rev. Lett.,* **1997***, 78*, 1667.

[69]   Lakowicz, J. R. *Plasmonics,* **2006***, 1*, 5.

[70]   Fu, Y.; Lakowicz, J. R. *Plasmonics,* **2007***, 2*.

[71]   Zeman, E. J.; Schatz, G. C. *J. Phys. Chem.,* **1987***, 91*, 634.

[72]   Malinsky, M. D.; Kelly, K. L.; Schatz, G. C.; Van Duyne, R. P. *J. Am. Chem. Soc.,* **2001***, 123*, 1471.

[73]   Le Ru, E. C; Etchegoin, P. G. *Principles of Surface-enhanced Raman spectroscopy*, Elsevier, Amsterdam, **2009**.

[74]   Lakowicz, J. R. *Principles of Fluorescence spectroscopy,* New York, Springer, **2006**.

[75]   Willis, R. C. *Anal. Chem.,* **2007***, 79*, 1785.

[76]   Brolo, A. G.; Kwok, S. C.; Moffitt, M. G.; Gordon, R.; Riordon, J.; Kavanagh, K. L. *J. Am. Chem. Soc.,* **2005***, 127*, 14936.

[77]   Lakowicz, J. R.; Geddes, C. D.; Gryczynski, I.; Malicka, J.; Gryczynski, Z.; Aslan, K.; Lukomska, J.; Matveeva, E.; Zhang, J. A.; Badugu, R.; Huang, J. *J. Fluoresc.,* **2004***, 14*, 425.

[78]   Gryczynski, Z.; Malicka, J.; Matveeva, E.; Gryczynski, I.; Lakowicz, J. R. *Biophys. J.,* **2004***, 86*, 359A.

[79]   Corrigan, T. D.; Guo, S.; Phaneuf, R. J.; Szmacinski, H. *J. Fluoresc.,* **2005** *15*, 777.

[80]   Lakowicz, J. R. *Anal. Biochem.,* **2001***, 298*, 1.

[81]   Aslan, K.; Gryczynski, I.; Malicka, J.; Matveeva, E.; Lakowicz, J. R.; Geddes, C. D. *Curr. Opin. Biotechnol.,* **2005***, 16*, 55.

[82]   Sugawara, Y.; Kelf, T. A.; Baumberg, J. J.; Abdelsalam, M. E.; Bartlett, P. N. *Phys. Rev. Lett.,* **2006***, 97*, 266808.

[83]   Cosgrave, L.; Devocelle, M.; Forster, R. J.; Keyes, T. E. *Chem. Commun.*, **2010***, 46*, 103.

[84]   Neugebauer, U.; Pellegrin, Y.; Devocelle, M.; Forster, R. J.; Signac, W.; Morand, N.; Keyes, T. E. *Chem. Commun.,* **2008**, 5307.

[85]   Balzani, V.; Juris, A. *Coord. Chem. Rev.,* **2001***, 211*, 97.

[86]   Nazeeruddin, M. K.; Kay, A.; Rodicio,I.; Humphry-Baker, R.; Mueller, E.; Liska, P.; Vlachopoulos, N.; Graetzel M. *J. Am. Chem. Soc.,* **1993***, 115*, 6382.

[87]   Rubinstein, I.; Bard, A.J. *J. Am. Chem. Soc.,* **1980***, 102*, 6641.

[88]   Adam Webb, M.; Knorr, F. J.; McHale, J. L. *J. Raman Spectrosc.,* **2001***, 32*, 481.

[89]   Juris, A.; Balzani, V.; Barigelletti, F.; Campagna, S.; Belser, P.; von Zelewsky, A. *Coord. Chem. Rev.,* **1988***, 84*, 85.

[90] Forster, R. J. and Keyes, T.E. *J. Phys. Chem. B,* **1998**, *102*, 10004.

[91] Vijaya Sarathy, K.; Narayan, K. S.; Kim, J.; White, J. O. *Chem. Phys. Lett.,* **2000***, 318*, 543.

[92] Cotton, T. M.; Schultz, S. G.; Van Duyne, R.P.; *J. Am. Chem. Soc.,* **1980***, 102*, 7960.

[93] Kneipp, K.; Kneipp, H.; Itzkan, I.; Dasari, R. R.; Feld, M. S. *Chem. Rev.,* **1999***, 99*, 2957.

[94] Doering, W. E.; Nie, S. *J. Phys. Chem. B,* **2002***, 106*, 311.

[95] Stockman, M. I. *Top. Appl. Phys.,* **2006***, 103.*

[96] Campion, A.; Kambhampati, P. *Chem. Soc. Rev.,* **1998***, 27*, 241.

[97] Otto, A. *J. Raman Spectrosc.,* **2005***, 36*, 497.

[98] Fromm, D. P.; Sundaramurthy, A.; Kinkhabwala, A.; Schuck, P. J.; Kino, G. S.; Moerner, W. E. *J. Chem. Phys.,* **2006**, *124*, 061101.

[99] Brolo, A. G.; Arctander, E.; Gordon, R.; Leathem, B.; Kavanagh, K. L. *Nano Lett.,* **2004***, 4*, 2015.

[100] Mahajan, S.; Abdelsalam, M.; Suguwara, Y.; Cintra, S.; Russell, A.; Baumberg, J.; Bartlett, P. *Phys. Chem. Chem. Phys.,* **2007***, 9*, 104.

[101] Cintra, S.; Abdelsalam, M. E.; Bartlett, P. N.; Baumberg, J. J.; Kelf, T. A.; Sugawara, Y.; Russell, A. E. *Faraday Discuss.,* **2006***, 132*, 191.

[102] Kelf, T. A.; Sugawara, Y.; Baumberg, J. J.; Abdelsalam, M.; Bartlett, P. N. *Phys. Rev. Lett.,* **2005**, *95*, 116802.

[103] Hao, E.; Schatz, G.C; Hupp, J. T. *J. Fluoresc.,* **2004**, *14*, 331.

[104] Van Duyne, R. P. *Abstracts of Papers of the American Chemical Society,* **2002**, *223*, 003.

[105] Haes, A. J.; Van Duyne, R. P. *Abstracts of Papers of the American Chemical Society,* **2004**, *227*, 228.

[106] Kinkhabwala, A.; Yu, Z. F.; Fan, S. H.; Avlasevich, Y.; Mullen, K.; Moerner, W. E. *Nat. Photonics,* **2009**, *3*, 654.

[107] Mahajan, S.; Cole, R. M.; Soares, B. F.; Pelfrey, S. H.; Russell, A. E.; Baumberg, J. J.; Bartlett, P. N. *J. Phys. Chem. C,* **2009**, *113*, 9284.

[108] Cole, R. M.; Mahajan, S.; Bartlett, P. N.; Baumberg, J. J. *Opt. Express,* **2009**, *17*, 13298.

[109] Dreier, J.; Eriksen, R. L.; Albrektsen, O.; Pors, A.; Simonsen, A. C. *J. Phys. Chem. Lett.,* **2010**, *1*, 260.

[110] Vos, J. G., Forster, R. J, Keyes, T.E. *Interfacial supramolecular Assemblies,* Wiley, Chichester, **2003**.

[111] Blaaderen, A.; Ruelt R.; Wiltzius, P. *Nature,* **1997***, 385*, 321.

[112] Lee, Y.; Pruzinsky, S. A.; Braun, P. V. *Langmuir,* **2004***, 20*, 3096.

[113] Napper, D. H. *Polymeric stabilization of colloidal dispersions,* **1983**.

[114] Bossel, C.; Dutta, J.; Houriet, R.; Hilborn, J.; Hofmann, H. *Mater. Sci. Eng., A,* **1995,** *204,*107**.**

[115] John, M. C. *J. Polym. Sci. Polym. Lett. Ed.,* **1977**, *15*, 632.

[116] Forster, R. J.; Keyes, T. E. *Coord. Chem. Rev.,* **2009**, *253*, 1833.

[117] Fendler, J. H. *Membrane mimetic chemistry,* John Wiley & Sons, **1982**.

[118] Harrison, R.; Lund, G.G. *Biological membranes,* Blackie and Sons Ltd., London, **1980**.

[119] Gortel, E.; Grendel. E. *J. Exp. Med.,* **1925**, *41*, 439.

[120] Singer, S. J.; Nicolson, G. L. *Science,* **1972**, *175*, 720.

[121] Tanford, C. *Science,* **1978**, *200*, 1012.

[122] Mueller, P.; Rudin, D. O.; Tien, H. T.; Wescott, W. C. *Nature,* **1962**, *194*, 979.

[123] Bartlett, P. *Bioelectrochemistry*, John Wiley & Sons Ltd., Chichester, **2008**.

[124] Montal, M.; Mueller, P. *Proc. Natl. Acad. Sci. U. S. A.,* **1972**, *69*, 3561.

[125] Castellana, E. T.; Cremer, P. S. *Surf. Sci. Rep.,* **2006**, *61*, 429.

[126] Sackmann, E. *Science,* **1996**, *271*, 43.

[127] Tien, H. T.; Salamon, Z. *Bioelectrochem. Bioenerg.,* **1989**, *22*, 211.

[128] Spinke, J.; Yang, J.; Wolf, H.; Liley, M.; Ringsdorf, H.; Knoll, W. *Biophys. J.,* **1992**, *63*, 1667.

[129] Zhang, L. Q.; Longo, M. L.; Stroeve, P. *Langmuir,* **2000**, *16*, 5093.

[130] Shen, W. W.; Boxer, S. G.; Knoll, W.; Frank, C. W. *Biomacromolecules,* **2001**, *2*, 70.

[131] Elender, G.; Kuhner, M.; Sackmann, E. *Biosens. Bioelectron.,* **1996**, *11*, 565.

[132] Tanaka, M.; Sackmann, E. *Nature,* **2005**, *437*, 656.

[133] Glazier, S. A.; Vanderah, D. J.; Plant, A. L.; Bayley, H.; Valincius, G.; Kasianowicz, J. J. *Langmuir,* **2000**, *16*, 10428.

[134] Majewski, J.; Wong, J. Y.; Park, C. K.; Seitz, M.; Israelachvili, J. N.; Smith, G. S. *Biophys. J.,* **1998**, *75*, 2363.

[135] Kugler, R.; Knoll, W. *Bioelectrochemistry,* **2002**, *56*, 175.

[136] Hausch, M.; Zentel, R.; Knoll, W. *Macromol. Chem. Phys.,* **1999**, *200*, 174.

[137] Hillebrandt, H.; Wiegand, G.; Tanaka, M.; Sackmann, E. *Langmuir,* **1999**, *15*, 8451.

[138] Volker, K.; Marta, K. D.; David, M.; Chen, W.; Lukas, K. T. *Wiley encyclopedia of chemical biology*, John Wiley and sons, Virginia, **2008**.

[139] Janshoff, A.; Steinem, C. *Anal. Bioanal. Chem.,* **2006**, *385*, 433.

[140] Lang, H.; Duschl, C.; Vogel, H. *Langmuir,* **1994**, *10*, 197.

[141] Cheng, Y. L.; Bushby, R. J.; Evans, S. D.; Knowles, P. F.; Miles, R. E.; Ogier, S. D. *Langmuir,* **2001**, *17*, 1240.

[142] Ogier, S. D.; Bushby, R. J.; Cheng, Y. L.; Evans, S. D.; Evans, S. W.; Jenkins, A. T. A.; Knowles, P. F.; Miles, R. E. *Langmuir,* **2000**, *16*, 5696.

[143] Wilk, S. J.; Goryll, M.; Laws, G. M.; Goodnick, S. M.; Thornton, T. J.; Saraniti, M.; Tang, J.; Eisenberg, R. S. *Appl. Phys. Lett.,* **2004**, *85*, 3307.

[144] Goryll, M.; Wilk, S.; Laws, G. M.; Thornton, T.; Goodnick, S.; Saraniti, M.; Tang, J.; Eisenberg, R. S. *Superlattices Microstruct.,* **2003**, *34*, 451.

[145] Simon, A.; Girard-Egrot, A.; Sauter, F.; Pudda, C.; D'Hahan, N. P.; Blum, L.; Chatelain, F.; Fuchs, A. *J. Colloid Interface Sci.,* **2007**, *308*, 337.

[146] Schmitt, E. K.; Nurnabi, M.; Bushby, R. J.; Steinem, C. *Soft Matter,* **2008**, *4*, 250.

[147] Steinem, C.; Janshoff, A.; Galla, H. J.; Sieber, M. *Bioelectrochem. Bioenerg.,* **1997**, *42*, 213.

Chapter 2

Photophysical and spectroscopic studies of dye filled nanocavity arrays

2.1 Introduction

One of the key advantages of using plasmonic negative curvature structures filled with fluid is that these surfaces may be used as a nano-vial. We were interested in examining the ability of these substrates to fill and once filled, to enhance emission or Raman from solution. Filling is particularly important because in the ultimate application of these arrays, it is hoped to support protein which requires fluid at both interfaces.[1,2,3] Gold nanocavity arrays can be fabricated reproducibly on different electrodes such as smooth gold substrates or conductive glass substrates using nanosphere lithography[4,5,6] followed by electrochemical deposition.[7,8] A key challenge is to investigate the filling properties of the voids with solvents. If the gold nanocavity arrays are able to fill with solvents then the voids can act as an aqueous compartment for the lipid bilayers and this water filled voids fulfils the major requirement for the lipid bilayer to mimic the biological environment. Therefore, in this chapter the filling properties of the gold nanocavity arrays as investigated using confocal microscopy are reported.

The main issue to be addressed is the capability of the gold nanocavity arrays to enhance the spectroscopic signals. The spectroscopic signal enhancement from nanostructured metal surfaces mainly arise due to the presence of electron density at the surface of the arrays, which oscillates with incident light when the oscillation frequency of electrons matches with the frequency of the incident light.[9,10] These surface charge oscillations localized at the metal surface can influence the electric field experienced by a species adsorbed at or near the interface, and is the basis for enhanced spectroscopies such as SERS[11,12], SERRS[13] and SEF.[14,15,16,17,18] SERRS occurs when the laser excitation overlaps with an electronic transition of the adsorbed species and with the excitation of surface plasmon at the substrate.[19] The combination of both SERS and resonance gives an overall intensity enhancement for SERRS, which makes the technique very sensitive

i.e., single molecule detection.[20,21,22] Bartlett and co-workers have systematically studied the plasmonic properties, especially SERS, of gold nanocavity arrays using adsorbed benzenethiol molecule.[1] They reported approximately six orders of magnitude enhancement in Raman signal intensity from the adsorbed thiol on gold nanocavity arrays. In addition, SERRS from the gold nanocavity arrays was studied using indocarbocyanine dyes, and they reported approximately nine orders of magnitude enhancement in signal intensity.[23] In this chapter, SERRS from gold nanocavity arrays were studied using self-assembled monolayers of an inorganic luminophore. Another issue to be addressed is the ability of the arrays to enhance emission intensity from dye filled arrays. In addition to SERS and SERRS, nanostructured features on gold metal films such as nanoholes have been shown to exhibit strong localized surface plasmons, which enhances the emission from fluorophores near the metal surface.[24,25,26] The interaction of a fluorophore with the metal surface can enhance the emission intensity by altering the radiative decay rates or by amplifying the incident light intensity at the metal surface.[27]

A key goal of exploiting gold nanocavity arrays is to suspend lipid film across the cavity and then investigate the possibility to use their plasmonic properties to enhance Raman or luminescence signals from protein or membrane components adsorbed on or near the array. It is instructive to investigate the influence of this array on the photophysical and spectroscopic properties of molecules adsorbed or close to the metal surface. In order to investigate the affect of gold nanocavity array on the properties of the dyes, a surface active luminescent metal complex; $[Ru(bpy)_2(Qbpy)]^{2+}$ complex, where bpy is 2,2'-bipyridyl and Qbpy is 2,2':4,4":4,4"-quarterpyridyl, is used. This dye has been selected because of their interesting photophysical properties such as large Stoke shift and relatively low quantum yields. Ruthenium polypyridyl complexes typically have quantum yields in the range ~3-8 % with long luminescence lifetimes (>100 ns). The presence of free nitrogen atom on Qbpy ligand permits the complex to form a monolayer dye on the metal surface, which enables monolayer studies as well as solution phase luminescence measurements. The influence of the gold nanocavity arrays on emission properties of $[Ru(bpy)_2(Qbpy)]^{2+}$ complex and fullerene (C_{60}) suspended within 820 nm diameter gold nanocavity arrays were compared to the dye filled cobalt cavities which are expected to have plasmons outside the visible spectral region. In order to investigate the mechanism of enhancement in emission intensity, the lifetime of $[Ru(bpy)_2(Qbpy)]^{2+}$ dye

on gold nanocavity arrays is studied using a fluorescence lifetime imaging microscope (FLIM). Finally, SERRS from the gold nanocavity arrays were studied using a monolayer of $[Ru(bpy)_2(Qbpy)]^{2+}$ dye self-assembled on the array under 514 nm excitation.

2.2 Experimental

2.2.1 Materials

Cysteamine (98%), cobalt acetate (99.995%), sodium acetate (98.5%), tetrahydrofuran (THF, 99%) and fullerene (C_{60}) were purchased from Sigma-Aldrich. The sulphate modified polystyrene latex spheres with different diameters (240, 430, 600 and 820 nm) were obtained from Duke scientific. The size distribution of polystyrene spheres was ≤3 % with a concentration of 10% w/w. FDTO glass slides were purchased from Hartford Glass Co. Inc. $[Ru(bpy)_2(Qbpy)]^{2+}$ dye was synthesized and characterized by Reena Marthi and Yann Pellegrin from cis-$[Ru(bpy)_2Cl_2]$ as described previously.[28]

2.2.2 Fabrication of gold nanocavity arrays

Gold nanocavity arrays were prepared on a fluorine-doped tin-oxide (FDTO) substrate by electrochemical deposition of gold through the voids of self-assembled polystyrene spheres. The overall scheme for the fabrication of nanocavity arrays using nanosphere lithography is shown in Scheme 2.1. The FDTO glass slides were used as a substrate due to their electrical conductivity and low cost. The slides were cut into small pieces to give a geometric surface area of approximately 1.75 cm^2. Then, the slides were thoroughly cleaned by rinsing successively with water and acetone, and then heated up to 400 ^{o}C for 10 minutes to remove all the contaminants from the surface. The thoroughly cleaned slides were then immersed in piranha solution, which is expected to increase the efficiency of assembly of the polystyrene spheres on the FDTO substrate. Then, the FDTO substrate was washed with deionised water and dried under a stream of nitrogen.

The first stage of the fabrication of nanocavity arrays involves self-assembly of polystyrene spheres on a FDTO slide as shown in Scheme 2.1. This is a crucial step for the fabrication of different sizes of arrays, in which the diameter of the cavity can be controlled by selecting the appropriate sphere diameter.[1] In this chapter, polystyrene latex spheres with a diameter of 820 nm, were used as the template. The sphere solution was diluted to 1% w/v with water. The deposition of the colloidal template layer was carried out in a thin layer cell made up of two FDTO electrodes in which the electrodes were held 1 mm apart by using approximately five sheets of parafilm. The space between

the two electrodes was filled with aqueous 1 % suspensions of polystyrene latex spheres and evaporated to dry at room temperature.
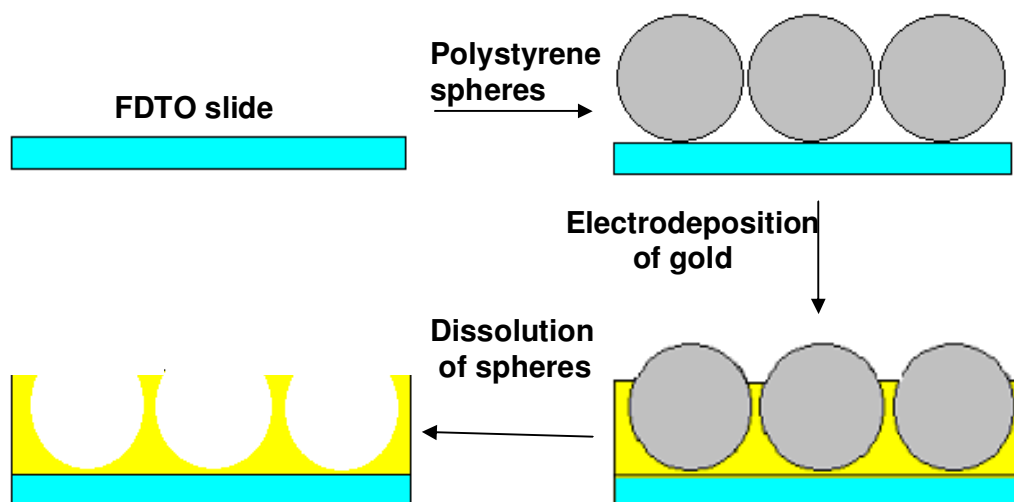
Scheme 2.1: Schematic representation of fabrication of nanocavity arrays using nanosphere lithography. The first step is the self-assembly of polystyrene spheres on FDTO electrode. Second step is the electrochemical deposition of metal through the voids of polystyrene spheres. Finally, the polystyrene spheres dissolved in THF resulting nanostructured surfaces.

All electrochemical measurements were carried out in a standard three-electrode cell at room temperature using CH electrochemical workstations. In electrodeposition, the template-coated FDTO plates were incorporated as a working electrode in the three-electrode cell and a platinum mesh was used as counter electrode. The surface area of the working electrode was controlled by wrapping insulating teflon tape around half of the electrode. A gold film deposited electrochemically through the templates from a commercially obtained aqueous gold plating solution (Technic Inc. Sodium gold sulphite solution, Cranston, RI, USA) in which the gold concentration was 6.8 g/L. Electrolyte solutions were degassed for 30 minutes before deposition. A potential of –0.95 V versus an Ag/AgCl (sat. KCl) electrode was applied by a CH Instruments Model 660 electrochemical workstation until a charge of approximately -0.35 C.cm^{-2}. If the coulometric efficiency is 1, a charge of -0.35 C.cm^{-2} should result a thickness of approximately 600 nm. This ideal is accurate if the spheres pack perfectly on the electrode. The thickness of the cavities can be tuned by controlling the charge passed through the electrochemical cell. After deposition, the Au-covered electrodes were

sonicated in THF for 1 hour to dissolve and remove the template. The resulting gold nanocavity arrays were characterised using scanning electron microscope (SEM) and atomic force microscopy (AFM).

2.2.3 Preparation of cobalt nanocavities

Cobalt nanocavity arrays were also prepared by nanosphere lithography according to the Scheme 2.1. In this instance, cobalt metal deposition was carried out using electrochemical deposition via reduction of cobalt ions from an aqueous solution of cobalt acetate through the interstitial voids of templated polystyrene spheres on FDTO. A nanostructured cobalt film of controlled thickness was deposited through the voids of polystyrene spheres from an aqueous solution of 0.1 M $Co(Ac)_2$ and 0.1 M sodium acetate. The potential of –0.90 V versus an Ag/AgCl (sat. KCl) electrode was controlled by a CH Instruments Model 660 electrochemical workstation until a charge of -0.74 $C.cm^{-2}$ is passed. After passing this charge, a film with a thickness of approximately 600 nm should form, if the spheres pack perfectly on the electrode. After deposition of the cobalt, the deposited electrode was thoroughly rinsed with deionised water and then sonicated in THF for 1 hour to dissolve and remove the template. The cobalt cavity array was characterised by SEM.

2.2.4 Filling and surface modification of gold nanocavity arrays

Metal enhanced emission and surface enhanced resonance Raman scattering from the gold nanocavity arrays were studied using a surface active $[Ru(bpy)_2(Qbpy)]^{2+}$ complex. The structure of $[Ru(bpy)_2(Qbpy)]^{2+}$ molecule is shown in Scheme 2.2. Filling of both gold and cobalt nanocavity arrays with dyes was achieved by sonication in 1 mM methanolic solution of $[Ru(bpy)_2(Qbpy)]^{2+}$ for 30 minutes. The nanocavity arrays were filled with 1 mM fullerene by sonication and toluene was used as a solvent. A monolayer of dye on gold cavities were prepared by soaking the array in 1 mM methanolic solution of $[Ru(bpy)_2(Qbpy)]^{2+}$ dye for two days after 30 minute sonication, so that enough time was given for the monolayers to form. Excess physisorbed material was removed from the electrode by sonicating the electrode with methanol prior to the measurements.
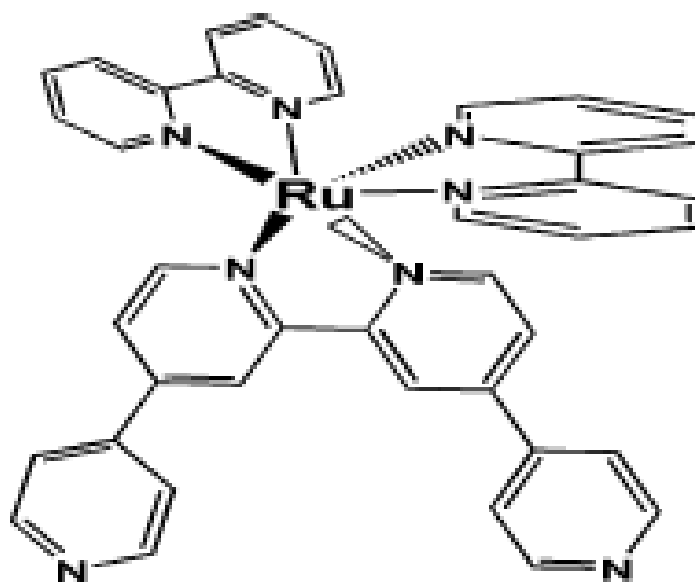
Scheme 2.2: Structure of a [Ru(bpy)$_2$(Qbpy)]$^{2+}$ complex. *Taken from reference Forster et al., J. Phys. Chem. B, 1998, 102, 10004.*[28]

2.2.5 Methods

The structure and morphology of the self-assembled polystyrene templates and the subsequent nanocavity arrays were investigated using a Hitachi S-3000N scanning electron microscope. The statistics of the pore opening sizes were obtained using Image J version 1.37d image analysis software. The reflectance measurements of the gold nanovoid structures were recorded with a Perkin Elmer Lambda 900 UV-Vis spectrophotometer. Resonance Raman spectra of the luminophore on a plain FDTO slide as well as on the nanocavity arrays were recorded using a confocal HR micro-Raman setup (HR800, Jobin-Yvon, Horiba) with an 600 groves/mm grating. The 514 nm or 458 nm lines of an argon ion laser (Coherent, Innova) were employed for excitation and the scattered light was collected in a 180° alignment. Typical acquisition times were between 1 and 20 s. Each measurement was replicated across three different spots of the sample. Emission spectra of the dye filled cavities were collected with Horiba Jobin Yvon HR800UV spectrometer using an argon ion laser.

Luminescence images of the nanocavity arrays were recorded with a confocal fluorescence microscope (LSM 50, Zeiss) using a 64x oil immersion objective. The

principle behind this technique is discussed below. An argon ion laser provided 514 nm and 488 nm excitation wavelengths. The scanned images contain 512x512 pixels. Emission spectra were collected using the Raman protocol described above. Luminescence lifetime measurements were carried-out on the Zeiss system with a fluorescence lifetime upgrade kit from PicoQuant, Germany, equipped with a pulsed 405 nm excitation laser and SymPhoTime software. The effective confocal volume, V_{eff} of the microscope was estimated by imaging 60 nm diameter fluorescent beads (Bangs Labs) in lateral and axial dimensions.

2.2.5.1 Confocal fluorescence microscopy

A schematic representation of a confocal microscope setup is shown in Scheme 2.3. In confocal fluorescence microscopy, the light is focussed through a pinhole to the condenser lens and then, this lens focuses the light to the focal point. The fluorescence signal coming from the sample is collected using an objective lens. To eliminate the signal from out-of-focus the collected light passes through the second pinhole before reaching the detector. This second pinhole eliminates out of focus rays from the sample as shown in Scheme 2.3. As a result, confocal microscope setup improves the z-resolution of the image.

A confocal microscope provides the opportunity of optical slicing the sample, which gives information from different focal planes.[29] Optical sectioning technique can be used to build up an image of a three-dimensional object. This technique is actually the collection of a set of two-dimensional images from different z-planes of the sample.
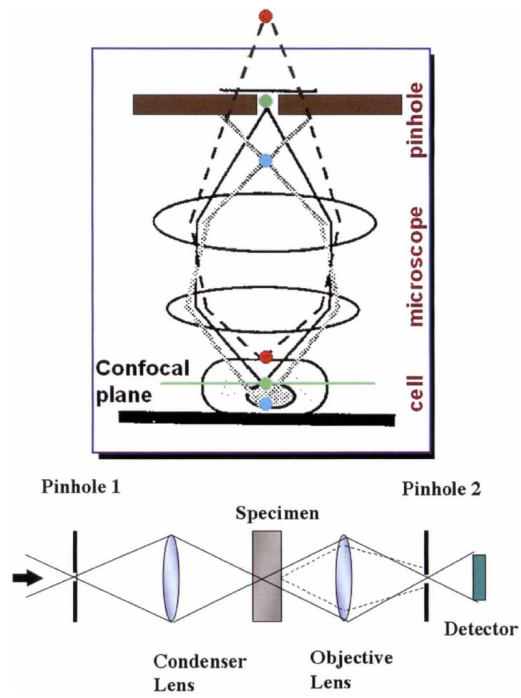
Scheme 2.3: Schematic representation of confocal setup. *Taken from reference 29.*

2.3 Results and Discussion

2.3.1 Characterisation of gold nanocavities by scanning electron microscopy (SEM)

Self-assembly of polystyrene spheres is a very simple and flexible method for producing different nanostructured arrays such as nanotriangles[30] and nanocavities[7] with controlled interparticle distance as discussed in Chapter 1. A number of different methods have been used to prepare self-assembled polystyrene spheres such as drop-coating method, gravity sedimentation, and direct evaporation.[31,32] Van Duyne and co-workers have prepared a 2-dimensional array of polystyrene spheres on chemically modified glass substrates by a drop-coating method.[31] In this approach, the negatively charged polystyrene spheres were repelled from the negatively charged glass substrate until the spheres reach lowest energy configuration. When solvent evaporates, the spheres stick to the surface due to capillary forces and form a hexagonally close packed pattern on the substrate. The size of defect-free domain was in the range of 10-100 µm using this method. Gravity sedimentation is the other popular way to prepare ordered colloidal lattices but in this approach, it is difficult to control the thickness of the film.[32] In this thesis, an approach described by Bartlett et al. is used in which two-dimensional arrays of polystyrene spheres were prepared using a direct evaporation technique. This technique leads to well defined defect-free areas on the order of 1 cm^2.[33] In this approach, diluted latex sphere solution is deposited in between two smooth gold slides, which was sealed using a parafilm. In the direct evaporation technique, as the fluid dries, strong capillary forces develop at the meniscus between the substrate and the colloidal solution, which pulls the spheres to the evaporation line resulting in close packed monolayers on the substrate. The evaporation technique gives large defect-free areas in the range of centimetres compared to drop-coating method. In this thesis, the latter method is exploited for the preparation of self-assembled monolayers of polystyrene spheres. The main drawback of this approach is that a long time is needed to evaporate the solvent (water). However, this is compensated by the long-range order achieved. SEM measurements were taken from the self-assembled monolayers of polystyrene spheres formed on FDTO in order to understand the packing efficiency of spheres using the direct evaporation technique on this substrate. Figure 2.1 shows the SEM image of self-assembled monolayers of 820 nm diameter polystyrene spheres self-assembled on the

FDTO substrate. The sulphate modified polystyrene spheres formed thermodynamically stable hexagonally close packed monolayers of polystyrene spheres on the FDTO over a range of 2 mm^2.
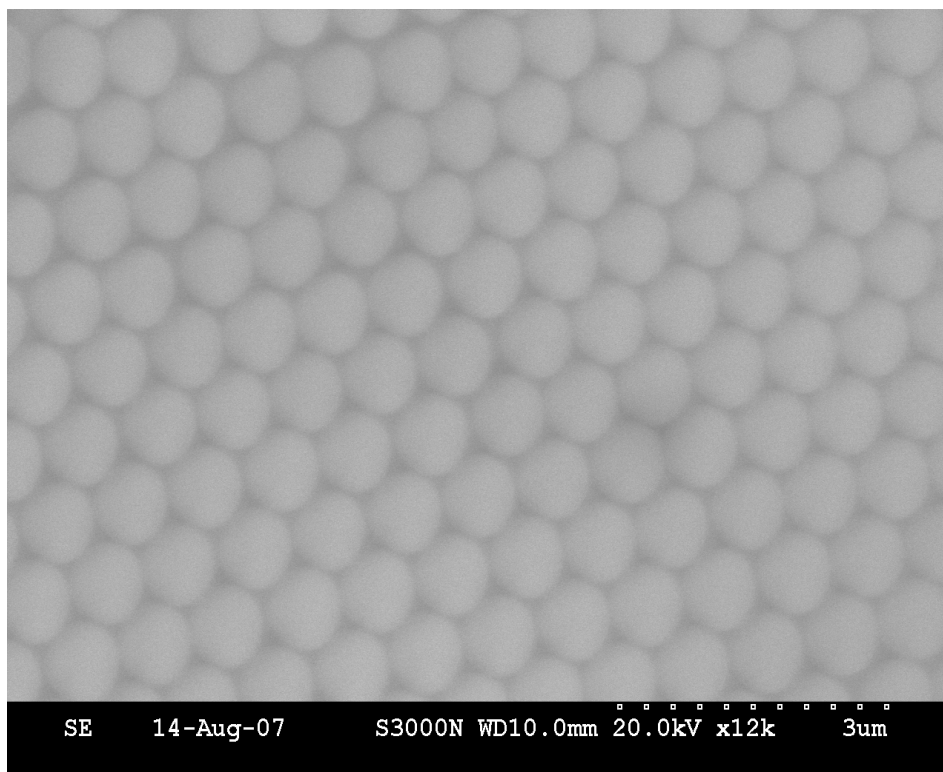

Fig. 2.1: SEM image of self-assembled monolayer of polystyrene spheres with a diameter of 820 nm on FDTO formed from a solution of 1 % polystyrene solution. The accelerating voltage was 20 kV.

Gold nanocavity arrays were prepared by electrochemical deposition of gold through the voids of the close packed monolayers of the polystyrene colloidal particles on FDTO. The diameter of the resulting voids corresponded approximately to the diameter of the templating spheres, and the depth of the voids was controlled by monitoring the amount of charge passed during metal deposition. After deposition, the metal deposited slides were sonicated in THF for one hour to remove the polystyrene spheres. Figure 2.2 (A) and (B) show the resulting nanostructured gold cavities at different magnifications after dissolution of the template in THF. The resulting nanocavities formed a well-ordered, close-packed array, which extended uniformly over an area of approximately 2 mm^2. The open diameter of the cavities was determined from scanning electron microscopy, SEM, to be approximately 700 nm. The majority of the cavities showed a mean diameter

74
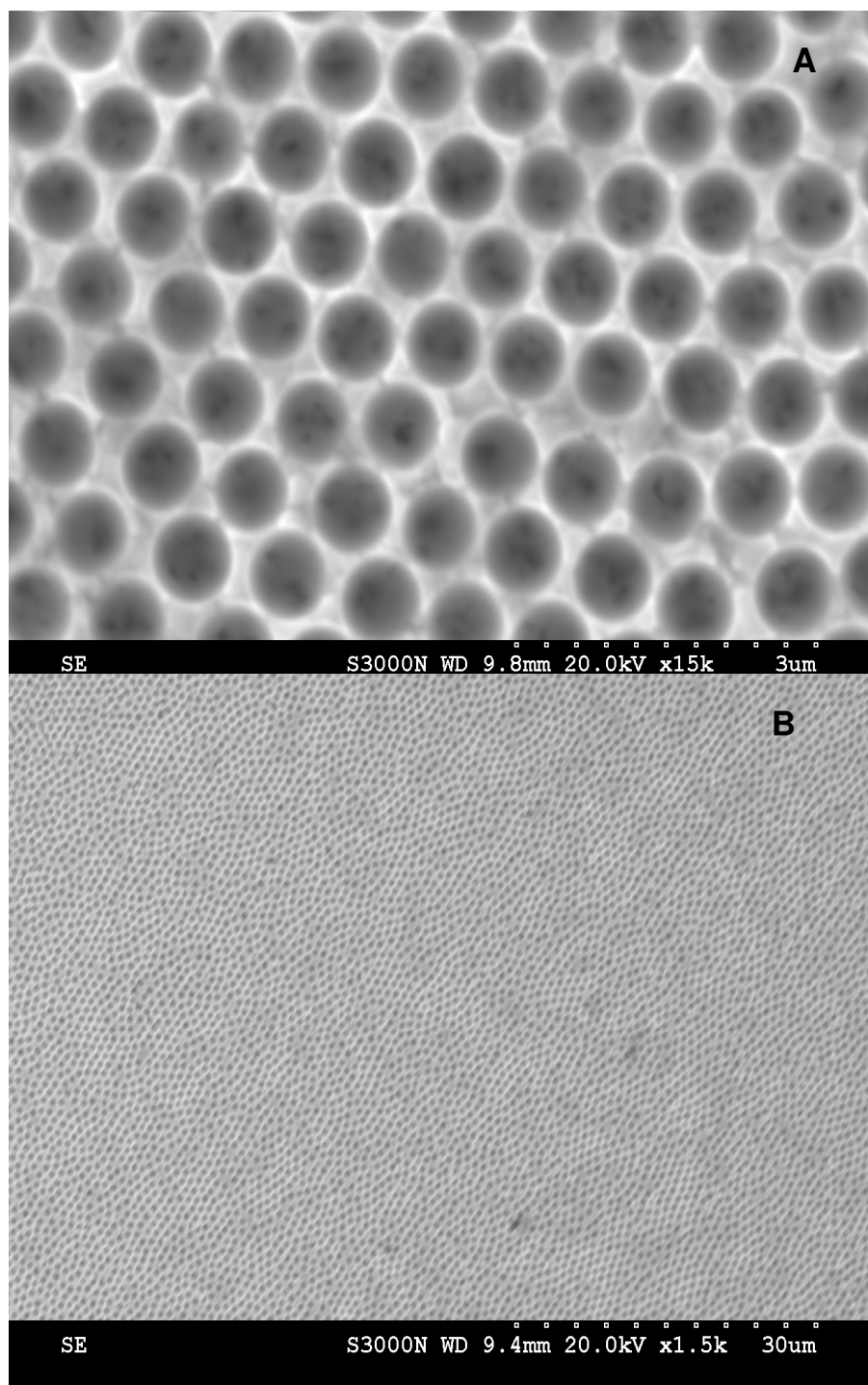
Fig. 2.2: SEM images of gold nanocavity arrays formed on FDTO by electrochemical deposition through the voids of 820 nm diameter arrays. The electrochemical deposition was carried out at a potential of -0.95 V and passing a charge of -0.35 C.cm^{-2}. The images were taken at different magnifications after the dissolution of the polystyrene spheres in THF. The accelerating voltage was 20 kV.

of approximately 700 nm and this is reflected in the cavity size distribution obtained from the analysis of SEM image using Image J software as shown in Figure 2.3. However, the appearance of cavity diameters between 100 and 500 nm were observed in the distribution histogram and these are attributed to artefacts arising from the way in which Image J counts cavities at the edges of the SEM image.

The film thickness 't' of the cavities was calculated from simple trigonometry using Equation 2.1:

$$t = r \pm (r^2 - r^2_{pore})^{1/2} \qquad\qquad 2.1$$

where r is the radius of the template sphere and r_{pore} is the radius of the pore mouth. The choice of the sign for the ± term depends on whether the film is thicker or thinner than the radius of the template sphere. For the 410 nm radius spheres employed here and an open radius of 350 nm, the film thickness could be either 620 or 200 nm. During gold deposition, a potential of -0.95 versus Ag/AgCl (sat. KCl) was applied until a charge of approximately -0.35 C.cm^{-2} is achieved which corresponds to a thickness of around 600 nm if the coulometric efficiency is unity. The actual thickness of the cavity was then experimentally confirmed by side-on SEM measurements after cleaving a gold nanocavity array on smooth gold surface is shown in Figure 2.4. The thickness of the FDTO was approximately 3 mm, therefore, it was impossible to cut the slide after deposition in order to get the SEM images from the side of the slide. Therefore, in order to confirm the thickness of the array by cleaving the slide, the electrochemical deposition were carried out using a smooth gold surface on silicon substrate. The amount of charge passed was approximately the same as on the FDTO substrate. More experimental details about the fabrication of gold nanocavity array on the smooth gold substrate is described in the following chapter. The side-on SEM study confirmed that the array corresponds to a normalised thickness of t_N= t/d = 0.76.[1]

Multilayers of gold cavities could also be formed readily on FDTO. For example, Figure 2.5 shows a multilayer of gold nanocavities formed through a template of 820 nm diameter polystyrene spheres on FDTO. Multilayers of gold cavities were prepared using a multilayer of polystyrene spheres as a template by passing a charge of approximately -0.7 C.cm^{-2} during electrochemical deposition. Highly ordered 3-dimensional

nanostructured spherical voids remained after the dissolution of polystyrene spheres and the connectivity between the layers can be clearly seen from Figure 2.5. Bartlett et al. have shown that the electrochemical deposition of metal through the multilayer of colloidal spheres produces similar three-dimensional microporous structures.[34] Colvin and co-workers have shown that the thickness of the colloidal film (number of layers) can be varied by controlling parameters such as concentration of the colloidal solution and the sphere size.[35] The thickness of the colloidal film is independent of the evaporation conditions but the rate of evaporation can have an impact on the uniformity of the film. The thickness of the multilayer structures can be controlled by monitoring the amount of charge passed during electrochemical deposition. SEM of multilayer gold cavity reveals that the arrays are not hexagonally close packed in whole area of the electrode. Controlled electrodeposition of metals through the self-assembled polystyrene spheres can produce different layers of interconnected spherical voids with different optical and electronic properties. The multilayer of gold nanocavity arrays could be useful as sensors due to its plasmonic properties. In this work, only two dimensional gold nanocavity arrays are further studied in detail.
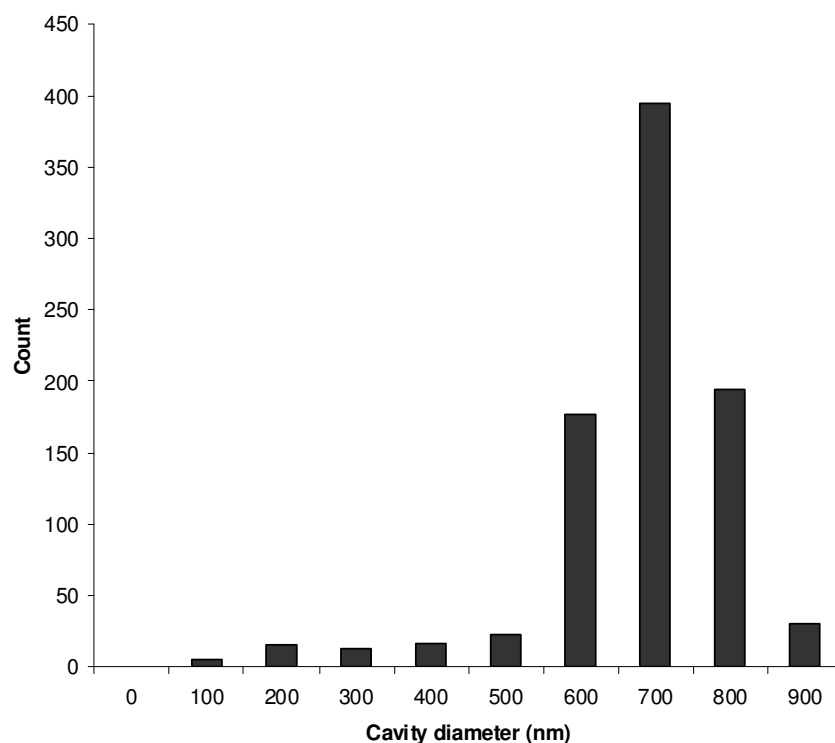

Fig. 2.3: Particle size distribution histograms for gold nanocavity array determined from SEM image using Image J software.
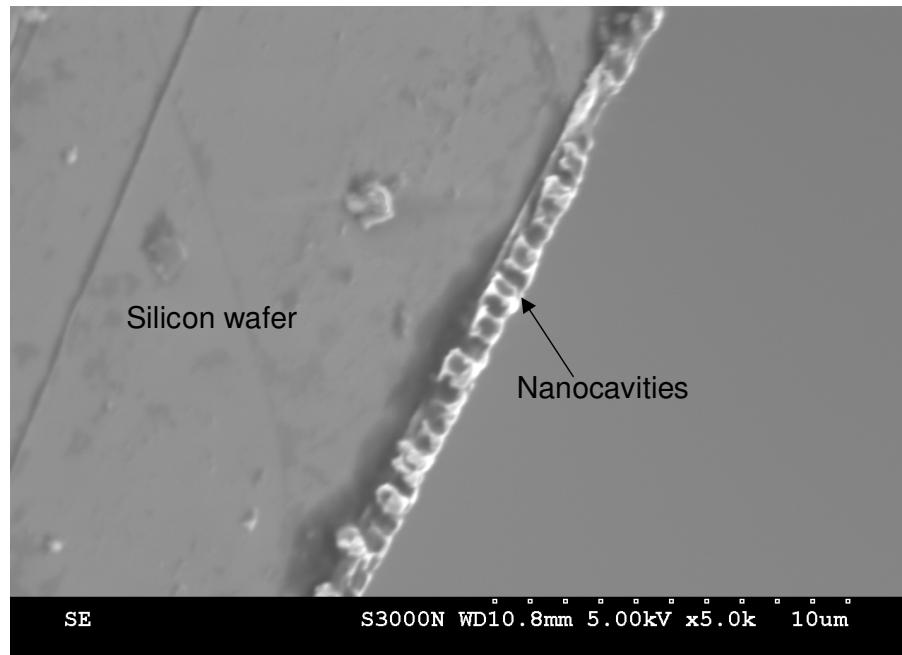
Fig. 2.4: Cross sectional SEM image of the gold nanocavity formed on smooth gold surface by electrochemical deposition through the voids of self-assembled polystyrene spheres.
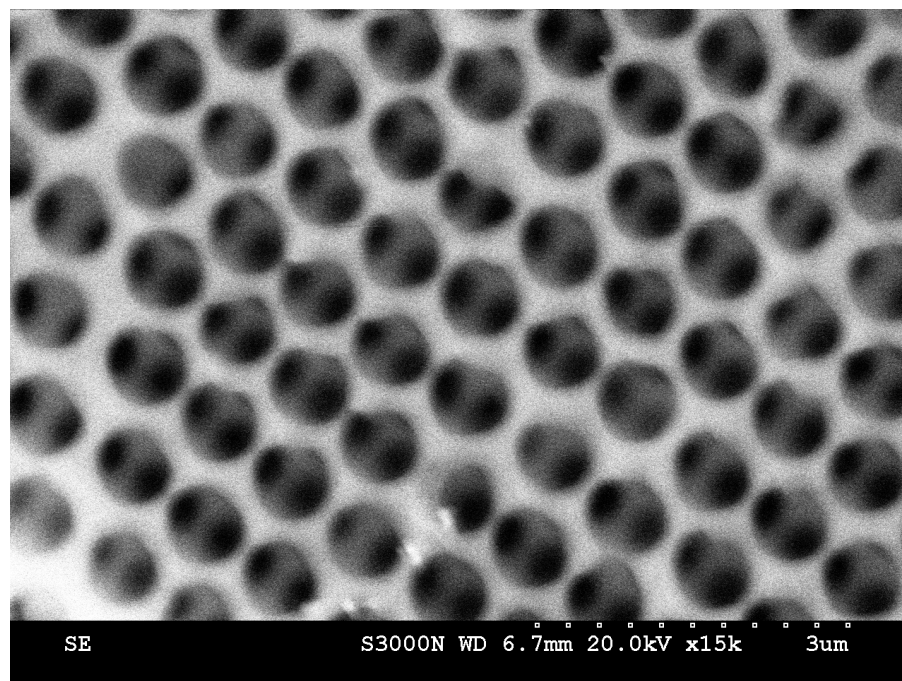

Fig. 2.5: SEM image of a multilayer of gold nanocavities formed by electrochemical deposition of gold through multilayers of 820 nm diameter polystyrene spheres formed on FDTO. The electrochemical deposition was carried out at a potential of -0.95 V and passed a charge of -0.7 C.cm^{-2}. The polystyrene spheres were dissolved in THF by sonication.

2.3.2 Characterisation of cobalt cavities by SEM

The presence of very weak surface plasmons in the visible region for cobalt arrays, makes them a useful comparison for the emission enhancement measurement because the size parameters in context of confocal volume could be controlled. Highly ordered cobalt cavities were prepared in an analogues way to gold cavities by using electrochemical deposition of cobalt through a template of polystyrene spheres on FDTO. Nanocavities were prepared using 820 nm diameter polystyrene spheres as a template. A charge of -0.74 $C.cm^{-2}$ is passed at a potential of -0.9 V to create a 600 nm thick cobalt film. Figure 2.6 (a) shows the SEM image of nanostructured cobalt substrates on FDTO. The hexagonally close packed cobalt nanocavities were prepared on FDTO with negligible defects over dimensions of 1 mm^2. The pore aperture of the nanocavity calculated from the SEM image was around 700 nm as shown in Figure 2.6 B, which is an excellent match for the gold arrays. Similarly, the particle size distribution histogram of cobalt nanocavity arrays show some features above and below 700 nm which is probably an artefact due to counting cavities at the edges of the image or due to the counting of the defects in the packing of spheres.

2.3.3 Diffuse reflectance measurements using UV-visible spectrophotometer

Several reports have shown that nanoscale features on highly reflecting metal surfaces can have strong absorption in the visible region.[36,15] For instance, Whittaker and co-workers have shown that gold nanocavity arrays absorb strongly in the UV-visible region depending on the size and thickness of the film.[36] Therefore, in this work diffuse reflectance measurements were carried out to study the optical reflectivity of gold and cobalt nanocavities in the visible region. The reflectance measurement from gold nanocavity array reveals the presence of strong absorption of light in the visible region. Whereas, the absorption of cobalt cavities in the same region was very weak as shown in Figure 2.7. It has been previously demonstrated that the strong absorption of gold nanocavity arrays arise due to the excitation of localized surface plasmons.
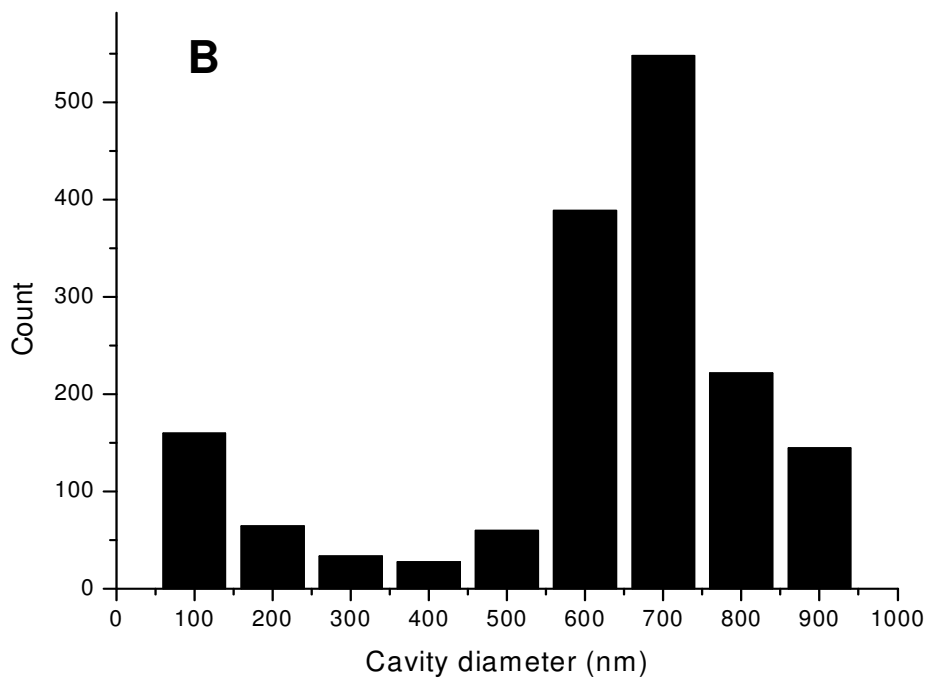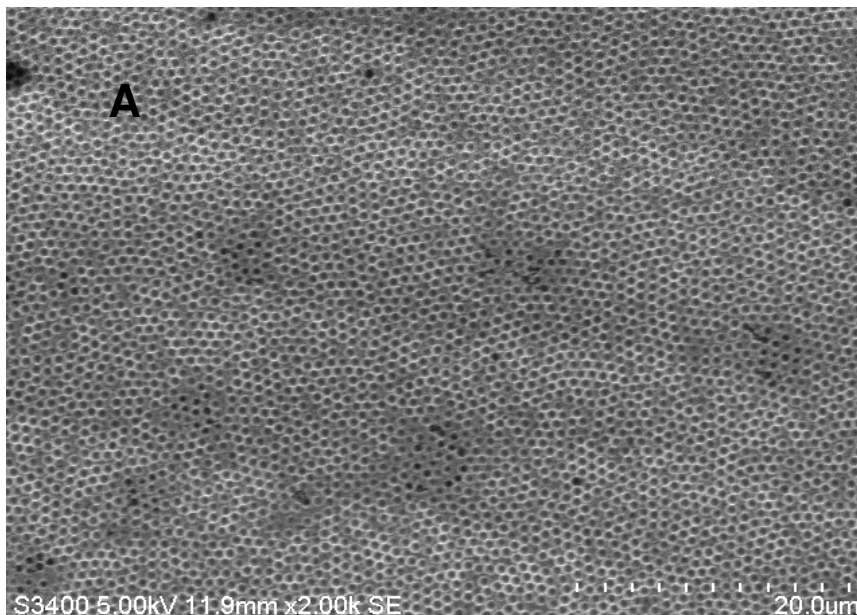
Fig. 2.6: SEM image of (A) electrodeposited cobalt film formed by electrochemical deposition of cobalt through the voids of templated 820 nm diameter spheres on FDTO. The electrochemical deposition was carried out at a potential of -0.9 V. The image was taken after dissolution of polystyrene spheres in THF by sonication. (B) Particle size distribution histogram for cobalt nanocavity array was measured using Image J software.
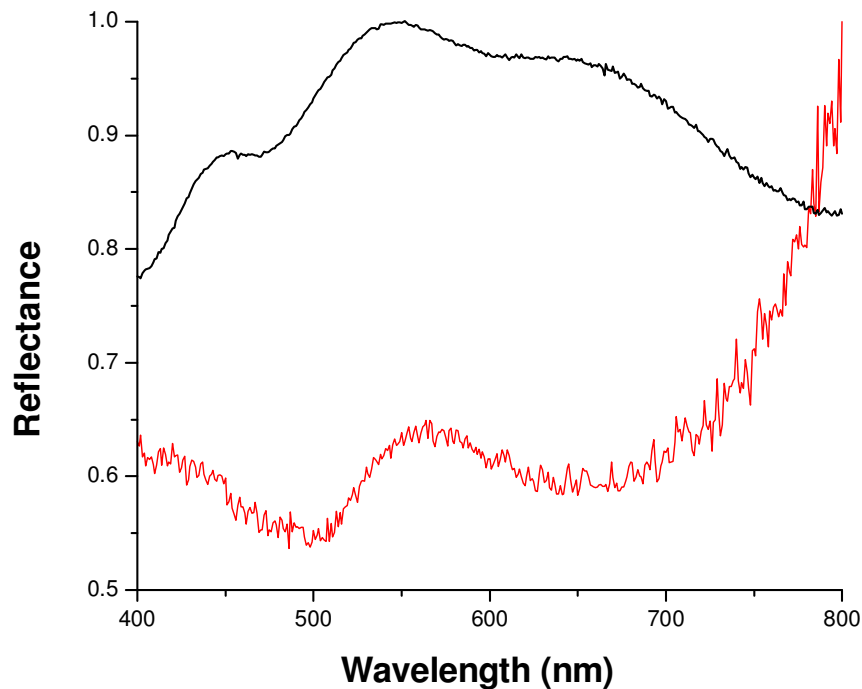
Fig. 2.7: Diffuse reflectance spectra for (—) gold nanocavity arrays and (—) cobalt cavity arrays on FDTO formed by electrodeposition of gold through the voids of 820 nm templated polystyrene spheres. The measurements were carried out in contact with air.

2.3.4 Characterisation of gold cavity arrays by Atomic Force Microscopy (AFM)

The gold nanocavity array prepared on the FDTO glass substrate appears relatively flat in the SEM images, this is somewhat misleading as the FDTO is actually nanoscopically rough. Therefore, the surface roughness and nanoscale features of the gold nanocavity films on FDTO substrates were also characterised using AFM. Figure 2.8 shows the AFM images of the gold cavity film on the FDTO substrate at different magnifications. The nanoscale roughness of FDTO substrates can be clearly seen as bright features in the image and, consistent with SEM, the opening diameter of the gold cavity was around 700 nm as shown in Figure 2.8. Figure 2.9 shows the height profile for the gold nanocavity on FDTO. AFM measurements indicate that the thickness of the gold cavity array is around 550 nm, which is smaller when compared to the thickness calculated from SEM measurements and charge passed during the deposition step. This smaller depth is attributed to a tip convolution artefact, which arises due to the negative curvature of cavity walls and dimension of the tip.[37] This artefact arises because of the tip aspect ratio. The tip height was approximately 10 μm and tip radius was less than 20 nm radius.

81
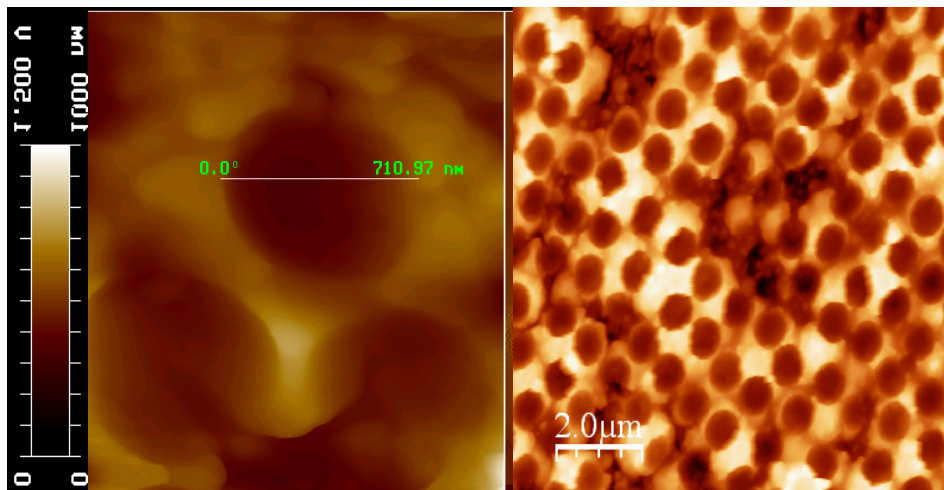
Fig. 2.8: Contact mode AFM images of 820 nm diameter gold cavity array formed by electrochemical deposition of gold through the voids of polystyrene spheres on FDTO at different magnifications. The electrodeposition was carried out at a potential of -0.95 V from gold plating solution. The polystyrene template was dissolved in THF by sonication.
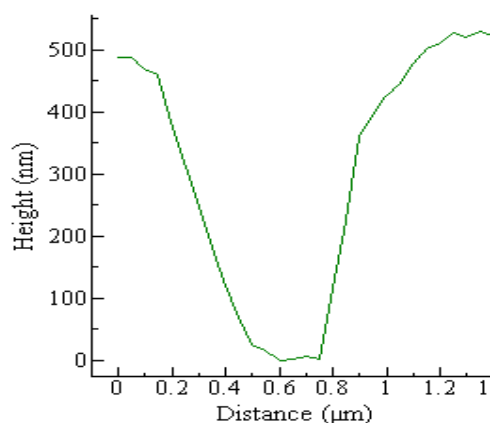
Fig. 2.9: The height profile of the gold nanocavity arrays (820 nm diameter) measured from AFM image. The gold nanocavity arrays were prepared on FDTO using nanosphere lithography followed by electrochemical deposition.

2.3.5 Contact angle measurements

Baumberg and co-workers systematically studied the wettability of gold nanocavity arrays.[38] Their report revealed that the wettability of patterned gold surface depends on the thickness of the film but is independent of the pore diameter over the range 400-800 nm. As the desire is to fill the arrays with aqueous solution, an important parameter to measure is wettability which dictates the spread of water on a surface which will dictate filling. The hydrophilicity of a substrate is usually evaluated using contact angle measurements. A surface is considered as hydrophobic when the contact angle is greater than 90 °C and a surface is considered as hydrophilic when the contact angle is less than 90 °C. Here, in order to understand the wettability of 820 nm diameter array on FDTO, with a normalized thickness of 0.8, contact angle measurements were carried out using water and methanol. For water, θ values of 93±7° and 94±7° were obtained for gold deposited on FDTO and for the gold nanocavity array on FDTO respectively, indicating
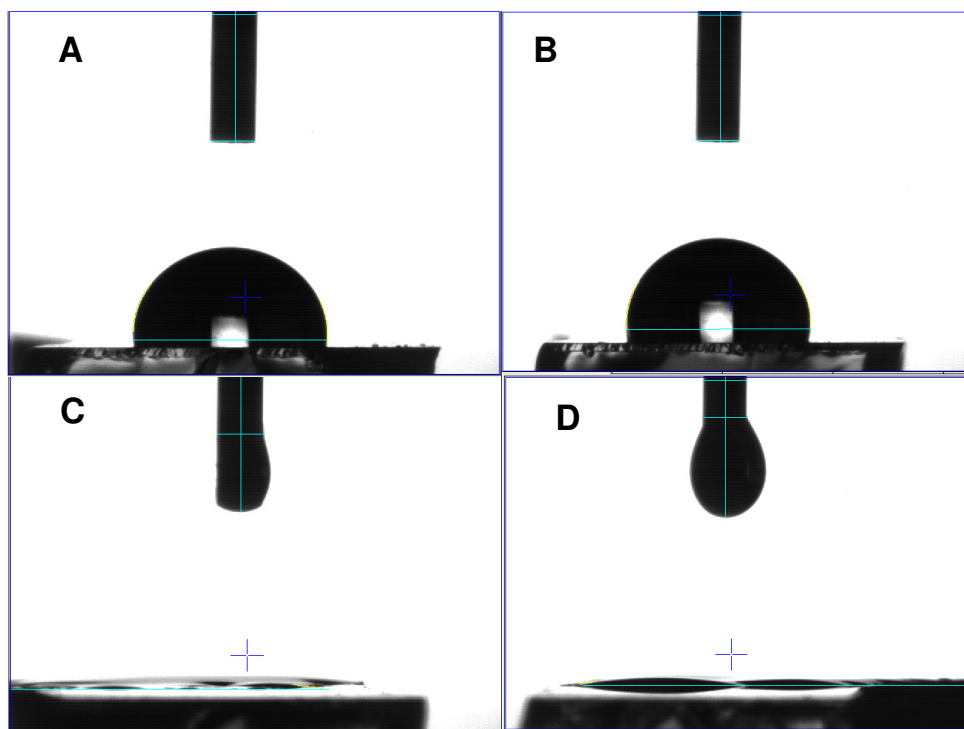
Fig. 2.10: Contact angle measurements using water and methanol (A) electrodeposited gold on FDTO (water) (B) gold nanocavities on FDTO (water) prepared using nanosphere lithography followed by electrochemical deposition (C) gold cavities on FDTO (methanol) and (D) gold deposited on FDTO (methanol).

both surfaces are similar and modestly hydrophobic. In contrast, both surfaces showed very high wettability by methanol with contact angles of 29±5° for bare electrodeposited gold on FDTO and 7±3° on the cavity array as shown in Figure 2.10. In summary, gold nanocavity arrays fabricated on FDTO were modestly hydrophobic therefore, it will be necessary to modify the substrate to make it hydrophilic and then to support bilayer.

2.3.6 Investigation of filling property of gold cavities using confocal microscopy

As discussed earlier, the ultimate application of the arrays in this project is to prepare a biomimetic platform by spanning lipid bilayers across the array and an essential factor for the proper function of lipid bilayers is the aqueous environment at both sides of the membrane. Therefore, a critical issue in this work is the ability of the arrays to fill with fluid. Here, a study of filling capability of these arrays were carried out using confocal microscopy with a luminescent $[Ru(bpy)_2(Qbpy)]^{2+}$ molecule.

Initially, the arrays were placed in contact with methanolic solution of $[Ru(bpy)_2(Qbpy)]^{2+}$ dye, and the array was studied after various time periods by fluorescence microscopy. It was found that merely placing the substrate in contact with a methanolic solution of the dye, even over a period of several hours, was insufficient to achieve filling of the nanocavities. Some partial filling was noted but the majority of the cavities were failed to fill at all. Recently, Antonio and co-workers have shown that the trapping of air nanobubble occurs at the interface between water and hydrophobic nanopatterned silicon substrate and this air bubble can block water penetration into the pores.[39] Baumberg et al. have discussed the possibility that the gold nanocavity arrays can trap air inside the voids, which can make the substrate hydrophobic depending on the thickness.[38] In order to force the dye into the cavity and disrupt any air nanobubble inside the void, the sample was sonicated in a methanolic solution of dye at different time intervals. Figure 2.11 shows the changes in intensity recorded from the nanocavity array after 5 minutes, 15 minutes and 30 minutes of sonication in a methanolic solution of $[Ru(bpy)_2(Qbpy)]^{2+}$ dye. The figures on the left show the intensity profile collected from approximately five cavities after sonication. After 5 minutes of sonication, the gold cavities had begun to fill and in contrast to simple immersion or deposition of solution onto the arrays. Importantly, as indicated in the intensity profile (Figure 2.11, left) filling was quite even across the cavities (Figure 2.11 (A)) and the intensity was approximately 1000 ± 100 as shown in intensity profile. Figure 2.11 (B) and (C) show that intensity increased with time over a further 15 and 30 minutes sonication, wherein the intensity
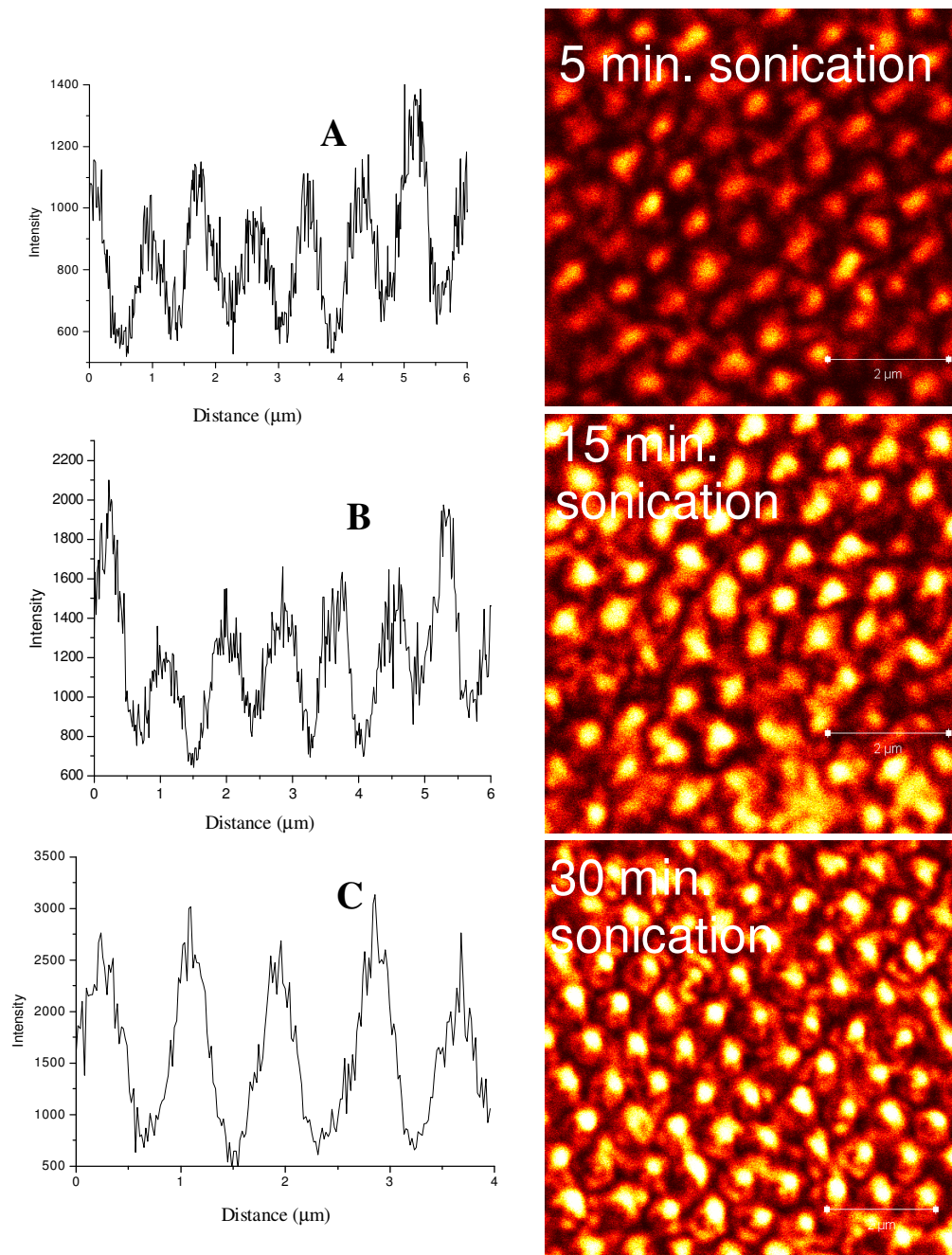
Fig. 2.11: Confocal luminescence microscopy profiles (left) and images (right) of gold nanocavities following sonication with 1 mM $[Ru(bpy)_2(Qbpy)]^{2+}$ dye, laser excitation intensity and detector gain are identical throughout each measurement. (a) 5 minutes (b) 15 minutes and (C) 30 minutes of sonication of gold nanocavities with the dye solution. The excitation wavelength was 488 nm.

was approximately 1500 ± 200 and 2500 ± 300 for 15 and 30 minutes sonication, respectively. Figure 2.12 shows the dynamics of filling of gold nanocavity arrays at different time intervals. This is calculated from the confocal microscope images (Figure 2.11) and shows that 30 minutes of sonication is required to completely fill the arrays with solvents. Further sonication, beyond 30 minutes, did not increase the intensity further. This suggests that all the cavities are completely filled at this point, which is reflected by the reproducible signal intensity from each cavity in scanning across the array. This experimental data suggests that sonication was required in order to achieve effective filling of the cavities. As described, the incomplete filling of the nanocavities in the absence of sonication is speculated to arise due to the presence of air bubbles trapped inside the pores, which blocks complete filling with solution and sonication is likely to disrupt air bubbles.
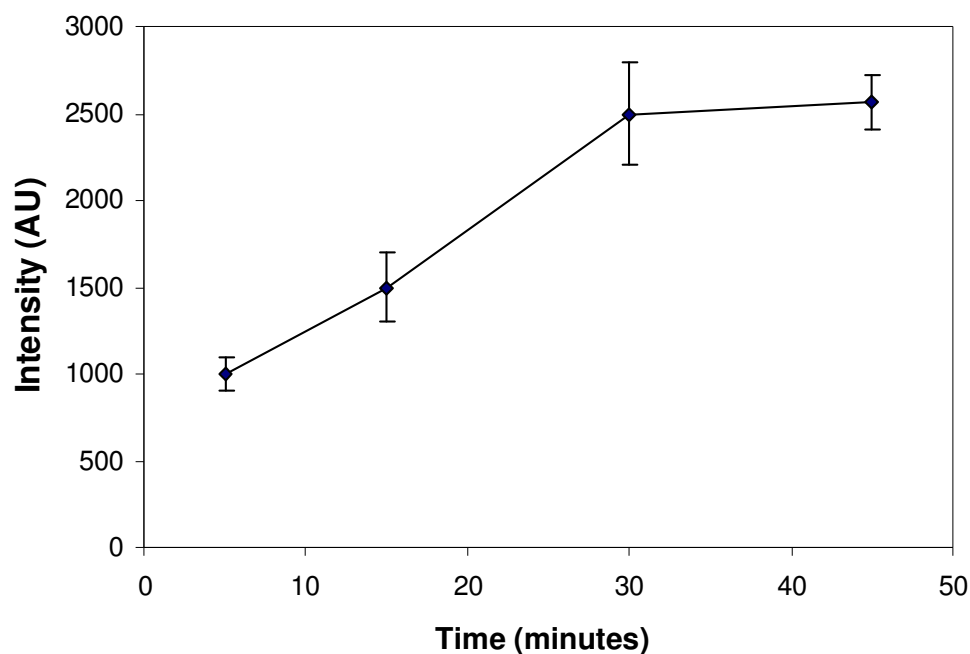
Fig. 2.12: Dynamics of filling of gold nanocavity arrays calculated from confocal microscope images (Figure 2.11). 1mM methanolic solution of $[Ru(bpy)_2(Qbpy)]^{2+}$ dye used as a probe molecule.

It is important to consider whether sonicating for extended periods has any impact on the topography of the gold substrate. Therefore, the SEM image of the gold nanocavities was collected after 30 minutes of sonication confirmed that this process does not affect the nanocavities structure. After filling of the arrays with the dye, the exchange of material in/out of the cavities was investigated using fluorescence microscopy. The filled array

kept upside down in contact with methanol solution and recorded the changes in luminescence intensity of the solvent with time. This experiment reveals that, the methanolic solution of $[Ru(bpy)_2(Qbpy)]^{2+}$ could be readily cleared from the cavity by washing the array with pure methanol without sonication. The array after washing out of dye is shown in Figure 2.13. The graph (right) in Figure 2.13 shows the intensity profile and image from the gold nanocavity array after washing with methanol. This study confirmed that over 30 minutes sonication little monolayer formation had occurred within the cavity and meant that over such short time-scales the $[Ru(bpy)_2(Qbpy)]^{2+}$ solution could be used to study the effect of the array on the photophysics of a solution phase luminophore without the complication of monolayer formation. That filling and washing out of the dye solution in nanostructured metal surface is possible indicates that sonication facilitates the exchange of dye molecules both inside and outside the cavity.
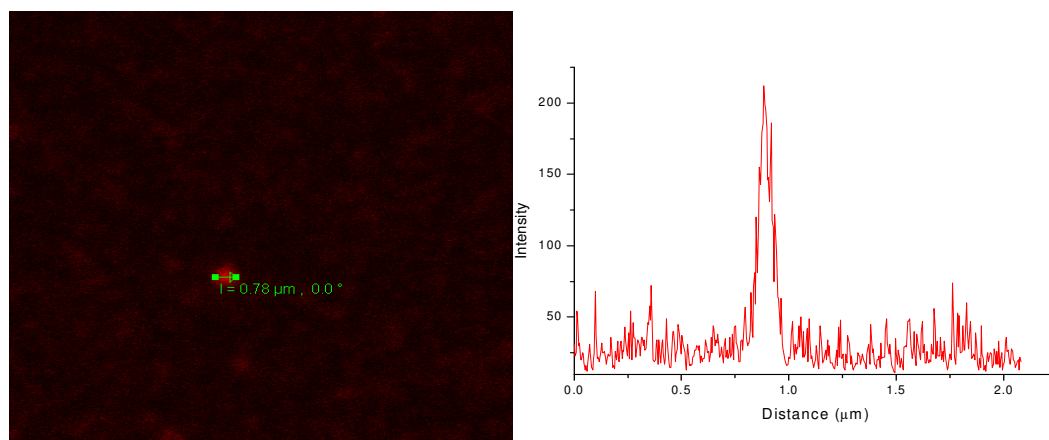

Fig. 2.13: Gold nanocavities with 820 nm diameter array after washing out of the free $[Ru(bpy)_2(Qbpy)]^{2+}$ dye solution using methanol.

2.3.7 SERRS studies of $[Ru(bpy)_2(Qbpy)]^{2+}$ complex on gold nanocavities

As discussed in Section 1.5, gold nanocavity arrays possesses localized surface plasmon resonance in the visible region, which are the basis for surface enhanced Raman and surface enhanced resonance Raman spectroscopies. Previous reports have shown that gold nanostructured surfaces can be useful in SERRS studies.[23] For instance, Bartlett et al. reported 8 orders of magnitude enhancement in resonance Raman from Cy5 dyes compared with Cy3 adsorbed on gold nanocavity arrays.[23] In this work, it is expected that labelled biomolecules incorporated into a suspended bilayer will exploit the surface plasmons from the underlying array. Therefore, it was decided to assess both SERRS and luminescence enhancement from the gold cavity arrays. As the $[Ru(bpy)_2(Qbpy)]^{2+}$ complex is surface active, self assembled monolayers of $[Ru(bpy)_2(Qbpy)]^{2+}$, were prepared by sonicating 1 mM solution of dye in methanol with cavities for 30 minutes. Then, the solution was left in contact with the array for 24 hours. Following this period, the arrays were washed extensively with methanol under sonication to eliminate unbound dye. The arrays were then dried under a stream of nitrogen. To confirm monolayer assembly on the gold nanocavity array, Raman microscopy was employed. Figure 2.14 shows the Raman spectrum of the monolayer modified array (thick line) and for comparison, a thin solid film of $[Ru(bpy)_2(Qbpy)]^{2+}$ dried onto a clean FDTO (thin line). The excitation wavelength was 514 nm. This wavelength is post-resonant with the broad Ru ($d\pi$)-ligand (π^*) MLCT transition of this complex as shown in Figure 2.15. Therefore, the Raman spectrum of the dye, both as solid and monolayer is anticipated to be resonantly enhanced. The Raman bands can be assigned almost exclusively to ligand centred vibrations. The most intense Raman peaks around 1611, 1557, 1530, 1483 cm^{-1} are attributed to pyridine C-C stretching modes. C-H deformation modes are found around 1320 and 1275 cm^{-1}, and ring vibration modes occur around 1026 and 668 cm^{-1}. A moderately intense feature around 1170 cm^{-1} is attributed to a coupled C-H bend and stretching mode. There are some very weak bands for the solid film of dye on FDTO slide compared to a monolayer on gold nanocavity array. These bands are in the region between 450-1100 cm^{-1} (460, 630, 600, 780, 810, 860 and 1100 cm^{-1}) which can be seen in Figure 2.14. These weak bands were disappeared for the molecules on gold nanocavity arrays which is attributed to the huge enhancement of specific bands

compared to these weak signals. A significant enhancement in signal intensity from dye molecules is evident in the monolayer on the nanocavity array after normalization for the number of molecules in the laser spot. The Raman signal intensity of the dye on the gold surface is highly reproducible and shows little variation (<2 %) in intensity when recorded from different spots across the surface. The defect free areas from the slides were selected for the measurements using white light imaging.
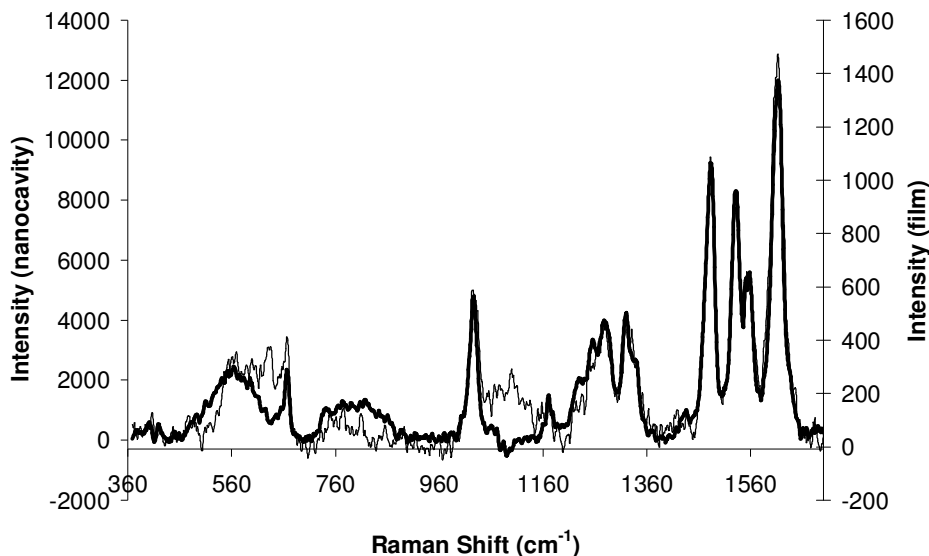
Fig. 2.14: Resonance Raman spectrum of thin film of $[Ru(bpy)_2(Qbpy)]^{2+}$ on FDTO (light line, right hand axis) and the surface enhanced resonance Raman of a monolayer of $[Ru(bpy)_2(Qbpy)]^{2+}$ on nanostructured gold surface (heavy line, left hand axis). The excitation wavelength was 514 nm. Both measurements were conducted at identical conditions. The laser spot size was 2 μm.

The surface enhancement factor (SEF) for molecules on the gold nanocavity array was determined using Equation 2.2.

$$SEF = (I_{Au}/N_{Au})/(I_{fdto}/N_{fdto}) = (I_{Au}/I_{fdto})*(N_{fdto}/N_{Au}) \qquad 2.2$$

where I_{Au} and I_{fdto} denote the integrated intensities of Raman peaks of the Ru complex on the gold nanocavity arrays and as a solid film on FDTO, respectively, whereas N_{Au} and N_{fdto} represent the corresponding number of molecules estimated to be present in the focus of the gold and FDTO samples respectively. The ratio of I_{Au} and I_{fdto} was determined from the area under the curve of the four most intense Raman bands of the Ru complex, which are seen at 1611, 1557, 1530 and 1483 cm^{-1}. The average ratio from

these bands was 10.3 ± 1.5. The number of molecules in the laser focus on the gold nanocavity arrays was estimated by assuming complete monolayer surface coverage at the array and taking the increased surface area due to spherical shape of the nanocavities into account. The area occupied by a single $[Ru(bpy)_2(Qbpy)]^{2+}$ complex was taken to be 150 Å^2 as reported earlier.[40] The number of molecules resident in the laser focus on the FDTO slide was determined electrochemically. The charge under the oxidation curve from the cyclic voltammogram is used to calculate the number of molecules in the laser focus. It was found that 5×10^6 more molecules occupied the confocal volume for the thin film compared with the monolayer on the gold substrate. This gives an overall enhancement factor (SEF) of 5×10^7 for the gold nanocavity array. As $[Ru(bpy)_2(Qbpy)]^{2+}$ is resonant with 514 nm excitation to the same degree in both instances, this value corresponds directly to the plasmonic enhancement by the array. This surface enhancement factor is comparable to the values reported for the nanostructured metal surfaces by other groups.[1,41] The suitability of such arrays as SERS substrates has been discussed before.[42] Due to the excellent reproducibility of the Raman signal intensity across the array, this material shows an outstanding promise as SERS platforms. Comparison of SERRS from the gold cavity array with cobalt cavities is useful to confirm the influence of plasmons on the signal of gold cavities but the cobalt cavity was not sufficiently stable in methanolic solution for 24 hrs. The cobalt cavities were immersed in methanolic solution of dye for 24 hrs in order to form monolayers of dye on the cobalt however, the arrays were disrupted, resulting loosing their structure. Therefore, the formation of monolayers of dye inside the cobalt cavity was not possible.

2.3.8 The effect of nanocavity array on luminescence

Several groups have reported that metallic surfaces can enhance emission from fluorescent tags attached to the biomolecules such as DNA, or antibody. Metal enhanced fluorescence can increase the sensitivity of fluorescence based analysis.[43,44] However, there have been relatively few studies on molecule close to gold cavity structures. The effect of gold nanocavity arrays on the luminescence properties of two weak and modest luminophores were investigated using $[Ru(bpy)_2(Qbpy)]^{2+}$ dye and fullerene as probe molecules. Lakowicz and co-workers have reported that the metal enhanced fluorescence is greatest for low quantum yield dyes when it is near a metal surface as there is more

capacity for enhancement of Φ when its value is low.[27] Therefore, $[Ru(bpy)_2(Qbpy)]^{2+}$ dye which has a low quantum yield was selected to investigate the influence of 820 nm diameter gold nanocavity array on the photophysical properties of the dye. Figure 2.15 shows the absorption and emission spectra of $[Ru(bpy)_2(Qbpy)]^{2+}$ dye (100 μM) in methanol. The MLCT transition for $[Ru(bpy)_2(Qbpy)]^{2+}$ dye is around 475 nm and the emission is around 650 nm.
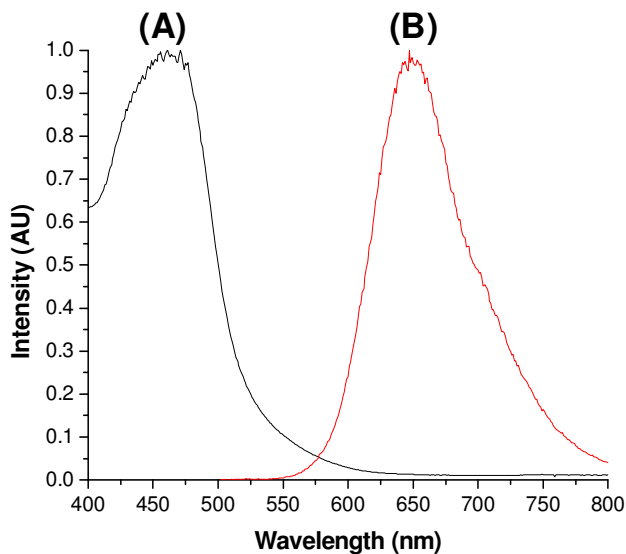

Fig. 2.15: The absorption (A) and emission (B) spectra of $[Ru(bpy)_2(Qbpy)]^{2+}$, 100 μM in methanol. The excitation wavelength for emission spectrum was 450 nm. The slit width was 5 nm. Both spectra were normalized to the maximum intensity value.

The impact of 820 nm diameter gold nanocavity array on the luminescent properties of $[Ru(bpy)_2(Qbpy)]^{2+}$ dye was studied using confocal microscopy under two different excitation wavelengths, 488 and 514 nm. Confocal microscopy is used here to visualize the luminescent enhancement from the gold nanocavity array due to its optical sectioning capability. This special feature provides an opportunity to get optical slices to form a three-dimensional object. In this work, Z-stack measurements were carried out to visualize the localized emission enhancement from the spherical gold nanocavities. The confocal volume of the laser in the Z-direction was around 700 nm, so it was difficult to accurately locate the exact enhancement position from the nanocavities. The experimental set up for Z-stack measurements is shown in Scheme 2.4. The filling solution containing free dye molecule was kept in between the cover glass and the dye filled array for direct comparison of the emission intensity from the solution and the enhanced emission from the dye filled cavities.

Figures 2.16 and 2.17 show the excitation wavelength dependent emission from the $[Ru(bpy)_2(Qbpy)]^{2+}$ dye filled gold cavities at 488 nm and 514 nm excitation. These two wavelengths were chosen due to their close match with the absorbance of 820 nm diameter gold cavities (514 nm) and the absorbance of ruthenium dye (488 nm). As discussed in Chapter 1, enhancement in emission intensity can be due to the increased rate of excitation and/or due to the increased rate of radiative decay induced by the metal substrate.

Figures 2.16 and 2.17 show the Z-stack images collected from $[Ru(bpy)_2(Qbpy)]^{2+}$ dye filled cavities under 488 nm and 514 nm excitation respectively and these measurements were carried out using confocal microscope. In this experiment, the dye filled gold nanocavity arrays were placed upside down on the cover glass with the free dye solution in between the cover glass and the gold cavity array as described in Scheme 2.4. 1 mM methanolic solution of dye was used for the measurements. The scan started from the cover glass, then proceeded through the dye solution and finally collected the emission from the dye filled arrays. The green colour shows the luminescence signal collected from the dye solution. Figure 2.16 shows the emission from the dye filled gold cavities under 488 nm excitation, clearly demonstrating that the emission from the dye was comparatively low, even though the MLCT transition is most strongly coincident with this wavelength than 514 nm. As the emission intensity from the dye filled gold cavity array excited at 488 nm was not strongly enhanced compared with bulk solution, it was easy to collect emission from both dye solution and the dye filled gold cavity with the same experimental settings. The slices between 10 and 27 show the emission from the dye solution above the array and the slice 30 shows the emission intensity collected from the dye filled gold cavity. Under 488 nm excitation, the luminescence intensity from the dye filled gold cavities was comparable with the emission from the free dye solution. However, excitation at 514 nm exhibits (Figure 2.17) a large enhancement in emission from dye solution inside the cavity compared with bulk, therefore it was hard to see emission from the dye in between the cover glass and the filled cavity under the experimental conditions used to collect the cavity emission i.e., without increasing laser power or detector gain to collect both emission. The Z-stack interval between slices was approximately 400 nm but the images look somewhat longer than the expected scale,

which is attributed to the elongation of the confocal width in the z-direction caused by the optics.
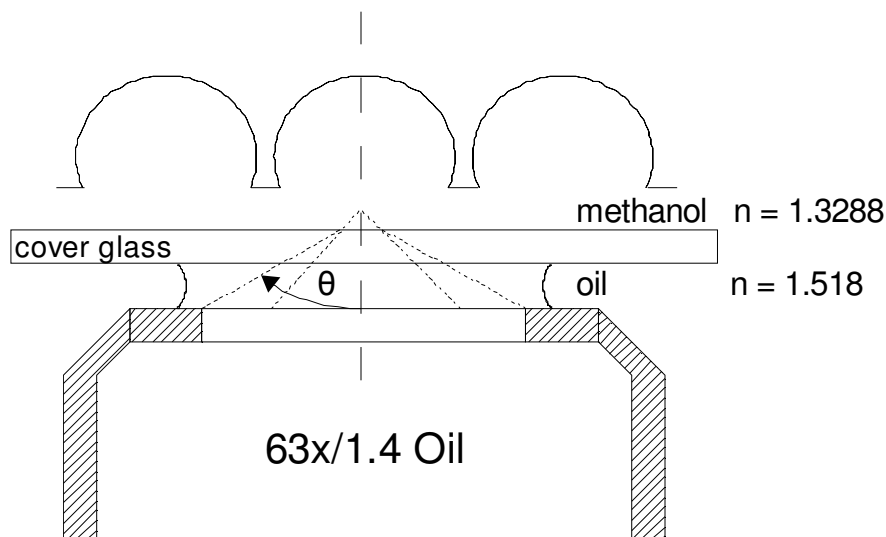
Scheme 2.4: Experimental set up on confocal microscope. The laser is focussed to the array through cover glass using a high resolution, oil immersion objective 63x. The solvent/dye solution kept in between the cover glass and dye filled arrays.

During the measurement, the luminescence and reflectance were separated using appropriate filters from the dye filled cavities and collected using separate channels. Figures 2.18 (A) and (B) show the combined images of luminescence and reflectance from the dye filled cavities under 488 and 514 nm excitation. The red line shows the emission intensity and the black trace shows the reflectance coming from the dye filled 820 nm diameter array. It can be seen that the reflectance (black trace) is dominating at 488 nm excitation whereas the luminescence trace (red line) is significantly stronger than reflectance signal at 514 nm excitation. The blue colour in the image shows the reflectance collected through the channel 1 and the green colour shows the luminescence collected through the channel 2 from the dye filled cavity. The inset of Figure 2.18 (B) reflects the enhancement of luminescence intensity from the dye filled gold cavities from different Z-planes at 514 nm excitation. These Z-stack measurements shows a 10-fold enhancement from the $[Ru(bpy)_2(Qbpy)]^{2+}$ dye filled gold cavities compared to the free dye solution at 514 nm excitation. This enhancement factor is calculated from Z-stack measurements using image J software. Slices from 10 to 20 give the emission from the dye in bulk solution and 20-30 shows the enhanced emission from the dye filled gold cavities. In this way, the luminescence from the dye in bulk solution and in the gold

cavity array could be measured and compared directly using the same experimental settings.
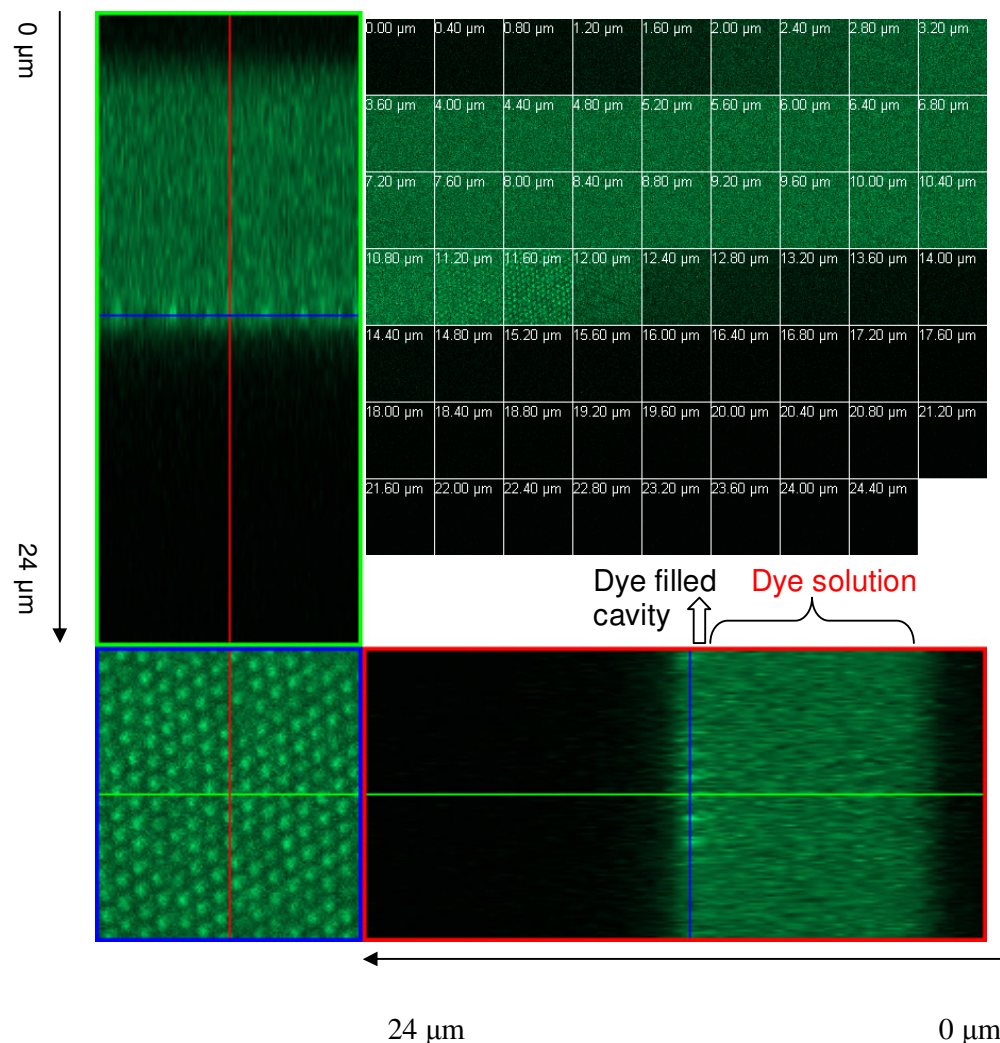
Fig. 2.16: Emission from $[Ru(bpy)_2(Qbpy)]^{2+}$ dye filled gold cavities at 488 nm excitation. The Z-stack measurement was carried out by recording the X-Y image from different Z-plane. The scanning started from the cover glass and then proceeded through free dye solution to the filled cavity. The green colour shows the emission collected through the fluorescence channel.
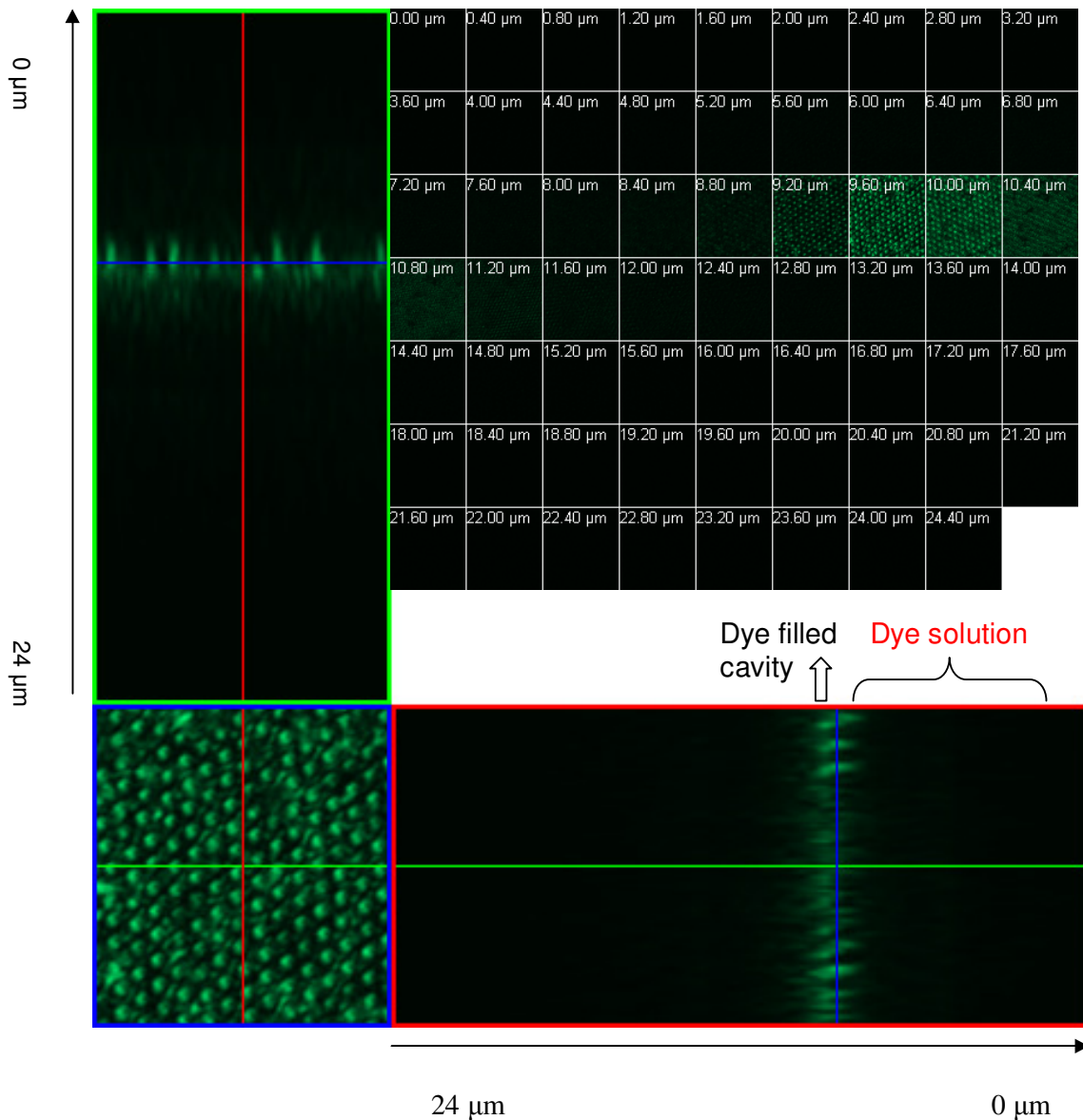
Fig: 2.17: Emission from $[Ru(bpy)_2(Qbpy)]^{2+}$ dye filled gold cavities at 514 nm excitation. The Z-stack measurement was carried out by recording the X-Y image from different Z-plane. The scanning started from the cover glass and then proceeded through free dye solution to the filled cavity. The green colour shows the emission collected through the fluorescence channel.
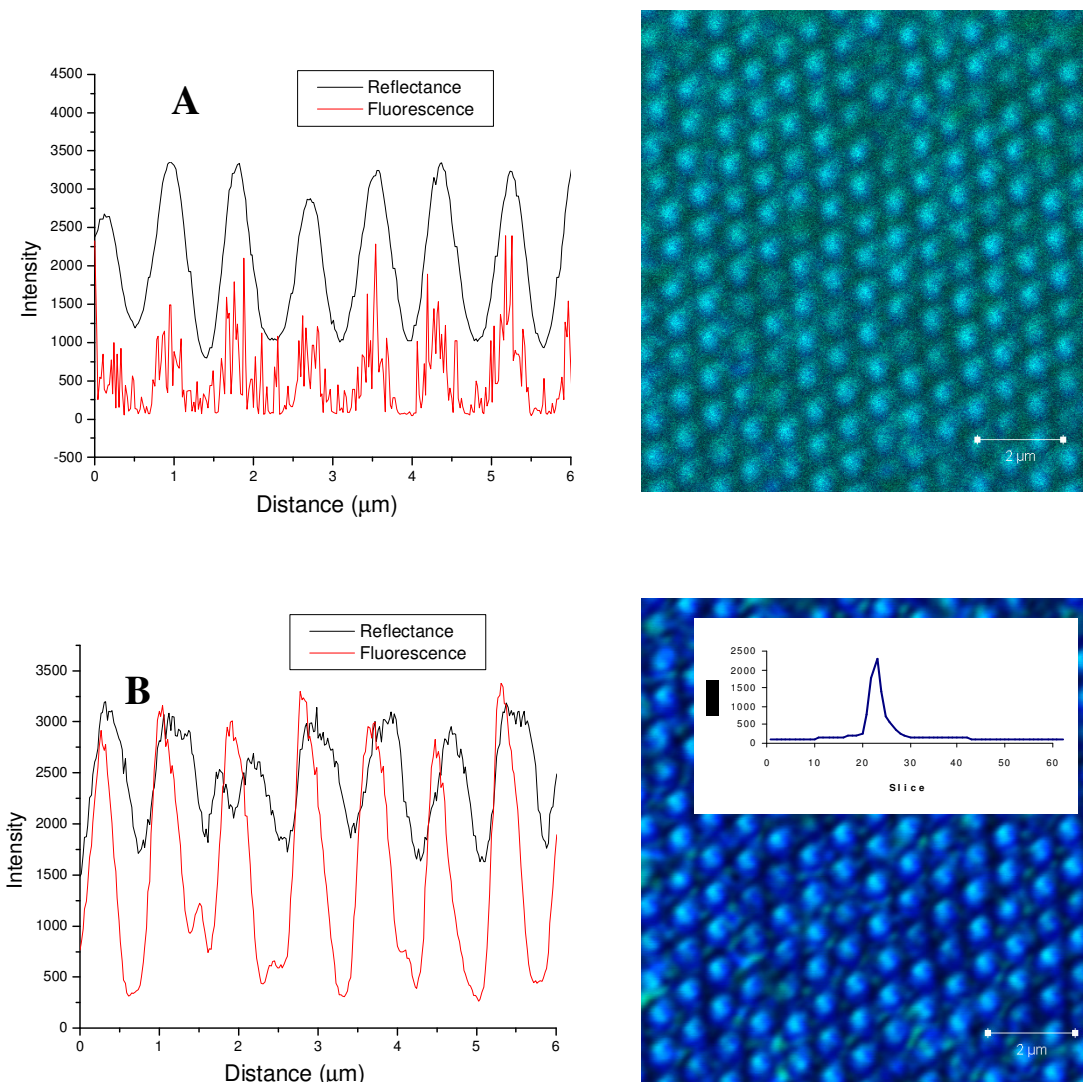
Fig. 2.18: Wavelength dependent emission from $[Ru(bpy)_2(Qbpy)]^{2+}$ dye filled gold cavities at (A) 488 nm excitation and (B) 514 nm excitation. The red trace in profile shows emission and the black trace shows the reflectance from dye filled arrays. The inset shows the enhancement between the slices at 514 nm excitation.

The Z-stack measurements reveal that dye filled gold nanocavity arrays show a 10-fold enhancement in emission intensity at 514 nm excitation compared to the bulk dye solution. Although, identical experimental settings were used to measure the emission from both the dye solution and the dye filled array, the accurate measurement of the enhancement factor was difficult due to the increased volume of spherical shape nanocavity and the thickness of the bulk dye solution in the confocal volume. Therefore, cobalt cavities were also used as a control platform for the direct comparison of the plasmonically enhanced emission from the dye filled gold nanocavities. Cobalt cavities

were selected due to their very weak absorption in the visible region compared to gold cavities as shown in Figure 2.7. Figures 2.19 and 2.20 show the Z-stack measurements for the dye filled cobalt cavities under 488 and 514 nm excitation, respectively. The Z-stack measurements were carried out using the $[Ru(bpy)_2(Qbpy)]^{2+}$ dye solution in between the dye filled cobalt cavity and the cover glass. Here, it is expected to see similar luminescence intensity at two excitation wavelengths due to the weak absorption of cobalt arrays at this region. However, it can be clearly seen that the emission signal intensity at 514 nm excitation was greater than 488 nm. This indicates that there is an other contribution to emission at 514 nm that may be due to the reflectance coming through the fluorescence channel. The dye filled cobalt cavities are not well defined at either 488 or 514 nm excitation, the reason for this is unclear.
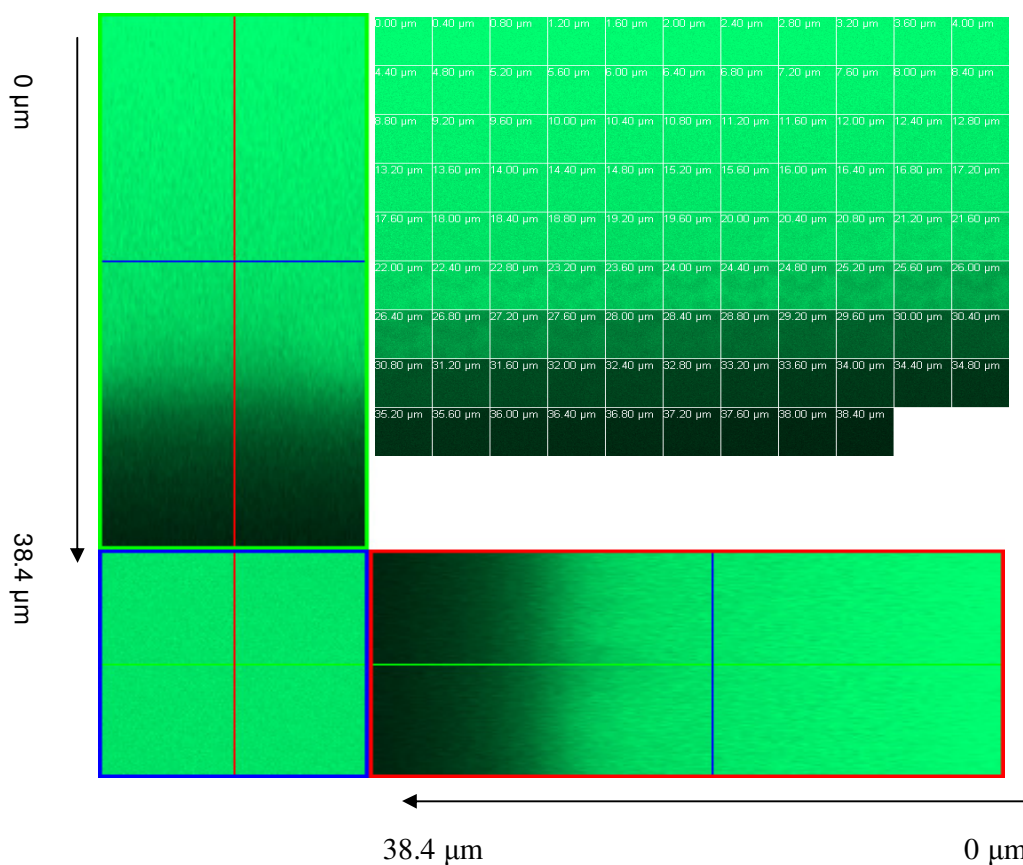
Fig. 2.19: Emission from $[Ru(bpy)_2(Qbpy)]^{2+}$ dye filled cobalt cavities at 488 nm excitation. Z-stack measurements were obtained by scanning across the filled cavity using the dye in between cover glass and filled cavity.
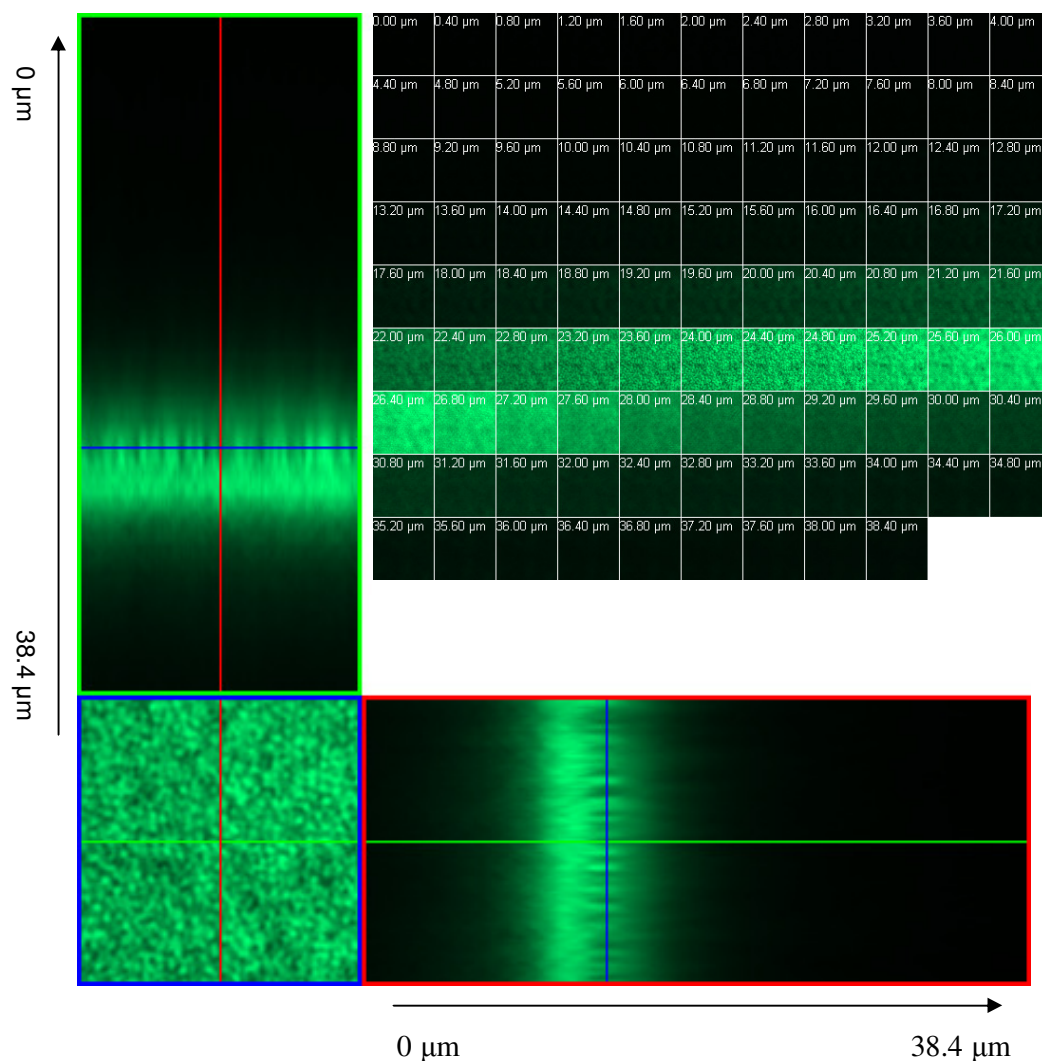
Fig. 2.20: Emission from $[Ru(bpy)_2(Qbpy)]^{2+}$ dye filled cobalt cavities at 514 nm excitation. Z-stack measurements were obtained by scanning across the filled cavity using the dye in between cover glass and filled cavity.

Therefore, an accurate enhancement factor calculation from the dye filled gold nanocavities was again difficult even after using cobalt cavities in the confocal microscope set up. As an alternative, luminescence measurements were carried out with a Raman spectroscopy to differentiate between the reflectance and enhanced emission from the dye filled gold nanocavities. The dye filled cobalt cavities were used as a control platform, which makes the calculation of enhancement factor easier than the free dye solution. The enhancement of emission from the $[Ru(bpy)_2(Qbpy)]^{2+}$ dye filled cavities at 514 nm excitation is shown in Figure 2.21. The emission signal intensity was

99

very weak from the dye filled cobalt cavities compared to gold cavities, indicating a significant impact of the gold nanocavities on the luminescence of dye. The enhancement factor was approximately 15-fold compared to the dye filled cobalt cavity array.
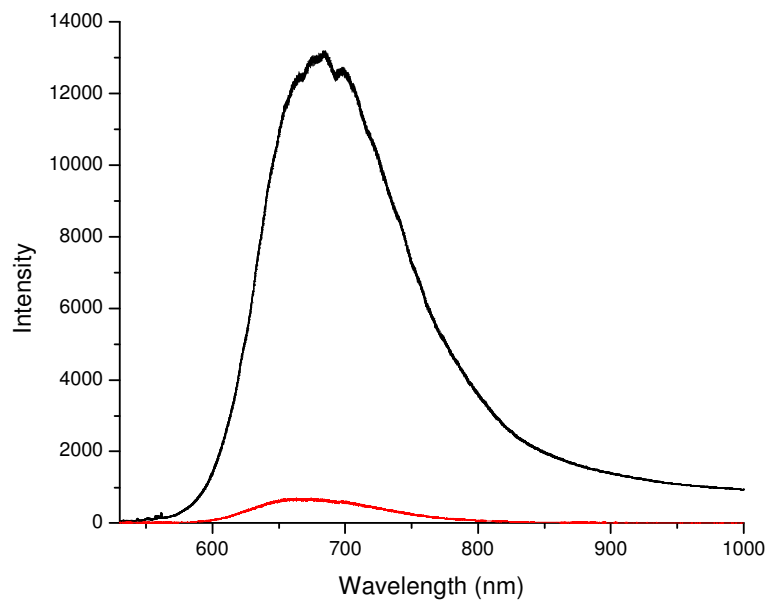
Fig. 2.21: Emission spectra of $[Ru(bpy)_2(Qbpy)]^{2+}$ complex filled gold cavity (—) and (—) cobalt cavity at 514 nm excitation. Methanol was used as a solvent.

2.3.9 Fluorescence lifetime measurements using FLIM

The excitation wavelength dependence of emission from $[Ru(bpy)_2(Qbpy)]^{2+}$ dye filled gold nanocavity arrays suggest that the enhancement in emission intensity occurs due to the plasmonically enhanced excitation rather than increased rate of radiative decay. Changes in the radiative decay rate of the fluorophore should change the lifetime of the fluorophore. But, the lifetime of the fluorophore should remain unchanged if the enhancement in emission intensity is due to the increased rate of complex excitation.[45] Therefore, in order to confirm the origin of the enhancement in emission intensity from the $[Ru(bpy)_2(Qbpy)]^{2+}$ dye filled gold cavity, lifetime measurements were carried out using fluorescence lifetime imaging microscopy (FLIM).

Previous reports have shown that if the emission is enhanced due to the changes in the radiative decay rate, then the quenching of the lifetime could be simulated using following equations.[46]

$$\varphi_m = (k_r + G*k_r)./(k_r + G*k_r + k_{nr}) \tag{2.3}$$

$$\tau_m = 1./(k_r + G*f + k_{nr}) \tag{2.4}$$

where φ_m and τ_m are the quantum yield and the lifetime of the dye in presence of metal surface respectively. k_r is the radiative decay rate and k_{nr} is the non-radiative decay rate. G is the "plasmonic enhancement factor" since it does not include any contributions from increased absorption or spatially directed emission and $G = k_{rm}/k_r$, k_{rm} = metal enhanced rate. According to this simulation, If we take the emission enhancement factor of Φ_m/Φ = 15 we get G = 19 and τ/τ_m of 1.3, i.e. we would expect a decrease in lifetime τ_m to about 230 ns if the ratio Φ_m/Φ = 15 is due to plasmonic enhancement. Therefore, a lifetime of 230 ns is expected if the increase in emission intensity occurs due to the changes in the radiative decay.

The luminescence lifetime of free dye solution was compared with the lifetime of dye in gold nanocavity arrays. The excited lifetime of dye is calculated after fitting the experimental decay curve to a monoexponential equation,

$$I(t) = I_0 \exp(-t/\tau) \tag{2.5}$$

Where I_t is the time-dependent intensity, I_0 is the intensity at time 0 and $\tau = (k_r + k_{nr})^{-1}$.
If the decay is biexponential, the experimental data curve fitted to the equation 2.6.

$$I(t) = A_1 \exp(-t/\tau_1) + A_2 \exp(-t/\tau_2) \qquad\qquad 2.6$$

where A_1 and A_2 are the amplitudes of τ_1 and τ_2, respectively .
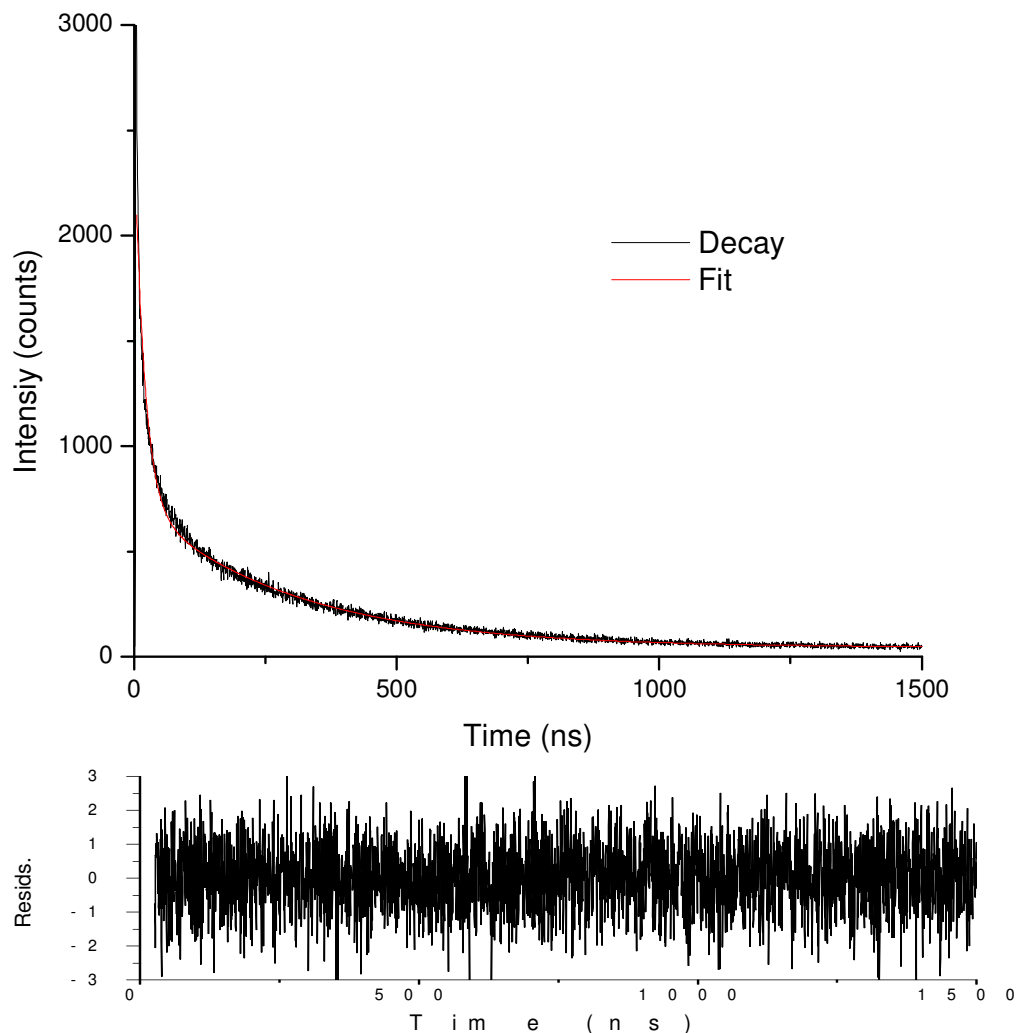
Fig. 2.22: Luminescent decays for $[Ru(bpy)_2(Qbpy)]^{2+}$ dye in bulk aerated solution. The dye is dissolved in 80/20 water and methanol mixture and the concentration of the solution was 100 μM. The excitation wavelength was 405 nm.

The luminescent decays for $[Ru(bpy)_2(Qbpy)]^{2+}$ dye in bulk aerated solution followed first order kinetics characterised by a single lifetime of 306±5 ns as shown in Figure 2.22. The black line shows the experimental decay curve and the red curve is the fit to the Equation 2.5. Figure 2.23 shows the lifetime measurements collected from the dye filled 820 nm diameter gold cavity arrays. The top image shows the lifetime image of the dye

filled cavity and the scale bar in the image indicates the lifetimes arising from the dye filled cavity. The scale bar shows the lifetimes in between 15 and 300 ns. Blue represents the lower lifetime and the red colour represents the longest lifetime components from the dye-filled arrays excited at 405 nm. The decay of dye solution within the gold nanocavities exhibited a biexponential decay with τ_1 (25%) of 295 ± 30 ns and τ_2 (75%) of 19 ± 3 ns. There is no significant change in the long lifetime component compared to the lifetime of the bulk dye solution as the small change in the long lifetime component from the dye filled array falls within experimental error. A second short-lived component with a lifetime of 19 ns was also observed from the dye filled gold cavity which contributed 75 % of the signal amplitude. To find out the origin of this short lived component a control experiment is carried out using blank solution. A signal lifetime of 19 ± 3 ns was observed for the gold cavities filled with blank solution (*i.e.,* in the absence of dye). Therefore, this second component might be due to the scattering or the reflectance from the gold nanocavity array. This short lifetime component for the dye probably contains short-lived signal from the ruthenium dye, but this will effectively mask any shorter decay components that may be present near the metal surface due to the effect of plasmons. Previous studies have shown that the presence of metal surfaces can enhance the emission intensity and decrease the lifetime of the dye due to the influence of surface plasmons. As discussed before, Lakowicz has shown that, the lifetime of the fluorophore decreases dramatically when it is very close to metal surface.[48] The fluorescence intensity from rhodamine B for example, is enhanced approximately 20 fold near silver islands and the lifetime of the dye on silver islands showed multiexponential decay. The lifetime of the rhodamine dye was 1.81 ns on the quartz plates whereas the lifetime of the dye was reduced to 0.14 ns on silver film. A long-lived component was also present on silver island film attributed to free molecules far from the metal surface. The report reveals that the enhancement of the fluorescence and the quenching of the lifetimes were comparable with the simulated data based on Equations 2.3 and 2.4 . Therefore, the enhanced emission from the rhodamine B on silver islands was attributed to increased rate of radiative decay.[45] In this present study, the dye filled gold nanocavity array shows biexponential decay with the long lifetime component, which is close to the lifetime of the free dye solution. Part of the short lifetime component from the dye filled array is thought to arise due to the scattering or the reflectance of the gold nanocavity array. Therefore, the enhancement in emission

intensity arises due to the increased rate of excitation rather than changes in the radiative decay. The enhancement in emission intensity with 514 nm excitation compared with 488 nm is attributed mainly to the increased rate of excitation due to the presence of strong localized surface plasmons on the surface.

In order to investigate the influence of the gold cavity array on the luminescence lifetime of the dye close to the metal surface, the luminescence lifetime of the self-assembled monolayers of dye were measured using FLIM. Figure 2.24 shows the luminescence lifetime of self assembled monolayers of $[Ru(bpy)_2(Qbpy)]^{2+}$ dye on the gold nanocavity arrays. Self-assembled monolayers of the dye on gold nanocavity arrays were prepared as described in Section 2.2.2 and then the arrays were filled with buffer solution. Surprisingly, the self-assembled monolayers of the dye showed a single exponential decay with a lifetime of 5 ns. The long lifetime component, 300 ns and the short lifetime component of 19 ns observed for the solution measurements were not observed. The presence of monolayer of ruthenium dye on the gold metal surfaces seems to affect background signal attributed to the reflection or scattering from the metal surface, which might be the reason for the disappearance of the 19 ns component in monolayer experiments. The quenching of the lifetime of the metal complex in monolayers might be due to the influence of surface plasmons close to the metal surface. Previous reports have shown that the presence of metal surfaces can influence the photophysical properties of the dye molecule and the effect is greater when the molecules are close to the metal surface.[47] Geddes and co-workers have shown a 7-fold enhancement in emission intensity from monolayers of R-phycoerythrin on silver island film and a 7-fold decrease in lifetime of the protein.[47] Solution phase measurements using a thin liquid layer showed a 6-fold enhancement in emission intensity whereas the lifetime decreased approximately 2-fold. For the monolayer sample, the entire molecule is in the near-field of silver particles therefore, the monolayer displayed a large change in lifetime. These results were similar to the observations found for $[Ru(bpy)_2(Qbpy)]^{2+}$ dye inside 820 nm diameter gold cavity array. In summary, the lifetime measurement from self-assembled monolayers of ruthenium dye on gold nanocavity array shows at least 60-fold quenching in excited state lifetime of the dye. The lifetime measurements of the dye filled arrays reveal that the enhancement in emission intensity from the dye filled arrays arises mainly from metal enhanced excitation, whereas, in the case of self-assembled monolayers

changes in the radiative decay rate occurs due to the proximity of the molecule to the metal surface.
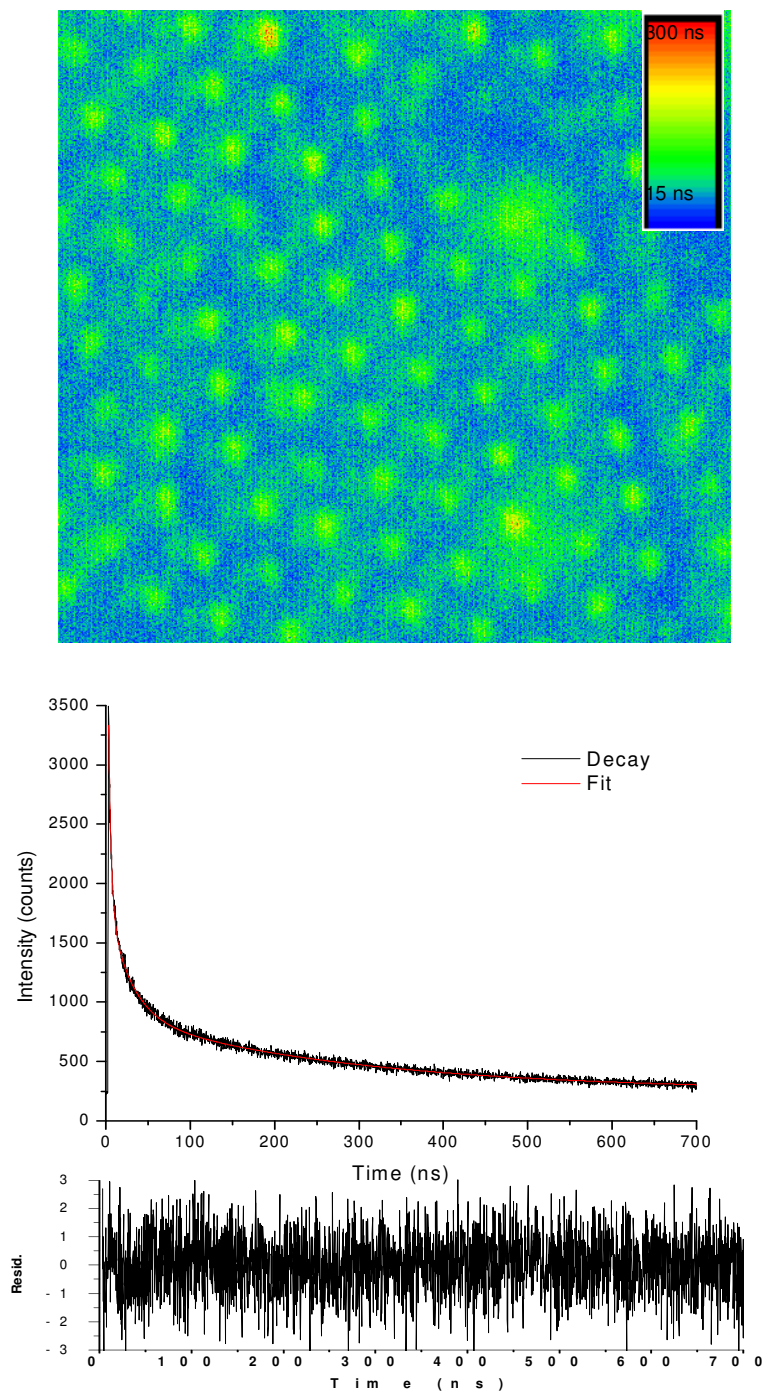
Fig. 2.23: Confocal scanning emission lifetime images (top) and (bottom) the luminescence decays were fitted to biexponential model for [Ru(bpy)$_2$(Qbpy)]$^{2+}$ dye filled gold nanocavity array. The excitation wavelength was λ_{ex} 405 nm.
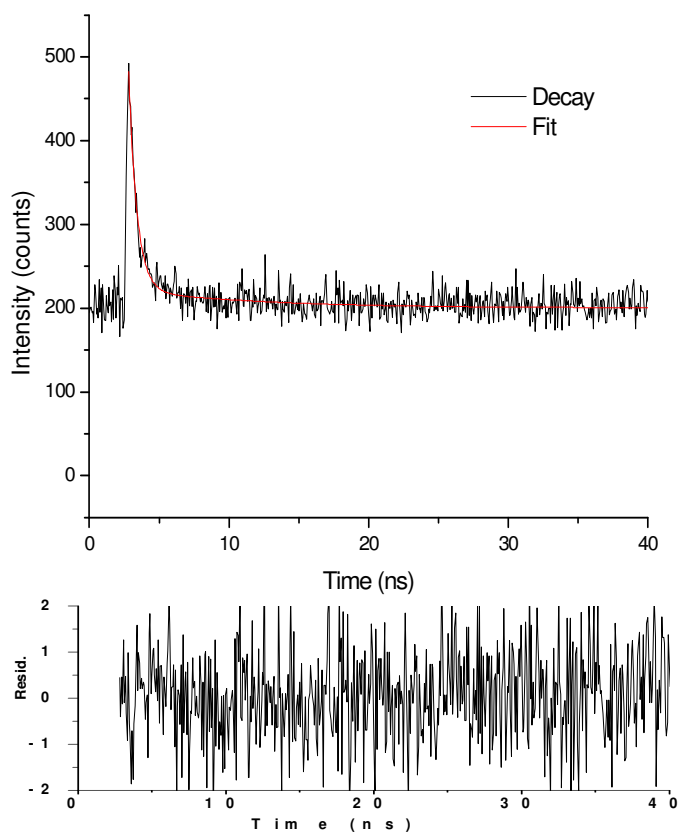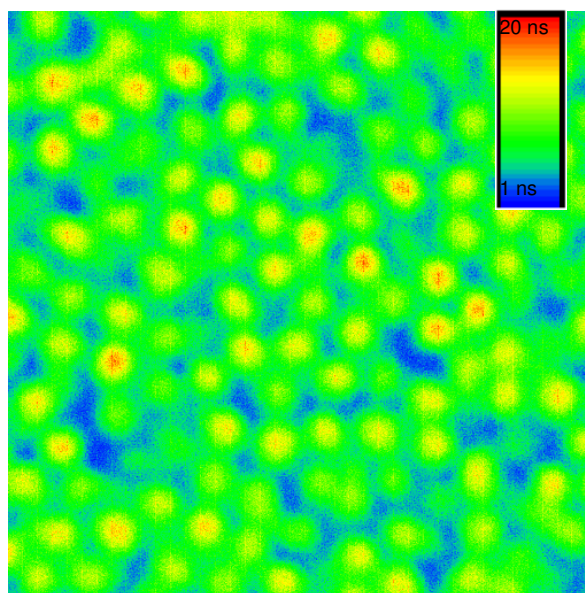
Fig. 2.24: Confocal scanning emission lifetime images (top) and (bottom) the luminescence decays were fitted to biexponential model for a self-assembled monolayer of $[Ru(bpy)_2(Qbpy)]^{2+}$ dye on the gold cavities. The measurements were carried out after filling the arrays with blank solution of methanol–water 80/20 v/v at λ_{ex} 405 nm.

2.3.10 Effect of gold nanocavity array on Fullerene emission

As discussed in Section 1.4, plasmonic enhancement and radiative decay is expected to have most impact on low quantum yield dyes. Therefore, in order to investigate the influence of the gold nanocavity array on the photophysics of a very low quantum yield dye, we studied the photophysics of fullerene on the array. Fullerene is a very weak fluorophore with an emission quantum yield (Φ) of 1×10^{-4}, and this low quantum yield is attributed to efficient intersystem crossing resulting in the formation of an excited triplet state.[48,49] The electronic transition is also very weak leading to the excited state in fullerene molecules. However, fullerene and its derivatives are important across a range of domains because of their structural and excellent electron accepting properties.[50,51]

Figure 2.25 shows the absorption and emission spectra of fullerene in toluene at a concentration of 1 mM. The inset of Figure 2.25 shows the structure of fullerene (C_{60}). The enhanced emission from fullerene filled gold nanocavity arrays was studied using confocal fluorescence microscopy. Figures 2.26 and 2.27 show the emission recorded from the fullerene filled 820 nm diameter gold cavity arrays at two different excitations, 514 nm and 488 nm. The Z-stack experiments were performed as described for $[Ru(bpy)_2(Qbpy)]^{2+}$ solution filled cavities. i.e., the scan started from the cover glass and then passed through the free fullerene solution between the cover glass and the fullerene filled arrays. In the case of the $[Ru(bpy)_2(Qbpy)]^{2+}$ complex it was possible to collect emission from both the free dye solution under 488 nm excitation with the same experimental settings. Whereas, under 514 nm excitation the enhancement in emission from the ruthenium dye filled gold nanocavity array was considerably greater than bulk solution therefore could not collect the emission from the dye solution with the identical experimental set up. In this case, the emission from fullerene in bulk solution was very low; therefore it was impossible to collect emission from the free fullerene even at 488 nm excitation using the same detector gain in both experiments. Indeed, it can be seen that there is little contribution from the emission of fullerene from gold nanocavity under 488 nm excitation but a signal can be seen at 514 nm excitation.
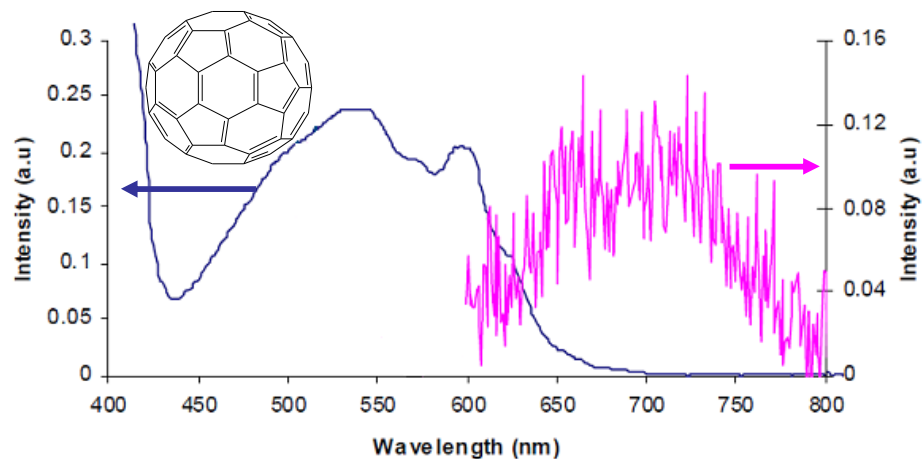
Fig. 2.25: UV/Vis absorption (—) and emission (—) spectra of fullerene in toluene at a concentration of 1 mM. The inset shows the structure of fullerene (C_{60}) molecule. The excitation wavelength for the emission spectrum was 550 nm.

Figure 2.28 shows the combined images of fluorescence and reflectance collected from fullerene filled gold cavity at 488 nm and 514 nm excitation. The inset shows the emission enhancement from the fullerene filled gold nanocavity array at 514 nm excitation. The black trace shows the reflectance and the red trace shows the fluorescence from the fullerene filled gold nanocavity arrays. The fluorescence and reflectance from the fullerene filled nanocavity arrays were separated using two different channels. The blue colour shows the reflectance channel and the green colour shows the fluorescence channel in Figure 2.28. It is clear that at 488 nm excitation, the reflectance signal intensity dominates whereas at 514 nm excitation, an enhancement in emission is observed from the fullerene-filled cavity. The enhancement was more than 10 fold at 514 nm excitation wavelength compared to free fullerene solution.
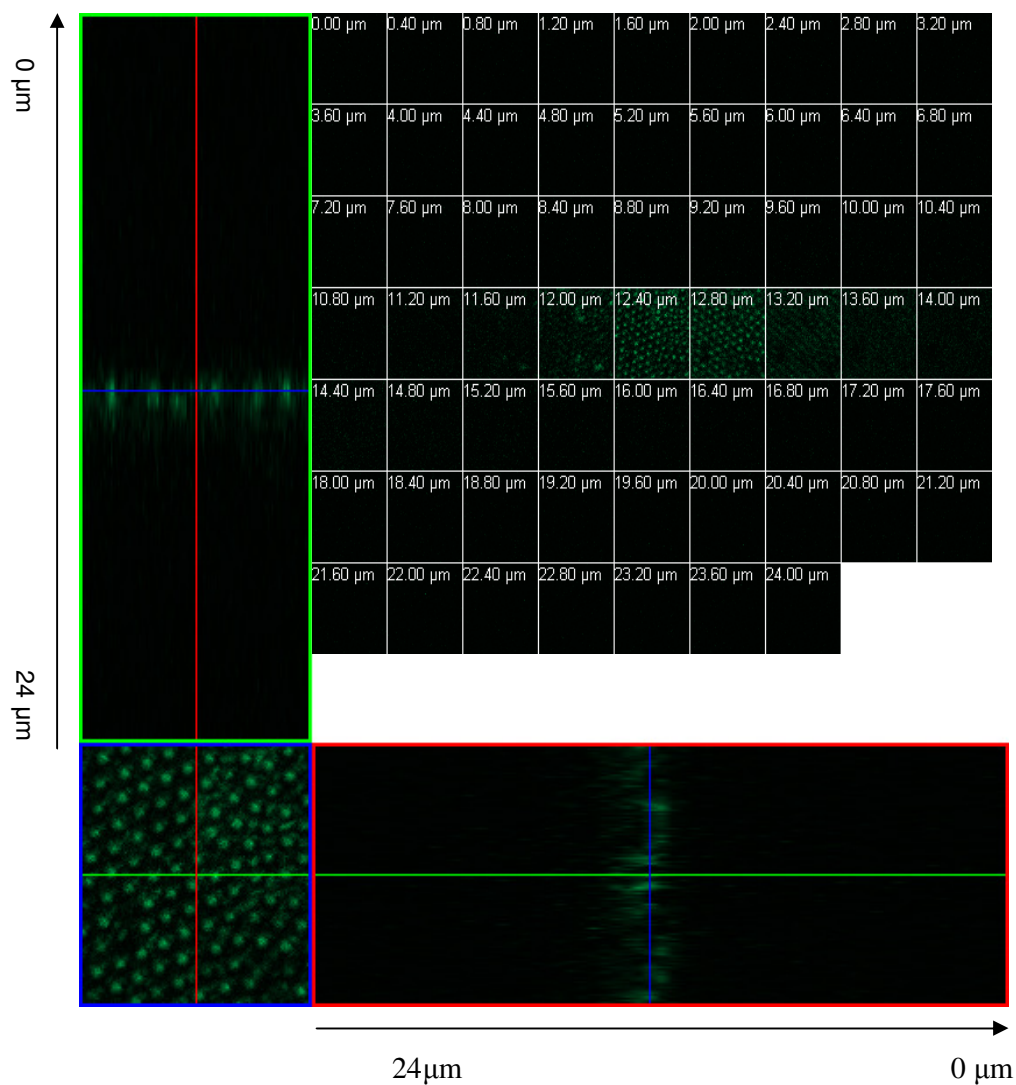
Fig. 2.26: Emission from the fullerene filled gold cavities at 488 nm excitation. The Z-stack measurements were carried out using the dye solution in between cover glass and the filled array. The scanning started from the cover glass and then passed through the dye solution to the filled array. The top slices show the emission from the free dye solution and then the fullerene-filled array. The step size was 400 nm.
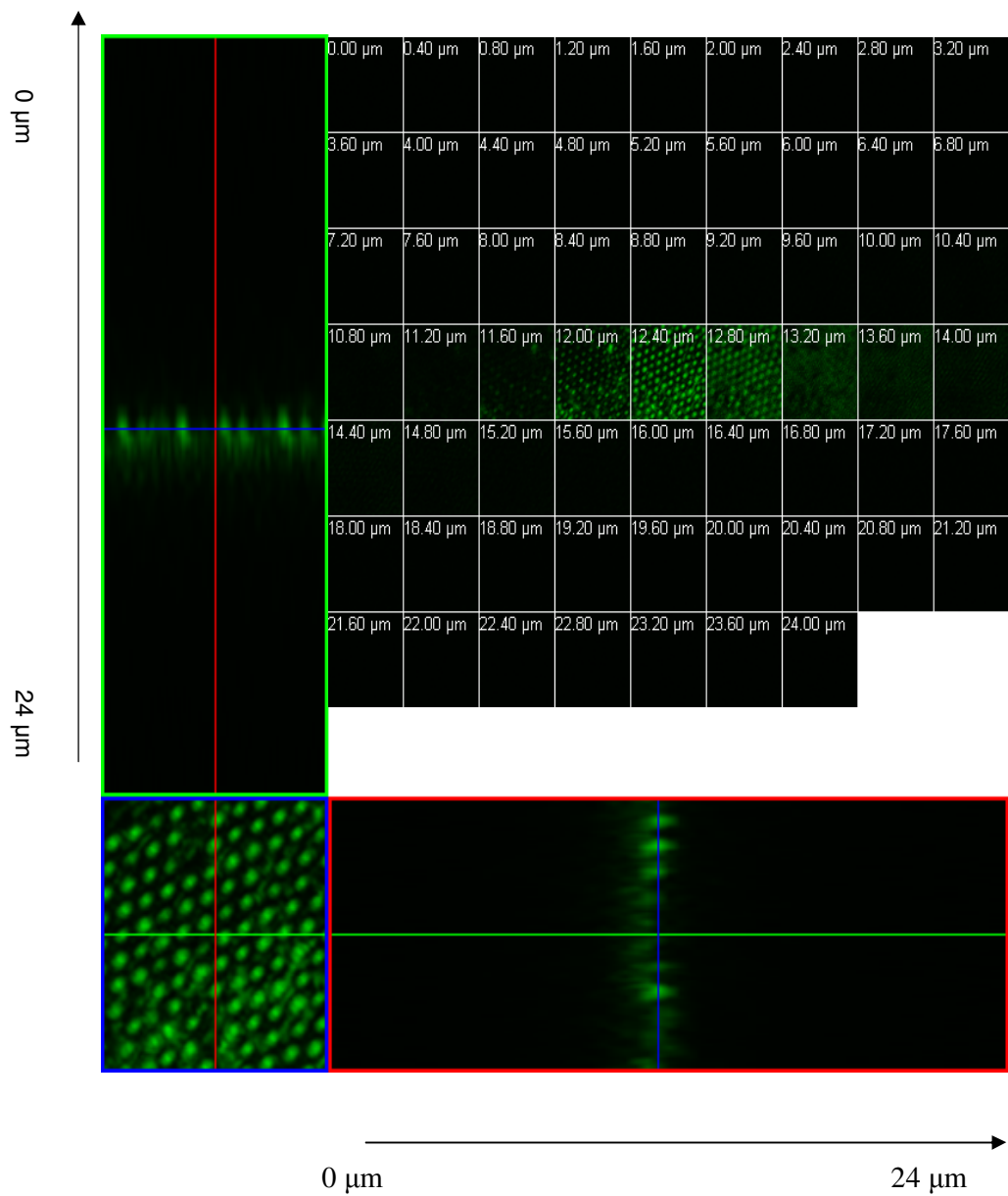
Fig. 2.27: Enhanced emission from the fullerene filled gold cavities at 514 nm excitation. The Z-stack measurements were carried out using the dye solution in between cover glass and the filled array. The scanning started from the cover glass and then passed through the dye solution to the filled array. The top slices show the emission from the free dye solution and then the fullerene filled array.
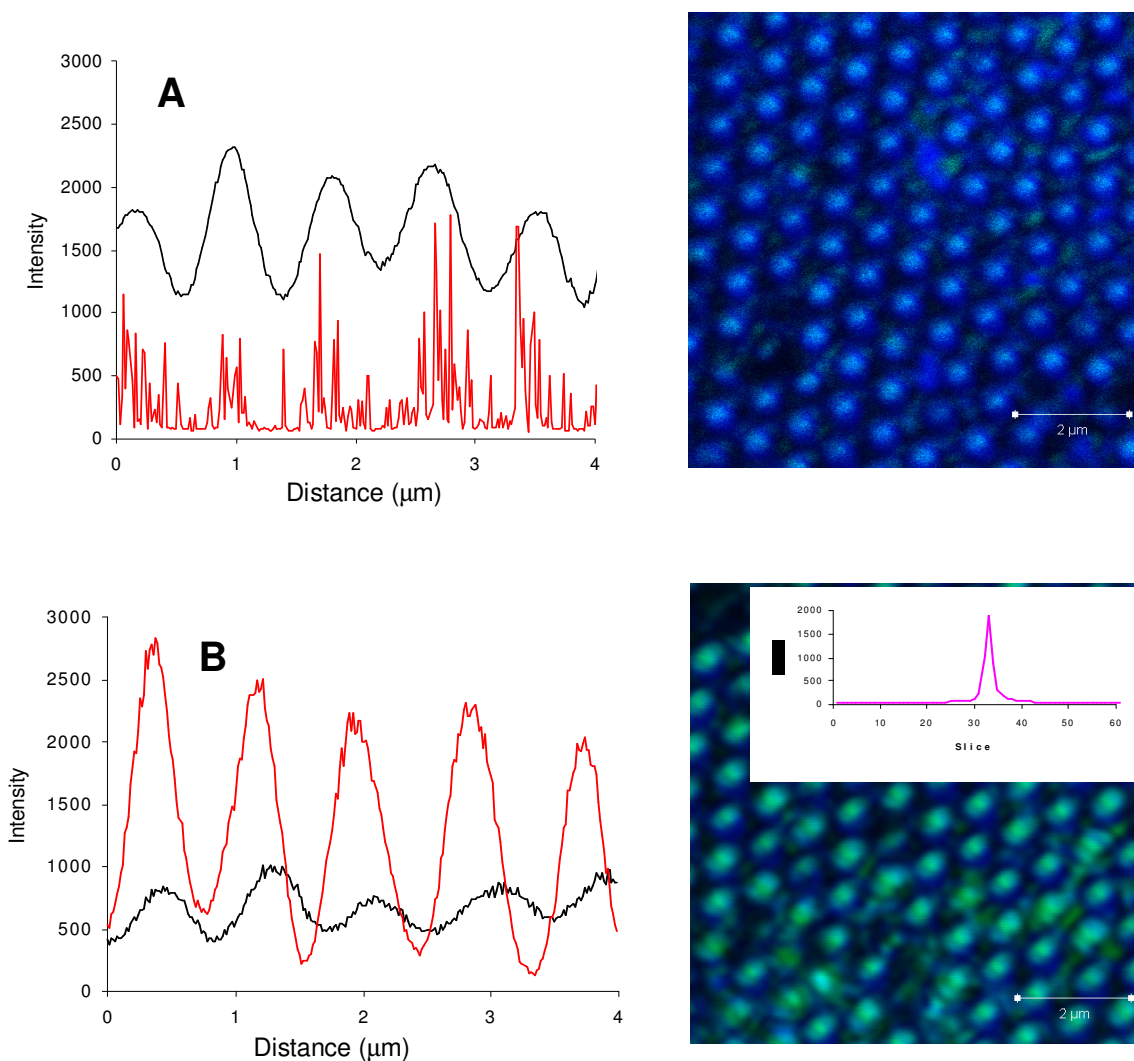
Fig. 2.28: Enhanced emission from fullerene filled gold cavity arrays at (a) 488 nm and (b) 514 nm excitation. The red trace in profile shows the emission and the black trace shows the reflectance from the dye filled arrays. The inset shows the emission intensity from the slices at 514 nm excitation. The blue colour in the image shows the reflectance and the green colour shows the emission from the dye filled arrays.

The enhancement in emission intensity was greater from the fullerene filled gold cavities at 514 nm excitation than at 488 nm and this is consistent with the behaviour seen for $[Ru(bpy)_2(Qbpy)]^{2+}$ dye filled arrays. The calculation of correct enhancement factor was difficult from the above measurements due to the spherical shape of the array. Therefore, fullerene filled cobalt nanocavities were used to compare the enhanced emission from the fullerene filled gold nanocavity arrays as models of similar structure but less plasmonic

111

contribution. Figure 2.29 shows the emission collected from fullerene filled cobalt cavities at (A) 488 and (B) 514 nm excitation using confocal microscopy. The blue colour shows the reflectance and the green colour shows the emission from fullerene filled cobalt cavities. There is very weak emission from the fullerene filled cobalt cavity under 488 nm excitation as shown in Figure 2.29 (A). However, it is clear that there is emission from the fullerene filled cobalt cavity at 514 nm excitation (Figure 2.29 (B)). The origin of this emission from fullerene filled cobalt cavities is unknown, and this might be due to the reflectance leaking through the fluorescence channel.
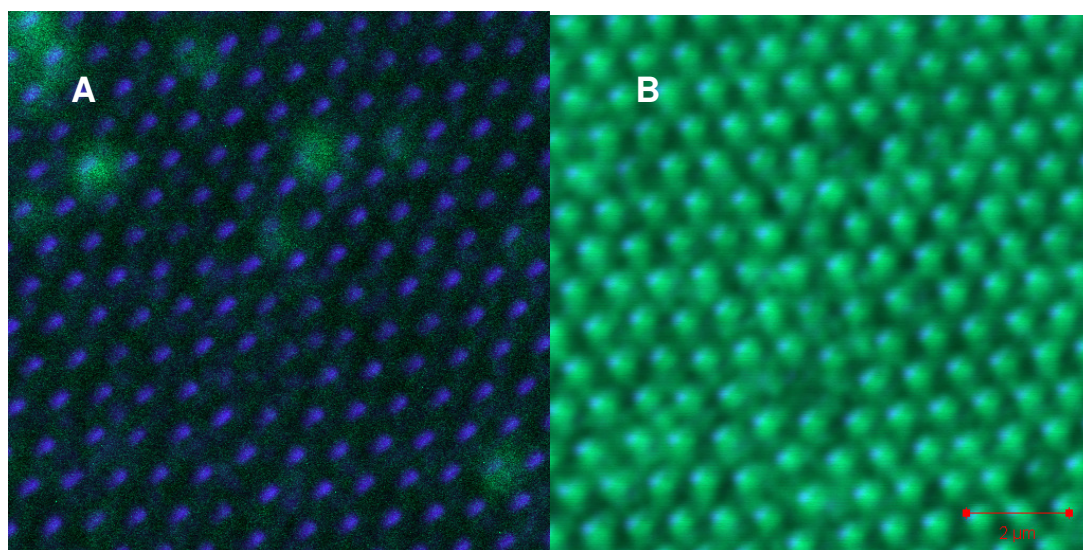
Fig. 2.29: Fullerene filled cobalt cavities at (A) 488 nm and (B) 514 nm excitation. The images are the combination of both emission and reflectance. The blue colour shows the reflectance and the green colour shows the emission from the dye filled arrays.

The enhancement factor calculated using confocal fluorescence microscopy experiments was around 10 fold. This enhancement factor was calculated by comparing the intensity of the emission from the dye solution between the filled cavity and the cover glass. To obtain spectral data and eliminate any contribution from background a Raman microscope is used to confirm the enhancement in emission intensity from the fullerene filled gold nanocavity array. In this experiment toluene is used as a solvent and the measurements were carried out at 514 nm excitation. Figure 2.30 shows the emission spectra of fullerene filled cavities. The black line shows the enhanced emission from the fullerene filled gold nanocavities and the red colour shows the emission from the fullerene filled cobalt cavities. Cobalt cavities enable to directly calculate the enhanced emission from the fullerene filled gold nanocavities without the normalization of number

of molecules. The enhancement was approximately 6 fold for the fullerene filled gold cavity array compared to cobalt cavities.
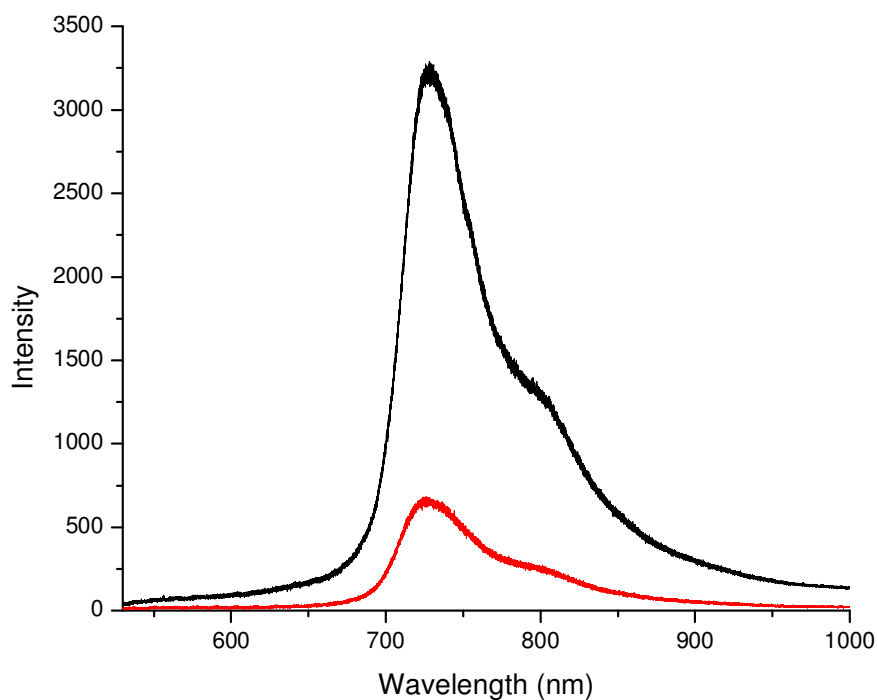
Fig. 2.30: Emission spectra of fullerene filled gold cavity (—) and (—) cobalt cavity at 514 nm excitation. Gold and cobalt nanocavity with 820 nm diameter arrays were fabricated using nanosphere lithography followed by electrochemical deposition. The solution with 1 mM concentration of fullerene in toluene was filled in both arrays by sonication. Both spectra were recorded using identical experimental conditions.

2.4 Conclusions

The ability of gold nanocavity arrays to enhance Raman signal from adsorbed species is well known, however, much less is known about their ability to enhance emission through plasmonic interactions, resident in solution in pores and as thin film on the surface. Here, we have investigated the impact of 820 nm diameter gold cavities on the photophysics of luminophores with modest to low luminescent quantum yields. Gold and cobalt nanocavity arrays were fabricated for the first time on FDTO using nanosphere lithography, followed by electrochemical metal deposition. This fabrication technique is highly reproducible and inexpensive compared to other lithographic techniques. The ability of 820 nm diameter gold spherical nanocavity arrays to enhance the Raman and the emission signal intensity from solutions and monolayers of luminophores was studied using confocal microscopy and Raman spectroscopy. The filling of the cavity, which is important parameter in any applications, was first explored and it was found that sonication of the luminophore solution was required in order to achieve complete filling of the nanocavity arrays which permits to study both solution and monolayer measurements. The requirement for sonication is tentatively attributed to trapping of air within the cavities.

Emission enhancement properties of the gold cavity array was studied using fullerene and $[Ru(bpy)_2(Qbpy)]^{2+}$ complex at two different wavelengths, 488 nm and 514 nm. A detailed study on the impact of excitation wavelength on emission enhancement from different quantum yield dyes indicate that the presence of surface plasmons on the gold nanocavity array plays a key role in the enhancement process. Comparisons were made between emission intensities from solutions of fullerene and $[Ru(bpy)_2(Qbpy)]^{2+}$ within gold nanocavities, in bulk solution and within cobalt nanocavities. It was observed that approximately an order of magnitude enhancement was achieved from ruthenium dye filled gold nanocavity arrays compared to cobalt cavities. The relatively unchanged luminescence lifetimes of the metal complex solutions within the array suggests that the metal enhanced excitation plays a major role in enhancement of emission intensity rather than the metal enhanced radiative decay rate. However, the monolayer of ruthenium dye formed on gold substrate shows a dramatic quenching of the lifetime which might be due to the change in radiative decay rate of the dye, although energy transfer to metal probably plays a role.

The $[Ru(bpy)_2(Qbpy)]^{2+}$ complex adsorbs onto the gold surface to form a self-assembled monolayer. This allowed the impact of the metal plasmons on the emission and Raman properties to be investigated both in solution and as a monolayer. Approximately 7 orders of enhancement in SERRS signal intensity were observed from monolayers of dye on gold nanocavity arrays. A comparison of enhancement in spectroscopic signal intensity from the top surface versus the interior walls of the gold nanocavity array is presented in next chapter.

2.5 References

[1]   Mahajan, S.; Abdelsalam, M.; Suguwara, Y.; Cintra, S.; Russell, A.; Baumberg, J.; Bartlett, P. N. *Phys. Chem. Chem. Phys.,* **2007***, 9*, 104.

[2]   Kelf, T. A.; Sugawara, Y.; Cole, R. M.; Baumberg, J. J.; Abdelsalam, M. E.; Cintra, S.; Mahajan, S.; Russell, A. E.; Bartlett, P. N. *Phys. Rev. B,* **2006,** *74*, 24.

[3]   Kelf, T. A.; Sugawara, Y.; Baumberg, J. J.; Abdelsalam, M.; Bartlett, P. N. *Phys. Rev. Lett.,* **2005,** *95*, 11.

[4]   Deckmann, H. W.; Dunsmuir, J.H. *Appl. Phys. Lett.,* **1982***, 41*, 377.

[5]   Burmeister, F.; Schäfle, C.; Keilhofer, B.; Bechinger, C.; Boneberg, J.; Leiderer, P. *Adv. Mater.,* **1998***, 10*, 495.

[6]   Haynes, C. L.; Van Duyne, R. P. *J. Phys. Chem. B,* **2001***, 105*, 5599.

[7]   Bartlett, P. N.; Baumberg, J. J.; Coyle, S.; Abdelsalam, M. E. *Faraday Discuss.,* **2004**, *125*, 1172.

[8]   Bartlett, P. N.; Baumberg, J. J.; Birkin, P. R.; Ghanem, M. A.; Netti, M. C. *Chem. Mater.,* **2002**, *14*, 2199.

[9]   Schwartzberg, A. M.; Zhang, J. Z. *J. Phys. Chem. C,* **2008**, *112*, 10323.

[10]   Wang, H.; Brandl, D. W.; Nordlander, P.; Halas, N. J. *Acc. Chem. Res.,* **2007**, *40*, 53.

[11]   Kelley A. M. *J. Chem. Phys.,* **2008**, *128*, 224702.

[12]   Campion, A.; Kambhampati, P. *Chem. Soc. Rev.,* **1998***, 27*, 241.

[13]   Zhao, J.; Jensen, L.; Sung, J.; Zou, S.; Schatz, G. C.; Van Duyne, R. P. *J. Am. Chem. Soc.,* **2007**, *129*, 7647.

[14]   Kneipp, K.; Kneipp, H.; Itzkan, I.; Dasari, R. R.; Feld, M. S. *Chem. Rev.,* **1999***, 99*, 2957.

[15]   Doering, W. E.; Nie, S. *J. Phys. Chem. B,* **2002***, 106*, 311.

[16]   Stockman, M. I. *Top. Appl. Phys.,* **2006***, 103*, 47.

[17]   Jackson, J. B.; Halas, N. J. *P. Natl. Acad. Sci.,* **2004***, 101*, 17930.

[18]   Le Ru, E. C.; Blackie, E.; Meyer, M.; Etchegoin, P. G. *J. Phys. Chem. C,* **2007**, *111*, 13794.

[19]   Jernshoj, K. D.; Hassing, S. *J. Raman Spectrosc.,* **2010**, *7,* 727.

[20]   Doering, W. E.; Nie, S. *J. Phys. Chem. B,* **2002**, *106*, 311.

[21]   Tian, Z. Q. *J. Raman Spectrosc.,* **2005**, *36*, 466.

[22]   Moskovits, M. *J. Raman Spectrosc.,* **2005**, *36,* 485.

[23]   Mahajan, S.; Baumberg, J. J.; Russell, A. E.; Bartlett, P. N. *Phys. Chem. Chem. Phys.,* **2007**, *9*, 6016.

[24]   Brolo, A. G.; Kwok, S. C.; Moffitt, M. G.; Gordon, R.; Riordon, J.; Kavanagh, K. L. *J. Am. Chem. Soc.,* **2005***, 127*, 14936.

[25]   Strekal, N.; Kulakovich, O.; Askirka, V.; Sveklo, I.; Maskevich, S. *Plasmonics,* **2009**, *4*, 1.

[26]   Corrigan, T. D.; Guo, S.; Phaneuf, R. J.; Szmacinski, H. *J. Fluoresc.,* **2005***, 15*, 777.

[27]   Lakowicz, J. R. *Anal. Biochem.,* **2001**, *298*, 1.

[28]   Forster, R. J.; Keyes *J. Phys. Chem. B,* **1998***, 102*, 10004.

[29]   Alberto, D. *Confocal and Multiphoton microscopy*, Lavoiseir, France, **2002**.

.

[30]   Haes, A. J.; Zou, S.; Zhao, J.; Schatz, G. C.; Van Duyne, R. P. *J. Am. Chem. Soc.,* **2006***, 128*, 10905.

[31]   Dieringer, J. A.; McFarland, A. D.; Shah, N. C.; Stuart, D. A.; Whitney, A. V.; Yonzon, C. R.; Young, M. A.; Zhang, X. Y.; Van Duyne, R. P. *Faraday Discuss.,* **2006**, *132*, 9.

[32]   Mayoral, R.; Requena, J.; Moya, J. S.; Lopez, C.; Cintas, A.; Miguez, H.; Meseguer, F.; Vazquez, L.; Holgado, M.; Blanco, A. *Adv. Mater.,* **1997**, *9*, 257.

[33]   Lacharmoise, P. D.; Tognalli, N. G.; Goni, A. R.; Alonso, M. I.; Fainstein, A.; Cole, R. M.; Baumberg, J. J.; de Abajo, J. G.; Bartlett, P. N. *Phys. Rev. B,* **2008**, *78*, 125410.

[34]   Bartlett, P. N.; Birkin, P. R.; Ghanem, M. A. *Chem. Commun.,* **2000**, *5,* 1671.

[35]   Jiang, P.; Bertone, J. F.; Hwang, K. S.; Colvin, V. L. *Chem. Mater.,* **1999**, *11*, 2132.

[36]   Netti, M. C.; Coyle, S.; Baumberg, J. J.; Ghanem, M. A.; Birkin, P. R.; Bartlett, P.

N.; Whittaker, D. M. *Adv. Mater.,* **2001**, *13*, 1368.

[37]   Van, C. M.; Holt, S. A.; Watson G. S.; Myhra, S. *J. Microsc.,* **1996**, *181*, 2.

[38]   Abdelsalam, M. E.; Bartlett, P. N.; Kelf, T.; Baumberg, J. *Langmuir,* **2005**, *21*, 1753.

[39]   Checco, A.; Hofmann, T.; DiMasi, E.; Black, C. T.; Ocko, B. M. *Nano Lett.,* **2010**, *10*, 1354.

[40]   Forster, R. J.; Pellegrin, Y.; Leane, D.; Brennan, J. L.; Keyes, T. E. *J. Phys. Chem. C,* **2007***, 111*, 2063.

[41]   Hayes, C. L.; Van Duyne, R. P. *J. Phys. Chem. B,* **2003***, 107*, 7426.

[42]   Baumberg, J.J.; Kelf T. A.; Sugawara Y.; Cintra S.; Abdelsalam M. E.; Bartlett P. N.; Russell A. E. *Nano Lett.*, **2005**, *11*, 2262.

[43]   Zhang, J.; Matveeva, E.; Gryczynski, I.; Leonenko, Z.; Lakowicz, J. R. *J. Phys. Chem. B,* **2005**, *109*, 7969.

[44]   Malicka, J.; Gryczynski, I.; Gryczynski, Z.; Lakowicz, J. R. *J. Biomol. Screen.*, **2004**, *9*, 208.

[45]   Lakowicz, J. R.; Shen, Y.; D'Auria, S.; Malicka, J.; Fang, J.; Gryczynski, Z.; Gryczynski, I. *Anal. Biochem.*, **2002**, *301*, 261.

[46]   Bierig, K.; Morgan, R. J.; Tysoe, S.; Gafney, H. D.; Strekas, T. C.; Baker, A. D. *Inorg. Chem.,* **1991**, *30*, 4898.

[47]   Chowdhury, M. H.; Ray, K.; Aslan, K.; Lakowicz, J. R.; Geddes, C. D. *J. Phys. Chem. C,* **2007**, *111*, 18856.

[48]   Lakowicz, J. R., *Principles of Fluorescence spectroscopy*, 3rd edition, Springer, New York, **2006.**

[49]   Bin, M.; Sun, Y. *J. Chem. Soc., Perkin Trans. 2,* **1996***, 10*, 2157.

[50]   Dirk, M. G., http://www.photobiology.com/reviews/6/index.html.

[51]   Nicole, L.; Roy, R. H.; Mark, O. L., David, L. C.; Gaddamanugu, L. P. *J. Nanobiotechnology,* **2006**, *4*, 14.

Chapter 3

Selective Surface Modification of Spherical Nanocavity Arrays: Identifying regions of plasmonic enhancement

3.1 Introduction

The frequency of charge density oscillations present at the surface of gold nanocavity arrays can be tailored by tuning their thickness and diameter, which can be controlled easily during fabrication.[1,2,3] Gold nanocavity arrays can enhance emission from molecules adsorbed on or close to the metal surface as discussed in Chapter 2. Moreover, the surface plasmon modes[4,5,6] present at the surface of gold nanocavity arrays can enhance Raman scattering from molecules adsorbed at or near the metal surfaces.[7] Recent studies revealed that the enhancement in signal intensity arising from nanostructured metal surfaces is not homogeneous across the surface. The electric field is typically concentrated at nanoscopic regions on the SERS substrate, referred to as "hot spots" and they are mainly responsible for the surface enhanced spectroscopies such as surface enhanced Raman spectroscopy (SERS),[8,9] surface enhanced resonance Raman spectroscopy (SERRS),[10,11,12] and surface enhanced fluorescence spectroscopy.[13,14,15] Furthermore, specifically for cavity structures theoretical calculation indicates that understanding the distribution of the enhancement in Raman signal intensity is desirable in efforts to exploit the surface plasmons for further development of sensors and optical devices.[16,17,18,19]

Reproducible fabrication of nanostructured metal surfaces with "hot spots" is desirable due to their ability to amplify the both Raman and luminescence signal intensity from molecule adsorbed on these fractile or disorganized structures. Attempts to reproducibly generate hot spots have been made by a number of groups.[20,21,22] For example, Moerner et al. have reported the enhancement of both Raman and fluorescence signal intensity from molecules adsorbed on gold bowtie antennas.[20,21] As discussed in section 1.9, this report revealed that the greatest enhancement in signal intensity originates from the gaps

between the triangles. Similarly, Van Duyne and co-workers also reported enhancement in Raman signal intensity from the sharp edges of triangular nanoparticles formed by nanosphere lithography.[22]

Dreier et al. have simulated the distribution of electric field in a single gold nanocavity using finite element software COMSOL multiphysics 3.5a.[23] They have shown that a gold nanocavity with 100 nm diameter and with 40 nm thickness showed the presence of concentrated electric field at the rim of the cavity. Indeed, Cole et al. reported theoretical calculations of surface plasmon modes distribution at the edges and interior walls of the gold nanocavity.[24] Their theoretical treatments predict that gold nanocavity arrays possess two different plasmon modes, Bragg surface plasmon modes, which are present at the top surface of the array and Mie plasmon modes, which are trapped inside the cavity. It is perhaps important to note that theoretical treatments typically focus only on a single cavity not on extended arrays, which excludes the top surface of the array. There has to our knowledge been only one aimed at differentiating plasmon contribution to SERS from top vs. cavity reported by Bartlett and co-workers. They have investigated the plasmon field distribution on gold nanocavity arrays by fabricating hybrid Ni/Au voids using a two-step metal deposition. Their study revealed that in gold nanocavity arrays, the best enhancement of SERS signals occurred from the top surface of the arrays which they attributed from comparison with theory to the rim plasmon modes. They suggested that the void acts as an antenna to aid coupling of light with the rim plasmon modes.[25] Detailed theoretical investigations on 2-D gold nanocavity arrays fabricated using nanosphere lithographic techniques have shown that both propagating and localized surface plasmons are distributed to different extents at the metal top surface and cavity interior.[26] In this chapter, the plasmon distribution in gold cavity arrays, especially on top surface and interior walls, is investigated using a two-step adsorption method by exploiting nanosphere lithography[27] to selectively modify the arrays with adsorbate,[28,29] which is luminescent and Raman active.

In this chapter, spherical gold nanocavity arrays with different diameters (240, 430, 600 and 820 nm) have been fabricated on smooth gold surfaces. Selective modification of top surface and interior walls of gold nanocavity arrays with $[Ru(bpy)_2(Qbpy)]^{2+}$, where bpy is 2,2'-bipyridyl and Qbpy is 2,2':4,4'':4,4''-quarterpyridyl, has been achieved by using a two step adsorption process as shown in Scheme 3.1. As described in Chapter 1,

$[Ru(bpy)_2(Qbpy)]^{2+}$ is a surface active dye, which can readily form self-assembled monolayers on metal surfaces such as gold and platinum. This dye is selected for the selective modification measurements due to its large Stoke shift and its surface-active properties as described in the previous chapter. Moreover, the photophysical properties of this complex are well studied by our group.[30] The wavelength dependent excitation of localized surface plasmons was studied using monolayers of $[Ru(bpy)_2(Qbpy)]^{2+}$ dye adsorbed at the top surface of gold nanocavity arrays to determine the optimum wavelength for SERS study. The plasmonically enhanced emission from $[Ru(bpy)_2(Qbpy)]^{2+}$ dye adsorbed at the top surface and interior walls of the nanocavity arrays was also compared.

3.2 Experimental

3.2.1 Materials

Cysteamine (98%), 1-nonane thiol (95%) and tetrahydrofuran (THF, 99%) were purchased from Sigma. Sulphate modified polystyrene latex spheres with different diameters (240, 430, 600 and 820 nm) were obtained from Duke scientific. $[Ru(bpy)_2(Qbpy)]^{2+}$ dye was synthesized by Reena Marthi and Yann Pellegrin from cis-$[Ru(bpy)_2Cl_2]$ as described previously.[30] Gold coated (400 nm) silicon, with a roughness factor ~ 1.3, was obtained from the Tyndall institute in Cork.

3.2.2 Preparation of gold nanocavity arrays

Spherical gold nanocavities with diameters of 240, 430, 600, and 820 nm (t_N = t/d = 0.8±0.04, where 't' is the thickness of the film and 'd' is the diameter of the cavity) were prepared using nanosphere lithography in a similar way to that described in Chapter 2. However, here smooth gold coated silicon substrates were used instead of FDTO glass slide. The gold coated (400 nm) silicon wafers were rinsed with acetone and then cleaned with piranha solution. Cysteamine was self-assembled onto the freshly cleaned smooth gold surface by immersing the substrate in a 10 mM ethanolic solution of cysteamine at room temperature for 24 hours. This chemical modification of the substrate aids the assembly of the sulphate modified polystyrene spheres on the gold substrate. Cysteamine reduces the contact angle of the latex solution which helps to form a sweeping meniscus during evaporation. This sweeping meniscus pulls the spheres from the solution to the evaporation line which results in the formation of a monolayer of spheres on the substrate.[31] Self-assembled monolayers of polystyrene spheres were prepared by placing the surface modified gold substrates upright in an aqueous solution of polystyrene spheres (0.01%) and allowing the solvent to evaporate. Through these 2-D pre-assembled templates, a gold film of controlled thickness was electrochemically deposited from gold electroplating solution as described in Chapter 2.

3.2.3 Selective surface modification of gold templated arrays

Selective modification of the top surface of the gold cavity array was achieved using the templating sphere to block adsorption at the cavity surface.[28] Following metal deposition
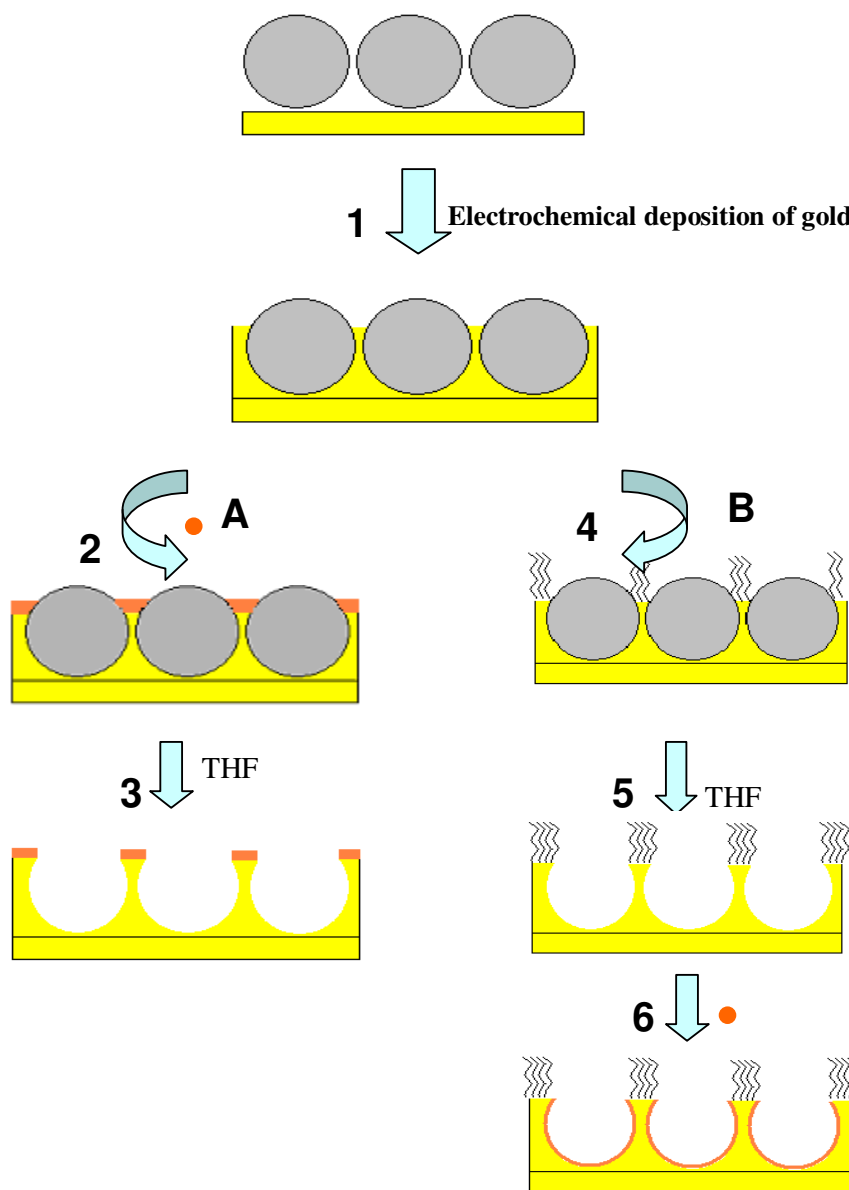
Scheme 3.1: Schematic of the approach to selective adsorption of surface active species at the top surface and interior walls of gold nanocavity arrays. After metal deposition, the spheres are retained in the array and the top surface is selectively modified through one of two routes. Route (A) Shows the selective modification of top surface of arrays using $[Ru(bpy)_2(Qbpy)]^{2+}$ dye (●). Route (B) shows the selective modification of interior walls of nanocavity arrays after functionalizing the top surface with ⌇⌇⌇ thiol ( ). (1) Illustrates the electrochemical deposition of gold through the voids of self-assembled polystyrene spheres. (2) Selective modification of top surface with ruthenium dye using self-assembly technique. (3) Dissolution of polystyrene spheres in THF after top surface modification resulting selectively top modified array. (4) Blocking of the top surface of the array using thiol. (5) Dissolution of polystyrene spheres in THF. (6) Selective modification of interior walls of the array using ruthenium dye. (Not drawn to scale for clarity).

the Au-covered electrodes were selectively modified either by alkanethiol or $[Ru(bpy)_2(Qbpy)]^{2+}$ dye as shown in Figure 3.1 (A) and (B). Self assembled monolayers of $[Ru(bpy)_2(Qbpy)]^{2+}$ at the top surface of the array were prepared by placing the templated gold electrode in 1 mM methanolic $[Ru(bpy)_2(Qbpy)]^{2+}$ dye solution overnight as shown in Scheme 3.1.2. The polystyrene spheres prevent modification of interior walls with dye. Then, the polystyrene template was removed by sonicating the surface modified slide in THF for one hour (Scheme 3.1.3). The interior walls of the array are selectively decorated using the ruthenium dye after blocking the top surface with alkane thiol. The top surface of the gold deposited slide is modified with thiol by keeping the slide with the templating sphere in ethanolic solution of thiol for overnight (Scheme 3.1.4). The top surface modified substrate was then sonicated in THF for 1 hour to dissolve and remove the templating spheres (Scheme 3.1.5). The interior walls of the cavities were then modified by filling the arrays with $[Ru(bpy)_2(Qbpy)]^{2+}$ dye solution by 30 minutes sonication. The array was then allowed to stand in contact with the ruthenium solution for 24 hours for the formation of monolayer at the interior walls as shown in Scheme 3.1.6. Excess physisorbed molecules were removed from the electrode by sonicating in blank solvent after this period.

3.2.4 Methods

Electrochemical measurements were carried out in a standard three electrode cell using CH Instruments Model 660 electrochemical workstation. The topology of gold nanocavity array was investigated using a Hitachi S-3000N scanning electron microscope. Reflectance measurements were recorded using a SPM-002 spectrometer with a tungsten halogen light source. Raman spectra were recorded on a Horiba Jobin Yvon HR800UV microscope using 514 nm, 633 nm, and 785 nm laser lines as excitation. The light intensity at the sample was approximately 4.75 mW for 633 nm laser and 5 mW for 785 nm laser line. The laser intensity for 514 nm excitation was 16 mW. Typical acquisition times were between 1 and 20 s and five acquisitions were performed to acquire a spectrum. Any emission background from the Raman spectra was subtracted using LabSpec software. Luminescence spectra from monolayers of $[Ru(bpy)_2(Qbpy)]^{2+}$ dye on nanocavity arrays were collected using a Horiba Jobin Yvon LabRAM spectrometer with a 100x objective (NA = 0.95). The excitation wavelength was 473 nm. Both Raman and luminescence measurements were repeated three times across a single slide in order to study the reproducibility of the measurement.

3.3 Results and discussion

3.3.1 Characterisation of gold nanocavity arrays using SEM

As discussed in Chapter 2, the FDTO electrode is nanoscopically rough, therefore, the top surface of the deposited array appears to be rough in atomic force microscope (AFM). In this chapter the gold nanocavity arrays were fabricated on a smooth gold surface wherein, templating was conducted on a silicon wafer coated with gold (400 nm), using a method similar to that described by Bartlett et al.[1] To assess the relative contribution of top vs. cavity plasmons to Raman enhancement as a function of cavity dimensions, four different diameters of cavities were investigated. Figure 3.1 shows scanning electron microscope images of the gold nanocavity arrays on smooth gold surface. The arrays with cavity diameters of (A) 240, (B) 430, (C) 600 and (D) 820 nm were prepared by templated electrochemical deposition through the voids of different diameters of polystyrene spheres. The images of the four different arrays were taken under identical conditions using a 10 kV accelerating voltage and are shown with the same magnification for direct comparison. The gold nanocavities formed well-ordered, hexagonal close-packed arrays, which extend with a low defect density over an area of approximately 50 mm^2 in the case of larger spheres. The packing efficiency was less for the smaller spheres (240 & 430 nm diameter) and the defect-free area for the smaller spheres was approximately 20 mm^2. Sphere sizes greater than 1 µm were very difficult to self assemble on different substrates such as gold or glass. Small defective areas of smooth gold appeared in all cases where the spheres failed to pack correctly. However, these are easily identified using the white light imaging function of the Raman microscope and only highly ordered regions were selected for the SERS study.

Kelf and co-workers have reported that gold nanocavity arrays deposited to a thickness below the equator of the sphere exhibit strong Bragg surface plasmon modes, which propagate through the 2-D lattice whereas arrays with greater thickness possess Mie surface plasmon modes which are trapped inside the cavity.[3] We were interested to find out the relative role of surface plasmon modes in such films where the thickness of gold deposition exceeds the equator. The thickness of the film is controlled by the amount of charge passed during metal deposition. In each case, the gold film was grown to a normalised thickness of approximately 0.8±0.04 (t_N= t/d = 0.8).[1] Therefore, the actual

thickness of each array is approximately 202, 320, 465, and 689 nm for films with cavity diameters of 240, 430, 600, and 820 nm respectively. The thicker arrays, i.e., gold deposited above the equator of polystyrene sphere are of particular interest as we hope to exploit the porous nature of the array wherein the cavity can acts as an aqueous compartment for the cytoplasmic tail of the transmembrane protein such as integrin.
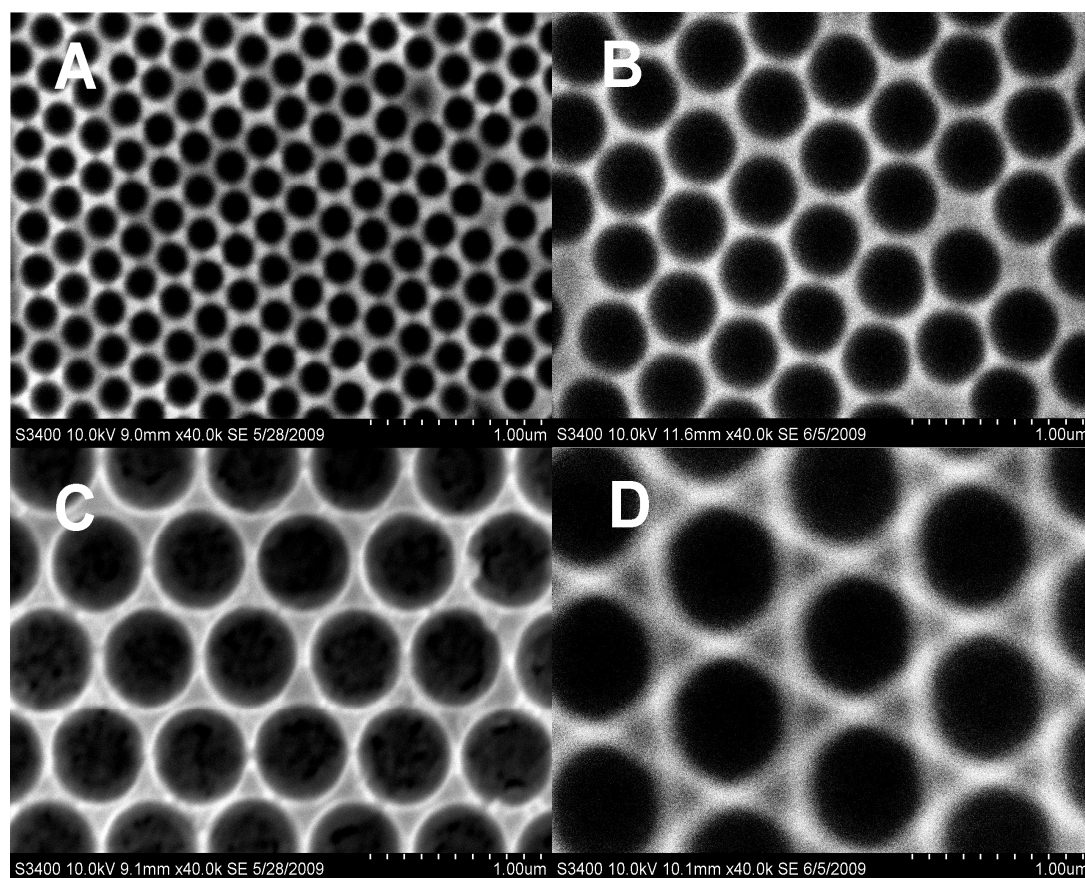
Fig. 3.1: SEM images of gold cavity arrays with cavity diameters of (A) 240 nm (B) 430 nm (C) 600 nm and (D) 820 nm. The gold nanocavity arrays were fabricated on a smooth gold substrate by nanosphere lithography followed by electrochemical deposition. All images were taken under identical conditions using 10 kV accelerating voltage. The film thickness is approximately 0.8 ± 0.04 ($t_N = t/d = 0.8$).

3.3.2 Selective modification of arrays confirmed by Raman

The previous chapter described the enhancement in emission intensity from solution encapsulated in cavity and SERRS from self-assembled monolayers of a probe molecule across the entire gold nanocavity arrays. The objective of this study was to identify the regions of enhancement from the gold nanocavity arrays as mentioned earlier. The use of templated adsorption permitted comparison of the surface enhancement of both Raman and luminescence signals of adsorbate localised separately across the top surface of the array and within the nanocavities. The novel selective templated adsorption approach used in this chapter is illustrated in Scheme 3.1, where two modification pathways, (A) and (B) are followed to produce the required pattern of adsorption of probe molecule. i.e., $[Ru(bpy)_2(Qbpy)]^{2+}$ dye separately either at the top surface or inside the cavity.

The formation of monolayers of dye or alkane thiol was achieved by self-assembly of the selected adsorbate on the top surface of the gold nanocavity arrays while the template is still in place. Then, the templated polystyrene spheres were dissolved by sonicating in THF for 1 hour sonication. A key issue is the stability of monolayers after sonication of the selectively modified array in THF. In order to confirm their stability, Raman spectra were recorded before and after the removal of spheres following monolayer adsorption. Figure 3.2 shows the Raman spectra of 1-nonanethiol selectively adsorbed at the top surface of 820 nm diameter gold nanocavity arrays before and after the removal of polystyrene spheres. The black line in Figure 3.2 shows the Raman spectra of the top surface modified array before dissolution of the polystyrene spheres. It is clear that the spectrum is dominated by polystyrene features before removal of spheres, especially aromatic ring breathing modes at 1001, 1026, 1602 cm^{-1}. In particular, the strong peak at 1001 cm^{-1} is attributed to aromatic C-H deformation, which is typical of polystyrene. Also aromatic ring stretching vibrations from polystyrene occur in the spectral region 1600-1430 cm^{-1}.[32] The stretching vibration of the aliphatic group occurs between 3000-2800 cm^{-1}. The alkanethiol peaks are not visible due to the intensity of the peaks of polystyrene spheres, which is reasonable when one compares the large quantity of polystyrene compared to the single monolayer of alkane thiol assembled at the top surface of the arrays. The SEM images of the gold nanocavity arrays after the removal of spheres indicated that one hour sonication in THF was sufficient to remove the polystyrene spheres completely from the substrate. Removal of the spheres was further

confirmed by the absence of Raman peaks associated with the polystyrene spheres after sonication of the arrays in THF. However, the red line in Figure 3.2 confirms the Raman modes associated with alkane thiol self- assembled at the top surface of nanocavity array are evident after the removal of spheres. The features around 1001 cm^{-1} and 1500 cm^{-1} arise from skeletal vibrations of C-C stretching mode and CH_2 scissor vibrations respectively.
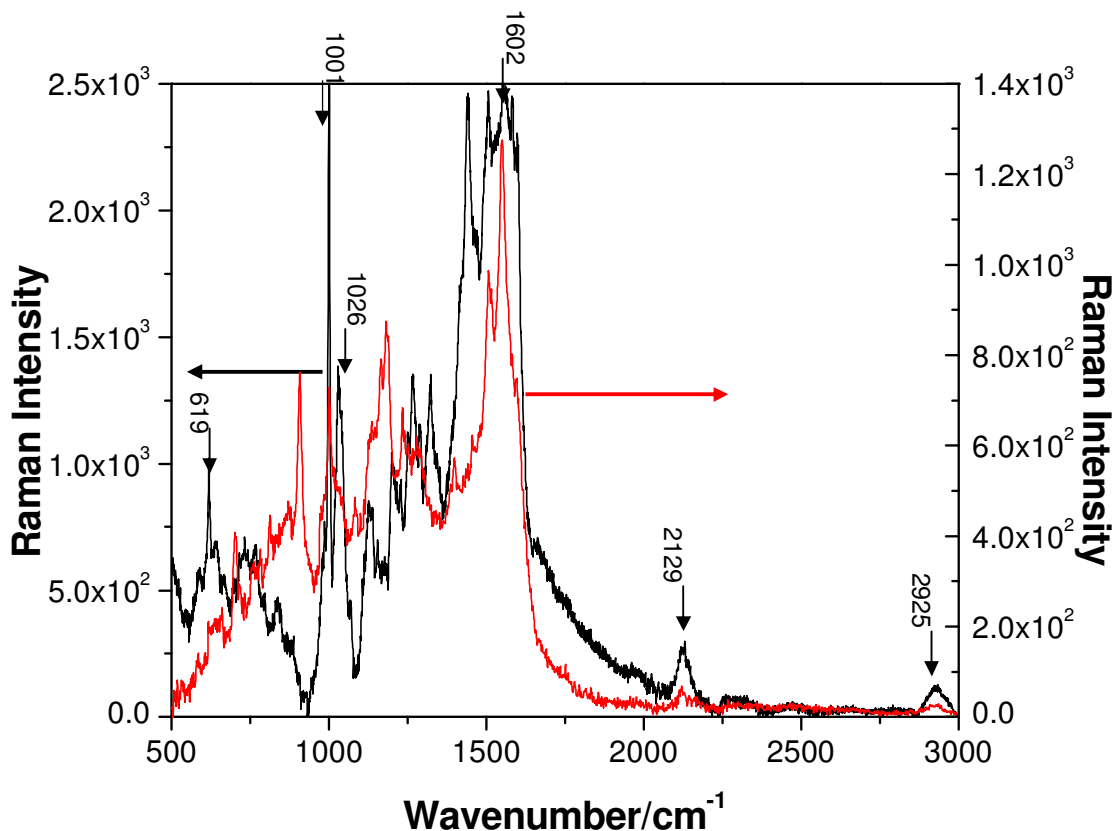
Fig. 3.2: Raman spectra of top surface modified 820 nm diameter gold nanocavity arrays with 1-nonanethiol (—) before and (—) after dissolving polystyrene spheres in THF by sonication. The excitation wavelength was 633 nm. Typical acquisition time was 10 s and the laser spot size was 2 μm. The spectra recorded with a 100x objective.

Similarly, the formation and stability of monolayers of [Ru(bpy)$_2$(Qbpy)]$^{2+}$ dye on the top surface of the array was confirmed using Raman spectroscopy. Figure 3.3 shows the Raman spectra of spontaneously adsorbed monolayers of [Ru(bpy)$_2$(Qbpy)]$^{2+}$ dye adsorbed at the top surface of the gold nanocavity arrays (black) before and (red) after the dissolution of the templating polystyrene spheres. The spectrum is dominated by strong polystyrene peaks before the removal of spheres. The red line in Figure 3.3 shows the

SERS signal coming from $[Ru(bpy)_2(Qbpy)]^{2+}$ dye adsorbed at the top surface of the array after dissolving the polystyrene spheres. An intense band around 1600 cm^{-1} is attributed to pyridine C-C stretching modes. The peak around 1000 cm^{-1} arises from the aromatic ring stretching vibrations of the ruthenium dye. A detailed description of the Raman vibrational modes of Ru(bpy)$_2$(Qbpy)]$^{2+}$ dye is given in the following section. The persistence of strong Raman signals after the dissolution of polystyrene spheres confirms that one hour sonication of the array in THF did not remove the adsorbed monolayers of $[Ru(bpy)_2(Qbpy)]^{2+}$ dye. The stability of monolayers of both thiol and $[Ru(bpy)_2(Qbpy)]^{2+}$ dye on top surface of the array during an hour sonication is confirmed for the four different diameter arrays, the spectra for only 820 nm diameter arrays are shown here as an example. The extent of exchange of first adsorbed molecules (for example, thiol) with the second adsorbing molecules (for example ruthenium dye) at the top surface of the arrays has to be addressed in future.
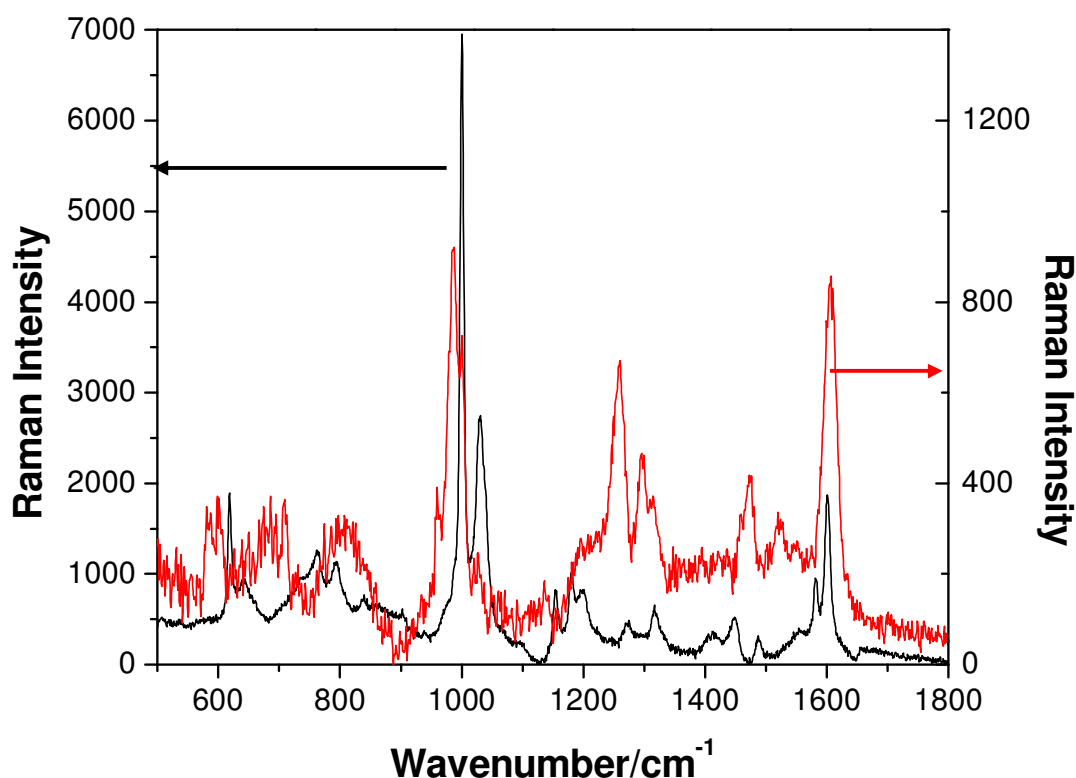
Fig. 3.3: Raman spectra of top surface modified 820 nm diameter gold nanocavity arrays with [Ru(bpy)$_2$(Qbpy)]$^{2+}$ (——) before and (——) after dissolving polystyrene spheres in THF by sonication. The excitation wavelength was 633 nm. Typical acquisition time was 10 s and the spot size was 2 μm. The collection angle was 72 degree.

Raman spectroscopy suggests that monolayers of both alkane thiol and $[Ru(bpy)_2(Qbpy)]^{2+}$ dye were stable toward sonication which is due to the high bond strength of gold-sulphur and gold-pyridine. It is important to note that the smooth gold surface was modified with cysteamine before self-assembly of polystyrene spheres. The interaction between the smooth gold surface and sulphate modified polystyrene spheres is expected to be non-covalent. Therefore, the sonication of arrays in THF are expected to remove those weakly attached polystyrene spheres readily compared to covalently attached monolayers of thiol or ruthenium dye. The Raman measurements on the top surface modified arrays have shown that the sonication of the gold nanocavity arrays in THF for an hour completely removed the polystyrene spheres.

3.3.3 Calculation of the ratio of top surface area versus interior surface area

A key goal of this chapter is to identify the relative enhancement in Raman signal intensity from top surface and interior walls of gold nanocavity arrays. It should be noted that, the number of molecules expected to be adsorbed at the spherical interior cavity walls is far higher than that adsorbed at the top surface. Therefore, normalization of signal intensity to the number of molecules anticipated to lie within the laser spot for each type of surface area, top and cavity is essential to accurately estimating the enhancement factor. The top surface area versus the interior surface area of gold nanocavity arrays was determined by analysis of SEM images using Image J software. The surface area of a single cavity, with a height of 0.8±0.04, was calculated by using the equation for the area of a truncated sphere, $3\pi r^2$, where r is the radius of the sphere. The number of nanocavities in a defined area was calculated from SEM image using Image J software. The total interior surface area of nanocavity was determined by multiplying the number of cavities i.e., determined from SEM image, by the surface area of a single cavity. The area of top surface of cavity was determined by subtracting the area of all holes from the total area of the image. Table 3.1 shows the top surface and internal cavity areas estimated for each cavity diameter using this approach. These areas were calculated from a defined area (7 μm^2) and shows that the interior and edge areas vary little as a function of cavity size. The number of molecules within the laser focal area on the gold nanocavity arrays was estimated by assuming a complete close-packed monolayer surface coverage and taking the increased surface area due to the spherical shape of the nanocavities into account as described above. Previous investigations[30] on planar gold electrodes show that the surface coverage of $[Ru(bpy)_2(Qbpy)]^{2+}$ is $1.05\pm0.1\times10^{-10}$ mol cm^{-2}, corresponding to an area occupied per molecule of 158±17 Å^2. Table 3.1 shows the calculated surface area of top surface and interior walls of different diameter arrays for a 7 μm^2 area. This is useful for the calculation of enhancement factor for both Raman and emission measurements. The relative enhancement of Raman signal intensity from the top surface of the cavity compared to the inner surface of the cavity, REF, was estimated using equation 3.1 which accounts for the relative number of molecules adsorbed at each surface.

$$REF = (I_{edge}/ N_{edge})/ (I_{inside}/ N_{inside})$$

$$= (I_{edge}/ I_{inside})* (N_{inside}/ N_{edge})$$ 3.1

where

I_{edge}= Intensity of Raman Signal, at 1026 cm^{-1} from [Ru(bpy)$_2$(Qbpy)]$^{2+}$ at top surface of the array.

N_{edge} = Number of [Ru(bpy)$_2$(Qbpy)]$^{2+}$ molecules adsorbed at the top surfaces of the array.

I_{inside}= Intensity of Raman Signal at 1026 cm^{-1} from [Ru(bpy)$_2$(Qbpy)]$^{2+}$ at cavity walls.

N_{inside} = Number of [Ru(bpy)$_2$(Qbpy)]$^{2+}$ adsorbed at the cavity walls.

Cavity diameter (nm)	Edge Area (μm^2)	Interior Area (μm^2)
820	3.0±0.4	26±3
600	2.3±0.3	25±2
430	2.1±0.3	20±3
240	3.1±0.4	21±1.5

Table 3.1: Calculated surface area of top surface vs. interior walls of different diameters of gold nanocavity arrays for 7 μm^2 area.

The relative enhancement factor from the top surface of the gold nanocavity arrays were calculated using Equation 3.1. The enhancement in signal intensity from interior modified arrays was compared with self-assembled monolayers of ruthenium dye on a smooth gold surface. The details of the control experiments are provided in Section 3.3.5.

3.3.4 Wavelength dependent enhancement

As described, SERS enhancement is believed to arise primarily from two contributions, of which the dominant is the electromagnetic mechanism, which requires resonance between excitation wavelength and plasmonic frequency.[15,33] In order to relate the SERS enhancement to plasmonic frequency, we examined three different excitation lines (514 nm, 633 nm, 785 nm).[34] In order to assess the optimal wavelength for SERS enhancement under the conditions employed here, Raman spectra of $[Ru(bpy)_2(Qbpy)]^{2+}$ monolayers adsorbed only at the top surface of four different diameter arrays, in which the cavity is free of adsorbate, were assessed as a function of wavelength. The arrays were anticipated to exhibit greatest enhancement in Raman signal intensity under 514 nm excitation due to the post resonance of this frequency with the MLCT optical transition of the metal complex. Spectra of the $[Ru(bpy)_2(Qbpy)]^{2+}$ dye adsorbed at the top surface of 240 nm diameter cavity arrays at various excitation lines are shown in Figure 3.4. The
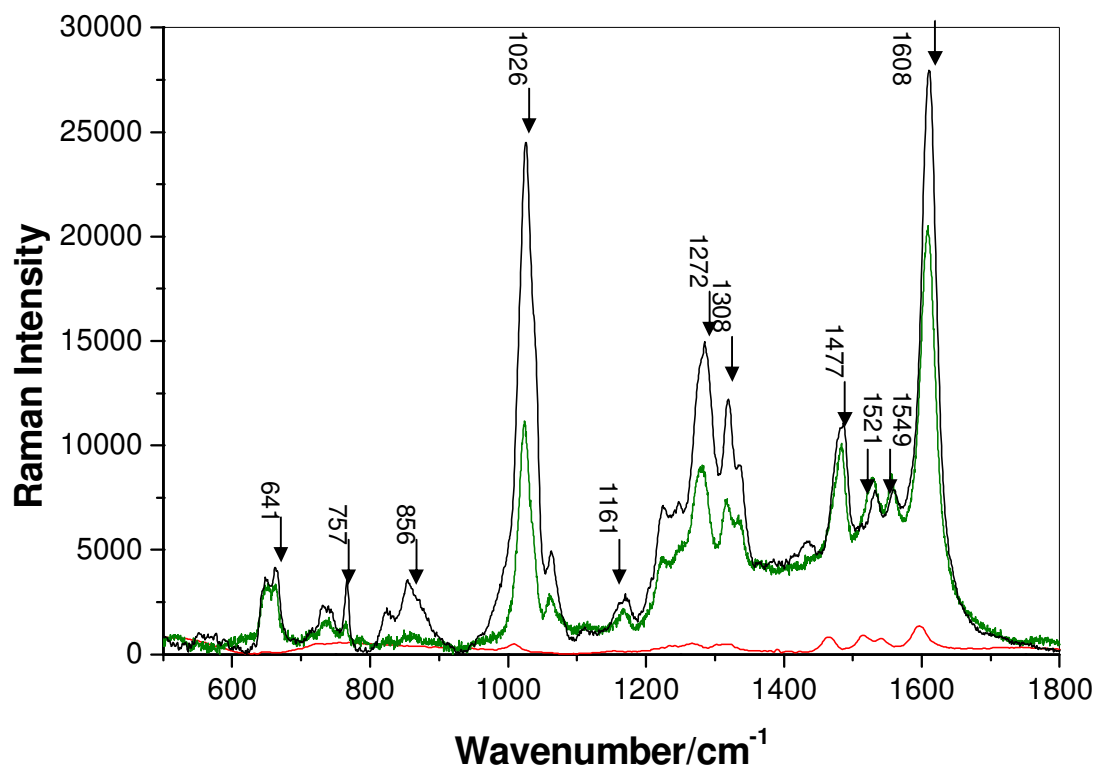
Fig. 3.4: Raman spectra of monolayers of $[Ru(bpy)_2(Qbpy)]^{2+}$ dye adsorbed at the top surface of 240 nm diameter nanocavity array at the following excitation wavelengths: (—) 785 (—) 633 (—) 514 nm with power intensity 5 mW, 4.75 mW and 16 mW respectively. Typical acquisition time was 10 s and the spot size was 2 μm. The collection angle was 72 degree.

black, red and green lines show the Raman signal intensity collected from the top surface modified 240 nm diameter arrays under 785, 633 and 514 nm excitation wavelengths, respectively. The spectra are not corrected for laser power intensity which was 5 mW, 4.75 mW and 16 mW for 785, 633 and 514 nm excitation wavelengths respectively. The laser power intensity is comparable for 785 and 633 nm excitation lines. However, the laser intensity was three fold greater for 514 nm wavelength compared to other two wavelengths.

The most intense Raman peaks around 1608, 1549, 1521 and 1477 cm^{-1} are attributed to pyridine C-C stretching modes. C-H deformation modes are found around 1308 and 1272 cm^{-1}, and ring vibration modes occur around 1026 and 641 cm^{-1}. A moderately intense feature around 1170 cm^{-1} is attributed to a coupled C-H bend and stretching mode. These modes are consistent with those reported previously for this complex adsorbed at the metal surfaces.[35] The relative intensity of the bands at 1026 and 1608 cm^{-1} appeared to be changing with the excitation wavelength. The intensity between these bands is comparable under 785 nm excitation, however, at resonance wavelength (514 nm) the peak intensity at 1608 cm^{-1} is two times greater than the band at 1026 cm^{-1}. At 514 nm excitation, it is expected to obtain SERRS from $[Ru(bpy)_2(Qbpy)]^{2+}$ dye. The reproducibility of the signal intensity between different spots of the sample was <7 %. However, reduced signal intensity was observed when the spectrum was recorded from the same spot due to bleaching of the dye molecules. After normalizing for the laser power intensity, the highest SERS intensity is observed when the arrays are excited at 785 nm. The Raman signal intensity was eight times greater when the molecules at the top surface were excited under 785 nm excitation compared to 514 nm. This increase in signal intensity at 785 nm excitation for these arrays suggests that the localized surface plasmon modes at the top of the array couple more effectively with 785 nm laser line in comparison to the other two excitation lines.
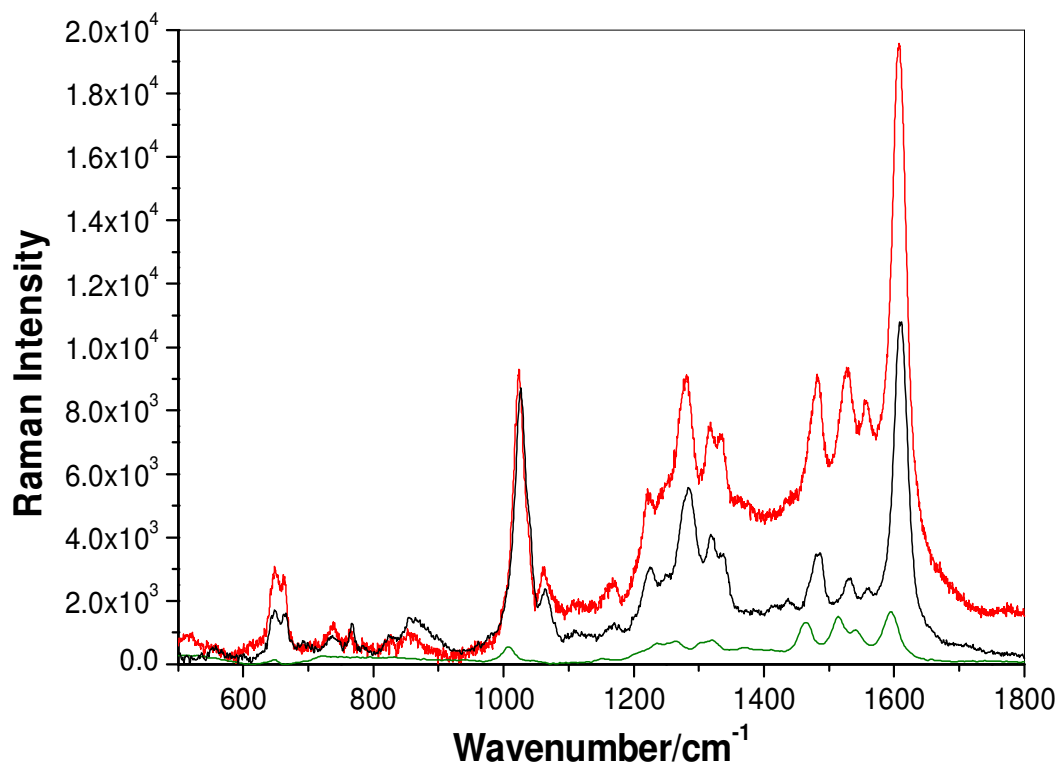
Fig. 3.5: Raman spectra of monolayers of $[Ru(bpy)_2(Qbpy)]^{2+}$ dye adsorbed at the top surface of 430 nm diameter nanocavity array at the following excitation wavelengths: (—) 785 (—) 633 (—) 514 nm with power intensity 5 mW, 4.75 mW and 16 mW respectively. Typical acquisition time was 10 s and the spot size was 2 μm. The spectra recorded with a 100x objective.

The wavelength dependent surface enhanced Raman scattering was also studied using top surface modified 430 nm diameter gold cavity arrays. The spectra are shown in Figure 3.5. In Figure 3.5, the red line shows the spectrum recorded from the top modified 430 nm array under 633 nm excitation. The green and black lines show the spectra collected under 785 and 514 nm excitation respectively, from the same sample. The reproducibility of signal intensity across the array was <7 %. For 430 nm diameter arrays, the Raman intensity is comparable at 633 and 785 nm excitations. However, the Raman signal intensity was 30 times greater when the sample was excited under 633 and 785 nm compared to 514 nm excitation after normalizing to the power intensity. The relative intensity of the bands at 1026 cm^{-1} and 1608 cm^{-1} was comparable for 633 and 785 nm excitation, consistent with SERS.

Figure 3.6 shows the Raman spectra collected from the top surface modified 600 nm diameter arrays at three different excitation wavelengths, 514, 633 and 785 nm. The

green line shows the Raman spectrum recorded from the 600 nm diameter arrays at 785 nm excitation after top surface modification of the array with ruthenium dye as described in Scheme 3.1. The red and black lines show Raman spectra collected from the same sample exciting at 514 and 633 nm respectively. After normalizing to laser power intensity, the Raman signal intensity was 10^2 times greater for the molecules excited at 785 nm compared to molecules excited under 514 nm wavelength. The signal intensity was 25 times greater under 633 nm excitation compared to 514 nm excitation. This difference in intensity values were estimated by directly comparing the peak height. In this array, the maximum signal intensity is observed at 785 nm after normalizing for laser power intensity. This suggests that the absorbance of localized surface plasmons at the top surface of 600 nm diameter arrays is closer in resonance to the 785 nm incident laser.
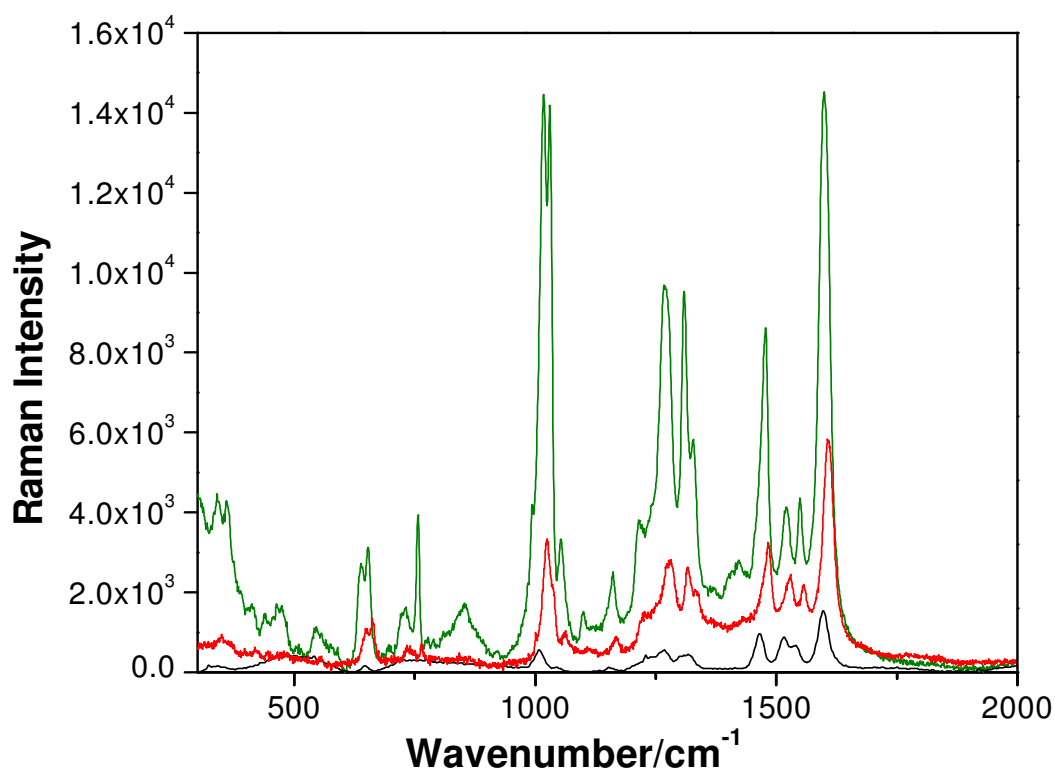

Fig. 3.6: Raman spectra of monolayers of $[Ru(bpy)_2(Qbpy)]^{2+}$ dye adsorbed at the top surface of 600 nm diameter nanocavity array at the following excitation wavelengths: (—) 785 (—) 633 (—) 514 nm with power intensity 5 mW, 4.75 mW and 16 mW respectively. Typical acquisition time was 10 s and the spot size was 2 μm. The collection angle was 72 degree.
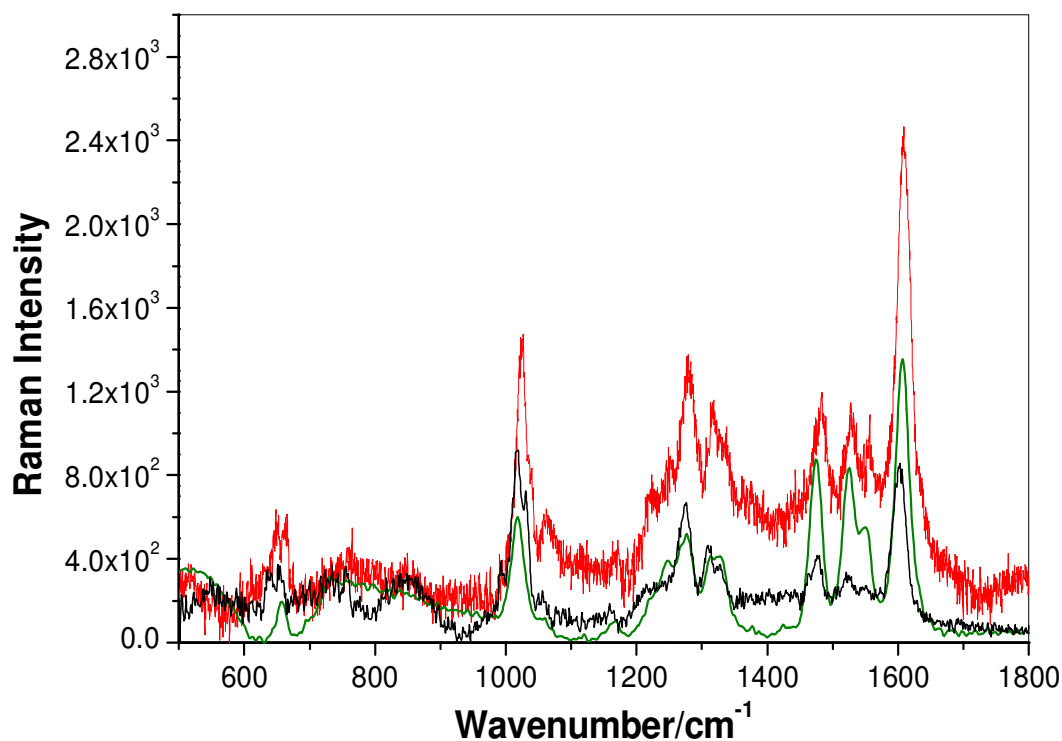
Fig. 3.7: Raman spectra of monolayers of $[Ru(bpy)_2(Qbpy)]^{2+}$ dye adsorbed at the top surface of 820 nm diameter nanocavity array at the following excitation wavelengths: (—) 785 (—) 633 (—) 514 nm with power intensity 5 mW, 4.75 mW and 16 mW respectively. Typical acquisition time was 10 s and the spot size was 2 μm.

Finally, Figure 3.7 shows the Raman spectra recorded from the top surface modified 820 nm arrays at three different excitation wavelengths, 514, 633, 785 nm. The red line shows the spectrum collected from the top surface modified array at 633 nm excitation. The green and black lines show the spectra obtained from the same sample at two different excitations, 514 and 785 nm respectively. The Raman signal intensity is nine times greater under 633 nm excitation compared to 514 and again, the signal intensity is six times greater with 785 nm excitation compared to 514 nm wavelength. This enhancement in SERS intensity at 633 nm excitation indicates that this incident laser is in resonance with the localized surface plasmons modes present at the top surface of the 820 nm arrays. Van Duyne and co-workers reported wavelength scanned surface enhanced Raman excitation spectroscopy (WS SERES) from benzene thiol adsorbed on triangular silver nanoparticles.[13] They found that maximum enhancement in Raman signal intensity is observed when the peak extinction wavelength of LSPR was located between excitation wavelength and the wavelength that is Raman-scattered by the analyte molecules. The report revealed the importance of selection of excitation wavelength in

single-molecule SERS. In our work, the gold nanocavity arrays with 240 and 600 nm diameter shows most enhancement in Raman signal intensity at 785 nm excitation whereas 430 and 820 nm diameter arrays show greater enhancement at 633 nm excitation. Therefore, subsequent studies focused on 633 nm and 785 nm excitation to compare the relative SERS enhancement from adsorbate on the top surface and cavity as these excitation wavelengths gave the best intensities.

3.3.5 SERS from arrays: 785 nm excitation

The influence of surface plasmon modes at the top surface of the arrays were investigated with three different excitation lines across four different diameters of arrays as shown in Section 3.3.4. The gold nanocavity arrays with 240 and 600 nm diameters show greatest enhancement in Raman signal intensity when the arrays excited at 785 nm. Therefore, these arrays were further investigated using the 785 nm laser line. In this instance, the top surface of the array was modified with nonanethiol after which the polystyrene spheres were removed and then the interior walls of the nanocavity arrays were selectively modified with the ruthenium dye, according to Scheme 3.1 (B). Figure 3.8 compares the Raman spectra of monolayers of $[Ru(bpy)_2(Qbpy)]^{2+}$ dye adsorbed at the top surface (black line, left axis) and interior walls (red line, right axis) of the 240 nm diameter nanocavity arrays under 785 nm excitation wavelength. The Raman signal intensity of the adsorbed dye on the gold array is highly reproducible and shows little variation (<7 %) in intensity when recorded from three different spots of the same sample across the surface. The emission background for all Raman spectra was subtracted using LabSpec software. The Raman spectral intensities were normalized to the number of molecules at the top surface and the interior walls of the arrays in confocal volume. Interestingly, the relative signal intensities of the features at 1026 cm^{-1} and 1608 cm^{-1} are significantly different for molecules on the top surface of the array compared to molecules adsorbed at the interior walls. The band intensity at 1026 cm^{-1} is greater at interior modified arrays whereas the intensity at 1608 cm^{-1} is highest for top surface modified arrays. The band intensity at 1026 cm^{-1} is used here to calculate the relative enhancement factor from whole arrays due to the greater intensity of this peak from interior modified arrays.

According to the geometric calculations described in Section 3.3.3, the number of molecules adsorbed at the interior walls of the nanocavity is approximately eight times greater than the number of molecules adsorbed at the top surfaces within the confocal volume. In spite of this, the Raman signal intensity from the top surface modified cavity arrays is significantly larger than that seen at the interior walls of the arrays. The enhancement factor for molecules adsorbed at the top surface over those at the interior cavity walls is approximately 170±10 for the 240 nm diameter arrays, after consideration
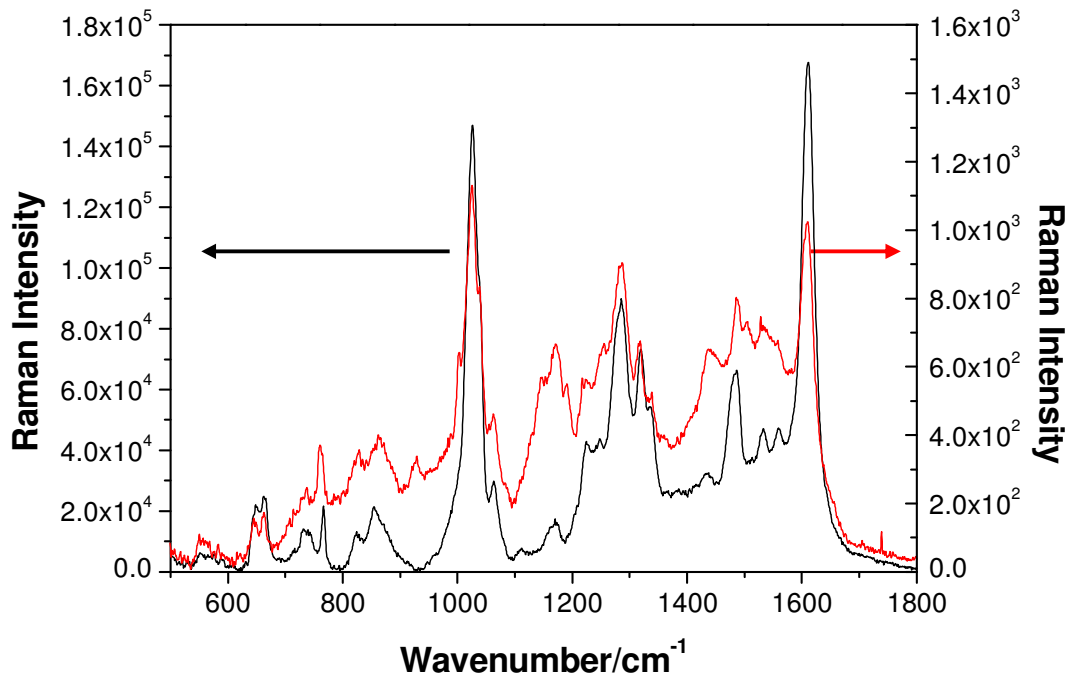
Fig. 3.8: Raman spectra of $[Ru(bpy)_2(Qbpy)]^{2+}$ adsorbed at (—) top surface and (—) interior walls of 240 nm nanocavity arrays. The spectra were recorded under identical conditions and normalized for number of molecules. The excitation wavelength was 785 nm. Typical acquisition time was 10 s and the spot size was 2 μm. The collection angle was 72 degree.

of the relative number of molecules in the confocal volume. The relatively greater enhancement in Raman signal intensity from the top surface of 240 nm diameter gold nanocavity arrays indicates effective coupling of plasmon modes at the top surface compared to the interior walls of the nanocavity array. However, it is important to note that the interior surfaces of 240 nm diameter arrays show a 10 fold enhancement in signal intensity compared to unroughened gold (roughness factor ~ 1.3). This enhancement from the interior decorated arrays compared to the unroughened surface suggests that there is a contribution of interior plasmon modes to the total enhancement from the gold nanocavity arrays. The enhancement factor obtained compared to the smooth gold surface is calculated using Equation 3.2.

$$EF = (I_{NC}/I_{Au})*(N_{Au}/N_{NC}) \qquad 3.2$$

where I_{NC} is the intensity of the 1026 cm^{-1} mode from the metal complex on the nanocavity array and I_{Au} for that on unroughened gold. N_{Au} is the number of molecules

estimated to be present on unroughened gold based on its surface area and the coverage associated with a close packed layer, and N_{NC} is the number estimated to be on the top surface of nanocavity array.

It is important to note that in the case of interior modified array, the top surface of the array is blocked with 1-nonane thiol. It is clear that the resonance excitation of ruthenium dye is not playing a role at 633 and 785 nm. Therefore, one would have expected significant enhancements in Raman signal intensity for the alkane thiol modes, when we consider the relative enhancements obtained by adsorption of ruthenium at the top surface. However, the Raman spectrum observed is dominated by the ruthenium complex whether the thiol is present or not. This might be either due to the relatively smaller Raman cross sections of the alkane thiols compared with the aromatic moieties of the ruthenium complex or due to the chemical enhancement mechanism for the observed SERS for $[Ru(bpy)_2(Qbpy)]^{2+}$ complex.

Raman spectra of $[Ru(bpy)_2(Qbpy)]^{2+}$ selectively adsorbed at the top surface and interior cavity walls of 430 nm nanocavity arrays excited at 785 nm are shown in Figure 3.9. The top surface of 430 nm diameter arrays showed greatest enhancement in Raman signal intensity at 633 nm excitation compared to 785 and 514 nm as discussed in Section 3.3.4. Here, the 785 nm laser line is used to investigate the excitation of surface plasmons at the interior walls of the array compared to the top surface at this wavelength. The black line shows the spectrum for $[Ru(bpy)_2(Qbpy)]^{2+}$ dye monolayers adsorbed at the top surface and the red line shows the spectrum for monolayers adsorbed at the interior walls of the nanocavity arrays. The number of molecules under confocal area, adsorbed at the inside walls of the nanocavity array is approximately 10 times greater than the number of molecules at the top surface based on geometrical calculations. Correcting for the relative greater number of molecules inside the cavity, the enhancement factor is 43±5 times greater for the monolayers adsorbed at the top surface compared to that obtained for the molecules adsorbed inside the cavity. The interior cavity modified 430 nm diameter arrays show an increase in Raman signal intensity approximately 25 times greater compared to unroughened gold substrate. The Raman spectra were collected from three different spots of the same sample and the measurements shown <7 % variation between the spots. Interestingly, similar to 240 nm diameter arrays, the bands

at 1026 and 1608 cm^{-1} show significant variations in relative intensity for selectively modified arrays. Raman spectra of [Ru(bpy)$_2$(Qbpy)]$^{2+}$ dye adsorbed at the top surface
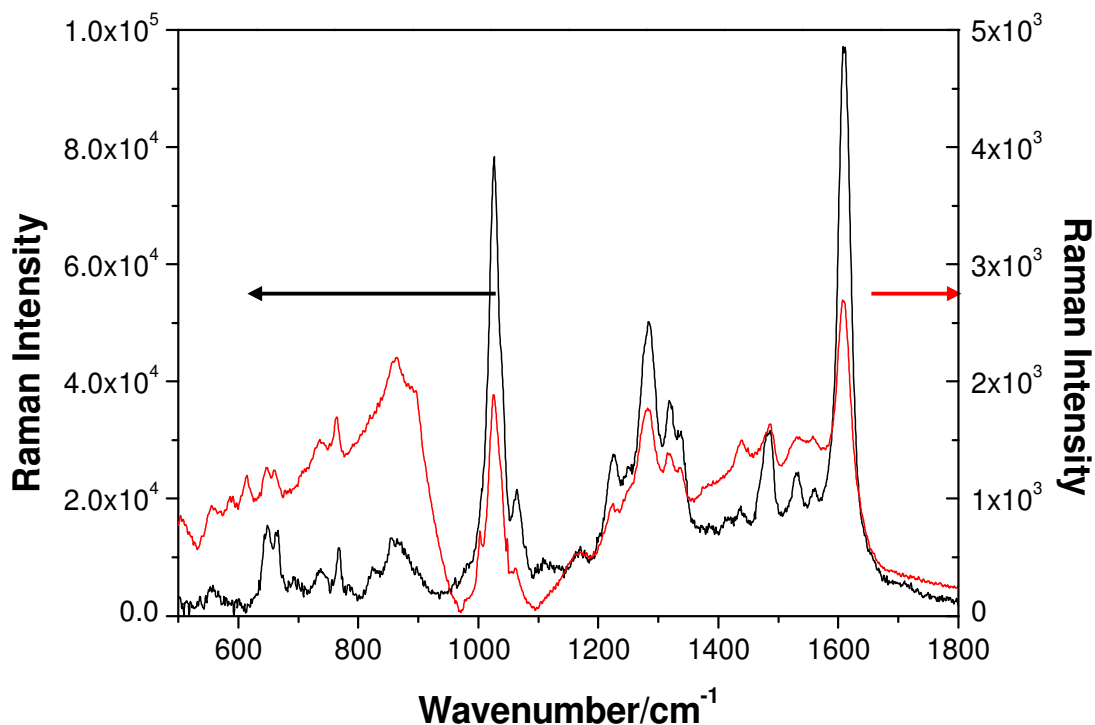

Fig. 3.9: Raman spectra of [Ru(bpy)$_2$(Qbpy)]$^{2+}$ adsorbed at (—) top surface and (—) interior walls of 430 nm nanocavity arrays. The spectra were recorded under identical conditions and normalized for number of molecules. The excitation wavelength was 785 nm. Typical acquisition time was 10 s and the spot size was 2 μm. The spectra recorded using a 100x objective.

(black, left axis) and the interior cavity walls (red, right axis) of 600 nm nanocavity arrays are shown in Figure 3.10. This figure shows that the SERS signals from selectively modified 600 nm gold nanocavity arrays also follow the same trend as seen for 240 nm and 430 nm gold cavity arrays. The gold nanocavity with 600 nm diameter array shows an enhancement in Raman signal intensity of approximately 39±4 times greater for the molecules selectively adsorbed at the interior walls compared to those adsorbed on the unroughened gold surface. The corrected enhancement factor for the monolayers adsorbed at the top surface is approximately 37±5 times greater compared to those seen adsorbed inside the cavity after considering the number of molecules in the confocal volume taken into account.

Raman spectra of $[Ru(bpy)_2(Qbpy)]^{2+}$ dye adsorbed at the top surface and the interior cavity walls of 820 nm nanocavity arrays are shown in Figure 3.11. As before, the black line shows the spectrum obtained from the top surface modified substrate and the red line shows the spectrum obtained from the interior modified arrays. Similar to the other arrays, the spectroscopic signal seen from the top surface modified arrays is greater than that seen for interior modified arrays, after normalization for the number of molecules present in the confocal volume. The relative enhancement factor of approximately 6±2 is observed for the top surface modified arrays compared to those seen for interior modified arrays.
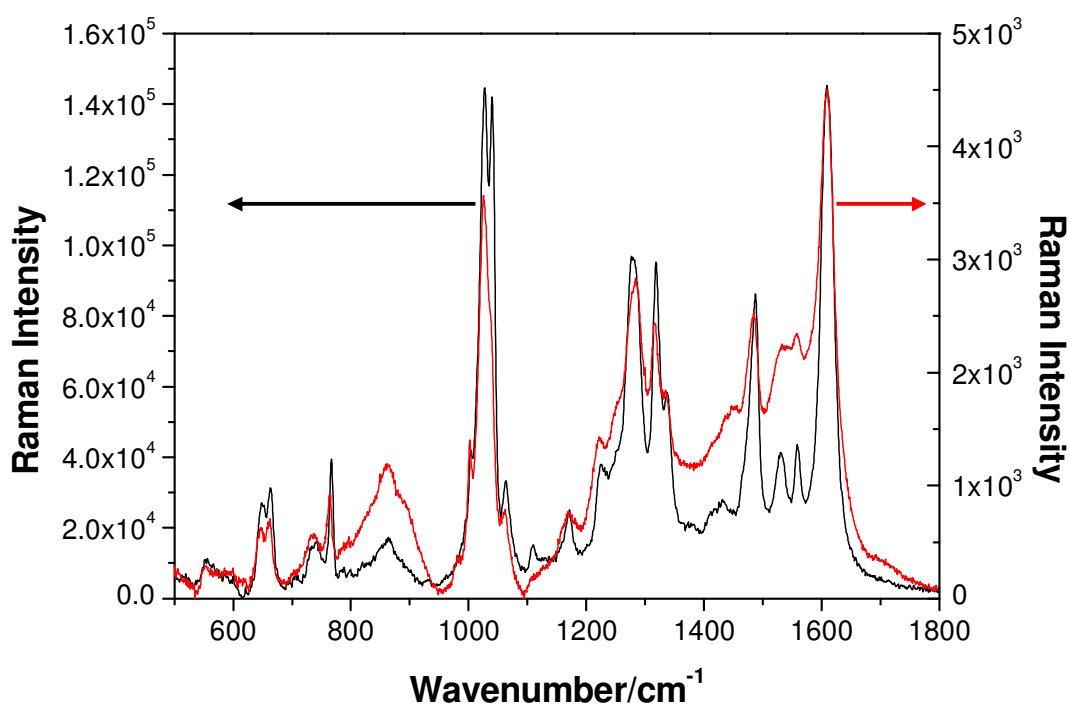

Fig. 3.10: Raman spectra of $[Ru(bpy)_2(Qbpy)]^{2+}$ adsorbed at (——) top surface and (——) interior walls of 600 nm nanocavity arrays. The spectra were recorded under identical conditions and normalized for number of molecules. The excitation wavelength was 785 nm. Typical acquisition time was 10 s and the spot size was 2 μm.

Theoretical calculations reported by Bartlett et al. have previously shown that the 600 nm diameter arrays with a normalized thickness of 0.8 exhibit a strong surface plasmon mode around 785 nm, which supports strong coupling of incident light with the molecules adsorbed at the metal rim.[16] Moreover, an experimental investigation into the plasmon field distribution using metal hybrid structures with this diameter disclosed that the nickel

void with gold rim shows similar SERS enhancement to that of gold only structure which again confirmed the strong field distribution at the rim of the array.[25] Here, the top surface modified substrates show significantly larger enhancement compared to interior modified arrays, which again suggests the presence of more intense or perhaps more accessible surface plasmon modes at the top surface of these arrays. This paper also revealed that the enhancement of Raman signal intensity was negligible within the gold void with thick nickel rim structure. This indicates that there is only a minor contribution from the void structure to total SERS enhancement.[25] Here, in selective modification experiment, the 600 nm diameter array contributes around 21 % of the SERS signal intensity to the fully decorated arrays which might be originating from the coupling of Bragg and Mie surface plasmon modes which is absent in hybrid structures.

Van Duyne and co-workers reported that the vapour deposition of silver through the voids of 400 nm diameter arrays on the glass substrate produces nanotriangles with in-plane width of ~ 100 nm, which provide enhancements in SERS intensity in the range of 10^5-10^8 depending on the height of the film.[36,37] The top surface of the nanocavity arrays prepared here are similar to the triangles prepared by Van Duyne et al. This group have demonstrated huge enhancements from the silver triangles and here it is interesting to compare the enhancement region due to similarity in structure. They have shown that the enhancement was mainly arising from the triangular tips. Here, the greatest Raman signal intensity is observed from monolayers adsorbed at the top surface of the nanocavity arrays indicating the presence of strong localized surface plasmon modes at the top surface of metal nanocavity rather than the negative curvature spherical nanocavity walls. The Raman spectra obtained from the four different diameters of cavities reveal that a more significant electric field might be created at the triangular edges of the arrays compared to the interior walls of the arrays. As reported by Bartlett, the presence of rim plasmon modes at the edges of metal nanocavity arrays couple with the incident light more efficiently than void plasmon modes, giving large enhancement in Raman intensity at these rims.[25] Mahajan et al. reported that the maximum signal intensity from the gold nanocavity arrays were obtained when the normalized thicknesses of the arrays were between 0.4-0.8.[1] In addition, Moerner reported that the bowtie structures can amplify both Raman and fluorescence signal intensity from the molecules adsorbed on these structures.[20,21] Here, significant enhancement in Raman signal

intensity from the top surface modified arrays could be arising from the hot spots present at the edges of triangular features. The reduced enhancement in Raman intensity for larger diameter cavity arrays suggests that the enhancement is mainly arising from the sharp tips at the edges, so called "hot spots". At larger diameter arrays, less of these hot spots are present in the confocal area, which is constant over the course of this work.
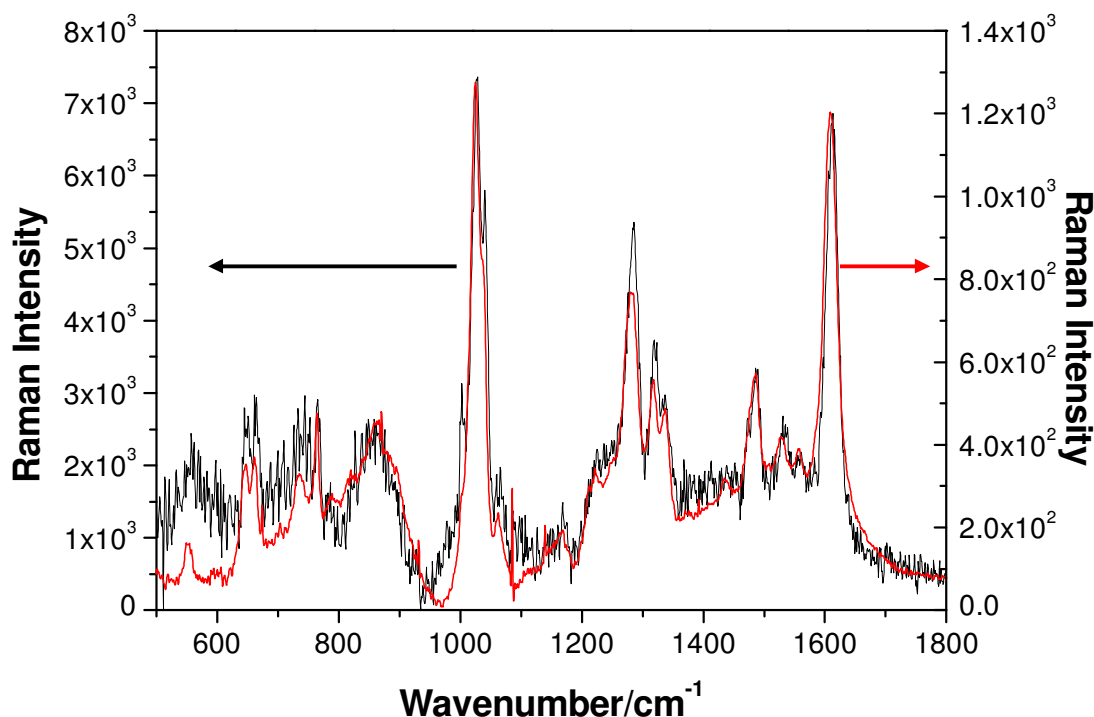
Fig. 3.11: Raman spectra of $[Ru(bpy)_2(Qbpy)]^{2+}$ adsorbed at (—) top surface and (—) interior walls of 820 nm diameter nanocavity arrays. The spectra were recorded under identical conditions and normalized for number of molecules. The excitation wavelength was 785 nm. Typical acquisition time was 10 s and spot size was 2 μm.

Table 3.2 shows the top surface and the internal cavity areas determined for each cavity size and the associated intensity of the 1026 cm^{-1} Raman band. These relative areas were calculated from a defined surface area (7 μm^2) and show that the relative areas of interior and the edge areas vary little as a function of cavity size. There is not much change in signal intensity collected from the interior walls of different diameters of arrays. The minor changes in signal intensity from the interior walls of different sizes of array rules out the notion that wavelength coming from the smaller diameter arrays are trapped inside the arrays. If there is significant difference in signal intensity for large diameter

arrays then that could be the reason for the large enhancement factor for smaller diameter top modified arrays compared to interior modified arrays.

Cavity diameter (nm)	Edge		Interior	
	Area (μm^2)	Raman Intensity	Area (μm^2)	Raman Intensity
820	3.0±0.4	900	26±3	1200
600	2.3±0.3	14000	25±2	4000
430	2.1±0.3	9000	20±3	2000
240	3.1±0.4	25000	21±1.5	1000

Table 3.2: Surface area and Raman intensity of the 1026 cm^{-1} peak for top surface and interior modified cavity arrays of various cavity diameters. The wavelength of excitation was 785 nm.

In order to calculate the enhancement from cavity interior modified arrays, it is necessary to compare the signal intensity from self-assembled monolayers of dye formed on a smooth gold surface (roughness factor ~ 1.3). Figure 3.12 shows the Raman spectrum collected from self-assembled monolayers of $[Ru(bpy)_2(Qbpy)]^{2+}$ dye adsorbed at the surface of unroughened gold surface at 785 nm excitation. It can be clearly seen that weak Raman signals are obtained from unroughened gold surface. The comparison of Raman signal intensity from the smooth gold surface with the interior modified arrays indicates the presence of surface plasmon modes even at the interior of the gold nanocavity arrays.
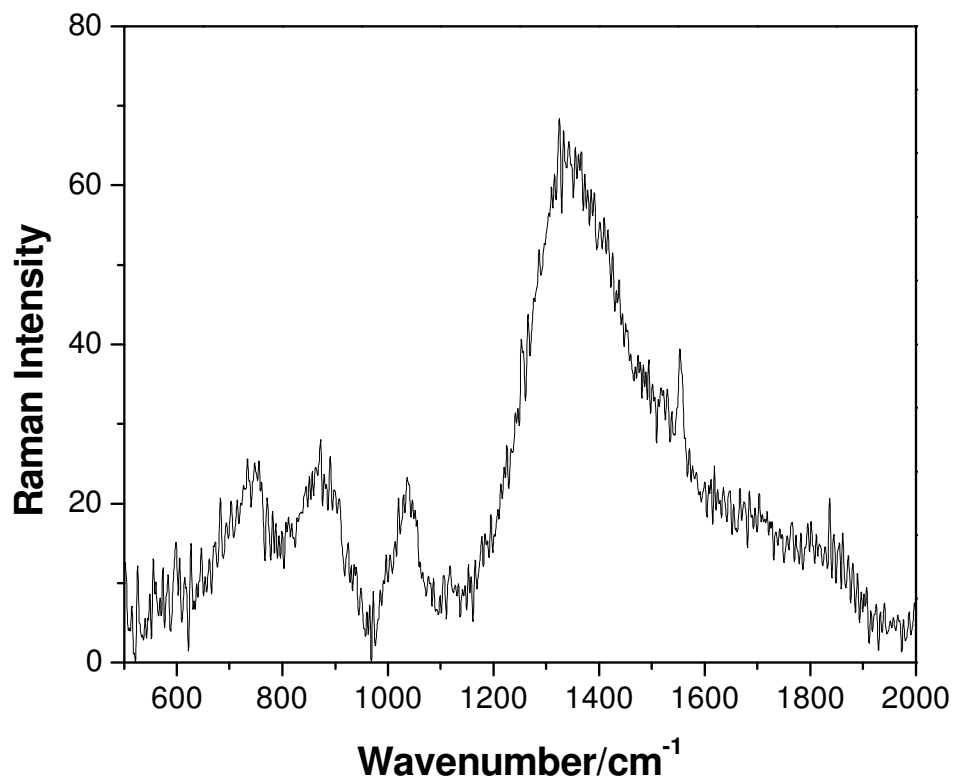
Fig. 3.12: Raman spectrum of monolayers of $[Ru(bpy)_2(Qbpy)]^{2+}$ dye adsorbed on a planar gold surface which has a roughness factor ~ 1.3. The excitation wavelength was 785 nm. The spot size was 2 μm. The collection angle was 72 degree.

3.3.6 SERS from arrays: 633 nm excitation

Gold nanocavity arrays with diameters 430 and 820 nm show greatest enhancement in Raman signal intensity at 633 nm excitation compared to 785 and 514 nm as discussed in Section 3.3.4. Therefore, 633 nm excitation was also used to study the location of best enhancement from different diameters of the arrays. Figure 3.13 shows the Raman spectra collected from monolayers of $[Ru(bpy)_2(Qbpy)]^{2+}$ adsorbed at the top surface (black, left axis) and interior walls (red, right axis) of 240 nm gold cavity arrays. The excitation wavelength was 633 nm. Here, greater signal intensity is expected from the interior walls of the array compared to top surface due to the greater concentration of molecules at the interior walls. However, the greatest enhancement in Raman signal intensity is observed at the top surface than the interior walls of the array.
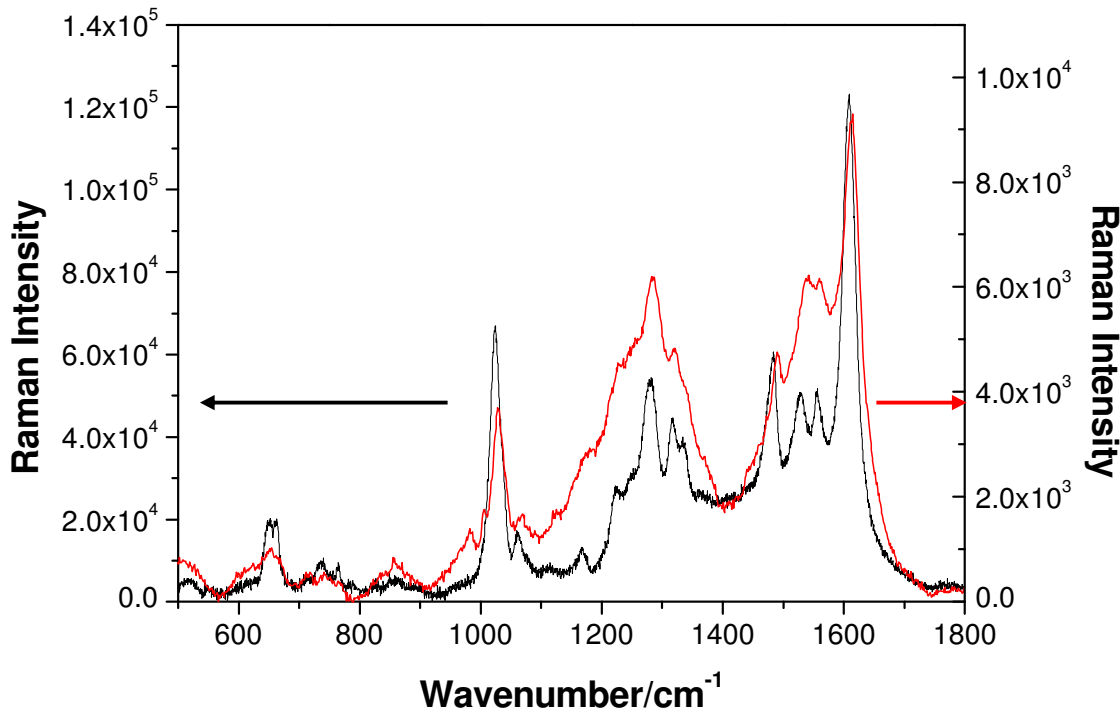
Fig. 3.13: Raman spectra of $[Ru(bpy)_2(Qbpy)]^{2+}$ adsorbed at (—) top surface and (—) interior walls of 240 nm nanocavity arrays. The spectra were recorded under identical conditions and normalized for number of molecules. The excitation wavelength was 633 nm. Typical acquisition time was 10 s and the spot size was 2 μm. The spectra recorded using a 100x objective.

As discussed before, the number of molecules presents in the laser spot was eight times greater for interior walls compared to the top surface modified array. The enhancement

of Raman signal intensity at the top surface was approximately 20±4 compared to the interior decorated arrays after normalizing for the number of molecules in the laser spot. This increase in intensity suggests the effective coupling of surface plasmons with incident laser at the top surface compared to the interior walls of 240 nm gold nanocavity arrays at 633 nm excitation similar to that of 785 nm excitation. The Raman signal intensity is collected from three different spots of the same sample and variation in intensity between the spots was less than 7 %.
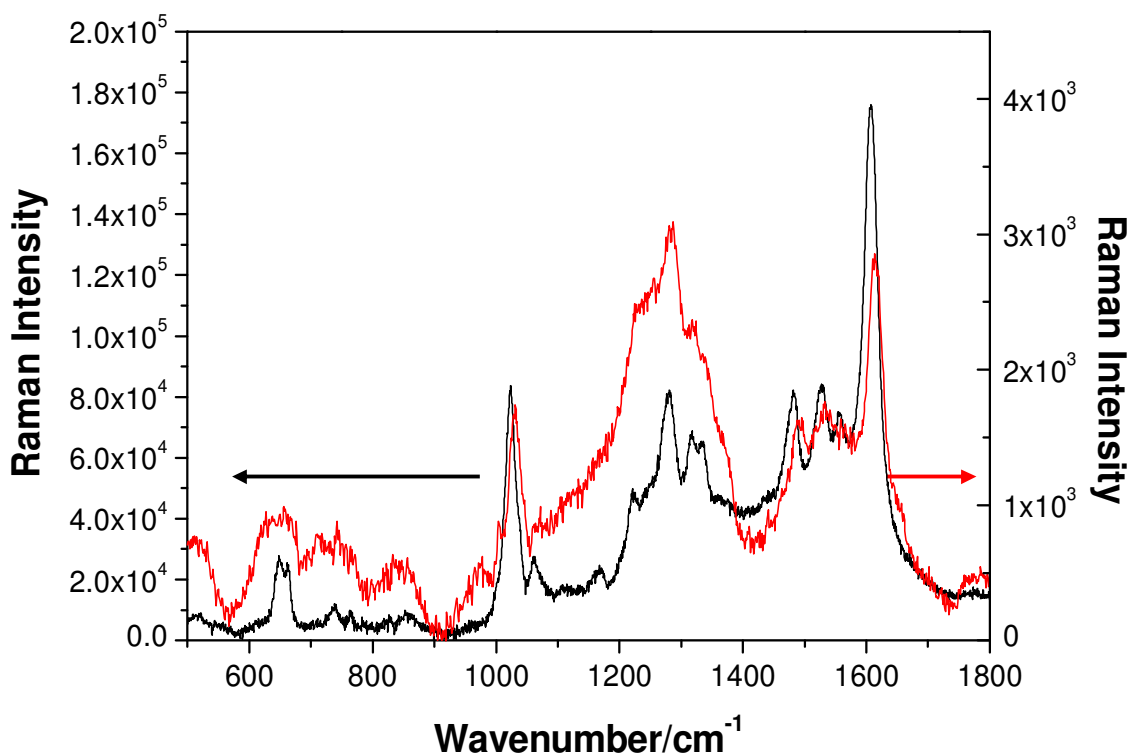
Fig. 3.14: Raman spectra of $[Ru(bpy)_2(Qbpy)]^{2+}$ adsorbed at (—) top surface and (—) interior walls of 430 nm nanocavity arrays. The spectra were recorded under identical conditions and normalized for number of molecules. The excitation wavelength was 633 nm. Typical acquisition time was 10 s and the spot size was 2 μm. The collection angle was 72 degree.

Figure 3.14 shows the Raman spectra of $[Ru(bpy)_2(Qbpy)]^{2+}$ dye adsorbed at the top surface (black, left axis) and the interior walls (red, right axis) of 430 nm diameter nanocavity arrays at 633 nm excitation. Again, the top surface of the arrays shows greater signal compared to interior walls of the 430 nm diameter arrays. The number of molecules in the confocal volume was 10 times greater for interior walls compared to the top surface modified arrays. The enhancement factor was determined to be around 44±5

from material adsorbed at the top surface compared to the interior walls after considering the number molecules at the interior walls in the confocal volume. Previous reports have
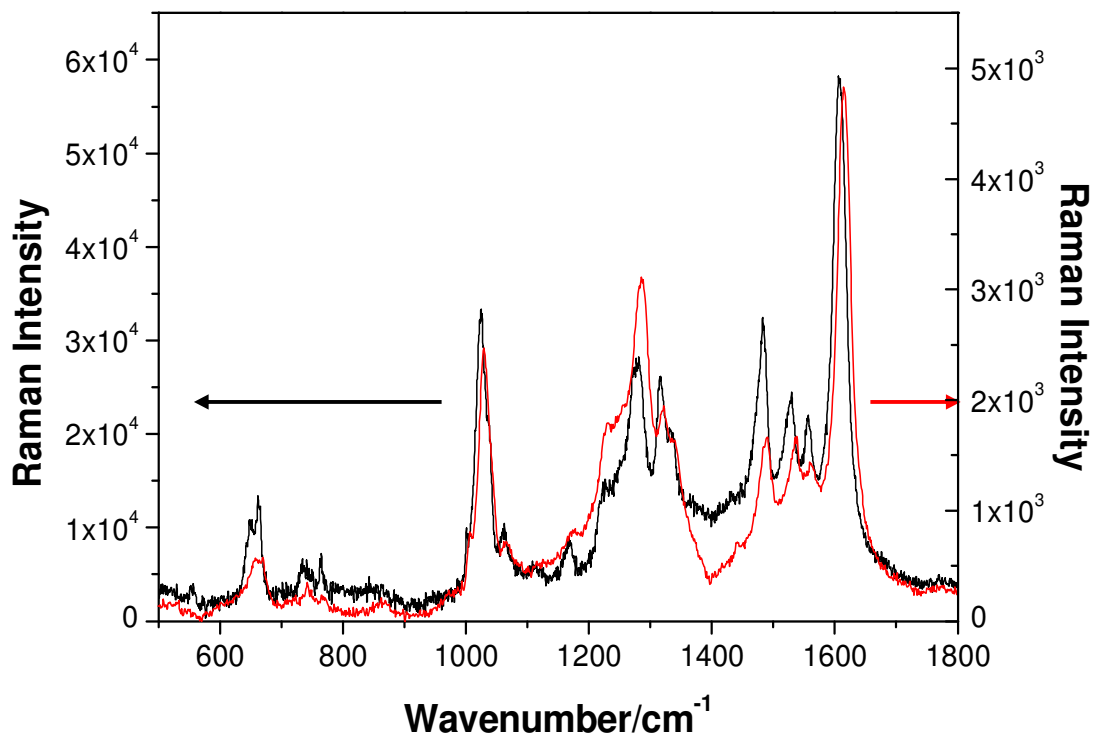

Fig. 3.15: Raman spectra of [Ru(bpy)$_2$(Qbpy)]$^{2+}$ adsorbed at (—) top surface and (—) interior walls of 600 nm nanocavity arrays. The spectra were recorded under identical conditions and normalized for number of molecules. The excitation wavelength was 633 nm. Typical acquisition time was 10 s and the spot size was 2 μm.

shown that the gold nanocavity array with 400 nm diameter (t=0.8) shows a strong plasmon mode at 633 nm excitation.[16]

Raman spectra of ruthenium dye selectively adsorbed at the top surface (black, left axis) and the interior walls (red, right axis) of 600 nm arrays collected under identical conditions are shown in Figure 3.15. The number of molecules in the confocal volume was 10 times greater at the interior walls compared to the top surface of the array and the enhancement factor was approximately 14±3 for the molecules adsorbed at the top surface compared to the selectively decorated interior walls. The 600 nm diameter arrays with a normalized thickness of 0.8 shows a weak surface plasmon mode at 633 nm whereas a strong surface plasmon mode at 785 nm.[16] Therefore, the enhancement in the signal intensity at 633 nm excitation might be due to the coupling of this weak plasmon

mode with 633 nm laser line. Similarly, Figure 3.16 shows the Raman spectra of $[Ru(bpy)_2(Qbpy)]^{2+}$ dye adsorbed at the top surface and the interior walls of 820 nm
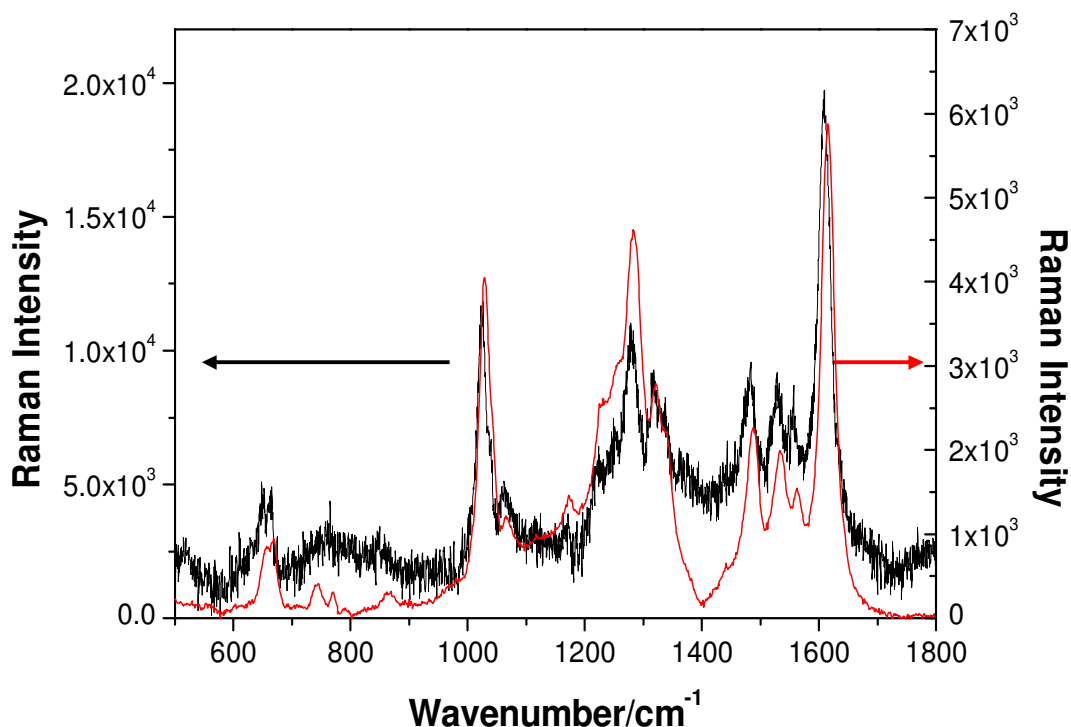
Fig. 3.16: Raman spectra of $[Ru(bpy)_2(Qbpy)]^{2+}$ adsorbed at (—) top surface and (—) interior walls of 820 nm nanocavity arrays. The spectra were recorded under identical conditions and normalized for number of molecules. The excitation wavelength was 633 nm. Typical acquisition time was 10 s and the spot size was 2 μm.

diameter arrays at 633 nm excitation. The enhancement factor was approximately 3±1 for molecules adsorbed at the top surface compared to the interior modified array. This increase in signal intensity suggests again the presence of strong surface plasmons modes at the top surface than the interior walls of the 820 nm diameter arrays. The gold nanocavity array with 800 nm diameter array (t=0.8) shows a weak surface plasmon mode at 633 nm, therefore this smaller enhancement in Raman signal intensity might be due to the coupling of these weak plasmon modes with the 633 nm excitation laser line. In conclusion, at both 785 and 633 nm excitation, the top surface of the arrays yields greater enhancement in Raman signal intensity than the interior decorated arrays. The origin of the enhancement is due to the effective coupling of localized surface plasmons with the appropriate incident laser line. However, the top surface of the array gives

higher enhancement for both 633 and 785 nm excitation lines which is clearly greater at the top surface of the array. The decrease in enhancement factor from bigger cavities suggests that the enhancement mainly arises from the sharp tips or "hot spots" present at the top surface. Van Duyne and co-workers have reported the presence of strong SERS signal intensity from similar triangular nanoparticles.[38,39] Kinkhabwala et al. have also reported the enhancement of Raman signal intensity from bowtie structures and the report reveals that the enhancement is mainly arising from the gap between the triangular structures.[20] In addition, they have reported the maximum enhancement from the small gaps between the triangles and enhancement decreases as a function of the gap size. Table 3.3 shows the top surface and internal cavity area determined for each cavity diameter and the associated intensity of the 1026 cm^{-1} Raman band, using 633 nm as an excitation source. A very similar pattern to that seen at 785 nm is observed wherein, the edge modified 240 nm cavity arrays provide the best enhancement and there is a little overall change in the signal seen from the cavity interior.

Cavity diameter (nm)	Edge		Interior	
	Area (μm^2)	Raman Intensity	Area (μm^2)	Raman Intensity
820	3.0±0.4	1800	26±3	4000
600	2.3±0.3	3500	25±2	3000
430	2.1±0.3	8300	20±3	2000
240	3.1±0.4	12000	21±1.5	3000

Table 3.3: Active surface area and Raman intensity of 1026 cm^{-1} peak for the top surface and interior modified cavity arrays of various cavity diameters. The wavelength of excitation was 633 nm.

In order to calculate the enhancement from interior modified arrays, it is necessary to compare the signal intensity from a comparable platform in which a monolayer is formed. Therefore, self-assembled monolayers of dye formed on a smooth gold surface used as a control. Figure 3.17 shows the Raman spectrum collected from self-assembled monolayers of [Ru(bpy)$_2$(Qbpy)]$^{2+}$ dye adsorbed at the surface of unroughened gold surface at 633 nm excitation. The Raman signal intensity from the smooth surface was weak at this excitation wavelength using the parameters used for the array therefore; it was difficult to acquire spectra using same experimental set up. The spectrum shown below was recorded using high laser power and more acquisition time compared to the

spectra recorded from gold nanocavity arrays. The enhancement factor for gold nanocavity arrays were calculated after correcting for the laser intensity and the number of molecules in the confocal volume. Comparison of Raman signal intensity from the smooth gold surface with the interior modified arrays indicates the presence of surface plasmon modes at both top and interior of the gold nanocavity arrays. Comparison of monolayer formed at three different surfaces, smooth gold surface, edges of the arrays and interior walls of the arrays, reveal the presence of strongest plasmonic enhancement at the top surface and relatively weaker plasmon modes in the interior of four different arrays.
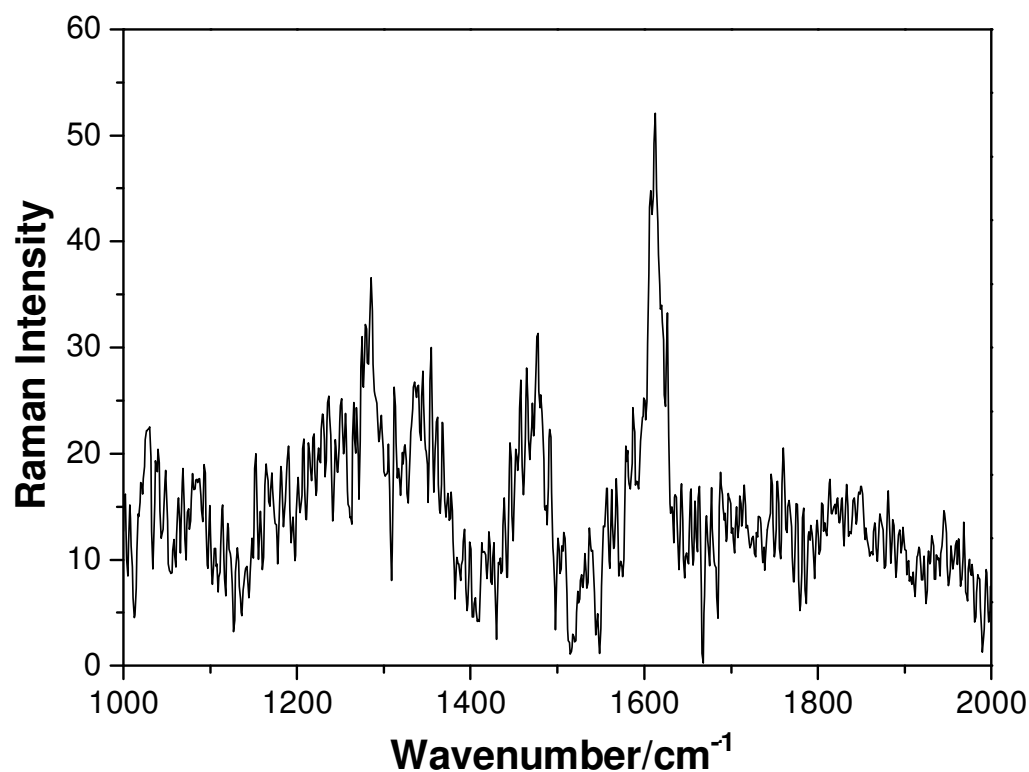
Fig. 3.17: Raman spectrum of monolayers of $[Ru(bpy)_2(Qbpy)]^{2+}$ dye adsorbed on a planar gold surface (roughness factor ~ 1.3). The excitation wavelength was 633 nm. The spot size was 2 μm. The collection angle was 72 degree.

Table 3.4 shows the relative Raman signal intensities from the top surface modified arrays compared to interior modified arrays at 785 and 633 nm excitation. In order to investigate the origin of this Raman signal enhancement, the reflectance measurements were carried out for four different arrays as shown in following section.

Cavity Diameter (nm)	Edge Vs Interior (785 nm)	Edge Vs Interior (633 nm)
820	6±2	3±1
600	37±4	14±3
430	43±5	44±5
240	170±7	19±4

Table 3.4: Relative Raman signal intensity at the top surface of the arrays vs interior at 633, and 785 nm excitation.

3.3.7 Reflectance measurements of gold nanocavity arrays

Raman measurements from selectively decorated gold nanocavity arrays suggests that the arrays with diameters 240 and 600 nm shows greatest enhancement at 785 nm excitation whereas the arrays with 430 and 820 nm diameter shows greater enhancement at 633 nm excitation. Therefore, it is expected that the arrays with diameters of 430 and 820 nm might exhibit strongest plasmon absorption at 633 nm whereas the other two arrays should shows strongest surface absorption at 785 nm. The reflectance measurements of gold nanocavity arrays were conducted to investigate the origin of the enhancement in Raman signal intensity for different diameter arrays at 633 and 785 nm excitations. Figure 3.18 shows the reflectance measurements were recorded from a smooth gold surface (black) and from the different diameter gold nanocavity arrays. The red, green, blue and cyan show the reflectance from 240, 430, 600 and 820 nm diameter arrays respectively. The reflectance spectra were plotted after removing the reflectance background by correcting with the spectra of white light. Then, the each spectrum was normalized to its maximum intensity value. The spectrum of smooth gold surface possesses absorbance around 490 nm which corresponds to the absorption of bulk gold surface. The smooth gold surface is highly reflective in UV-visible region as expected.

The absorbance curves of the gold nanocavity arrays with 240 and 430 nm diameter arrays show similar shapes in visible region. The 630 nm diameter arrays shows two absorption maxima in the spectrum. One is around 700 nm and the other one around 480 nm. The latter one is probably due to the absorption of bulk gold. The 820 nm diameter arrays show mainly three absorption in the spectra around 480, 630 and 800 nm. The absorption around 480 nm is attributed to the absorption of bulk gold. The absorption at 640 and 800 are attributed to the absorption of surface plasmon modes. Systematic studies of surface plasmons on gold nanocavity arrays have shown that the gold nanocavity arrays absorb at different regions depending on the diameter and thickness of the arrays.[40] Previous reports have shown that the enhancement of the Raman signal intensity can be optimized by using an excitation laser line that matches with the surface plasmon absorption of the SERS substrates.[15] As discussed in the previous section, the gold nanocavity arrays with 430 and 820 nm diameter show greatest enhancement in
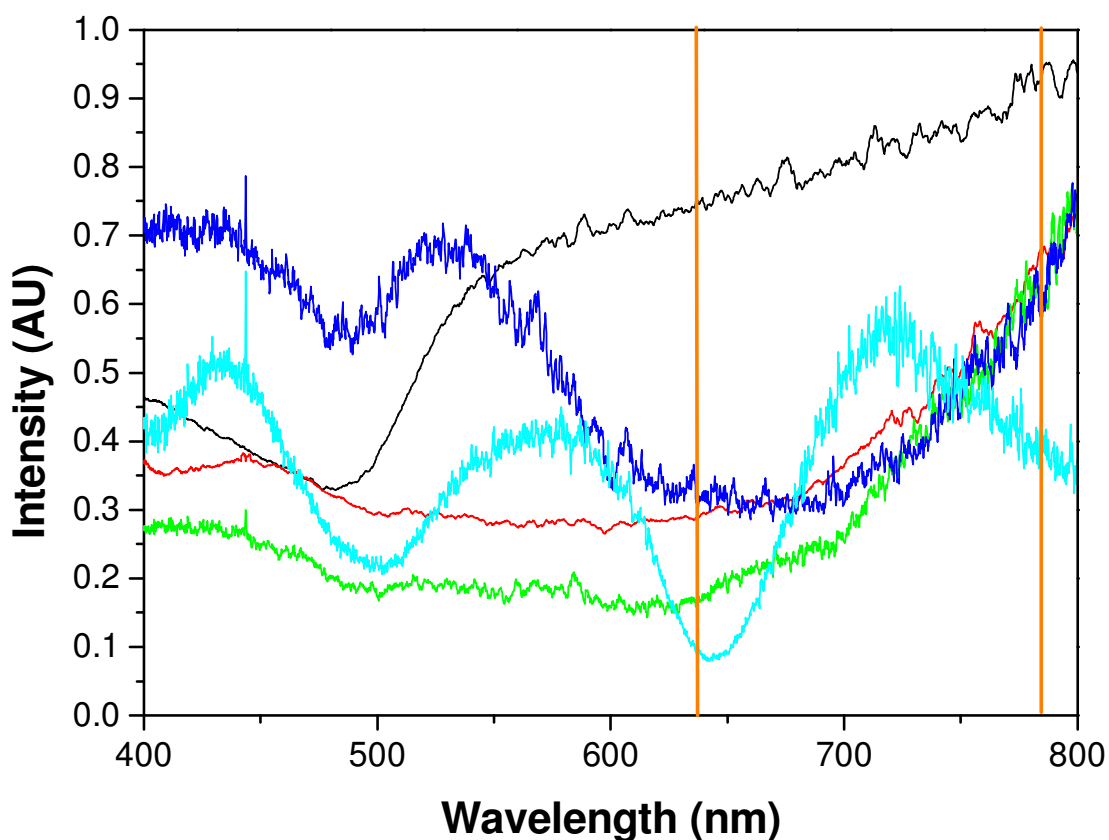
Fig. 3.18: Reflectance spectra of (——) smooth gold (——) 240 nm, (——) 430 nm, (——) 600 nm and (——) 820 nm diameter arrays. The film thickness is approximately 0.8±0.04 (t_N= t/d = 0.8).

adsorbate Raman signal intensity under 633 nm excitation than 785 nm. This is consistent with the reflectance measurements which also show that these arrays exhibit greater absorption at 633 nm than 785 nm. The arrays with 240 nm and 600 nm diameters show greater enhancement in Raman signal intensity at 785 nm compared to 633 nm excitation. However, these arrays show greater absorption at 633 nm than 785 nm. The origin of this discrepancy is unclear between the Raman signal enhancement and reflectance spectra.

3.3.8 Emission Enhancement

The preceding section clearly demonstrated the relative role of interior cavity and top surface in enhancing Raman signal where significantly greater contribution from SERS is derived from monolayer adsorbed at the top surface compared to cavity interior for smaller cavity sizes. In addition, Chapter 2 demonstrated that the dye filled gold nanocavity arrays provide enhancement in emission intensity. The very large Stokes shift of the luminescence of $[Ru(bpy)_2(Qbpy)]^{2+}$ allowed parallel study of luminescence and Raman from single array. Figure 3.19 compares the emission spectra of $[Ru(bpy)_2(Qbpy)]^{2+}$ dye adsorbed at the top surface (black line) and at the cavity walls (grey line) of 240 nm cavities using an excitation wavelength of 473 nm. The emission maxima for $[Ru(bpy)_2(Qbpy)]^{2+}$ dye in solution is approximately 650 nm, whereas that for the monolayer, as shown in Figure 3.19 is 720 nm. This red shifted λ_{max} has been
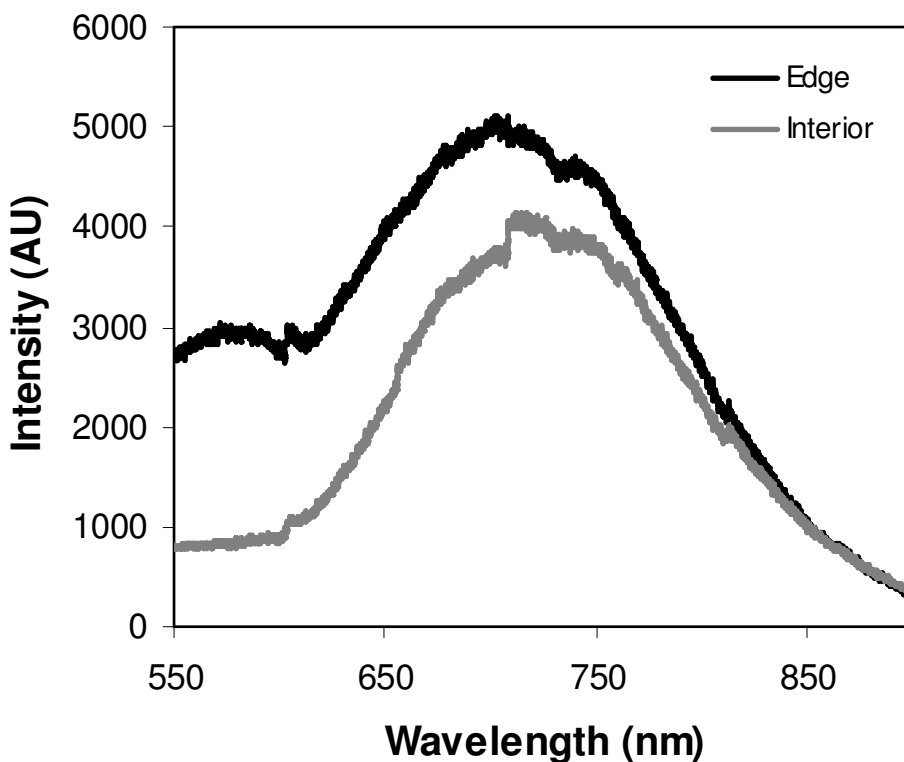
Fig. 3.19: Emission spectra of $[Ru(bpy)_2(Qbpy)]^{2+}$ adsorbed at the top surface (black) and interior walls (grey) of 240 nm nanocavity arrays. The spectra were recorded under identical conditions. The excitation wavelength was 473 nm. The spectra recorded using 100x objective.

reported previously for this complex adsorbed at platinum microelectrodes and is attributed to changes to the dielectric and rigidochromism the complex experiences in a close-packed monolayer.[30] The population of molecules adsorbed at the interior walls of the nanocavity array is eight times greater than the population of molecules adsorbed at the top surface. However, the emission intensity is greater from the top surface modified arrays compared to the interior wall modified array, which is consistent with the trend seen for the SERS signals. After correcting for the relative 2-D molecular concentrations of dye, a luminescence enhancement factor of approximately 8±2 was calculated for the molecules adsorbed at the top surface compared to those adsorbed at the interior walls of the 240 nm diameter arrays.
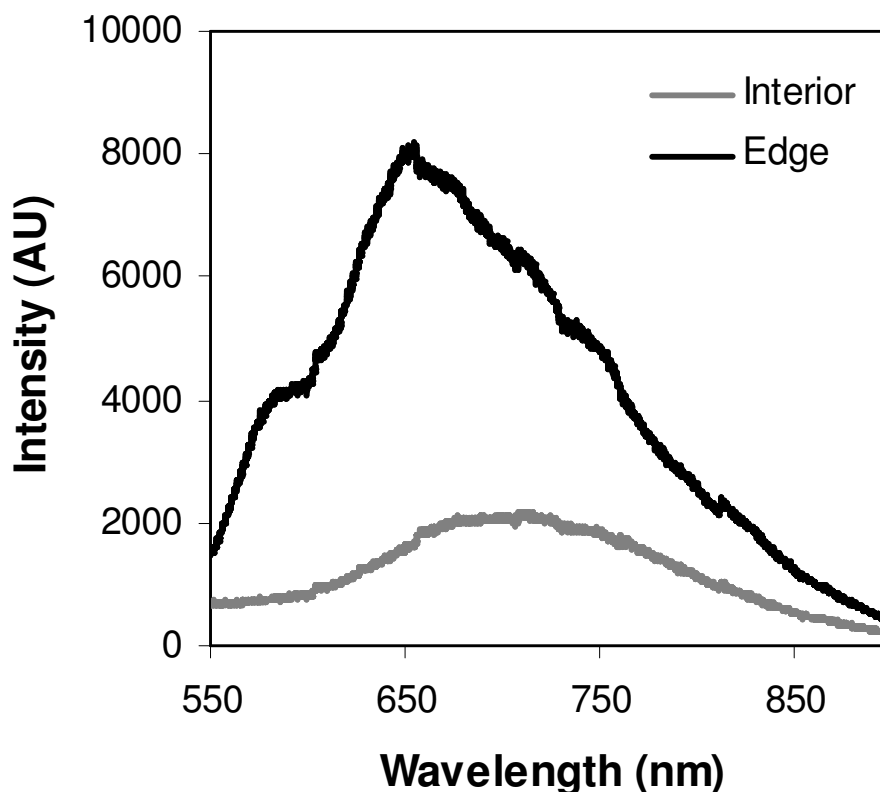
Fig. 3.20: Emission spectra of $[Ru(bpy)_2(Qbpy)]^{2+}$ adsorbed at the top surface (black) and interior walls (grey) of 430 nm nanocavity arrays. The spectra were recorded under identical conditions. The excitation wavelength was 473 nm. The collection angle was 72 degree.

Emission spectra of $[Ru(bpy)_2(Qbpy)]^{2+}$ dye adsorbed at the top surface and interior walls of 430 nm nanocavity arrays is shown in Figure 3.20. The black line shows the enhanced

emission collected from the top surface modified arrays and the grey line shows the enhanced emission recorded from the interior decorated arrays. Interestingly, the shape of the emission curve collected from the top decorated 430 nm diameter array appears to be broader and less gaussian compared to interior modified array. Spectra recorded from three different spots of the same sample and the shapes of the emission curves were identical. The enhancement factor for the top surface modified array was approximately 40±6 compared to the interior decorated array after taking number of molecules into account.

Figure 3.21 shows the enhanced emission collected from monolayers of $[Ru(bpy)_2(Qbpy)]^{2+}$ dye selectively self-assembled on the top surface and the interior walls of 600 nm array. The black line shows the emission recorded from the edge modified arrays and the grey line shows the emission collected from the interior walls of the array. The spectra were collected under identical conditions. The enhancement from the top surface is approximately 26±5 times greater than that seen for the material adsorbed within the cavity. This indicates that the gold nanocavity arrays with 600 nm diameter follow the same trend as 240 and 430 nm diameter arrays. The top surface of the array again shows greater enhancement than the interior decorated arrays. Bartlett and co-workers reported enhancement in emission intensity from thick film of oxazine dye on 600 nm diameter arrays. They reported an order of magnitude enhancement in emission intensity from Bragg modes compared to Mie modes[26] which are consistent with the results observed in this work. Finally, emission spectra of $[Ru(bpy)_2(Qbpy)]^{2+}$ dye adsorbed at the top surface and the interior walls of 820 nm nanocavity arrays is shown in Figure 3.22. Again, the top surface modified arrays show greater enhancement in luminescence compared with the interior decorated arrays at 473 nm excitation. In spite of the fact that the number of molecules in the confocal volume of the microscope is estimated to be six times greater for interior modified arrays compared to the top surface modified ones. The enhancement factor was approximately 12±3 after taking into account the number molecules in the confocal volume. The emission spectra were also collected from three different spots of the same sample and less than 10 % variation in emission intensity is observed between the spots. A greater reduction in emission intensity is observed when multiple spectra recorded from the same spot of the sample over time which is probably due to bleaching of the dye by the laser.
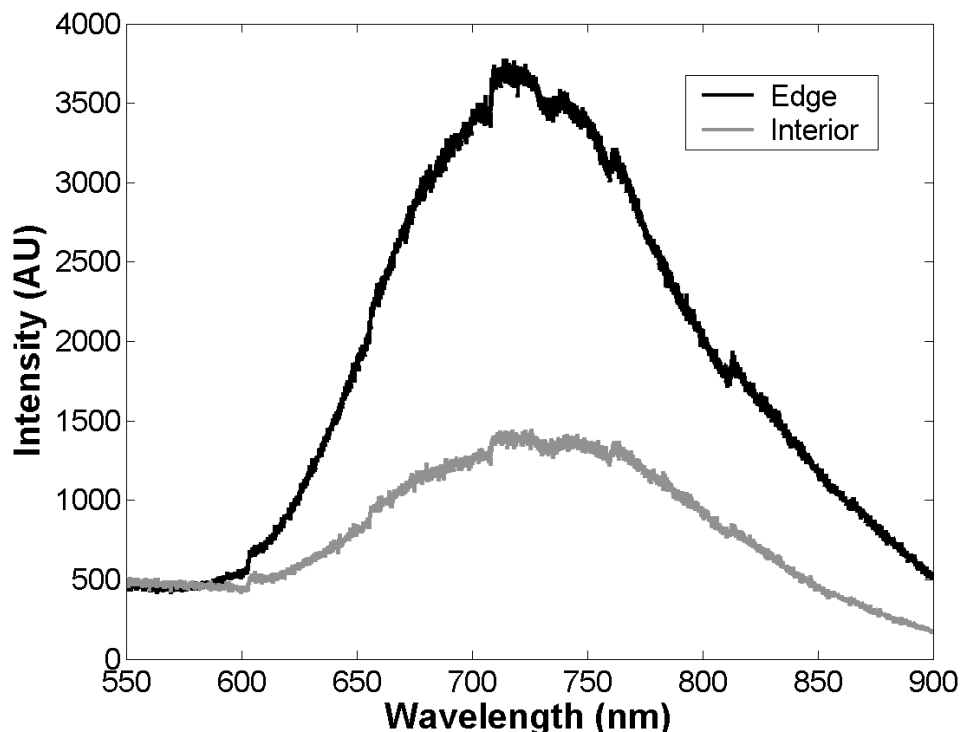
Fig. 3.21: Emission spectra of $[Ru(bpy)_2(Qbpy)]^{2+}$ adsorbed at the top surface (black) and interior walls (grey) of 600 nm nanocavity arrays. The spectra were recorded under identical conditions. The excitation wavelength was 473nm. The spot size was 2 μm.

The emission spectra were recorded for four different diameters of nanocavity arrays (240, 430, 600 and 820 nm), and in each case the results were broadly consistent with those seen for Raman studies. Figure 3.23 shows the relative trends where the top surface modified substrates consistently show greater signal intensity than the interior modified nanocavity arrays. This amplification in emission intensity is attributed to the effective coupling of molecular resonance of $[Ru(bpy)_2(Qbpy)]^{2+}$ dye with the localized surface plasmon resonance at the metal surface when the ruthenium dye is adsorbed at the top surface. Both Raman and emission enhancement measurements confirm the presence of strong surface plasmon modes at the top surface of nanocavity arrays compared to those adsorbed at the interior cavity walls. Figure 3.23 shows the calculated enhancement factors for both SERS and surface enhanced luminescence from ruthenium dye selectively adsorbed at the top surface and the interior walls of four different diameter arrays. The 240 nm diameter arrays show highest enhancement in Raman

intensity compared to other three different arrays. This enhancement in Raman signal intensity might be due to the roughness and discontinuities of the top surface and possibly triangular sharp edges in the confocal volume. Enhancement in luminescence measurements is confirming the presence of strong surface plasmon modes at the top surface of the array compared to interior walls. Fromm and co-workers have reported the enhancement in fluorescence signal from bowtie structures.[21] They have shown that the enhancement in signal intensity is mainly arising from the hot spots between the triangles.
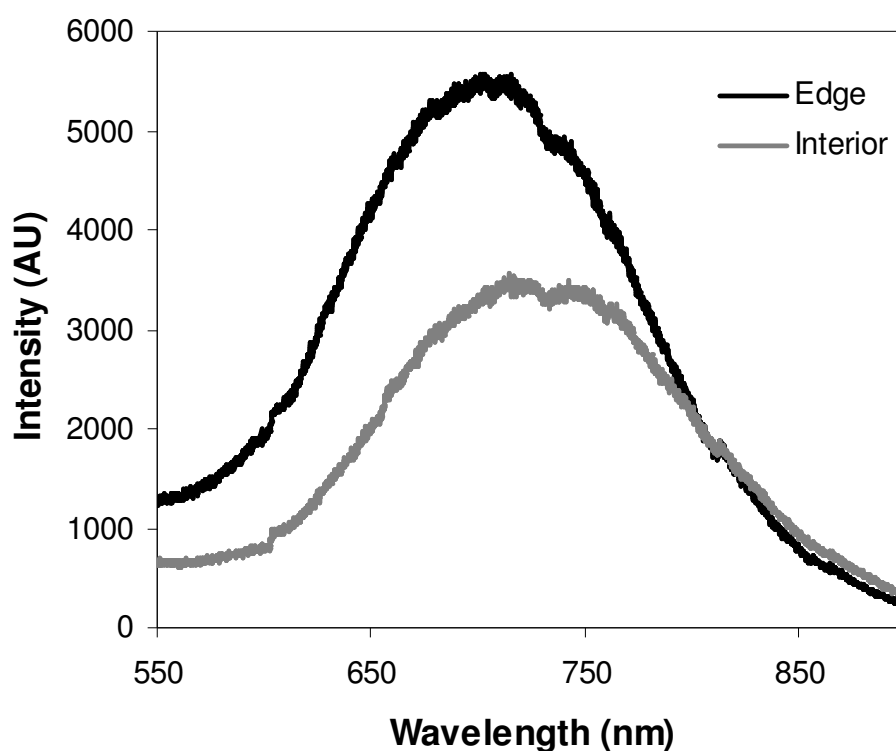

Fig. 3.22: Emission spectra of $[Ru(bpy)_2(Qbpy)]^{2+}$ adsorbed at top surface (black) and interior walls (grey) of 820 nm nanocavity arrays. The spectra were recorded under identical conditions. The excitation wavelength was 473 nm. The spectra recorded using 100x objective and the spot size was 2 μm.
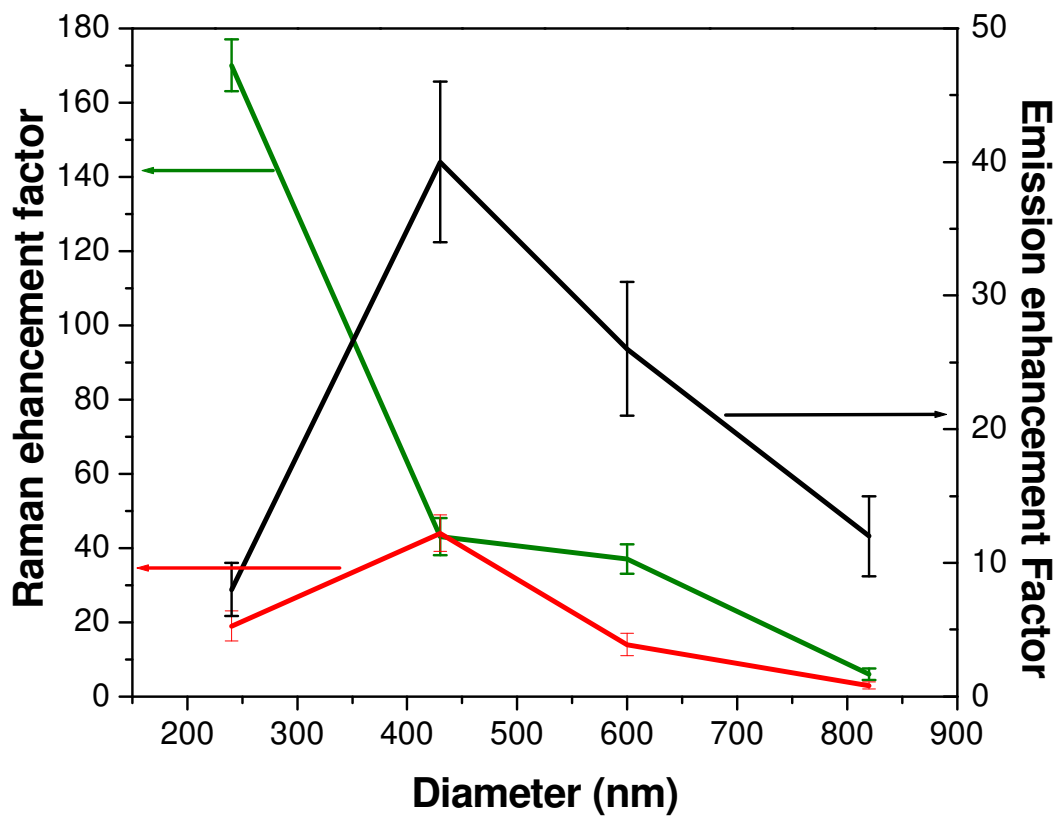
Fig. 3.23: Enhancement factor for both Surface enhanced Raman spectroscopy (SERS) at 785 nm (Green), 633 nm excitation (red) and surface enhanced luminescence (black) from top surface modified arrays (240, 430, 600, and 820 nm) with $[Ru(bpy)_2(Qbpy)]^{2+}$ dye under 473 nm excitation.

3.4 Conclusions

Four different diameters of gold nanocavity arrays on smooth gold substrates were fabricated using nanosphere lithography and followed by electrochemical deposition. Scanning electron microscopy images of these arrays reveal that the polystyrene spheres packed perfectly on a smooth gold surface leading to formation of close-packed gold nanocavity arrays after electrochemical deposition. A key objective of this chapter was to identify the location of strongest spectroscopic enhancement in different diameters of gold nanocavity arrays. A novel method is presented to interrogate the distribution of the plasmonic field on the surface of gold nanocavity arrays. The top surface and the interior walls of different diameters of gold nanocavity arrays could be separately selectively modified using this two-step adsorption process. In the first step, the top surfaces of the arrays are chemically modified with the ruthenium dye by exposure to an ethanolic solution overnight. Then, the spheres were dissolved in THF by one hour sonication. In the second step, the interior walls of the arrays were selectively modified with ruthenium dye after blocking the top surface with thiol. Raman spectra collected from the top surface modified gold nanocavity arrays before and after the sphere removal confirm the stability of monolayers on the top surface of the arrays during sonication.

SERS from selectively modified nanocavity arrays was studied using three different excitation wavelengths. Gold nanocavity arrays with 240 and 600 nm diameter show greatest enhancement when excited at 785 nm, whereas, arrays with 430 and 820 nm diameter shows greater SERS enhancement under 633 nm excitation. In all cases, the top surface modified gold nanocavity arrays show greatest enhancement in both Raman and luminescence signals compared to the interior modified arrays. This strongly suggests that the presence of strong localized surface plasmon modes at the top surface of nanocavity arrays contribute most to SERS from these arrays. A comparative study of selectively decorated arrays with different diameters of gold nanocavity arrays suggests that the intense plasmon modes contributing to SERS mostly from the top surface of the arrays, which might be from the triangular tips at the top surface. The enhancement in emission intensity also reveals the effective coupling of molecular resonance with the localized surface plasmons present at the top surfaces of the gold nanocavity arrays.

Identification of the precise location of these strong plasmon modes may have implication for subsequent design of photonic devices or sensors based on nanocavity arrays.

3.5 References

[1]   Mahajan, S.; Abdelsalam, M. E.; Suguwara, Y.; Cintra, S.; Russell, A. E.; Baumberg, J. J.; Bartlett, P. N. *Phys. Chem. Chem. Phys.,* **2007**, *9*, 104.

[2]   Kelf, T. A.; Sugawara, Y.; Cole, R. M.; Baumberg, J. J.; Abdelsalam, M. E.; Cintra, S.; Mahajan, S.; Russell, A. E.; Bartlett, P. N. *Phys. Rev. B,* **2006**, *74*, 24.

[3]   Kelf, T. A.; Sugawara, Y.; Baumberg, J. J.; Abdelsalam, M. E.; Bartlett, P. N. *Phys. Rev. Lett.,* **2005**, *95*, 11.

[4]   Barnes, W. L.; Dereux, A.; Ebbesen, T. W. *Nature,* **2003**, *424*, 824.

[5]   Ebbesen, T. W.; Lezec, H. J.; Ghaemi, H. F.; Thio, T.; Wolff, P. A. *Nature,* **1998**, *391*, 667.

[6]   Stewart, M. E.; Anderton, C. R.; Thompson, L. B.; Maria, J.; Gray, S. K.; Rogers, J. A.; Nuzzo, R. G. *Chem. Rev.,* **2008,** *108*, 494.

[7]   Jose, B.; Neugebauer, U.; Forster, R. J.; Keyes, T. E. *Phys. Chem. Chem. Phys.,* **2009**, *11*, 10923.

[8]   Kelley, A. M. *J. Chem. Phys.,* **2008**, *128*, 224702.

[9]   Campion, A.; Kambhampati, P. *Chem. Soc. Rev.,* **1998**, *27*, 241.

[10]   Haes, A. J.; Haynes, C. L.; McFarland, A. D.; Schatz, G. C.; Van Duyne, R. P.; Zou, S. L. *MRS Bull.,* **2005**, *30*, 368.

[11]   Haes, A. J.; Chang, L.; Klein, W. L.; Van Duyne, R. P. *J. Am. Chem. Soc.,* **2005**, *127*, 2264.

[12]   Haes, A. J.; Van Duyne, R. P. *J. Am. Chem. Soc.,* **2002**, *124*, 10596.

[13]   McFarland, A. D.; Young, M. A.; Dieringer, J. A.; Van Duyne, R. P. *J. Phys. Chem. B,* **2005**, *109*, 11279.

[14]   Aslan, K.; Wu, M.; Lakowicz, J. R.; Geddes, C. D. *J. Am. Chem. Soc.,* **2007**, *129*, 1524.

[15]   Le Ru, E. C; Etchegoin, P. G. *Principles of Surface-enhanced Raman spectroscopy* Elsevier, **2009**.

[16]   Mahajan, S.; Cole, R. M.; Soares, B. F.; Pelfrey, S. H.; Russell, A. E.; Baumberg, J. J.; Bartlett, P. N. *J. Phys. Chem. C,* **2009**, *113*, 9284.

[17]   Azzaroni, O.; Fonticelli, M.; Schilardi, P. L.; Benitez, G.; Caretti, I.; Albella, J. M.; Gago, R.; Vazquez, L.; Salvarezza, R. C. *Nanotech.,* **2004**, *15*, 197.

[18]   Haes, A. J.; Hall, W. P.; Chang, L.; Klein, W. L.; Van Duyne, R. P. *Nano Lett.,* **2004**, *4*, 1029.

[19]   Haes, A. J.; Zou, S. L.; Schatz, G. C.; Van Duyne, R. P. *J. Phys. Chem. B,* **2004**, *108*, 6961.

[20]   Kinkhabwala, A.; Yu, Z. F.; Fan, S. H.; Avlasevich, Y.; Mullen, K.; Moerner, W. E. *Nat. Photonics,* **2009**, *3*, 654.

[21]   Fromm, D. P.; Sundaramurthy, A.; Kinkhabwala, A.; Schuck, P. J.; Kino, G. S.; Moerner, W. E. *J. Chem. Phys.,* **2006**, *124*, 6.

[22]   Van Duyne, R. P. *Abstracts of Papers of the American Chemical Society,* **2002**, *223*, 003.

[23]   Dreier, J.; Eriksen, R. L.; Albrektsen, O.; Pors, A.; Simonsen, A. C. *J. Phys. Chem. Lett.,* **2010,** *1*, 260.

[24]   Cole, R. M.; Baumberg, J. J.; Garcia de Abajo, F. J.; Mahajan, S.; Abdelsalam, M. E.; Bartlett, P. N. *Nano Lett.,* **2007**, *7*, 2094.

[25]   Cole, R.M.; Mahajan, S.; Bartlett, P.N.; Baumberg, J. J. *Opt. Express,* **2009**, *17*, 13298.

[26]   Sugawara, Y.; Kelf, T. A.; Baumberg, J. J.; Abdelsalam, M. E.; Bartlett, P. N. *Phys. Rev. Lett.,* **2006**, *97*, 26.

[27]   Haynes, C. L.; Van Duyne, R. P. *J. Phys. Chem. B,* **2001**, *105*, 5599.

[28]   Mallon, C. T.; Jose, B.; Forster, R. J.; Keyes, T. E. *Chem. Commun.,* **2010**, *46*, 106.

[29]   Zhou, Q.; Zhao, H.; Pang, F.; Jing, Q.; Wu, Y.; Zheng, J. *J. Phys. Chem. C,* **2006**, *11*, 514.

[30]   Forster, R. J.; Keyes, T. E. *J. Phys. Chem. B,* **1998**, *102*, 10004.

[31]   Lacharmoise, P. D.; Tognalli, N. G.; Goni, A. R.; Alonso, M. I.; Fainstein, A.; Cole, R. M.; Baumberg, J. J.; Garcia de Abajo, J.; Bartlett, P. N. *Phys. Rev. B,* **2008**, *78,* 125410.

[32]   Socrates, G. *Infrared and Raman Characteristic of Group Frequencies*, Wiley, New York, **2001**.

[33]   Camden, J. P.; Dieringer, J. A.; Zhao, J.; Van Duyne, R. P. *Acc. Chem. Res.,* **2008**, *41*, 1653.

[34] McFarland, A. D.; Young, M. A.; Dieringer, J. A.; Van Duyne, R. P. *J. Phys. Chem. B,* **2005**, *109*, 11279.

[35] Forster, R. J.; Pellegrin, Y.; Leane, D.; Brennan, J. L.; Keyes, T. E. *J. Phys. Chem. C,* **2007**, *111*, 2063.

[36] Dieringer, J. A.; McFarland, A. D.; Shah, N. C.; Stuart, D. A.; Whitney, A. V.; Yonzon, C. R.; Young, M. A.; Zhang, X.; Van Duyne, R. P. *Faraday Discuss.*, **2006**, *132*, 9.

[37] McFarland, A. D.; Young, M. A.; Dieringer, J. A.; Van Duyne R. P. *J. Phys. Chem. B,* **2005**, *109*, 11279.

[38] Anker, J. N.; Hall, W. P.; Lyandres, O.; Shah, N. C.; Zhao, J.; Van Duyne, R. P. *Nature Mater.,* **2008**, *7*, 442.

[39] Haes, A. J.; Zou, S.; Zhao, J.; Schatz, G. C.; Van Duyne, R. P. *J. Am. Chem. Soc.,* **2006**, *128*, 10905.

[40] Bartlett, P. N.; Baumberg, J. J.; Coyle, S.; Abdelsalam, M. E. *Faraday Discuss.,* **2004**, *125*, 117.

Chapter 4

Thermal stability of gold nanocavity arrays

4.1 Introduction

An investigation into the effects of thermal annealing of gold nanocavity arrays was conducted to assess their thermal stability and the impact of annealing on the signal intensity from Raman and luminescence spectroscopy.

An important issue in the application of SERS platform is their thermal stability which can be particularly important in some and device applications. For instance, the study of nucleic acid hybridization assays involves heating and cooling of nucleic acids on the substrate to optimize the hybrid formation and decrease the mismatches.[1] The thermal stability of SERS platforms is essential in their application in situ monitoring of catalytic processes conducted at high temperature.[2,3]

The key difficulty with heating nanostructured surfaces is their changes in the morphology of the surface structures while annealing. For example, Mabuchi and co-workers have studied the effect of annealing of nanoporous gold surfaces and attributed the thermal coarsening of nanoporous gold to recrystallization rather than melting.[4] The recrystallization in the solid state of the nanoporous array was confirmed using differential scanning calorimetry. They reported that the nanoporous gold was coarsened at temperatures below the melting temperature of nanoparticles with sizes similar to the ligament sizes of nanoporous gold.

Vasiliuk et al. has shown that annealing of silver films changes the morphology of the sample, resulting in changes evident in the surface plasmon absorption of the substrate.[5] Van Duyne and co-workers have also studied the structural and optical changes occurring at silver island films after annealing at different temperatures.[6,7,8,9,10] They have shown that post deposition thermal annealing (300 °C) induced shape changes in

the nanoparticles from triangle to circular. The extinction spectra of silver triangles were blue shifted by approximately 160 nm after annealing. Surface enhanced Raman signal intensity from the silver triangles was reduced significantly after annealing at 300 °C. Therefore, to maintain the optical properties of the triangles at elevated temperatures, Al_2O_3 was coated on top of the triangles by atomic layer deposition to different thicknesses. AFM and localized surface plasmon resonance measurements show that this layer maintained its triangular structured integrity even at high temperatures, which permits its use as a SERS platform to monitor reactions conducted at elevated temperatures.

Geddes and co-workers have similarly reported a blue shift in the extinction spectra of a silver island film after annealing.[11] A red shift in the absorption spectra of the annealed film was expected due to a predicted increase in particle size.[12,13,14] Although they found that the shape of the particles became spherical and the spacing between the particles increased as a function of both temperature and time. The blue shift in the absorption spectra they attributed to the decreased interaction between neighbouring particles as the effect of temperature. The authors have shown that the annealed silver-island film enhances fluorescence from a 4 nm thick fluorescein labelled Human Serum albumin protein layer. A ten fold increase in fluorescence intensity was observed from fluorescein-labeled protein bound to annealed silver films. They rationalized this fluorescence enhancement as due to fluorophore-coupled radiating plasmons, i.e. energy transfer occurs from the excited fluorophore to the surface plasmons, followed by the surface plasmon emission with the characteristics of the fluorophore. The annealed silver island film was postulated to offer significant advantages including reusable autoclavable substrates for clinical assays and high temperature based sensing such as metal enhanced fluorescence hybridization assays.[15,16]

Despite their potential as SERS substrates, to our knowledge, the effect of increased temperature on the morphology and plasmonic behaviour of gold nanocavity arrays has not been studied. In this chapter, the effect of thermal annealing on gold nanocavity arrays was investigated on arrays with three different templating diameters. The structural and morphological changes of the arrays were studied using scanning electron microscopy (SEM) and atomic force microscopy (AFM). The changes in the reflectance spectra of gold nanocavity arrays were also studied after annealing.

Changes in the surface area of the gold nanocavity arrays were recorded using cyclic voltammetry. The effect of thermal annealing of the arrays on the emission properties of luminophore adsorbed on the arrays were investigated using monolayers of $[Ru(bpy)_2(Qbpy)]^{2+}$ complex as probe. Finally, the changes in the Raman signal intensity from this ruthenium dye adsorbed onto annealed arrays were compared with the signal intensity from unannealed arrays and smooth gold surface.

4.2 Experimental

Preparation and annealing of gold nanocavity arrays

Gold nanocavity arrays with three different diameters, 240, 430, 820 nm, were prepared on smooth gold surfaces using nanosphere lithography as described in Chapter 3. The topology of the gold nanocavity arrays were characterised using scanning electron microscopy (SEM) and atomic force microscopy (AFM). The arrays were heated up to 100 °C in an autoclave and then the slides were held at that temperature for 30 minutes. Similarly, fresh arrays were heated to 300, and 500 °C separately, and held at that temperature for 30 minutes. Then, the slides were cooled down slowly to room temperature, typically this required more than 3 hrs. The changes in the localized surface plasmons on the annealed samples were measured using a SPM-002 spectrometer with a tungsten halogen light source.

Self assembled monolayers of $[Ru(bpy)_2(Qbpy)]^{2+}$ dye, at the surface of annealed arrays were then prepared by sonicating the annealed slide in 1 mM methanolic solution of the dye for 30 minutes and then leaving the slide immersed in the same solution overnight. Excess physisorbed material was removed from the electrode by sonicating in blank solvent and rinsing and drying prior to the measurement. The measurements were conducted in dry conditions. The surface features of the annealed nanocavity arrays were investigated using a Hitachi S-3000N scanning electron microscope. AFM images were recorded with a Veeco Bioscope II in contact mode using commercial Si_3N_4 cantilever tips. These tips are pyramidal in shape with spring constants between 0.04 and 0.08 N/m, and tip sizes were nominally less than 20 nm radius. The same tip was used to image all the samples to minimize tip induced errors. The AFM imaging was carried out under dry conditions. The emission spectra were recorded on a Horiba Jobin Yvon HR800UV microscope using 473 nm laser line as excitation. The laser intensity at the sample was 30 µW. The laser intensity for 633 nm excitation was 10 µW. Typical acquisition times were between 1 and 20 s and five acquisitions were performed to acquire a spectrum. Both Raman and emission spectra were collected using a 100x objective (NA = 0.95, θ = 72°). The spectra were recorded from three different spots of the same sample.

4.3 Results and Discussion

4.3.1 Characterisation using SEM

In order to assess the morphological changes at the arrays while annealing, the topology of the substrate were studied before and after annealing using SEM. As previously reported, the gold nanocavity arrays have different optical properties depending on the thickness and diameter of the cavity.[17,18] To ensure the diameter and thickness of the film is uniform for each array, studies were conducted on a single array split into four samples. Each SEM image was collected under identical experimental conditions to permit their direct comparison. Figure 4.1 shows the SEM images of 240 nm diameter gold nanocavity arrays before and after annealing the samples at different temperatures. Figure 4.1 (A) shows the SEM image of this array before annealing where the opening diameter of the array is 160±10 nm. The arrays annealed at 100 ℃ reveal the formation of sharp triangular features at the top surface of the array. The surface roughness of the array appears to be increased and the feature changes remain visible after annealing the sample at 300 ℃. The hexagonal pattern of the array was still visible after annealing at 500 ℃ with surface features changes. It is noticeable that the opening diameter of the array decreased from 160±10 to 130±15 nm after annealing up to 500 ℃. The changes in the opening diameter might be due to the melting of the arrays or due to the recrystallization of gold in the solid state as described by Mabuchi et al. It can be clearly observed that the annealing of the arrays changes the underlying roughness of surface with increasing temperature. The top surfaces of the arrays become disordered and the size of the opening diameter becomes smaller during annealing at high temperatures.
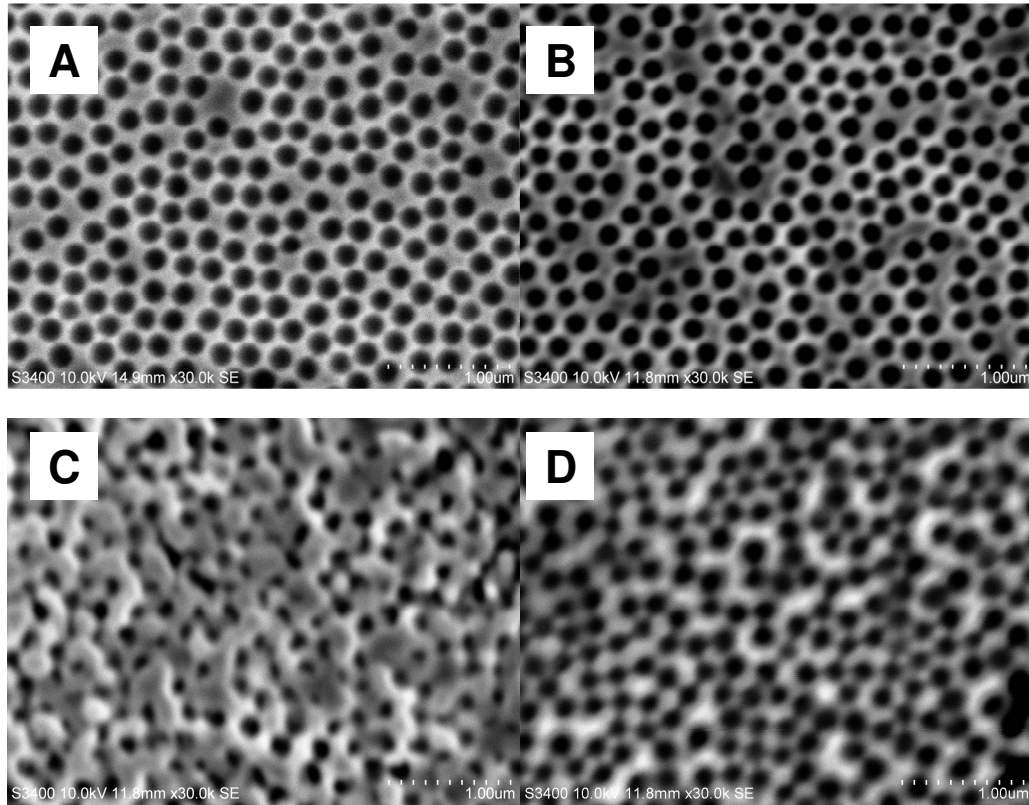
Fig. 4.1: SEM images of 240 nm diameter gold cavity arrays (A) before and after annealing in air for 30 minutes at different temperatures, (B) 100 (C) 300 and (D) 500 ºC. All images were collected using identical conditions at 10 kV accelerating voltage.

The SEM images of the gold nanocavity arrays with 430 nm diameters before and after annealing are shown in Figure 4.2. The opening diameter of these arrays was approximately 300±20 nm as shown in Figure 4.2 (A). Similar to the 240 nm diameter arrays the surface features of the array show narrowing of the inter-pore separation when annealed at 100 ºC compared to the unannealed array. However, the overall surface roughness of the array significantly increased after annealing the arrays at 300 ºC as shown in Figure 4.2 (C). Annealing of the array at 500 ºC significantly changes the structure of the top surfaces of the cavity. The underlying metal looks more contoured and the pore size looks larger than at 300 ºC. This might be due to the melting of the top surface of the array during annealing. Interestingly, at 500 ºC the arrays still appear as cavities and the hexagonal pattern of the array is also broadly maintained.
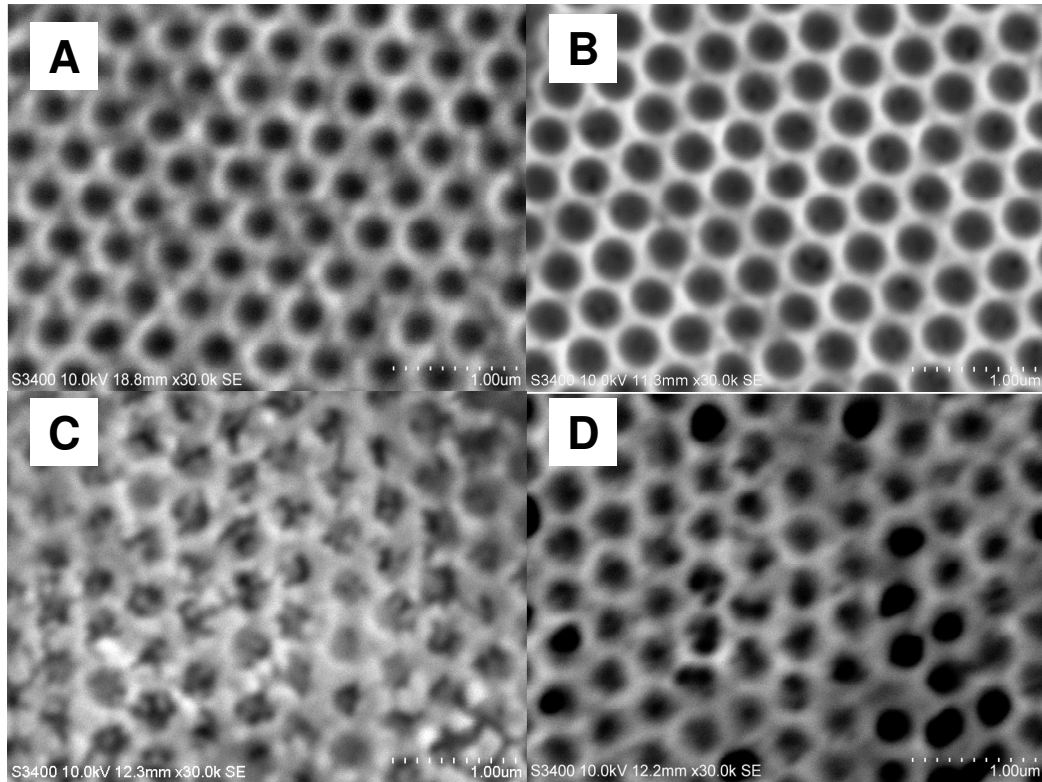
Fig. 4.2: SEM images of gold cavity arrays with cavity diameters of 430 nm (A) before and after annealing in air for 30 minutes at different temperatures, (B) 100 (C) 300 and (D) 500 °C. All images were taken using identical conditions at 10 kV accelerating voltage.

Figure 4.3 shows the SEM images of 820 nm diameter arrays before and after annealing at 100, 300, 500 °C for 30 minutes. The annealing of 820 nm diameter arrays show the same trend as seen for 240 and 430 nm arrays. The arrays annealed at 100 °C shows a small increase in aperture diameter at the top surface of the array. However, annealing of the arrays at 300 °C results in significant alterations to the cavity structure with significant roughening of the surface of the array. The arrays annealed at 500 °C shows evidence of melting of the top surface of the array. The opening of the cavity changes from circular to hexagonal shape after annealing the arrays at 500 °C. In summary, the SEM images of annealed arrays reveal that the surface features of the gold nanocavity undergo significant topological change at 300 °C. It is important to note that here, the SEM measurements were carried out using 10 kV accelerating voltage; therefore, the image might not be purely topographical. Imaging of the surface features at lower accelerating voltage was impossible due to charging therefore; the detailed information

174

about the surface features of the film in nanometre scale were investigated further using AFM.
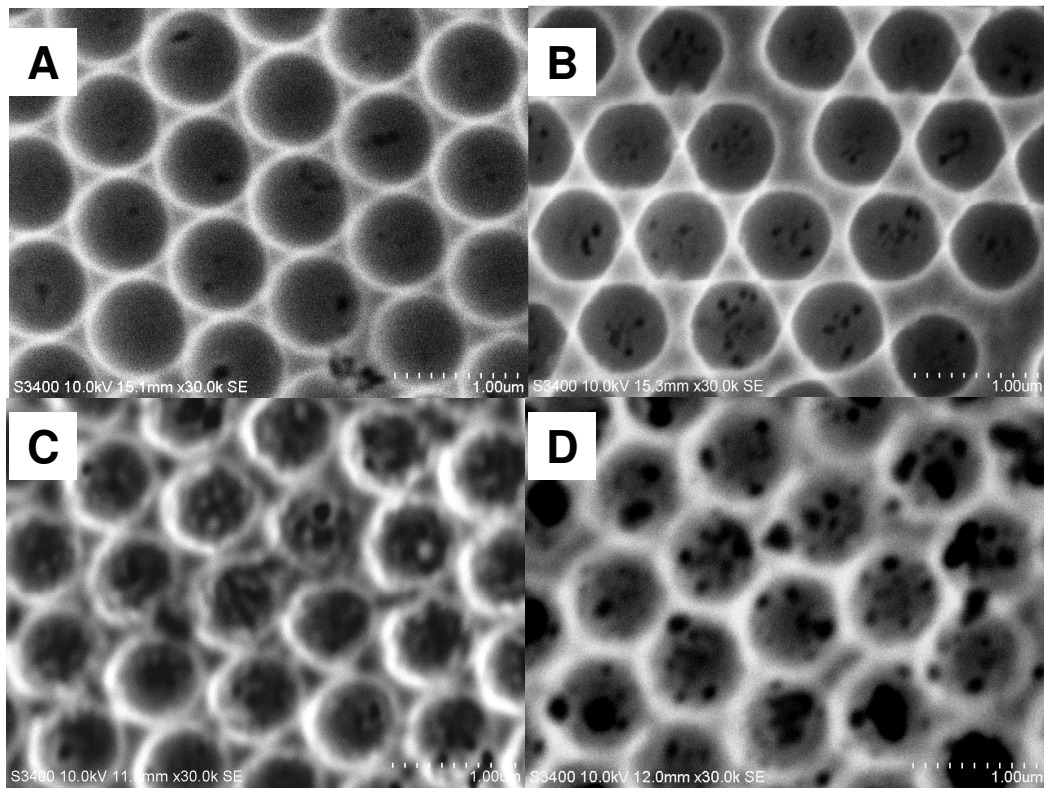

Fig. 4.3: SEM images of 820 nm diameter gold cavity arrays (A) before and after annealing in air for 30 minutes at different temperatures, (B) 100 (C) 300 and (D) 500 ºC. All images collected using identical conditions at 10 kV accelerating voltage.

4.3.2 Atomic force microscopy (AFM) of annealed arrays
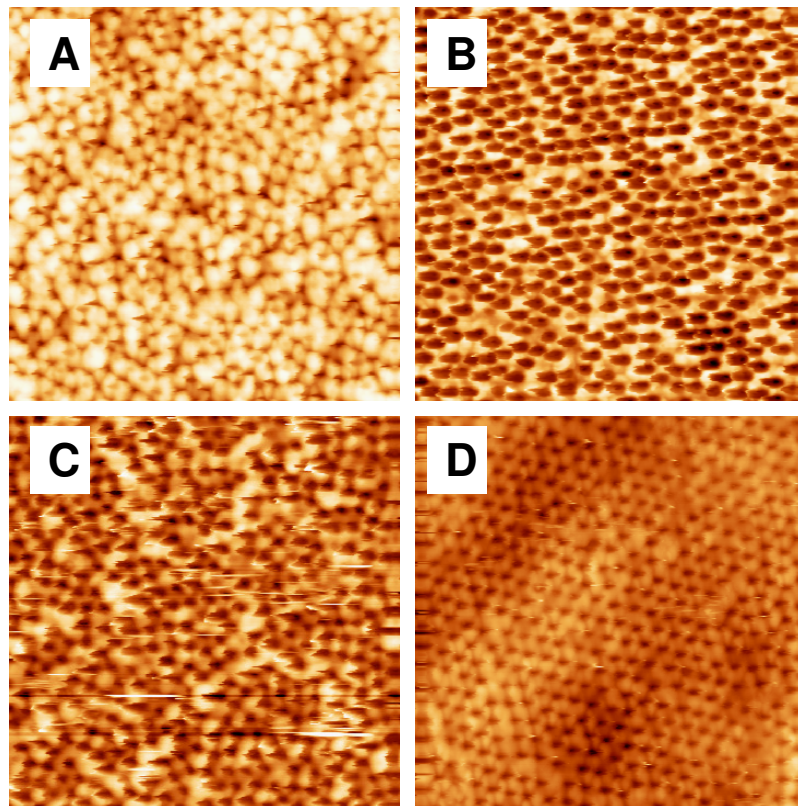
Fig. 4.4: Contact mode AFM images of 240 nm diameter gold nanocavity arrays (A) before and after annealing at different temperatures, (B) 100, (C) 300, and (D) 500 °C. The image dimensions are 5 µm by 5 µm.

As discussed earlier, the opening diameter of the arrays changed significantly after annealing the arrays at high temperatures and accurate measurements of the opening diameter of the arrays were uncertain using SEM. Therefore, AFM measurements were carried out in order to visualize the surface topology of the annealed arrays. Figure 4.4 shows the contact mode AFM images of 240 nm diameter arrays before and after annealing at temperatures 100, 300, and 500 °C. The surface features of the unannealed array appear to be rough which might be due to the over deposition of gold at the top surface during fabrication of arrays. However, the SEM images of the array show well packed nanocavity arrays as shown in Figure 4.1 (A). This contrast between the SEM and AFM images suggest that the SEM images collected using 10 kV accelerating voltage may not represent the top surface. But as described, it was difficult to measure SEM images from the annealed arrays at lower accelerating voltage due to charging.

The height profile in AFM measurements shows that the thickness of the unannealed array was approximately 140 nm. However, the thickness of the array with opening diameter of 160 nm should be either 210 or 30 nm according to Equation 4.1.

$$t = r \pm (r^2 - r^2_{pore})^{1/2} \qquad\qquad 4.1$$

The actual thickness of the array is 210 nm which corresponds to a normalized thickness $t_D = 0.87$. This difference in height between the calculated and in height profile is attributed to the tip induced error which arises due to the spherical shape of the deeper cavities and limited penetration of the tip due to its aspect ratio.[19] It was difficult to see any changes for the arrays annealed at 100 ℃ due to the tip induced errors. The arrays annealed at 300 and 500 ℃ show changes in the top surface features of the gold nanocavity arrays. The AFM image of array annealed at 500 ℃ reveals that the annealing leads to the melting of the top surface of the array which results in the formation of smoother surface compared to the unannealed arrays.
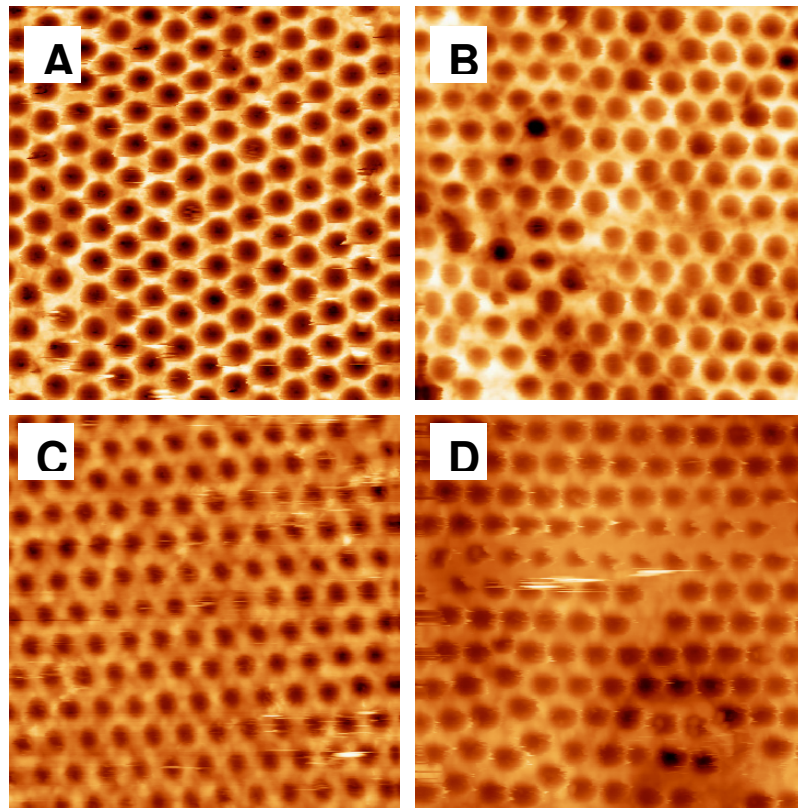
Fig. 4.5: Contact mode AFM images of 430 nm diameter gold nanocavity arrays (A) before and after annealing in air at different temperatures, (B) 100, (C) 300, and (D) 500 ℃. The image dimensions are 5 μm by 5 μm.

For the remaining arrays, behaviour under AFM is similar as shown in Figure 4.5-4.6. Figure 4.5 shows contact mode AFM images of the 430 nm diameter gold nanocavity array before and after annealing.   The top surface of the untreated array is homogeneous whereas the top surface features show significant changes after annealing at high temperatures. The array annealed at 100 ºC shows different heights between different regions of the slide which can be seen as different bright and dark spot in Figure 4.5 (B). However, after annealing the slide at 300 ºC the top surface of the array appears to be uniform compared to 100 ºC annealed arrays. The height profile in AFM measurements of the arrays shows that the thickness of the unannealed array was approximately 140 nm attributed to tip error as described.
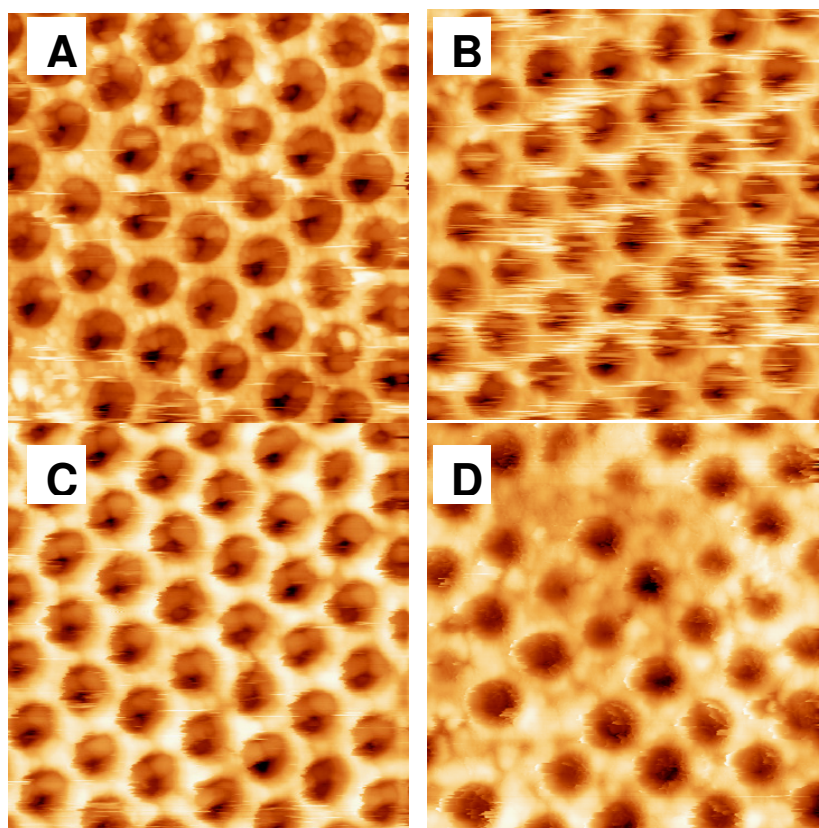
Fig. 4.6: Contact mode AFM images of 820 nm diameter gold nanocavity arrays (A) before and after annealing in air for 30 minutes at different temperatures, (B) 100, (C) 300, and (D) 500 ºC. The image dimensions are 5 µm by 5 µm.

The surface features of the array are changed at 300 ºC and the opening diameter of the array was reduced from 370 to 280 nm after annealing at 300 ºC. The reduction in the

opening diameter of the gold nanocavity arrays is attributed to the melting of the top surface of the array at higher temperatures.

The AFM images of the 820 nm diameter gold nanocavity arrays annealed at different temperatures are shown in Figure 4.6. Gold nanocavity arrays annealed at 100 ℃ shows some deformation at the edges of the array. The white stripes can be seen in the image of this array in Figure 4.6 (B) and the origin of these lines is unclear. This might be due to some impurity on the tip; however, this unlikely because the Figure 4.6 (C) is also taken using the same tip. The AFM image of the gold nanocavity arrays annealed at 300 ℃ reveals that the top surface features of the array are strongly disturbed and gold particles appear at the edges of the array after annealing. Heating of the gold nanocavity arrays, to 500 ℃ show melting of gold from the top surface of the array. The opening diameter of the array after annealing at 500 ℃ is dramatically reduced from 670 to 520 nm. The gold nanocavity array before annealing shows a height of approximately 200 nm. This is consistent with the height calculated from opening diameter of the array using the Equation 4.1.

4.3.3 Reflectance measurements

As the surface plasmon absorption of a nanostructured metal substrates depends on the size, shape and geometry of the surface features,[20,21] therefore it was expected that annealing particularly at higher temperatures would influence plasmon absorbance. For instance, Bartlett and co-workers have shown the changes in the optical properties of gold nanocavity arrays at different diameter and thickness.[22] Previous reports have shown that thermal annealing of nanostructured metal surfaces shift their surface plasmon resonance wavelength depending on the annealing temperature.[23,24] For example, as described a red shift in the extinction spectra were reported for annealed silver island films[12,13] which was interpreted as an increase in particle size after annealing and this was confirmed by SEM and AFM measurements. In contrast, a blue shift in the extinction spectra has also previously reported for annealed silver island films and speculated to be due to the break-up of silver particles.[25,26]

In order to investigate any shift in localized surface plasmon resonance for the gold nanocavity arrays as a function of annealing temperature, reflectance measurements were carried out for the three different diameter arrays. Figure 4.7 shows the reflectance spectra obtained from a smooth gold surface and the reflectance from 240 nm diameter arrays before and after annealing. The black line shows the reflectance recorded from the smooth gold surface for comparison. The red, green, blue and cyan shows the reflectance collected from 240 nm diameter arrays before annealing and after annealing at 100, 300 and 500 ℃ respectively. These measurements were carried out using 0 degree polarized light at an excitation angle of 45 degrees. A strong absorbance around 480 nm is observed for a smooth gold surface and is typical for gold absorption. The reflectance spectra of the annealed arrays show a blue shift in the spectra compared with unannealed arrays. However, the unannealed arrays show a greater absorbance compared with annealed arrays. The arrays annealed at 500 ℃ show quite dramatic changes in the reflectance spectra, with a strong absorbance around 500 nm and with loss of near IR absorbance. The increased reflectance of the arrays when annealed at 500 ℃ indicates the disappearance of some surface plasmon modes after annealing. SEM and AFM measurements from these arrays suggest that the thickness of the array changes from 160 to 130 nm after annealing up to 500 ℃

which corresponds to a normalized thickness changes from 0.66 – 0.54. As discussed earlier, previous reports have shown that the surface plasmon absorption of the gold nanocavity arrays depending on the thickness of the film.[22] Therefore, the changes in the reflectance spectrum for 500 ℃ annealed array either due to the change in the thickness of the array or due to the changes in the surface features of the arrays which is clearly seen in AFM images.
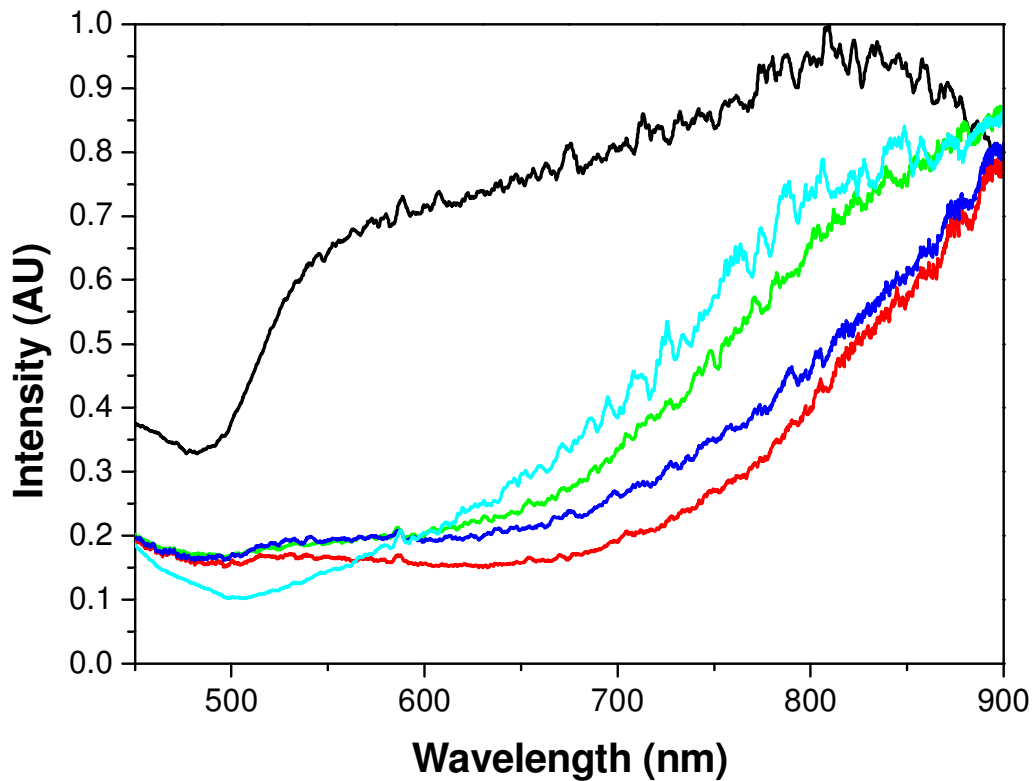
Fig. 4.7: Reflectance measurements of smooth gold surface (—) and 240 nm gold nanocavity arrays (—) before and after annealing at different temperatures (—) 100, (—) 300, and (—) 500 ℃. Spectra were normalized to the maximum intensity value. The measurements were recorded using 0° polarized light at an incident angle 45 degrees.

Figure 4.8 shows the reflectance measurements for 430 nm diameter gold nanocavity arrays before and after annealing. The black line shows the reflectance recorded from a smooth gold surface. The red, green, blue and cyan shows the reflectance collected from 240 nm diameter arrays before annealing and after annealing at 100, 300 and 500 ℃ respectively. In these arrays, there is a red shift in the surface plasmon absorption maxima for the arrays annealed at 100, 300, and 500 ℃ compared with untreated arrays. The untreated array shows less absorption than the annealed arrays. Especially,

the arrays annealed at 300 ℃ shows greater absorption above 600 nm. The AFM images of these arrays annealed at 300 ℃ show nanoparticle structured features on the top surface of the array. This greater roughness of the arrays tentatively attributed to the greater absorption of these arrays above 600 nm. In order to assess the impact of annealing on surface roughness, cyclic voltammetric measurements were conducted as described in the following section.
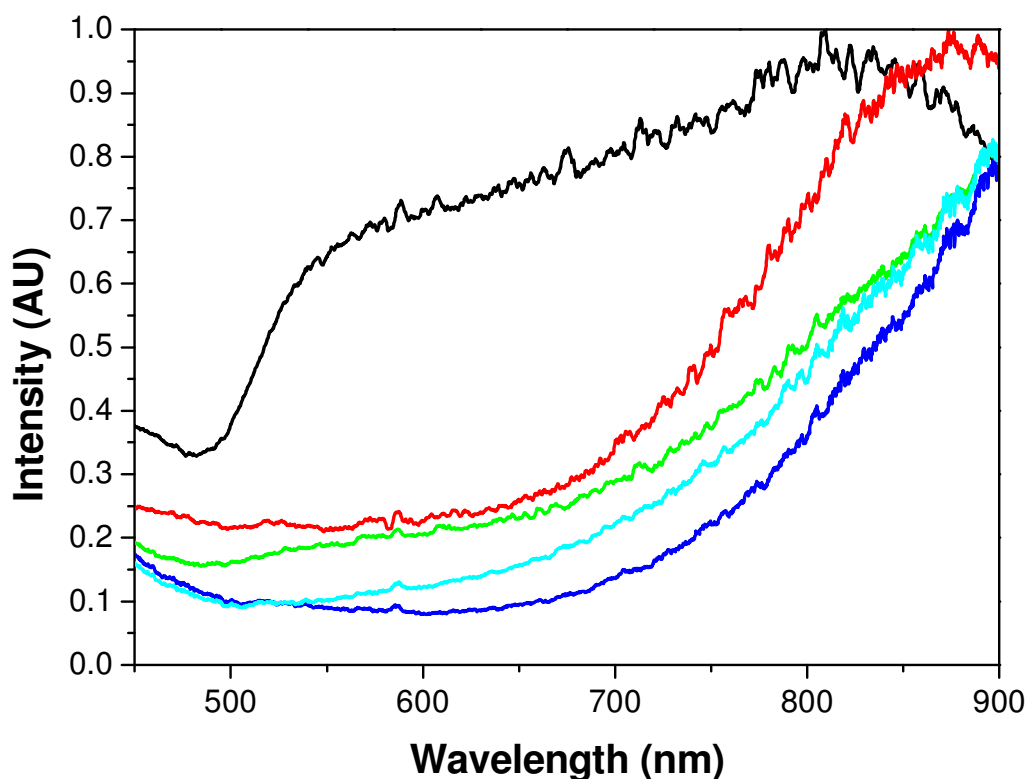

Fig. 4.8: Reflectance measurements of 430 nm gold nanocavity arrays (—) before and after annealing at different temperatures (—) 100, (—) 300, and (—) 500 ℃. (—) represents reflectance spectrum of smooth gold surface. The measurements were recorded using 0° polarized light at an angle 45 degree.

Figure 4.9 shows reflectance measurements recorded from the 820 nm diameter gold nanocavity arrays before and after annealing at different temperatures. The line colours are similar to the one described before. The absorption from the untreated array and the arrays annealed at 100 ℃ appear to be very similar. However, the array annealed at 300 ℃ shows increased absorption at 600 nm compared to other two arrays (untreated and annealed at 100 ℃). The arrays annealed at 500 ℃ show dramatic changes in the reflectance spectra which shows greater absorption compared with other annealed samples. The greater absorption of the annealed array at 500 ℃ might be due to the

changes in the roughness of the arrays or due to the changes in the thickness of the arrays.
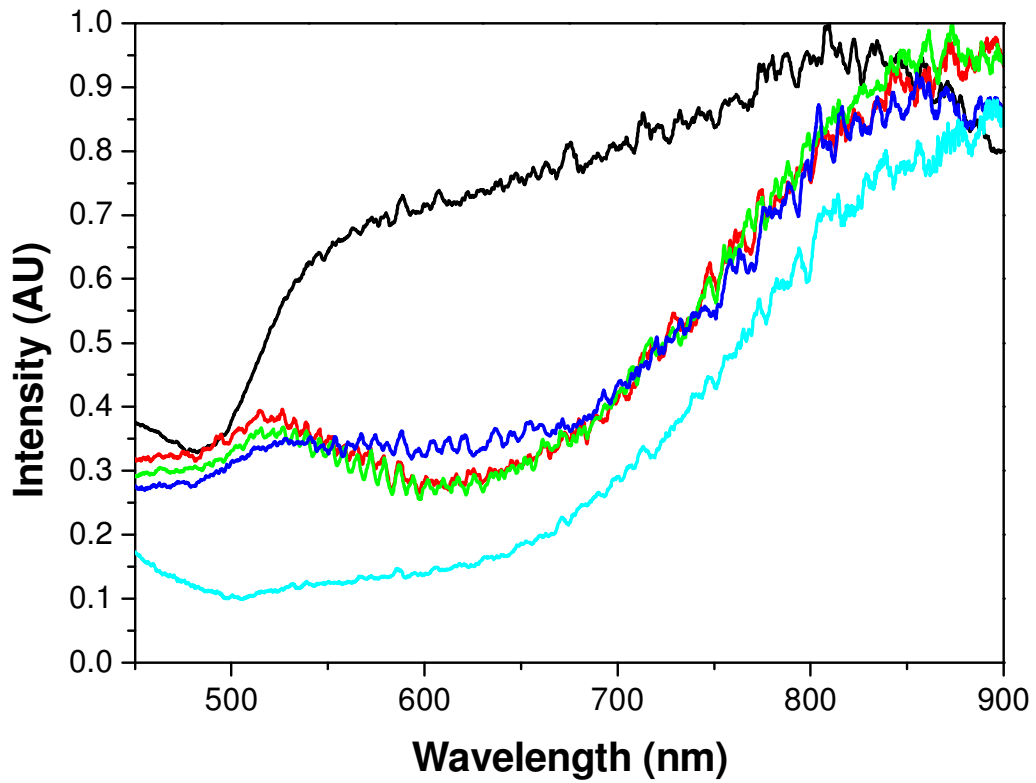

Fig. 4.9: Reflectance measurements of 820 nm gold nanocavity arrays (—) before and after annealing at different temperatures (—) 100, (—) 300, and (—) 500 ºC. (—) represents reflectance spectrum of smooth gold surface. The measurements were recorded using 0º polarized light at an angle of 45 degrees.

4.3.4 Surface area measurements
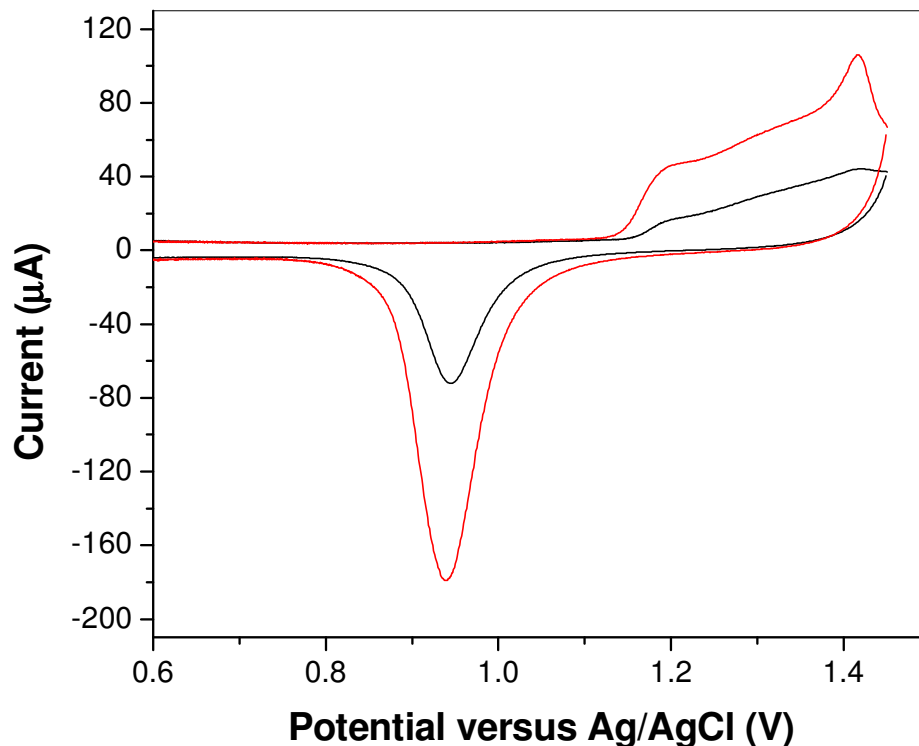
Fig. 4.10: Cyclic voltammetric measurement of 240 nm gold nanocavity arrays (—) before and (—) after annealing at 300 ºC. A 0.5 M H_2SO_4 was used as an electrolyte and the scan rate is 0.1 V/s. The reference electrode separated from the electrolyte by a salt bridge filled with 0.5 M H_2SO_4 to prevent contamination of the working electrode with chloride ions.

The reflectance measurements from the annealed arrays reveal that after annealing at higher temperatures > 300 ºC there are significant changes in the reflectance spectra. As discussed in Section 4.3.2, changes in the thickness as well as surface morphology of the arrays were evident after annealing. Therefore, changes in the reflectance spectra might be due to the changes in the thickness or due to the changes in the surface roughness of the gold nanocavity arrays after annealing. Cyclic voltammetric measurements were carried out before and after annealing the arrays to assess changes to surface area during annealing. The measurements were carried for all the arrays before and after annealing at each temperature. For example, Figure 4.10 shows the cyclic voltammetric measurements for 240 nm diameter arrays before and after annealing at 300 ºC. The surface area of the arrays was calculated using electrochemical cleaning of gold in 0.5 M H_2SO_4. The peak at 1.2 V corresponds to the

oxide formation and the peak at 0.95 V shows the subsequent oxide reduction. The surface area was calculated using the oxide reduction peak where the charge per cm^2 is 390 μC. Table 4.1 shows the surface area of different diameter arrays before and after annealing. The gold nanocavity arrays annealed at 100 ºC show approximately the same surface area as before annealing which indicates that the roughness of the surface remains unchanged. It is clear that the surface area of gold nanocavity arrays after

Diameter (nm)	100 ºC		300 ºC		500 ºC	
	Before (cm^2)	After (cm^2)	Before (cm^2)	After (cm^2)	Before (cm^2)	After (cm^2)
820	0.080	0.1072	0.0561	0.3251	0.071	0.064
430	0.042	0.035	0.037	0.135	0.468	0.006
240	0.095	0.045	0.171	0.434	0.07	0.006

Table 4.1: Surface area measurements for different diameter gold nanocavity arrays after annealing at different temperatures, 100, 300 and 500 ºC.

annealing at 300 ºC shows an increase in surface area, which suggests that the roughness of the surface is increased and this is in consistent with AFM measurements. Interestingly, in contrast the arrays annealed at 500 ºC show reduced surface areas compared to original arrays for 430 and 240 nm. This decrease in surface area is probably due to the melting of the array at this high temperature which results in a more homogenous, smooth surface. The difference in the surface area was less than 3 % after repeating the electrochemical measurements using the same sample. The measurements were conducted for three different samples to ensure the reproducibility of the experiment. However, the difficulty with this experiment was that, the thickness of the arrays was not identical for each arrays therefore, the direct comparison of reproducibility was not meaningful. However, surface area measurements from different arrays reveal that the surface area is increased for the arrays annealed at 300 ºC compared to untreated arrays and the arrays annealed at 500 ºC reveal the formation of homogeneous smooth surface. These surface area measurements before and after annealing can be helpful to compare the enhancement in signal intensity for both Raman and emission from the arrays.

4.3.5 Metal enhanced emission

Enhancement in emission intensity was observed from self-assembled monolayers of $[Ru(bpy)_2(Qbpy)]^{2+}$ complex adsorbed on gold nanocavity arrays and from fluid filled cavities as discussed in Chapter 2 and 3. The relative intensity of enhancement in emission from four different diameter arrays revealed that the enhancement factor depends on the diameter of the cavity. The influence of thermal annealing on the emission properties of a monolayer of $[Ru(bpy)_2(Qbpy)]^{2+}$ on the gold nanocavity arrays were investigated as a function of temperature. The emission intensity from luminescent monolayers at both annealed and untreated arrays were compared with the emission intensity from self-assembled monolayers of ruthenium dye formed at a smooth gold surface. The measurements were carried out using 473 nm excitation line under identical experimental conditions to those described for the array. Figure 4.11 shows the emission spectrum obtained from the monolayer of dye on vapour deposited gold on silicon with roughness factor of 1.3. The enhancement in emission intensity from both the annealed and unannealed arrays was calculated after normalizing the number of molecules within the confocal volume.
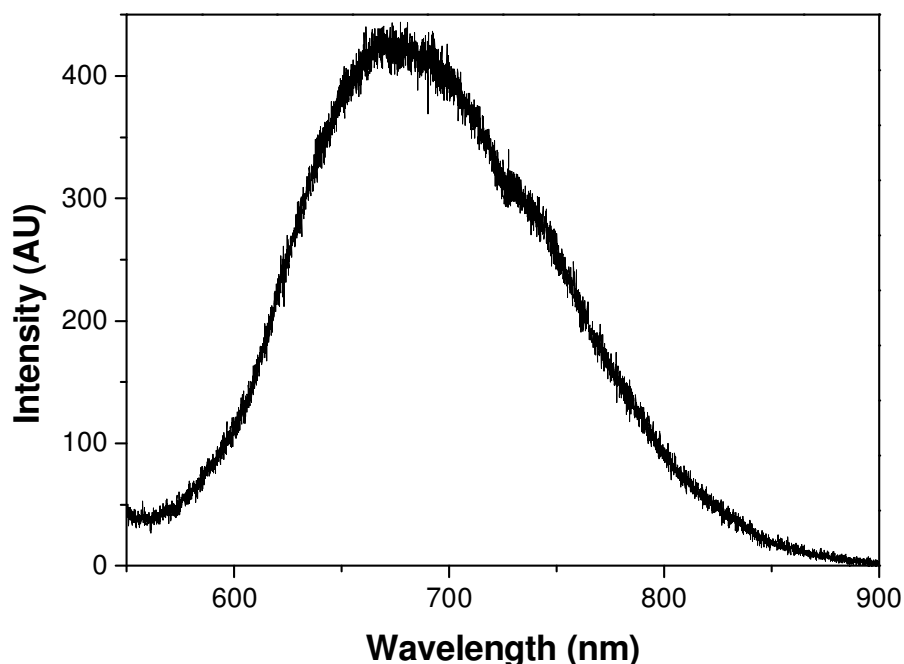

Fig. 4.11: Emission from self assembled monolayers of $[Ru(bpy)_2(Qbpy)]^{2+}$ complex on a smooth gold surface. The excitation wavelength was 473 nm at power of 30 μW. The laser spot size was 2 μm with a collection angle 72 degree.

In each instance, monolayers were formed by sonicating the slide in dye solution and then the gold nanocavity arrays were maintained in contact with 1 mM methanolic ruthenium dye solution overnight. After annealing, the arrays were treated in the same way to form a monolayer of dye. The luminescence spectra from a self-assembled monolayer of $[Ru(bpy)_2(Qbpy)]^{2+}$ adsorbed on 240 nm diameter gold nanocavity arrays before and after annealing at different temperatures are shown in Figure 4.12. The black line shows the emission spectrum recorded from the monolayer of dye adsorbed on the array prior to the temperature treatment and the red, green and blue lines show the emission from the self-assembled monolayer of dye on arrays annealed at 100, 300 and 500 ºC respectively. In order to investigate the reproducibility of the experiment, three spectra were recorded from different spots across the sample and variation in emission intensity was within the experimental error (< 7 %). The number of molecules estimated to be present in the confocal volume for the 240 nm diameter arrays before and after annealing is shown in Table 4.2. The enhancement factor is obtained compared to smooth gold surface according to Equation 4.2.

$$EF = (I_{NC}/I_{Au})*(N_{Au}/N_{NC}) \qquad\qquad 4.2$$

where I_{NC} is the intensity of emission from the metal complex on the annealed nanocavity array and I_{Au} for that on unroughened gold. N_{Au} is the number of molecules estimated to be present on unroughened gold based on its surface area and the coverage associated with a close packed layer, and N_{NC} is the number estimated to be on the annealed arrays.

As shown in Table 4.2 the number of molecules for 100 ºC annealed array is expected to be approximately two times less than the untreated arrays. Therefore, it is expected that a 50 % reduction in emission intensity will occur if the influence of surface plasmons at this wavelength is identical. Correspondingly, the intensity of emission is decreased by 50 % for the array annealed at 100 ºC as expected from the surface area measurements. However, annealing of the sample at 300 ºC increased the signal intensity to similar levels as those seen for the unannealed array. The number of molecules in the confocal volume for the 300 ºC annealed array was estimated to be two times greater than the untreated arrays. In fact, the emission intensity for 300 ºC
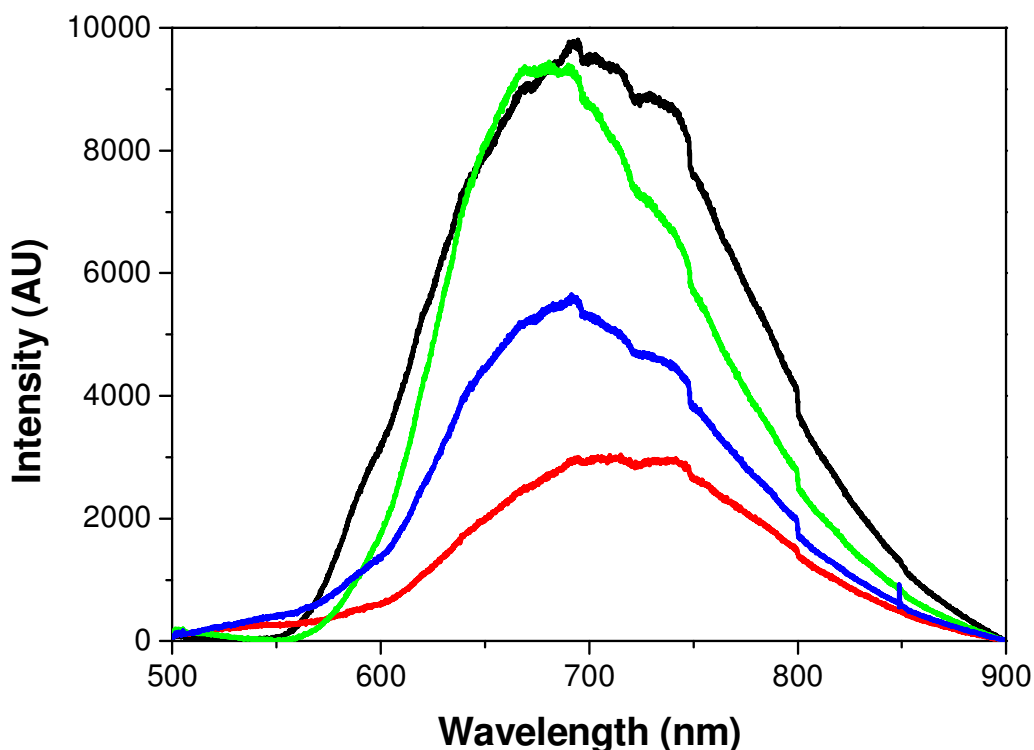
Fig. 4.12: Luminescence from monolayers of $[Ru(bpy)_2(Qbpy)]^{2+}$ complex adsorbed on 240 nm diameter gold nanocavity arrays before (—) and after annealing in air at different temperatures 100 (—), 300 (—), and 500 º C (—). The excitation wavelength was 473 nm at power of 30 µW. The laser spot size was 2 μm with a collection angle 72 degree.

annealed arrays was reduced by a factor of two times after normalization of the number of molecules compared to untreated arrays. The number of molecules for 500 ℃ annealed arrays was around ten times less than the untreated arrays. The emission intensity of the arrays after annealing at 500 ℃ reduced by a factor of two as shown in Figure 4.12. In fact, the enhancement factor was 5 for the arrays annealed at 500 ℃ compared to untreated arrays after normalization of number of molecules in the confocal volume. The lifetime measurements from self-assembled monolayers of ruthenium dye on gold nanocavity arrays reveal the changes in the radiative decay rate attributed to the presence of surface plasmons plays a major role in the enhanced emission from the monolayers of dye on gold cavity arrays. The reflectance measurements from both annealed and untreated arrays show that the reflectance from the array annealed at 500 ℃ was less at 473 nm compared to other arrays. The arrays shows similar reflectance for untreated array and the arrays annealed up to 100 ℃ and

comparatively greater reflectance is observed from the arrays annealed at 300 ℃. In summary, the enhanced emission from self-assembled monolayers of $[Ru(bpy)_2(Qbpy)]^2$ dye on gold nanocavity arrays reveal that the arrays annealed at 500 ℃ show the greatest enhancement in emission intensity after normalization for the number molecules under the confocal volume. The reflectance measurements from these arrays indicate that the enhancement in emission intensity from the arrays mainly due to the presence of strong surface plasmons at 473 nm. Monolayers of $[Ru(bpy)_2(Qbpy)]^{2+}$ complex adsorbed on the metal surfaces shows emission approximately 700 nm. It is clearly seen from the emission spectra that a blue shift in emission intensity is observed compared to previous reports.[27] The shift in emission wavelength was observed for the same sample at different spots. Therefore, it can be concluded that it is not a genuine shift for this annealed samples. The origin of this shift is unclear and in future, it will be studying using different luminescent dyes.

The changes in the emission intensity from monolayers of $[Ru(bpy)_2(Qbpy)]^{2+}$ complex at untreated and annealed arrays were measured for 430 nm diameter arrays as shown in Figure 4.13. All the measurements were carried out under identical conditions and the laser power used was 30 μW for the 473 nm laser line. The sample annealed at 100 ℃ shows similar emission intensity to the unannealed array and there is no significant difference anticipated in number of molecules in the confocal volume between untreated and the arrays annealed at 100 ℃. In the 430 nm diameter arrays, the emission intensity for the array annealed at 300 ℃ was approximately 15±2 fold compared to the unannealed sample. However, the number of molecules in the confocal volume was 3.5 times greater for the arrays annealed at 300 ℃. Giving an enhancement factor of 5 from 300 ℃ annealed arrays compared to untreated arrays after normalization to the number of molecules. An order of magnitude in emission enhancement is observed from the dye adsorbed on 500 ℃ annealed arrays compared to unheated array, whereas the number of molecules in the confocal volume was approximately 83 times less than the untreated arrays. Therefore, a greater enhancement in emission intensity (enhancement factor $8x10^2$) from 430 nm diameter arrays were obtained when annealed up to 500 ℃. The reflectance measurements from these arrays shows lowest reflectance for 500 ℃ annealed arrays at 473 nm. Therefore, this increase in emission intensity might be due to the greater contribution of plasmon-coupled emission for these annealed arrays.
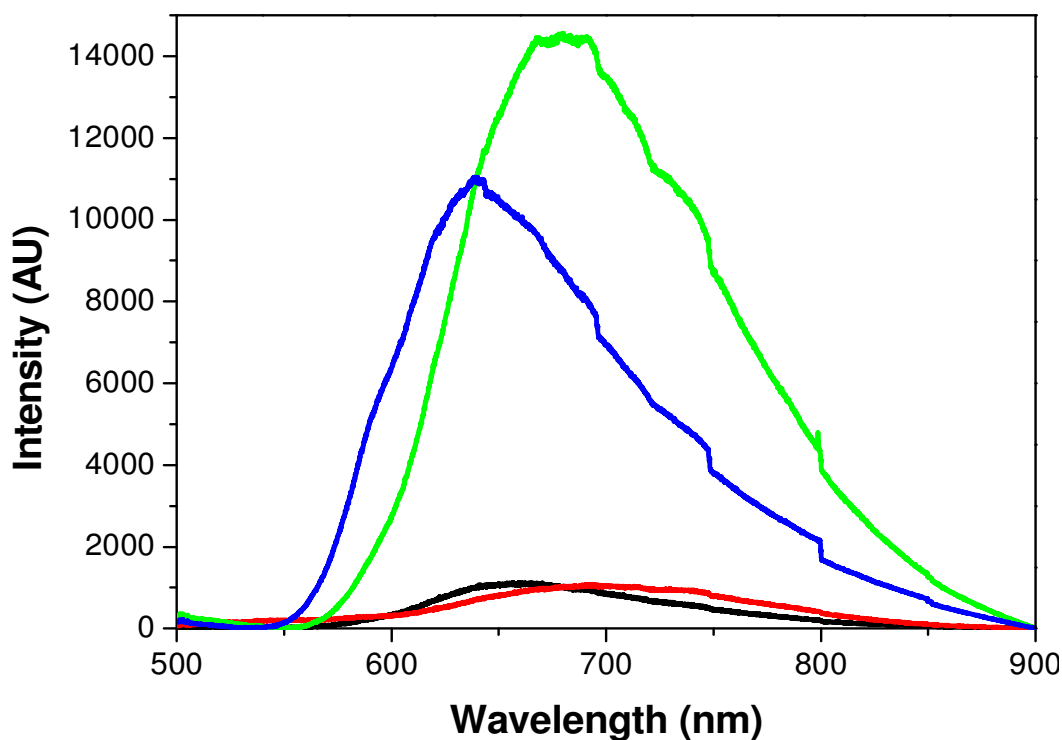
Fig. 4.13: Emission from self assembled monolayers of $[Ru(bpy)_2(Qbpy)]^{2+}$ complex on 430 nm diameter gold nanocavity arrays before (—) and after annealing at different temperatures 100 (—), 300 (—), and 500 ℃ (—). The excitation wavelength was 473 nm at power of 30 μW. The spectra were recorded with a 100x objective.

Figure 4.14 shows the luminescence spectra of $[Ru(bpy)_2(Qbpy)]^{2+}$ complex adsorbed on 820 nm diameter arrays before and after annealing of the arrays. The emission intensity of the dye was enhanced two fold for the 100 ℃ annealed arrays compared to an unannealed sample even though there were no significant changes in the number molecules in the confocal volume. The emission intensity decreased for the 300 ℃ annealed array compared to the untreated array. The number of molecules in the confocal volume for this array was anticipated on the basis of surface area to be five times greater than the untreated arrays which indicate that the enhancement in emission was less than the untreated arrays. The number of molecules in the confocal volume for 500 ℃ annealed arrays was unchanged within the experimental error to the untreated arrays but a two fold increase in emission intensity was observed.
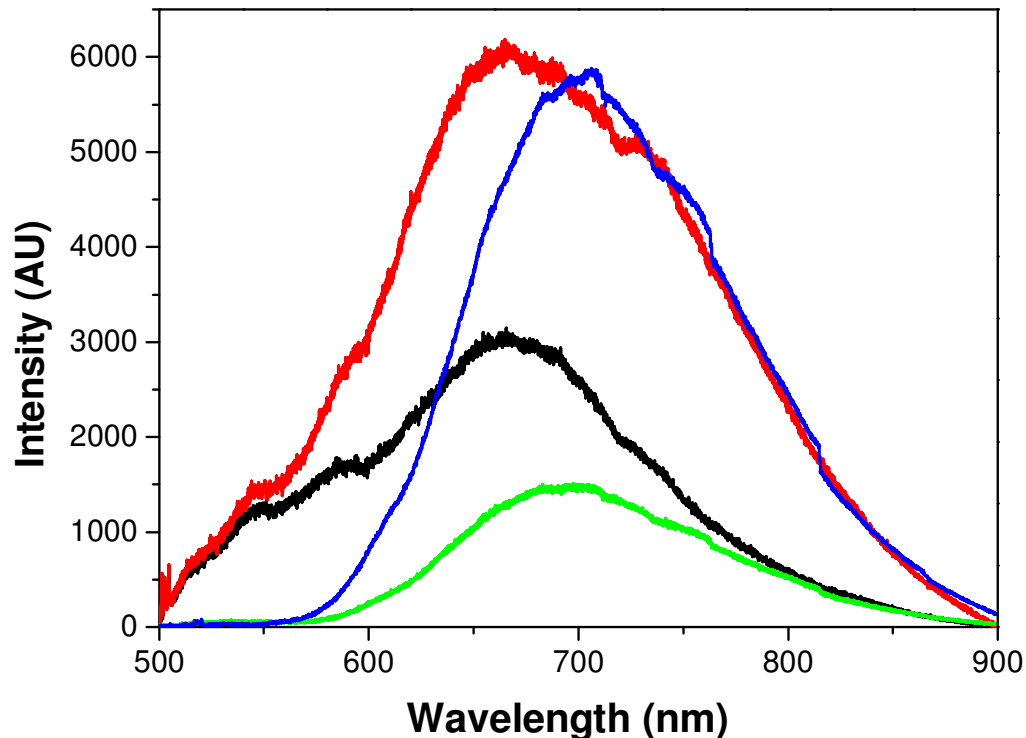
Fig. 4.14: Luminescence from monolayer of $[Ru(bpy)_2(Qbpy)]^{2+}$ complex adsorbed on 820 nm diameter gold nanocavity arrays before (—) and after annealing in air at different temperatures 100 (—), 300 (—), and 500° C (—) for 30 minutes. The excitation wavelength was 473 nm with a power of 30 µW. The laser spot size was 2 µm with a collection angle 72 degree.

The estimated enhancement factor for different arrays compared to smooth gold surface is shown in Table 4.2. The systematic study of enhancement in emission intensity for annealed arrays as a function of temperature reveals that the enhancement is not uniform for three different arrays which is in fact consistent with AFM and SEM which showed significant variation in the impact of heat on the arrays. The enhancement varies with cavity diameter and with annealing temperature. Overall, it is clear that, the greatest enhancement in emission intensity is observed for the arrays annealed at 500 °C. Geddes and co-workers reported 50 % enhancement in fluorescence intensity from annealed silver films compared to an unannealed sample.[11] They observed up to a 10-fold enhancement in fluorescence emission intensity from fluorescein labelled Human Serum Albumin adsorbed on annealed silver films. They attributed this enhancement to the increased surface area of the nanoparticles for annealed samples which increases the scattering cross sections. This increase in scattering cross section increases the extinction coefficient which is the combination of both absorption and scattering. They

have reported that the metal enhanced fluorescence is due to the fluorophore-plasmon coupled emission which depends on the scattering properties of the nanostructured film. In comparison, the enhancement in emission intensity from annealed silver island films with annealed silver colloids showed that the emission intensity is unchanged for annealed silver colloids. Here, larger gold nanocavity arrays show a greater increase in emission intensity as a function of temperature. Surprisingly, the surface roughness was significantly reduced for the arrays heated at 500 ºC and the larger arrays shows greater enhancement after annealing at this temperature. The reflectance measurements for three different arrays annealed at 500 ºC show greater absorption at 473 nm compared to unannealed arrays.

	240 nm		430 nm		820 nm	
	NM	EF	NM	EF	NM	EF
Untreated	5.5×10^6	7.6	6.2×10^6	1	2.2×10^6	5.7
100	2.6×10^6	4.8	5.1×10^6	1.02	2.8×10^6	9.2
300	1.3×10^7	2.8	2.2×10^7	2.7	1.2×10^7	0.532
500	4.7×10^5	50	7.4×10^4	185	1.9×10^6	13

Table 4.2: The enhancement factor for both annealed and unannealed arrays compared to smooth gold surface after normalizing to the number of molecules. NM – number of molecules, EF – enhancement factor.

4.3.6 SERS from annealed arrays
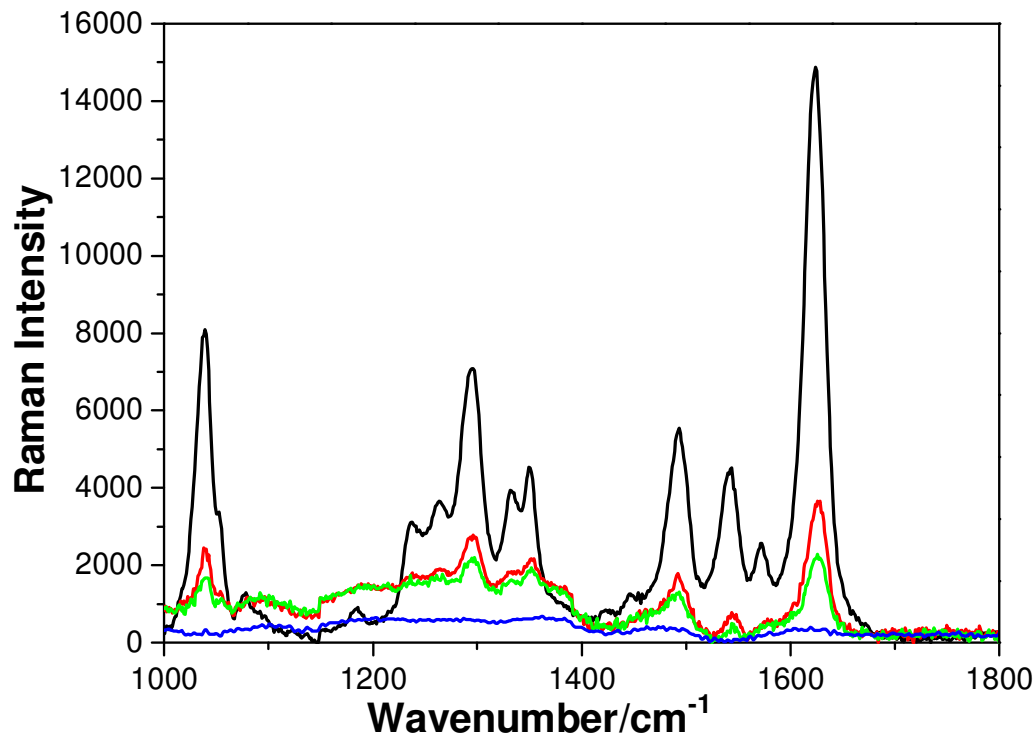
Fig. 4.15: Raman spectra of monolayers of $[Ru(bpy)_2(Qbpy)]^{2+}$ complex adsorbed on 240 nm diameter gold nanocavity arrays before (—) and after annealing in air at different temperatures 100 (—), 300 (—), and 500 ºC (—). The excitation wavelength was 633 nm at power of 10 µW. Typical acquisition time was 10 s and the laser spot size was 2 µm.

In order to investigate the effect of annealing on Raman signal intensity, the Raman spectra were collected from the $[Ru(bpy)_2(Qbpy)]^{2+}$ monolayer adsorbed onto the annealed arrays as described in each case following temperature treatment. The excitation wavelengths 633 and 785 nm were used here to study SERS from monolayers adsorbed on annealed arrays. The results obtained using 785 nm excitation were consistent with those observed under 633 nm excitation therefore, spectra were recorded using the 633 nm excitation are shown here. Figure 4.15 shows the Raman spectra collected from the monolayer of ruthenium dye on 240 nm diameter arrays before and after annealing. The black line shows the spectrum collected from the monolayer adsorbed on the untreated array and the red, green and blue lines show the Raman signal intensity recorded from monolayer of $[Ru(bpy)_2(Qbpy)]^{2+}$ dye adsorbed on annealed samples at 100, 300 500 ºC temperatures respectively. Interestingly, in contrast to luminescence signal it is clear that the Raman signal intensity of the array

decreases as the annealing temperature increases. The maximum signal intensity is observed from the dye adsorbed at the untreated arrays and correspondingly the reflectance measurements shows lower reflectance at 633 nm for untreated arrays. However, when one compares the number of molecules in the confocal volume (Table 4.3) a two fold enhancement in signal intensity for 300 ℃ annealed arrays would be expected but which is not observed in the experiment. The Raman measurements from both untreated and annealed arrays reveal that the enhancement in Raman signal intensity were reduced from the molecules adsorbed on to annealed arrays after normalizing to the number of molecules. In order to investigate the reproducibility of the experiment three spectra were collected from different spots of the sample. The signal intensity collected from different spots was within the experimental error.
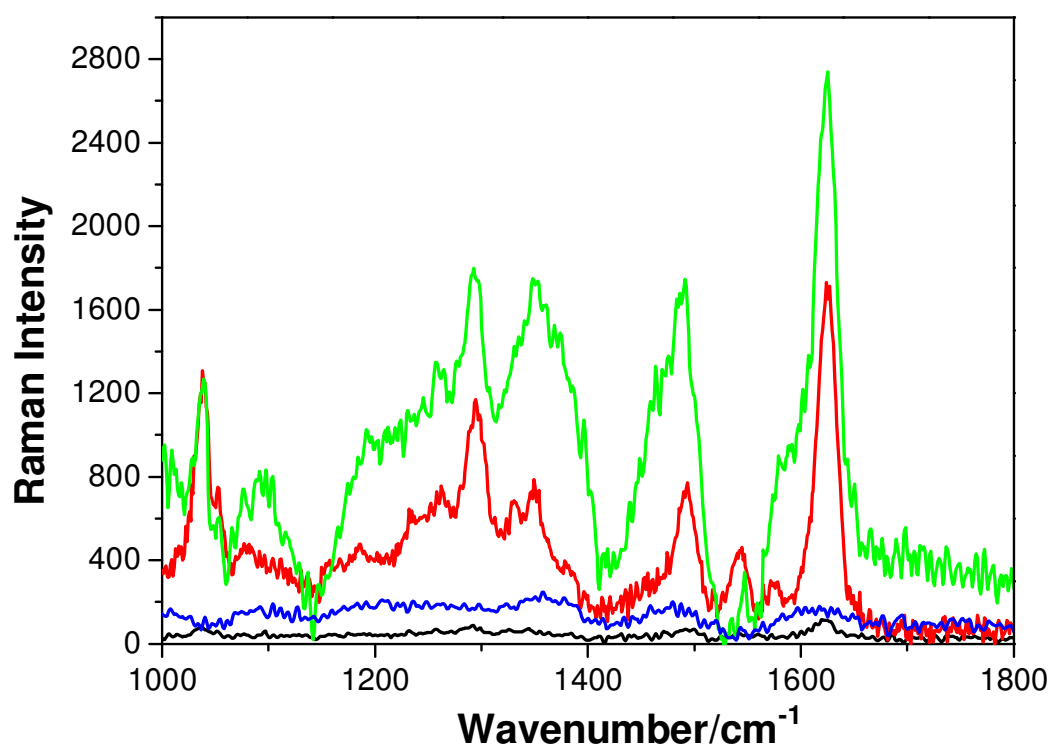

Fig. 4.16: Raman spectra of monolayers of $[Ru(bpy)_2(Qbpy)]^{2+}$ complex adsorbed on 430 nm diameter gold nanocavity arrays before (—) and after annealing in air at different temperatures 100 (—), 300 (—), and 500 ℃ (—). The excitation wavelength was 633 nm at power of 10 µW. Typical acquisition time was 10 s and the laser spot size was 2 µm.

Figure 4.16 shows the Raman spectra collected from a self assembled monolayer of $[Ru(bpy)_2(Qbpy)]^{2+}$ adsorbed onto the 430 nm diameter gold cavity arrays before and after annealing. The array annealed at 100 ℃ showed eight fold enhancement in signal

intensity compared to unannealed arrays but there is no significant change in the number molecules in the confocal volume based on surface area measurements. This increase in signal intensity suggests the increased absorbance from surface plasmons at 633 nm for 100 ℃ annealed arrays compared to untreated array which is in agreement with reflectance measurements. The reflectance measurements show that the arrays annealed at 300 ℃ showed highest absorbance at 633 nm compared to other arrays and correspondingly, the greatest enhancement in signal intensity was observed for the arrays annealed at 300 ℃. The number of molecules in the confocal volume for this array was three times greater and the total enhancement factor for this array was 3±0.4 which is smaller than the enhancement from 100 ℃ annealed arrays. Tuan and co-workers have reported the enhancement in Raman signal intensity from cresyl fast violet dye on annealed gold island films.[28] The greatest enhancement in signal intensity was reported from the dye on 200 ℃ annealed film compared to unannealed, 300 and 400 ℃ films.
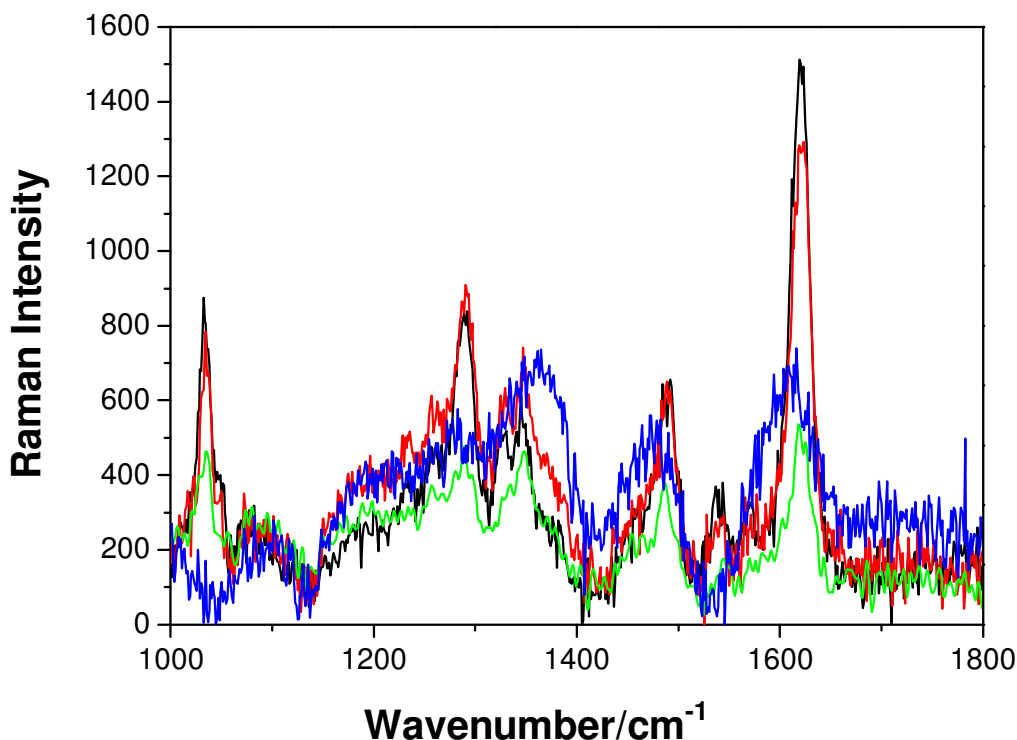

Fig. 4.17: Raman spectra of monolayers of $[Ru(bpy)_2(Qbpy)]^{2+}$ complex adsorbed on 820 nm diameter gold nanocavity arrays before (—) and after annealing in air at different temperatures 100 (—), 300 (—), and 500 ℃ (—). The excitation wavelength was 633 nm at power of 10 µW. Typical acquisition time was 10 s and the spot size was 2 µm.

Figure 4.17 shows the Raman signal intensity recorded from the dye adsorbed onto 820 nm diameter gold nanocavity arrays before and after annealing the sample. The unannealed array gives the best Raman signal intensity for 820 nm diameter arrays compared to annealed arrays. Changes in the signal intensity for the sample heated to
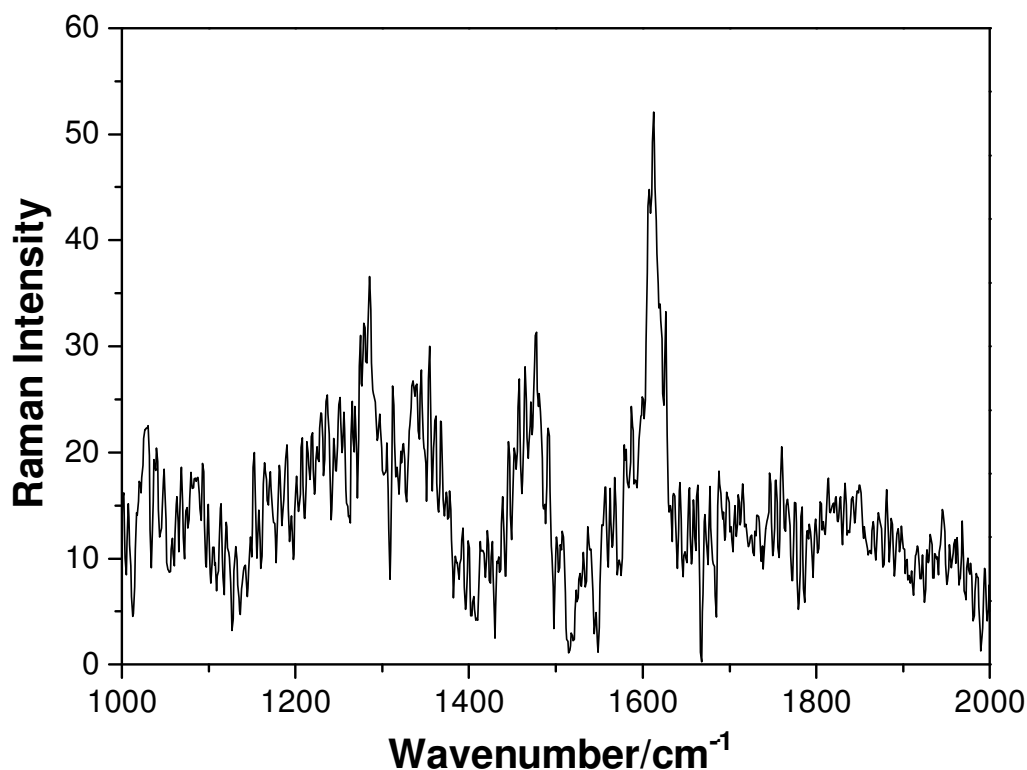
Fig. 4.18: Raman spectra of monolayers of $[Ru(bpy)_2(Qbpy)]^{2+}$ complex adsorbed on a smooth surface. The excitation wavelength was 633 nm. Typical acquisition time was 10 s and the spot size was 2 μm.

100 °C were comparable with the unannealed array. The gold nanocavity array annealed at 300 °C shows a reduction in signal intensity, even though the number of molecules in the confocal volume was greater for this compared to the unannealed arrays. The Raman signal intensity is further significantly decreased for the arrays annealed at 500 °C which is probably due to the decrease in surface roughness after annealing. In summary, greatest enhancement in Raman signal intensity is observed for unannealed arrays for 820 and 240 nm diameter arrays exciting at 633 nm. For 430 nm diameter arrays, the 300 °C annealed sample shows the highest signal intensity. In this chapter, the thicknesses of the arrays are different from those in Chapter 3. Therefore, the direct comparison of Raman signal intensity is insignificant.

The enhancement factor for $[Ru(bpy)_2(Qbpy)]^{2+}$ monolayer adsorbed on the gold nanocavity arrays was calculated by comparing the Raman intensity from molecule adsorbed on to unroughened gold surface. Figure 4.18 shows the Raman signal intensity from the molecule adsorbed onto a smooth gold surface. The Raman signal intensity from the smooth surface was exceedingly weak therefore; it was difficult to acquire spectra using an identical experimental set up. The spectrum shown above recorded therefore using high laser power and more acquisition time, compared to the spectra recorded from the gold nanocavity arrays. The enhancement factor for the gold nanocavity arrays were calculated after correcting for the laser intensity and the number of molecules in the confocal volume, using Equation 4.2. Table 4.3 shows the enhancement factor calculated for molecules adsorbed on both annealed and untreated arrays. In summary, for 240 nm and 820 nm diameter gold nanocavity arrays, the enhancement in Raman signal intensity is obtained for untreated arrays compared to annealed samples. However, the greatest enhancement is observed for 430 nm arrays under 633 nm excitation when annealed up to 500 ºC.

	240 nm		430 nm		820 nm	
	NM	EF	NM	EF	NM	EF
RT	5.5×10^6	$3 \times 10^3 \pm 200$	6.2×10^6	32 ± 5	2.2×10^6	$8 \times 10^3 \pm 75$
100	2.6×10^6	$1.9 \times 10^3 \pm 300$	5.1×10^6	$5 \times 10^2 \pm 70$	2.8×10^6	$5 \times 10^2 \pm 45$
300	1.3×10^7	$2 \times 10^2 \pm 70$	2.2×10^7	$1 \times 10^2 \pm 7$	1.2×10^7	75 ± 10
500	4.7×10^5	$8 \times 10^2 \pm 100$	7.4×10^4	$5 \times 10^3 \pm 400$	1.9×10^6	105 ± 10

Table 4.3: Enhancement factors for annealed and unannealed arrays compared to a smooth gold surface after normalizing to the number of molecule. Raman signals recorded from $[Ru(bpy)_2(Qbpy)]^{2+}$ dye adsorbed on annealed and unannealed arrays used for enhancement factor calculation. NM – number of molecules, EF – enhancement factor. The excitation wavelength was 633 nm.

4.4 Conclusions

The thermal stability of gold nanocavity arrays was investigated by annealing arrays at 100, 300 and 500 ℃. The arrays were studied by AFM and SEM to examine topology and surface structure, by CV to assess changes to surface area and by Raman and luminescence of an adsorbed monolayer to examine effect of temperature on 240, 430 and 820 nm diameter arrays. The gold nanocavity arrays appear to be thermally stable up to 100 ℃. SEM and AFM images of the annealed arrays reveal that greatest change in the nanoscale features occurs at the top surface of the array after annealing at 300 ℃. The AFM images of the arrays indicate that melting of the top surface of the arrays occurs at 500 ℃. However, the hexagonal pattern of the array was apparent even after annealing at 500 ℃. The roughness of the surface increases after annealing at 300 ℃ and then start melting the top surface of the array at 500 ℃. The cyclic voltammetric measurements of the arrays before and after annealing reveal that the surface roughness of 240 and 430 nm diameter arrays is significantly reduced after annealing at 500 ℃.

The greatest enhancement in emission intensity is observed for all three sizes of arrays after annealing at 500 ℃. Emission enhancement can arise from excitation or emission plasmonic interactions. The reflectance measurements show that the arrays annealed at 500 ℃ exhibit greater absorption at 473 nm attributed to the surface plasmons present on the metal surfaces. The Raman signal intensity of the gold nanocavity arrays decreased dramatically as a function of temperature for the 240 and 820 nm diameter arrays. Therefore, it may be necessary to coat with some layer such as Al_2O_3, for the application of these substrates in high temperature Raman sensing. However, the gold nanocavity arrays with 430 nm diameter exhibit greatest enhancement in Raman signal intensity at 300 ℃. In conclusion, the gold nanocavity arrays are not stable up to 300 ℃. However, the arrays annealed at 500 ℃ exhibit greater enhancement in emission intensity which can be useful for the fabrication high temperature based fluorescence sensors.

4.5 References

[1]   Beavers, K. R.; Marotta, N. E.; Bottomley L. A. *Chem. Mater.*, **2010**, *22*, 2184.

[2]   Banares, M. A. *Catal. Today,* **2005**, *100*, 71.

[3]   Guerrero-Perez, M. O.; Banares, M. A. *Catal. Today,* **2006**, *113*, 48.

[4]   Hakamada, M.; Mabuchi, M. *J. Mater. Res.,* **2009**, *24*, 301.

[5]   Feofanov, A.; Ianoul, A.; Kryukov, E.; Maskevich, S.; Vasiliuk, G.; Kivach, L.; Nabiev, I. *Anal. Chem.,* **1997**, *69*, 3731.

[6]   Haes, A. J.; Haynes, C. L.; McFarland, A. D.; Schatz, G. C.; Van Duyne, R. P.; Zou, S. L. *MRS Bulletin,* **2005**, *30*, 368.

[7]   Whitney, A. V.; Elam, J. W.; Stair, P. C.; Van Duyne, R. P. *J. Phys. Chem. C,* **2007**, *111*, 16827.

[8]   Haynes, C. L.; Van Duyne, R. P. *J. Phys. Chem. B,* **2001**, *105*, 5599.

[9]   Jensen, T. R.; Malinsky, M. D.; Haynes, C. L.; Van Duyne, R. P. *J. Phys. Chem. B,* **2000**, *104*, 10549.

[10]   Whitney, A. V.; Elam, J. W.; Zou, S. L.; Zinovev, A. V.; Stair, P. C.; Schatz, G. C.; Van Duyne, R. P. *J. Phys. Chem. B,* **2005**, *109*, 20522.

[11]   Aslan, K.; Leonenko, Z.; Lakowicz, J. R.; Geddes, C. D. *J. Fluoresc.,* **2005**, *15*, 643.

[12]   Hutter, E.; Fendler, J. H. *Adv. Mater.,* **2004**, *16*, 1685.

[13]   Yguerabide, J.; Yguerabide, E. E. *Anal. Biochem.,* **1998**, *262*, 137.

[14]   Yguerabide, J.; Yguerabide, E. E. *Anal. Biochem.,* **1998**, *262*, 157.

[15]   Aslan, K.; Gryczynski, I.; Malicka, J.; Matveeva, E.; Lakowicz, J. R.; Geddes, C. D. *Curr. Opin. Biotechnol.,* **2005**, *16*, 55.

[16]   Matveeva, E.; Gryczynski, Z.; Gryczynski, I.; Malicka, J.; Lakowicz, J. R. *Anal. Chem.,* **2004**, *76*, 6287.

[17]   Mahajan, S.; Abdelsalam, M.; Suguwara, Y.; Cintra, S.; Russell, A.; Baumberg, J.; Bartlett, P. N. *Phys. Chem. Chem. Phys.,* **2007**, *9*, 104.

[18]   Mahajan, S.; Baumberg, J. J.; Russell, A. E.; Bartlett, P. N. *Phys. Chem. Chem. Phys.,* **2007**, *9*, 6016.

[19]   Van Cleef, M.; Holt, S. A.; Watson, G. S.; Myhra, S. *J. Microsc.,* **1996**, *181*, 2.

[20]   Cintra, S.; Abdelsalam, M. E.; Bartlett, P. N.; Baumberg, J. J.; Kelf, T. A.; Sugawara, Y.; Russell, A. E. *Faraday Discuss.,* **2006**, *132*, 191.

[21]   Willets, K. A.; Van Duyne, R. P. *Annu. Rev. Phys. Chem.,* **2007**, *58*, 267.

[22]   Bartlett, P. N.; Baumberg, J. J.; Coyle, S.; Abdelsalam, M. E. *Faraday Discuss.,* **2004**, *125*, 117.

[23]   Bi, H. J.; Cai, W. P.; Zhang, L. D.; Martin, D.; Trager, F. *Appl. Phys. Lett.,* **2002**, *81*, 5222.

[24]   Semin, D. J.; Rowlen, K. L. *Anal. Chem.,* **1994**, *66*, 4324.

[25]   McCarthy, S. L. *J. Vac. Sci. Technol.,* **1976**, 13, 135.

[26]   Aussenegg, F. R.; Leitner, A.; Lippitsch, M. E.; Reinisch, H.; Riegler, M. *Surf. Sci.,* **1987**, *189*, 935.

[27]   Forster, R. J.; Keyes, T. E. *J. Phys. Chem. B,* **1998**, *102*, 10004.

[28]   Dhawan, A.; Du, Y.; Yan, F.; Gerhold, M. D.; Misra, V.; Vo-Dinh, T. *IEEE Sens. J.,* **2010**, *10*, 608.

Chapter 5

Formation of lipid bilayers across dried and prefilled gold nanocavity arrays

5.1 Introduction

A key challenge in the field of nanobiophotonics research is the application of nanostructured metal surfaces in biosensors which utilise proteins such as enzymes or antibodies as sensing elements.[1,2] The main problem associated with the nanostructured metal surfaces is their incompatibility with biomolecules. In living cells, proteins operate in an aqueous environment and many reside at membrane interfaces. Contact of such biomolecules with metal substrates typically results in non-specific adsorption and denaturation. Planar artificial lipid bilayers are most widely studied model applied to investigate the behaviour of transmembrane proteins. Artificial lipid membranes hold great promise due to their ability to mimic natural membrane properties such as the lateral mobility of constituents,[3,4,5] impermeability to ions and compatibility with protein incorporation.[3, 6 , 7] Lipids are broadly divided into three classes: phospholipids, glycolipids and sterols, in which phospholipids are the major lipids found in the biological membrane.[8] The phospholipids are further divided into two sub-classes, glycerophospholipids and sphingophospholipids. These phospholipids are mainly differentiated on the basis of their hydrophobic lipid chain. Most lipids exist in a bilayer structure in contact with aqueous solution as explained by Gorter and Grendel due to the hydrophobic effect.[9] As discussed in Chapter 1, the fluid mosaic model is the most widely accepted model for the lipid membrane.[10] The typical thickness of the lipid bilayer is 5-6 nm. Even though the thickness of the biomembrane is very small it is impermeable to most water-soluble ions, which enables cells to regulate the salt concentrations across the membrane. Many groups have prepared planar lipid bilayers on

a variety of platforms using different techniques from vesicle rupture technique to Langmuir-Blodgett technique.[11,12]

In biological membranes, lipids exist as planar bilayers and because of their small thicknesses, bilayers are treated as two dimensional sheets. The study of the role of biomembranes in live cells is hampered by the inhomogeneity in composition and the small thickness of the membrane. Therefore, there has been significant attention paid towards the preparation of artificial lipid bilayers, which incorporate proteins to understand the fundamental function of transmembrane proteins in a more controllable and biomimetic environment. Intensive research on the development of planar model membranes that mimic the features of the biological membrane has resulted in a variety of membrane models. The earliest bilayer model developed was known as the black lipid membrane (BLM) created using a painting method.[13] As discussed in Chapter 1, the main problem with black lipid bilayer membranes was their stability. Moreover, this model allowed only the electrical properties of the bilayer membrane to be investigated. The bilayers formed on the hole between the chambers were not accessible for studies using techniques other than electrochemistry due to the instability of the layers. It is crucial to study the fluidity of the membrane and dynamics of transmembrane protein in the membrane and these questions are best addressed using optical techniques such as Fluorescence recovery after photobleaching (FRAP) or fluorescence correlation spectroscopy (FCS).

There are numerous reports on the formation of self-assembled lipid layers on gold surfaces and the preparation of a second layer using physisorption techniques such as LB. Such methods can provide a defect-free bilayer on gold surface and exhibit membrane capacitance in the range of 0.5-1.0 $\mu F/cm^2$.[14,15] Unfortunately, this approach reduces the lateral mobility of the lipids because the inner layer is chemically bound to gold, which can prevent proper functioning of the membrane proteins as discussed in Chapter 1. The close packing of the self-assembled lipid also prevents insertion of proteins through the membrane. Even if a protein inserts in to membrane layer, the close proximity of the protein to the solid support can permit surface interaction, which may destroy the protein function and structure.

Recently, solid supported artificial bilayer membranes were used as an alternative bilayer model in biosensors to probe the dynamics of bio-macromolecules.[16,17] There are different types of solid supported lipid bilayers reported where the underlying layers are species such as polymer cushions or lipopolymer tethers and they were discussed in Chapter 1. However, issues still exist in respect of protein lateral motion, for example, Tanaka and co-workers prepared lipopolymers with 2-methyl-2-oxazoline as a supporting layer for lipid bilayers.[18] They investigated the mobility of incorporated cell-receptor integrin (integrin αIIbβ3) on the polymer support. The report revealed that only 20 % of the protein was mobile with a diffusion coefficient of 0.03 μm^2/s. In another example, Sackmann and co-workers reported cellulose supported lipid bilayers on glass support. The multilayer of trimethylsilyl cellulose was prepared on glass support using the Langmuir-Blodgett technique. Then the integrin was incorporated by introducing vesicles spread on these polymer cushions, which resulted in the protein incorporated into the lipid bilayers. The mobility of the integrin was greater on this substrate in comparison to 2-methyl-2-oxazoline lipopolymer supporting layer.[18] However, only 25 % of the integrin was mobile with a diffusion coefficient of 0.6 μm^2/s.[19] Here, the mobility fraction of the integrin on supported bilayers was investigated using FRAP. The major problem with the solid supported bilayer membrane was the thickness of the gap between the solid support and the membrane. The thickness between the membrane and the solid support was not sufficient to avoid the undesirable interactions between the transmembrane protein and the solid support. In such cases, where the protein is truly transmembranal and possesses a cytoplasmic region, one end of the protein makes direct contact with the solid surface which alters the structure of the membrane proteins.[20,21] For example, receptors such as integrin, have an extracellular head and cytoplasmic tail. In this type of protein, signalling occurs due to the binding of extracellular ligand to the head group of the integrin, which results the conformation changes in cytoplasmic tail. Biomimetic platform for the study of such proteins is important, as they are key target for a range of therapeutic agents. To study the dynamics of transmembrane proteins, the optimum platform is a substrate, which contains voids, which can freely support the cytoplasmic tails of the proteins with an aqueous phase at both interfaces of the membrane.[22] The design of an appropriate platform for supported bilayers that minimally perturb the conformation of membrane proteins is one of the current challenges in the field of membrane chemistry.

Recently, spanning lipid bilayers on porous substrates have attracted attention and several groups are now working in this field.[23,24] For example, Steinem and co-workers have suspended bilayers across porous silicon and alumina substrates using vesicle fusion.[25,26] The formation of spanning bilayers on porous alumina substrates have been used to aid the study of dynamics of protein using electrochemistry.[22] However, the study of biomolecules on spanning lipid bilayers using Raman and fluorescence spectroscopy which can be very informative, is difficult due to the weak signal intensity of these biomolecules and this has not to date been addressed on arrays in detail. To overcome lower sensitivity of Raman spectroscopy, several groups have focussed on surface enhanced platforms such as nanostructured metal surfaces, such as nanohole arrays. Hook and co-workers first reported the use of the shallow evanescent field of localized surface plasmons from nanoholes to study interaction of biotynated DHPE (phosphatidylethanolamine) with neutravidin.[27] They used SiO_x as a thin protective layer for biomolecules. In this study, lipid bilayers were assembled on a nanohole array and they reported a shift in localized surface plasmon when avidin binds to biotynated lipids. Spanning of lipid bilayers on a surface enhanced spectroscopic platform has not reported to date.

In this chapter, formation of a spanning lipid bilayer membrane, surrounded by an aqueous phase, formed on top of gold nanocavities as a biosensor platform is described. The key advantages of this platform are presented below.

- ❖ Spanning lipid bilayer formed on top of cavity is proximate to aqueous environments on both sides of the membrane.
- ❖ The composition of solution inside and outside the membrane can be varied by choosing appropriate solvents to fill the nanocavity arrays.
- ❖ This platform could also possibly make use of the surface plasmons from the gold nanocavity arrays, primarily for fluorescence and Raman enhancement.
- ❖ The gold nanocavity arrays allow selective modification of edges and inside the cavity by using thiol or nitrogen chemistry, for example, to make the surface either hydrophilic or hydrophobic.
- ❖ The diameter and thickness of the gold nanocavity array can be varied systematically.[28]

❖ As the platform is metallic, it can be studied using electrochemistry. For example, to study the ion channel formation in lipid bilayers or electrochemical releasing of proteins.[29]

The first part of this chapter describes the preparation of liposomes and exploration of different membrane probes to study the bilayers. Fluorescent membrane probes are indispensible tools for the investigation of different aspects of lipid membranes such as structure of liposomes on different substrates and lateral mobility of bilayers on a platform. Furthermore, biomolecules can be visualized and analysed within a short period of time using fluorescence microscopy.[30,31,32] Lipid membranes do not display intrinsic fluorescence; therefore, it is common to label membranes with fluorescent probes to study the dynamics of molecules in the membrane.[33,34]

The key idea behind using a nanocavity is to provide aqueous filled voids to maintain the lateral mobility of the bilayer and to provide enough space for the cytoplasmic tail of the transmembrane protein such as integrin. To confirm spanning we distinguished a difference in assembly of lipid bilayers on dried arrays and on top of buffer filled cavities. The formation of bilayer membrane at both buffer prefilled and dry cavity arrays was visualized using confocal fluorescence microscopy by including the fluorescent probe 5-dodecanoylaminofluorescein (DAF) in the bilayer. The lateral mobility, the most important feature of the membrane, of lipid bilayers assembled on dried arrays and the buffer filled arrays were investigated using Fluorescence recovery after photobleaching (FRAP) experiments. As discussed in Chapter 3, another advantage of the lipid/nanocavity design is that the interior walls and the top surface of the arrays can be selectively modified with different molecules. This selective decoration may permit the protein activators to be adsorbed inside walls of the array.[29] In future work, the slow release of these activators to activate the protein such as integrin in the spanned bilayer will be implemented. In order to confirm the bilayer width, fluorescence resonance energy transfer (FRET) measurements were carried out after filling the array with an FRET acceptor and incorporating FRET donor molecules (DAF) in the spanned lipid bilayer. It was expected to release the activators from the bottom of the cavity by electrochemistry, therefore, the insulating capability of the lipid bilayer membranes on top of both buffer prefilled and dry gold nanocavity arrays were assessed using capacitance measurements. Finally, as a model transmembrane protein, Gramicidin D

was injected to the electrolyte and the changes in the capacitance of the spanning lipid bilayer monitored during the formation of channels.

5.2 Experimental

5.2.1 Materials

Sodium hydroxide (99.99%), cysteamine (98%), tetrahydrofuran (THF), rhodamine B, polyethylene glycol, alkane thiol (C_9SH), 11-mercapto undecanoic acid and phosphate buffered saline (PBS) were purchased from Sigma-Aldrich. Polystyrene latex spheres (820 ± >3% nm) were obtained from Duke scientific. L-α- Dimyristoyl phosphatidylcholine (DMPC) was purchased from Avanti Polar Lipids and the membrane probe 5-dodecanoylaminofluorescein (DAF) was obtained from Molecular probes. Ruthenium membrane probes were synthesised in our group by Elena Lestini and Stephen Finn.

5.2.2 Preparation of liposome and spanning lipid bilayers

Gold nanocavities of 820 nm diameter were prepared on smooth gold substrates using nanosphere lithography as described in Chapter 3. Dimyristoylphosphatidylcholine (DMPC) lipid solutions with membrane probe in 1000:1 ratio, were prepared in 2 ml chloroform and the solvent evaporated completely by blowing N_2 gas until a lipid film was formed. This lipid film was then dissolved in 1 ml, 0.1 M PBS buffer solution (pH 7.4) to make a lipid suspension, which was then sonicated for 30 minutes to form liposomes. The liposome solution was then extruded through a 100 nm polycarbonate filter 5 times. Liposomes without dye were prepared for both electrochemical and atomic force microscopy (AFM) measurements using the same procedure but without adding the membrane probe. The assembly of lipid bilayers were prepared at both dried and buffer prefilled gold nanocavity arrays by sonication. The gold nanocavity arrays were prefilled with PBS buffer (pH 7.4, 0.1 M) for spanning the lipid bilayers across the array by 30 minutes sonication. In this technique, gold nanocavity arrays were sonicated in the liposome solution for 30 minutes after filling the array with buffer. For FRET measurements, gold nanocavities were filled with rhodamine (1 μM in water) by sonication for 30 minutes. Photophysical properties of the membrane probe in liposome solution were compared with the membrane probe in buffer. As membrane probes are hydrophobic, it was dissolved first in few drops of ethanol and then the solution made up in buffer. Lipid bilayers formed on gold nanocavity arrays were washed with buffer and kept in aqueous environment.

The top surface of gold nanocavity arrays were selectively modified with three different molecules, alkane thiol, polyethylene glycol and 11-mercapto undecanoic acid, in order to investigate the affect of gold surface on spanning lipid bilayers. The top surface of the arrays selectively modified according to the Scheme 3.1.

5.2.3 Methods

AFM images were recorded with a Veeco Bioscope II in contact mode using commercial Si_3N_4 cantilever tips. These tips are pyramidal in shape with spring constants between 0.04 and 0.08 N/m, and the tips were nominally less than 20 nm radius. All images were recorded with the AFM cantilever and substrate immersed in 0.1 M phosphate buffered saline.

Fluorescence lifetime studies were performed on a Pico-Quant PDL-800B pulsed diode laser controller and FluoTime 100 time-correlated single photon counting system (TCSPC) with a 450 nm pulsed laser source with a cut-on filter of 530 nm. TCSPC analysis was preformed using PicoQuant FluoFit software. Fluorescence microscopy was performed on a confocal fluorescence microscope (LSM 50, Zeiss) with a 64x oil immersion objective (NA = 1.4), under 488 nm excitation from an argon ion laser. The collected light was separated using a 505 nm long-pass filter, yielding a reflectance image ($\lambda<505$ nm) and fluorescence image ($\lambda>505$ nm). For FRET measurements, the gold nanocavities were filled with rhodamine (10 μM) by sonication for 30 minutes. Contact angle measurements were carried-out using First Ten Angstroms (FTA^0) 200 dynamic contact angle analyser. Capacitance measurements were conducted using a CH Instruments Model 660 electrochemical workstation at a frequency of 527 Hz and using an excitation signal of 5 mV.

5.3 Results and Discussion

5.3.1 Selection of membrane probes

Dimyristoylphosphatidylcholine (DMPC) lipid was used to prepare the spanning lipid bilayers over 820 nm diameter gold cavity arrays. Figure 5.1 shows the structure of DMPC lipid. This is a zwitter ionic lipid with transition a temperature around 23 ℃. This DMPC lipid was selected due to the future application of this platform to study the properties of transmembrane proteins, especially integrin. Previous reports have shown that the integrin can be incorporated efficiently to DMPC/DMPG (1:1 ratio) lipid vesicles with greater homogeneous size distribution.[35] The formation of planar lipid bilayers across the gold nanocavity arrays was carried out using vesicle rupture technique. We selected this technique over painting and LB methods due to the flexibility of the method to incorporate transmembrane proteins into the bilayer.
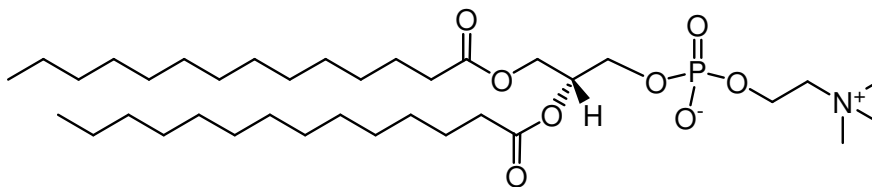

Fig. 5.1: Structure of dimyristoylphosphatidylcholine (DMPC) lipid. The acyl chain forms the hydrophobic part and the glycerol part forms hydrophilic part of the lipid bilayer.

Luminescent membrane probes were important to study the assembly of lipid bilayers at the arrays using confocal microscopy. Membrane probes have two major components: luminophore head and an acyl or alkyl chain. Potential application of the membrane probes includes lipid trafficking, membrane fusion and dynamics of membrane.[36] For a fluorescent membrane probe in liposome, the outer part of the membrane behaves as a polar solvent and the inner part as a non-polar solvent. The location of the fluorescent membrane probe in the lipid bilayer depends on the characteristics of the membrane probe and lipid. The distribution of a probe in the membrane is expected to be randomly distributed throughout the membrane. Here, two types of membrane probes are examined which is a fluorescent membrane probe 5-dodecanoylaminofluorescein (DAF) and long-lived ruthenium membrane probes. Commercially available fluorescent membrane probe DAF has a short fluorescent lifetime and high quantum yield. However, ruthenium was also used widely as a long-lived luminophore to avoid interference in the signal due to

the presence of scattered light and auto fluorescence of short lifetimes.[37] The changes of spectral properties of fluorescent membrane probes in the lipid membrane environment were studied after preparing liposomes with membrane probes as described in Section 5.2.2.

5.3.1.1 Photophysical properties of DAF membrane probe in DMPC lipid

5-dodecanoylaminofluorescein (DAF) is a commercially available fluorescent membrane probe, which contains a C-12 alkyl chain that can intercalate into the hydrophobic part of the lipid bilayer interior. The fluorescent polar part of the membrane probe is expected to lie at the aqueous interface of the DMPC lipid.   The structure of 5-dodecanoylaminofluorescein membrane probe and the predicted orientation of the commercially available fluorescent membrane probe in lipid membrane is shown in Figure 5.2.
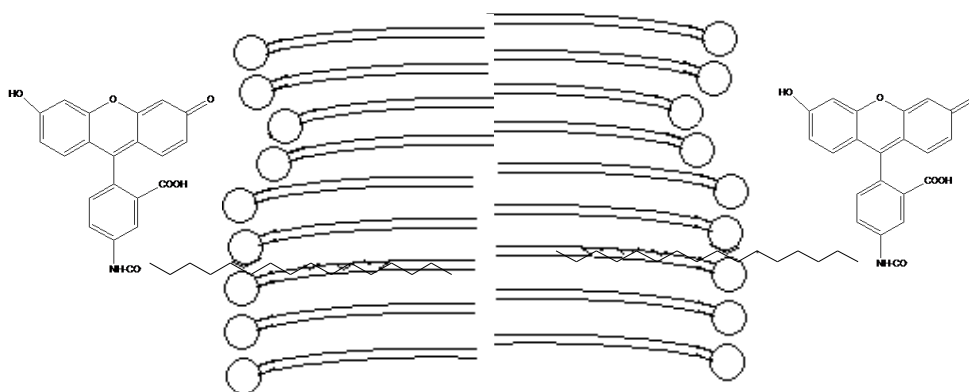

Fig. 5.2: Predicted location of the membrane probe in membrane. The horizontal lines show the non-polar part of the lipid and the circle shows the polar part. The alkyl chain of the probe sits in the hydrophobic region of the bilayer and the polar part of the dye extend out of the membrane.
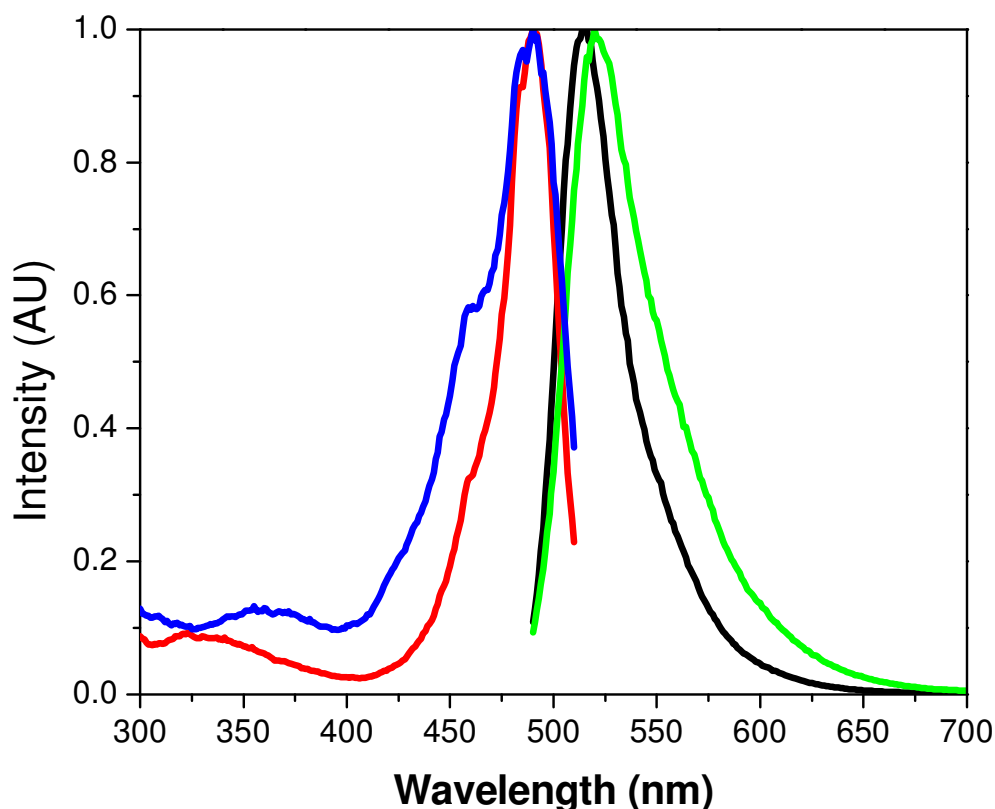
Fig.5.3: Excitation spectra of (Red) 5-dodecanoylaminofluorescein (DAF) dye in 0.1 M PBS buffer (Blue) and DAF in DMPC liposome and emission spectra of (Black) DAF (Green) in buffer and DAF in liposome. The excitation wavelength for the emission was 475 nm. Slit width was 5 nm.

Previous reports have been shown that the photophysical properties of membrane probes can depend on the solvent around the molecule.[33] Excitation and emission measurements were recorded in solution and in liposome for each of the probe explored. Figure 5.3 shows the excitation and emission spectra for 5-dodecanoylaminofluorescein in buffer solution and in liposome. The red and the blue lines show the excitation spectra of DAF in 0.1 M PBS buffer and in liposome solution respectively. The excitation spectra of the fluorescent membrane probe in the lipid environment and in the buffer shows similar absorption maxima but broadening of the spectrum occurs for the probe in the lipid environment. This broadening of spectra usually arises due to the fluctuations of the structure of the solvation shell surrounding the molecule. The resulting variation of the local electric field is caused by the fluctuations of the shell structure leading to statistical distribution of the frequencies of the electronic transition of the molecules and therefore to broadening of the dye spectrum.[33] The unchanged excitation and emission spectra of

the membrane probe suggests that the orientation of the fluorophore might be in the aqueous media above the bilayer. The lifetime of a fluorescent probe in membrane depends on the rigidity of the molecule in the membrane and the oxygen concentration.[38] The concentration of oxygen, which is a well-known quenching agent, is different outside and inside a liposome.[38] Fluorescence lifetime measurements for the dye in PBS buffer and in membrane were carried out to assess the influence of changes in the local environment of the dye. The experimental decay curve was fitted to the following equation,

$$I(t) = I_0 \exp(-t/\tau) \qquad\qquad 5.1$$

where I_0 is the intensity at time 0 and $\tau = (k_r + k_{nr})^{-1}$. After fitting the decay curve to the above equation, the membrane probe, 5-dodecanoylaminofluorescein in buffer shows a lifetime of 4 ± 0.4 ns with a single exponential decay. The membrane probe in liposome shows lifetime around 3.5 ± 0.4ns. The lifetime of the dye in PBS buffer and in liposome are shown in Table 5.1. The fluorescent lifetime of the dye is shorter in liposome compared to dye in buffer. This might be due to the influence of oxygen at the interface of the membrane. In summary, the exact location of DAF membrane probe in liposome was difficult to assess with these measurements. However, the unchanged excitation and emission spectra of the dye suggest that the fluorescent part of the probe might be at the polar part of the lipid.

Membrane probes	Lifetime (ns)			λ_{max} excitation (nm)		λ_{max} emission (nm)	
	Buffer	Liposome		Buffer	Liposome	Buffer	Liposome
		τ_1	τ_2				
DAF	4	3.5		490	490	525	530
[Ru(bpy)$_2$(pic-C$_{16}$)]$^{2+}$	393	944		460	460	610	615
[Ru(dpp)(ahap)]$^{2+}$	181	1360 (70%)	156 (30%)	460	460	625	630

Table 5.1: Photophysical properties of membrane probes in DMPC liposome and in aerated, 0.1 M PBS buffer solution. The lifetime measurements were carried out using 450 nm as an excitation wavelength. The variation in values between experiments was < 10 %.

5.3.1.2 Photophysical properties of $[Ru(bpy)_2(pic-C_{16})]^{2+}$ membrane probe in DMPC lipid

The DAF membrane probe exhibits a very short lifetime but is highly luminescent. However, ruthenium membrane probes are long-lived with low quantum yield so it may be useful to eliminate contribution to luminescent signal from scatter on metal substrates. Therefore, we were also interested in using a long-lived membrane probe, which may be useful in ascertaining longer-lived dynamics of membrane or associated macromolecules. For example, to measure the rotational motions of large proteins or membrane bound proteins requires long lifetime probes ranging from 200 ns to microseconds. Luminescent probes with ruthenium or rhenium also show large Stokes shift allowing detection far from excitation wavelength, which helps to reduce scattering from liposome solution.[37] Therefore, membrane probes, luminescent metal-ligand complex covalently attached to alkyl chain were synthesized in our group. Figure 5.4 shows the structure of $[Ru(bpy)_2(pic-C_{16})]^{2+}$ membrane probe. The complex has a liphophilic tail and the photophysics of the luminophore has been widely reported by our group.[39] The location of the membrane probes in liposomes can be predicted from its structure. It was anticipated that the ruthenium dye will orient with C_{16} tail intercalated in membrane with the 2+ charged metal oriented towards external solution. The spectral properties of dyes in liposome are expected to depend on the localization of the luminophore in the bilayer.
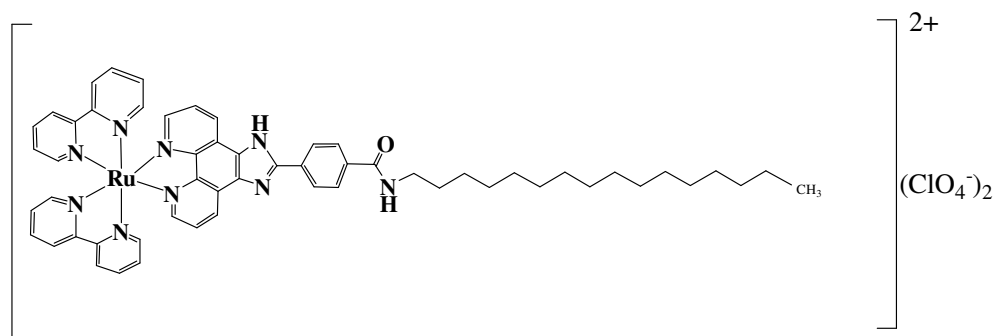

Fig. 5.4: Structure of $[Ru(bpy)_2(pic-C_{16})]^{2+}$ membrane probe. The non-polar alkyl chain lies in the polar part of the bilayer and the head group sits in the polar region of the membrane.

Figure 5.5 shows the excitation and emission spectra of $[Ru(bpy)_2(pic-C_{16})]^{2+}$ dye in DMPC liposomes and in 0.1 M phosphate buffered saline (PBS) buffer at pH 7.4. The black line shows the excitation spectra of the membrane probe in buffer and the blue line

shows the excitation spectra of membrane probe in liposome. The λ_{max} of the excitation spectrum of the dye is centered at 470 nm in PBS buffer an approximately 5 nm blue shift occurs in the excitation spectrum of the dye in lipid environment. The solubility of the membrane probe is low in water therefore the dye molecule is expected to associate strongly in the membrane rather than in buffer. The red line shows the emission spectra of the membrane probe in buffer and the green line shows the membrane probe in liposome. The emission spectrum of the dye in buffer is centered at 610 nm and the dye emits around 615 nm when it is associated with lipid membrane. These small changes in excitation and emission spectrum of dye in both buffer and in liposome suggests that the fluorescent part of the dye located in polar part of the liposome as expected from the structure.
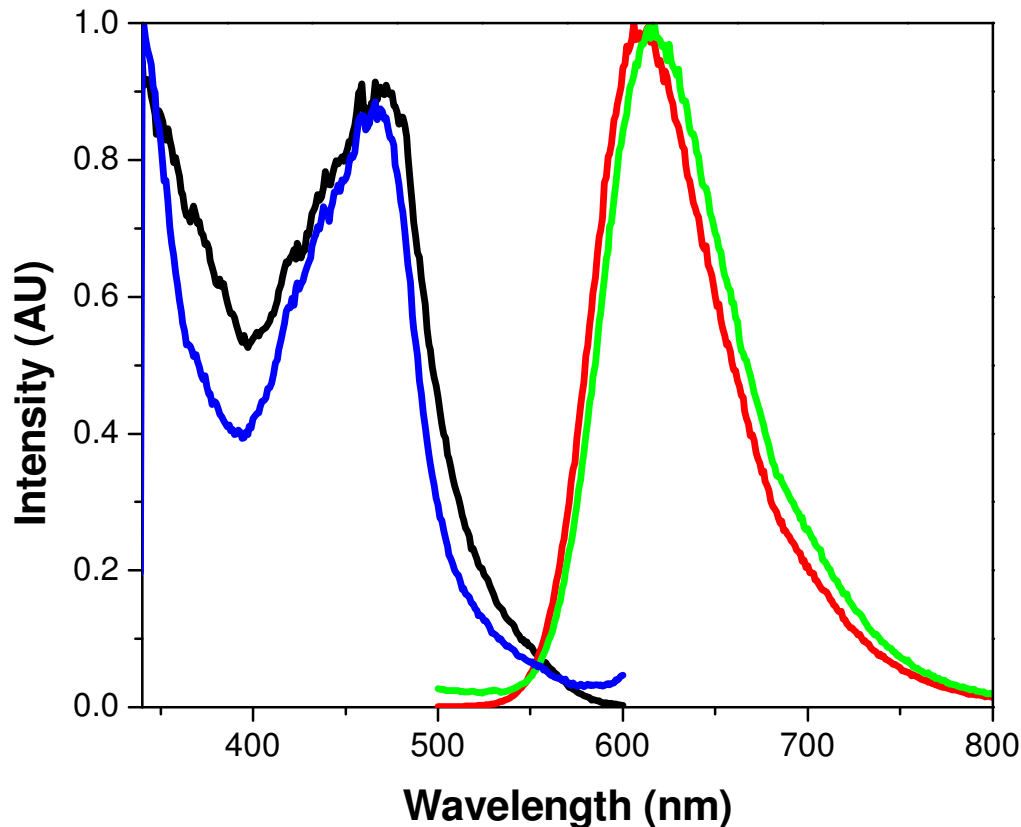

Fig. 5.5: Excitation spectra of (Black) $[Ru(bpy)_2(pic-C_{16})]^{2+}$ dye in 0.1 M PBS buffer (Blue) $[Ru(bpy)_2(pic-C_{16})]^{2+}$ dye in DMPC liposome and emission spectra of (Red) $[Ru(bpy)_2(pic-C_{16})]^{2+}$ dye in buffer and (Green) $[Ru(bpy)_2(pic-C_{16})]^{2+}$ dye in liposome. The excitation wavelength was 450 nm and slit width was 5 nm.

At room temperature, the radial motion of the luminescent membrane probe in lipid membrane is very slow. This slow translational motion of the membrane probes in membrane can affect the lifetime of the probe in lipid environment.[33] Table 5.1 shows the lifetime for the dye in PBS buffer and associated with liposome. The experimental decay curve fits to the Equation 5.1. The lifetime of pure dye was 393±30 ns in buffer with monoexponential decay but in lipid bilayers the lifetime of the membrane probe increased dramatically to 944±50 ns. This increased lifetime of the membrane probe is probably due to the restricted motion of the probe on association with the membrane. Previous reports have shown that luminescent metal-ligand complexes display lifetimes approximately 2.3 μs when bound to proteins.[37] Lakowicz reported that Ru(bpy)$_2$(mcbpy) complex (mcbpy is 4-methyl,4′-carboxylic acid-2,2′-bipyridine) attached to phosphatidylethanolamine (PE) in DPPG vesicles show lifetimes from 682 ns at 2 ℃ to 357 ns at 53 ℃.[37] The report revealed that metal-ligand complex probes are only moderately sensitive to dissolved oxygen therefore; removal oxygen is not needed for these probes. Their steady state anisotropies of Ru-PE in DPPG vesicles revealed that the luminophore is localized at the lipid-water interface. Briefly, here the unchanged excitation and emission spectra of luminescent membrane probe indicate the orientation of fluorophore in the polar part of the lipid whereas the lifetime of the dye is dramatically increased suggests the restricted motion of the membrane probe in lipid bilayers than in solution. In future, anisotropic decay measurements from this membrane probe in DMPC liposomes can provide more details about the rotational motion of the luminophore in membrane.

5.3.1.3 Photophysical properties of [Ru(dpp)$_2$(NH$_2$phenC$_{16}$)]$^{2+}$ membrane probe in DMPC lipid

An alternative ruthenium probe was explored in which the luminophore centre is hydrophobic unlike pic, which is hydrophilic. Figure 5.6 shows the structure of this second ruthenium membrane probe, [Ru(dpp)$_2$(NH$_2$phenC$_{16}$)]$^{2+}$ where dpp is diphenylphenanthroline and NH$_2$phenC$_{16}$ (16-(acetylthio)-hexadecanyl amidophen-anthroline). Liposomes were prepared using DMPC lipid with ruthenium membrane probe as described in Section 5.2.2. Figure 5.7 shows the confocal microscope image of the [Ru(dpp)$_2$(NH$_2$phenC$_{16}$)]$^{2+}$ membrane probe incorporated into liposome. The image reveals that the membrane probe is associated with lipid membrane as background luminescence is negligible. The size of the liposome was around 2 μm although the liposome was prepared after extrusion of liposome through 100 nm diameter filter. The particle size distribution histogram reveals that the size distribution of liposome was heterogeneous (100 nm – 3 μm). Extrusion of lipids through the polycarbonate filters is expected to produce liposomes in homogeneous size however, membrane probe incorporated liposome different sizes, and this might be due to the rupturing and reformation of liposomes after extrusion.
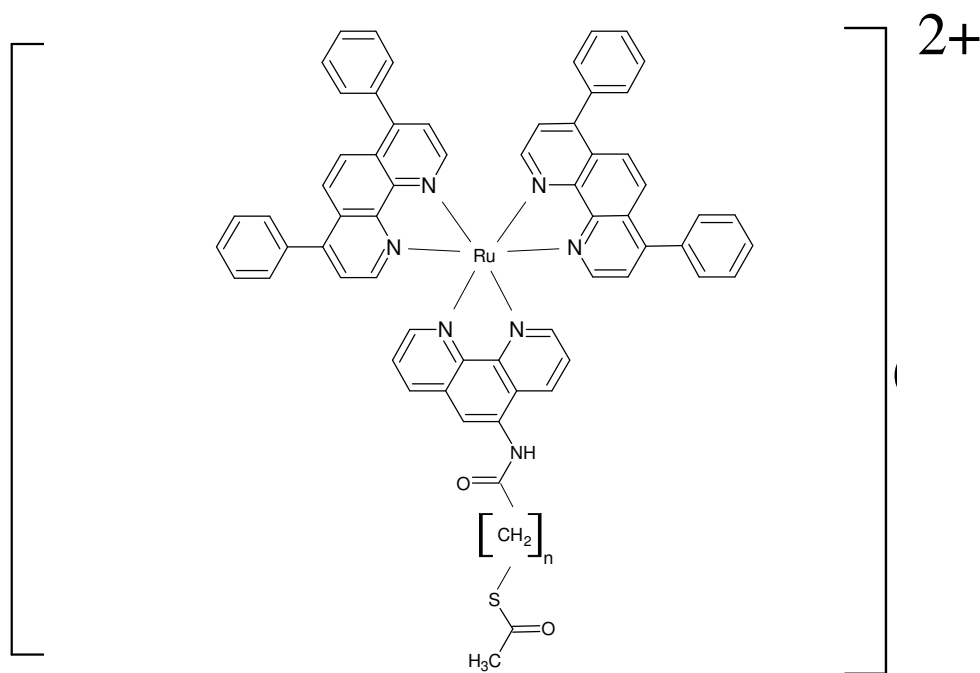

Fig. 5.6:   Structure of Ru (diphenylphenanthroline)$_2$ (16-(acetylthio)-hexadecanyl amidophenanthroline)(PF$_6$)$_2$ membrane probe and n = 16.
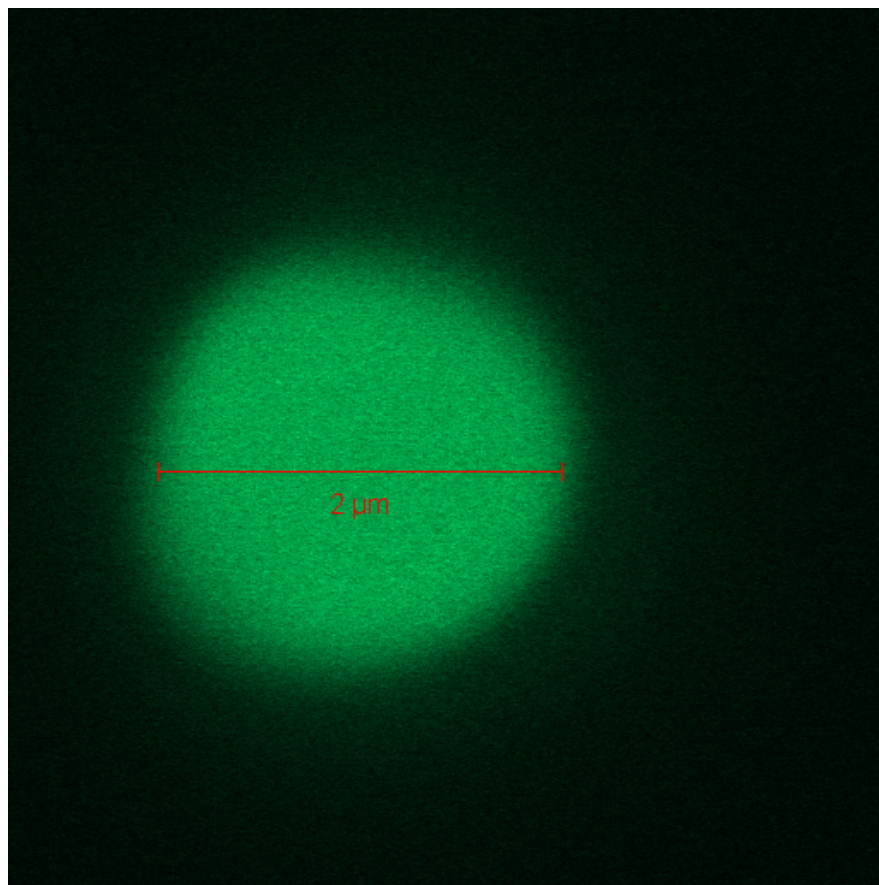
Fig. 5.7: Confocal microscope image of $[Ru(dpp)_2(NH_2phenC_{16})]^{2+}$ membrane probe incorporated in DMPC liposome. Excitation wavelength was 488nm.

This $[Ru(dpp)_2(NH_2phenC16)]^{2+}$ membrane probe exhibits a MLCT absorbance transition around 470 nm in buffer and this is unaltered in lipid membrane as shown in Figure 5.8. This dye shows emission around 625 nm in buffer but in membrane the emission peak is red shifted by around 5 nm to 630 nm (Figure 5.9). As for ruthenium pic the absorption and emission peaks are well separated from each other and this large separation is an advantage for a membrane probe because membrane suspensions usually scatter light, which is more easily removed when the excitation wavelength separated from the emission.
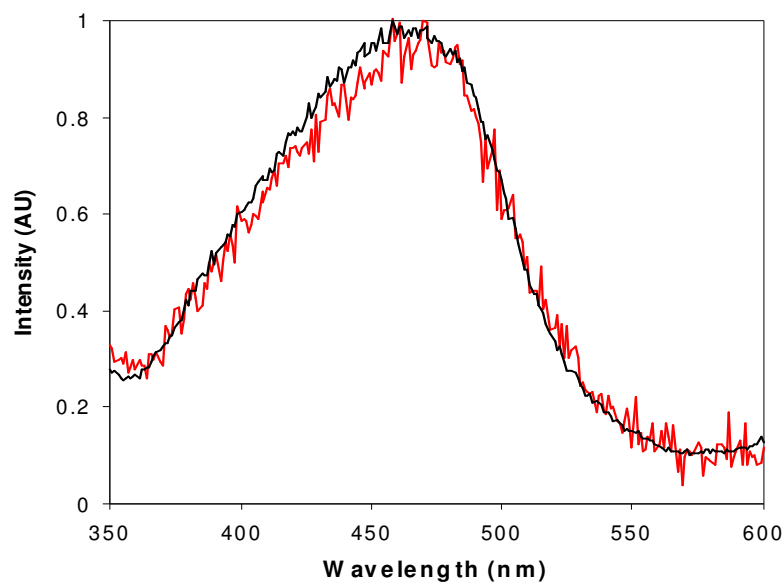
Fig. 5.8: Excitation spectra for (——) $[Ru(dpp)_2(NH_2phenC_{16})]^{2+}$ membrane probe in 0.1 M PBS buffer and (——) the membrane probe in liposome membrane.   The slit width was 5 nm.
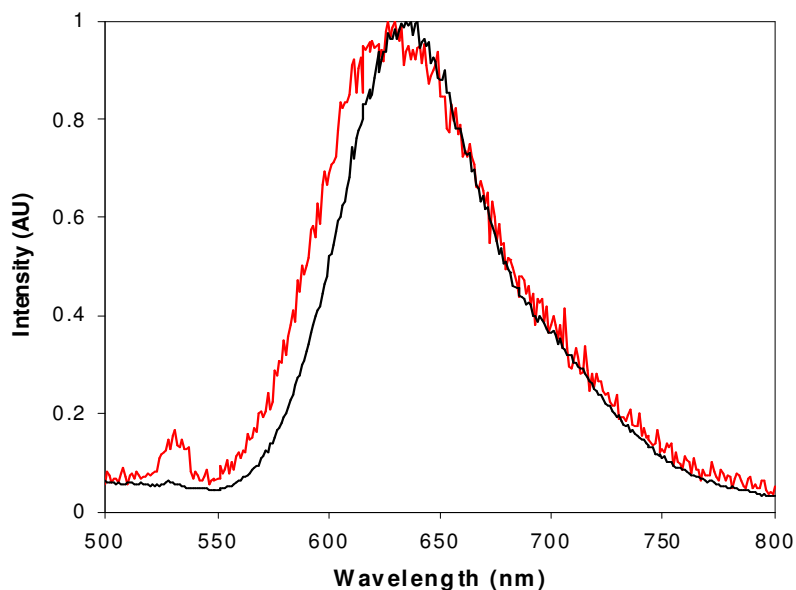
Fig. 5.9: Emission spectra for (——) $[Ru(dpp)_2(NH_2phenC_{16})]^{2+}$ membrane probe in 0.1 M PBS buffer (——) and the membrane probe in liposome membrane. The excitation wavelength was 450 nm with slit width 5 nm.

The lifetime measurements of the membrane probe associated with liposome shows interesting results as shown in Table 5.1. The lifetime of the ruthenium membrane probe in aerated solution was around 181±15 ns. The dye associated with liposome decays

biexponentially with lifetimes of 1366±60 ns and 156±13 ns. The shorter component is thought to arise from free dye molecule in the background solution. Whereas, the lifetime of the dye is increased by an order of magnitude in the membrane environment. This increase in the lifetime may be due to the structural rigidity of the molecule in membrane. In deaerated solution, the lifetime of the complex was around 3 μs and as discussed earlier, the dye in membrane shows the lifetime around 1.3 μs.

In summary, three membrane probes were explored to assess which would be best suited to study arrays. The changes in the lifetime of the fluorescent and luminescent membrane probes in the liposome indicate that all three probes associated with membrane, the viscosity of the membrane influences the rotational motion of the probe. The unchanged emission spectra of the dye indicate that the fluorescent part of the dye remains located in buffer as expected from the structure. The confocal microscope image of the liposome confirms that the membrane probe is located at the membrane and the background fluorescent signal was negligible indicating the absence of dye in the solution. In the following section, the spanning of lipid bilayers across gold nanocavity array was confirmed using high quantum yield commercially available DAF membrane probe. However, as discussed in the previous section long lived luminescent membrane probes can also be useful to study the rotational motion of macromolecules such as proteins.

5.3.2 Spanning of planar lipid bilayers by vesicle rupture technique

There are several methods available to prepare planar lipid bilayers on different substrates, which include painting, vesicle rupture technique, and Langmuir-Blodgett technique.[40,41,42,43] In this work, the spanning of lipid bilayers across dried and prefilled gold nanocavity arrays was investigated using a vesicle rupture technique. This technique is selected due to the ability of this method to permit the reconstitution of transmembrane proteins in the lipid bilayer. Liposomes with and without dye were prepared as described in Section 5.2.2. To investigate the potential for lipid bilayers to span the cavity openings, two methods of bilayer preparation were developed. The first approach involved sonicating the nanocavity array in the aqueous liposome solution, without prefilling of the cavities (i.e. dry cavities). In the latter case, the dried gold nanocavity arrays were dried by sonicating the slide in acetone for 5 minutes after dissolving polystyrene spheres in THF in order to remove trapped THF inside the cavity. Then, the slides were dried under a stream of nitrogen and stored in a Petri dish. Therefore, it was expected that the voids were filled with air prior to exposure as shown in Scheme 5.1 (A). The second approach involved prefilling of the cavity arrays with 0.1 M PBS buffer, by sonication before exposing the array to the liposome solution. Scheme 5.1 (B) shows the schematic representation of the buffer prefilled arrays. The prefilled or dry cavity arrays were then sonicated in liposome solution. The resulting lipid layers assembled on the gold nanocavity arrays were characterized then using electrochemical methods and advanced fluorescence microscopy.
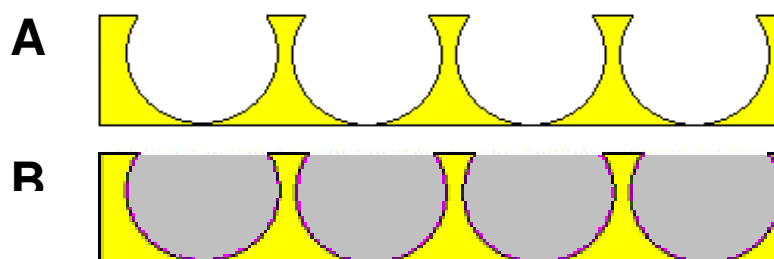
Scheme 5.1: Schematic of (A) dried and (B) prefilled gold nanocavity arrays. The yellow colour represents deposited gold and the ash color represents buffer.

5.3.3 Lipid assembly

Confocal microscopy is a versatile method to study arrays as demonstrated in Chapter 2. Therefore, liposomes were prepared with membrane probes and examined the liposome treated dried and prefilled arrays using confocal microscopy. As discussed in Section 5.2.2, liposomes were prepared using DMPC lipid after incorporating the fluorescent membrane probe, 5-dodecanoylaminofluorescein (DAF) which shows emission around 520 nm. This membrane probe was preferred compared to previously discussed ruthenium membrane probes due to the high quantum yield of the dye, which enable to distinguish the assembly of lipid bilayers on both dried and prefilled arrays. In addition, fluorescein is a well-studied molecule for FRET therefore this DAF membrane probe permits to study FRET on gold nanocavity arrays using suitable FRET pair.

Fluorescence images were collected using confocal microscopy after the assembly of DAF incorporated liposome onto both the prefilled and dried arrays. Figure 5.10 B and D show the confocal fluorescence images of the dried cavity arrays before and after sonication in aqueous liposome solution respectively, while Figure 5.10 A and C show the reflectance images of the dried cavity arrays, before and after the treatment with DAF modified lipids. The measurements were carried out using a 488 nm excitation laser line with 0.1 M PBS buffer solution between the lipid treated array and the cover glass. The fluorescence from the lipid treated arrays was collected using a 514 nm long pass filter which cuts off light below 514 nm and the reflectance from the sample is collected below 505 nm. The reflectance from the lipid treated arrays was collected since this permits the selection of defect free region of gold nanocavity arrays. Moreover, critically it reveals the presence of the nanocavity pattern underneath the fluorescence in case of the prefilled array.

Control measurements were carried out using identical experimental conditions before the arrays were modified with lipids to compare the difference in fluorescence intensity as shown top images (A&B) in Figure 5.10. The reflectance images show the presence of the ordered patterned nanocavity array in the region of investigation. As expected the fluorescence images show negligible signal intensity from dried arrays before treatment with liposome as shown in Figure 5.10 B. As shown in Figure 5.10 D, a localized fluorescence is observed from the dry cavity array after treatment with the liposome

solution under 488 nm excitation and the reflectance image (Figure 5.10 C) can be clearly superimposed on the fluorescence image, verifying that the fluorescence is arising from a region coincident with the individual cavities. When the dried gold cavity arrays are treated with liposome solution, a number of different ways of assembly of lipid bilayers is expected. The first one is that, the bilayers can span across the arrays on top of air filled arrays and the second expected way is the filling of liposome solution inside the cavity and span multilayer of lipid layers on top of the arrays. Another possible way of assembly is the formation of continuous lipid bilayers at the interior cavity walls as well as at the edges of the array. The confocal fluorescence image shown in Figure 5.10 shows a highly localized fluorescence from the lipid treated dried arrays, which rules out the first two possibilities. Since, if these were occurring then a homogeneous fluorescence image expected to be seen from these arrays. The cavity like fluorescence image observed suggests that lipid is assembled at the interior cavity walls as well as at the edges of the dry cavity arrays. Z-stack images show that (data is not shown) the fluorescence and reflectance from the lipid treated dried arrays started to be visible at the same slice which suggests the formation of lipid assembly at the walls of the array. The resolution of the confocal fluorescence microscope in z-direction is 700 nm therefore, the Z-stack measurement was not a proper measurement to study the assembly of lipid bilayers, which has a thickness 6 nm. As discussed in Chapter 3, most of the enhancement in gold nanocavity arrays arises from the top surface than the interior walls. If the enhancement in signal intensity arises from the top surface, it would be expected to see an inverse of the fluorescence image (Figure 5.10 D) for lipid treated dried arrays. i.e., higher intensity in fluorescence should be observed at the top surface than the inside walls. However, the spanning of liposome was carried out across the 820 nm diameter arrays due to the requirement of bigger void volume for the future applications. As discussed in Chapter 3, the gold nanocavity arrays with this diameter show only 3 fold enhancement at the top surface than the interior walls of the array. Therefore, the discrimination in the fluorescence image is rationalized to be due to the higher concentration of dye in the bilayers at the interior cavity walls.
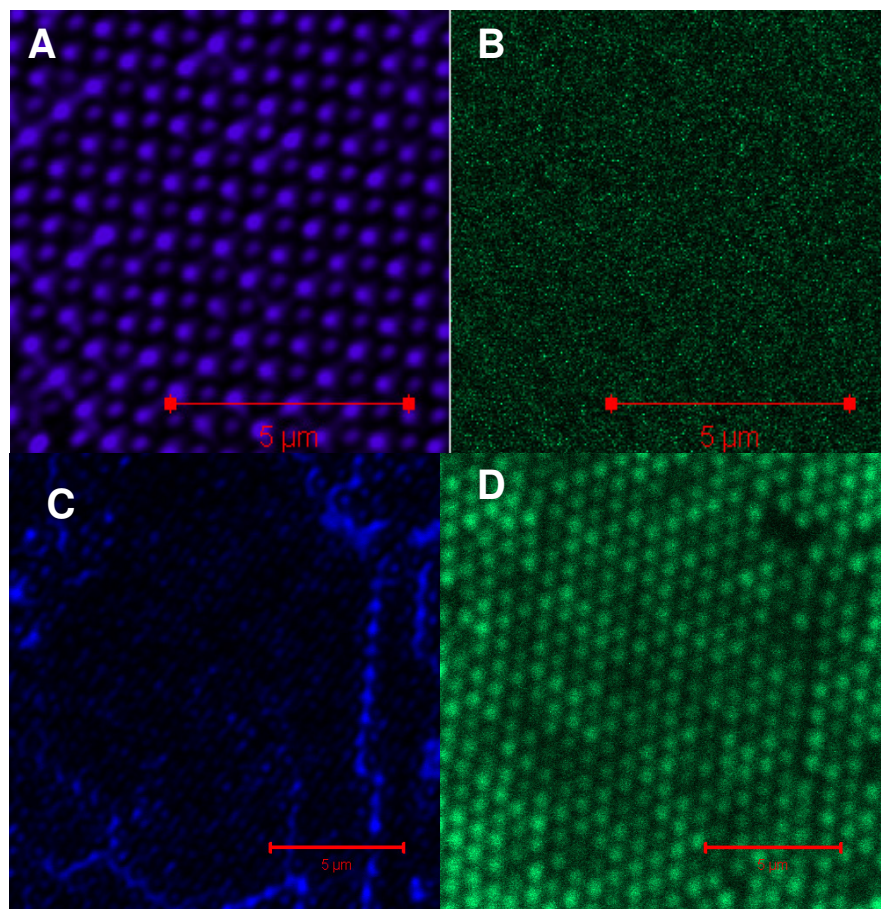
Fig. 5.10: Confocal microscope images of 820 nm diameter dried gold nanocavity array (top) before and (bottom) after treated with DAF incorporated liposome. The excitation wavelength was 488 nm. The collected light is separated using 505 nm filter yielding fluorescence (above 505 nm: B & D) and reflectance images (below 505 nm: A & C). Both fluorescence and reflectance images were taken simultaneously from the same region of the sample using two different channels. The measurements were carried out using 63x oil immersion objective with numerical aperture 1.4.

Figure 5.11 shows the confocal fluorescence images of buffer prefilled arrays before and after modification with DAF incorporated liposomes. Figure 5.11 (A) and (B) show the reflectance and fluorescence images of 820 nm diameter gold cavity which were filled by sonication with 0.1 M PBS buffer and Figure 5.11 (C) and (D) show the reflectance and fluorescence images of the prefilled arrays after treatment with DAF incorporated liposome. The confocal fluorescence image of the buffer prefilled array before treatment with liposome shows no fluorescence signal, as expected, whereas interestingly, a homogeneous, continuous fluorescence is observed from lipid treated prefilled arrays as

223
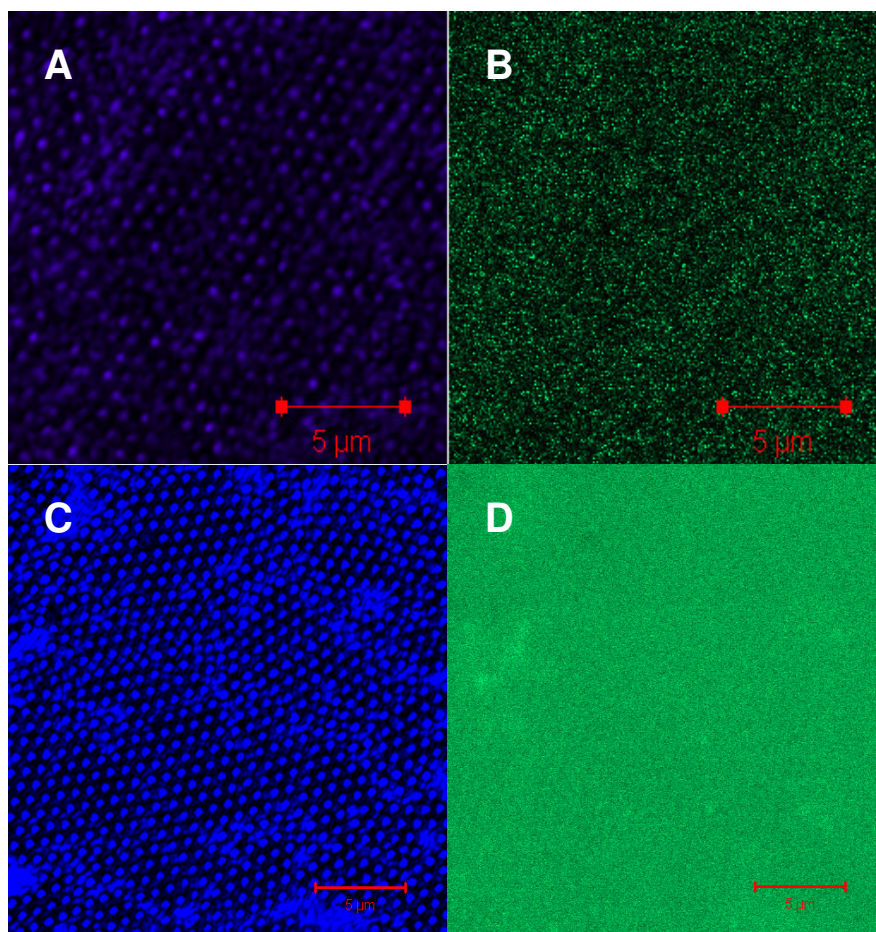
Fig. 5.11: Confocal microscope Images of buffer prefilled gold nanocavity (top) before and (bottom) after sonicating in DAF incorporated liposome. The collected light is separated using 505 nm filter yielding fluorescence (above 505 nm: B & D) and reflectance images (below 505 nm: A & C). Both fluorescence and reflectance images were taken simultaneously from the same spot of the sample using two different channels. The excitation wavelength was 488 nm. The measurements were carried out using 63x oil immersion objective with NA 1.4.

shown in Figure 5.11 D. The reflectance image for the same array confirms the presence of the gold nanocavities. Remarkably, the fluorescence image of the dye incorporated liposome treated prefilled arrays are completely different from the liposome treated dry arrays. This homogeneous fluorescence from the lipid treated prefilled array is attributed to the spanning of lipid bilayers across the top of buffer prefilled arrays. The spanned lipid bilayers were unstable in dry conditions; therefore, all the experiments were conducted in solution phase. In confocal experiments, buffer solution was used in between the cover glass and the spanned lipid bilayers. If the spanned bilayers (lipid

bilayers formed on top of prefilled arrays) were allowed to dry then, the homogeneous fluorescence disappeared. Instead, the lipid bilayers appeared to collapse and the fluorescence images became similar to Figure 5.10 D. After bleaching of collapsed spanning lipid bilayers (after dried out the layers), the recovery of fluorescence was not observed which reveals that the lipid layer was immobile. Z-stack measurements from prefilled arrays after drying show fluorescence arising from the cover glass as well as from the walls of the cavity which suggests that the spanned bilayers were not stable at dry conditions. Stienem et al. prepared lipid bilayers across porous alumina and silicon substrates. They deposited a thin film of gold on top of the pores to enable selective modification with polyethylene glycol. Then, spanned bilayers were formed across the pores using a vesicle fusion technique. The confocal fluorescence images of their spanned lipid bilayer on the porous arrays look very similar to Figure 5.10 D. They reported that the discrimination in the image might be due to the quenching of fluorescence from the gold at the top surface. However, in our case as discussed in Chapter 3 the top surface provides greater enhancement in emission intensity for monolayers of ruthenium dye. Therefore, a direct comparison of spanned lipid bilayers on different platforms is complicated. In summary, the confocal microscope images of the lipid treated both dried and prefilled arrays suggests the formation of spanning lipid bilayer on top of prefilled arrays whereas in the case of dried arrays the assembly of lipids occurred at the interior walls of the array.

5.3.3.1 Lipid assembly on selectively modified prefilled arrays

Confocal fluorescence microscope images reveal that the spanning lipid bilayers are continuous without defects over micrometer areas on top of prefilled arrays. In order to improve the surface coverage and film quality, the top surface of the gold nanocavity arrays were selectively modified with three different surface-active molecules. The species chosen for functionalizing the top surface were hydrophobic, modestly hydrophilic and highly hydrophilic: they were 11-mercapto undecanoic acid, polyethylene glycol (PEG), and alkane thiol (C_9SH) respectively. As discussed in Chapter 3, nanosphere lithography allows selective modification of the top surface and inside the cavity, as shown in Scheme 3.1. The selective modification of the top surface of the arrays was confirmed using Raman measurements as discussed Section 3.3.1. Figure 5.12 shows the confocal fluorescence images of spanned lipid bilayers formed on top surface modified gold nanocavity arrays. The green colour images show the fluorescence from spanned lipid bilayers and the blue colour images show the reflectance from the gold nanocavity arrays. Figure 5.12 (A) shows the fluorescence and reflectance from spanned lipid bilayers across the top surface modified with 11-mercapto undecanoic acid arrays. Similarly, Figure 5.12 (B) and Figure 5.12 (C) show the spanned lipid bilayers across PEG modified and alkyl thiol modified arrays.
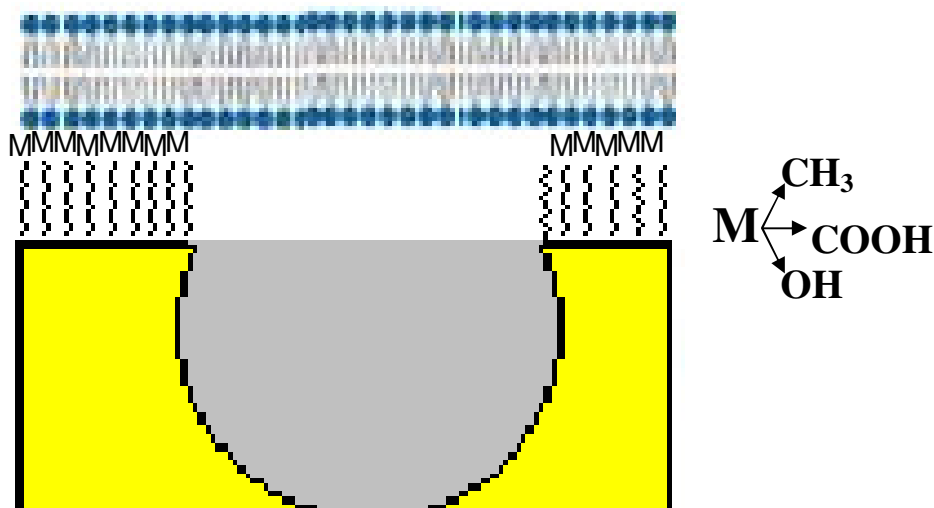
Scheme 5.2: Schematic representation of lipid bilayers formed on top surfaces selectively modified gold nanocavity arrays. The top surface of the gold array modified with, M = CH_3 (C_9SH), M = COOH (11-mercapto undecanoic acid) and M = OH (polyethylene glycol).
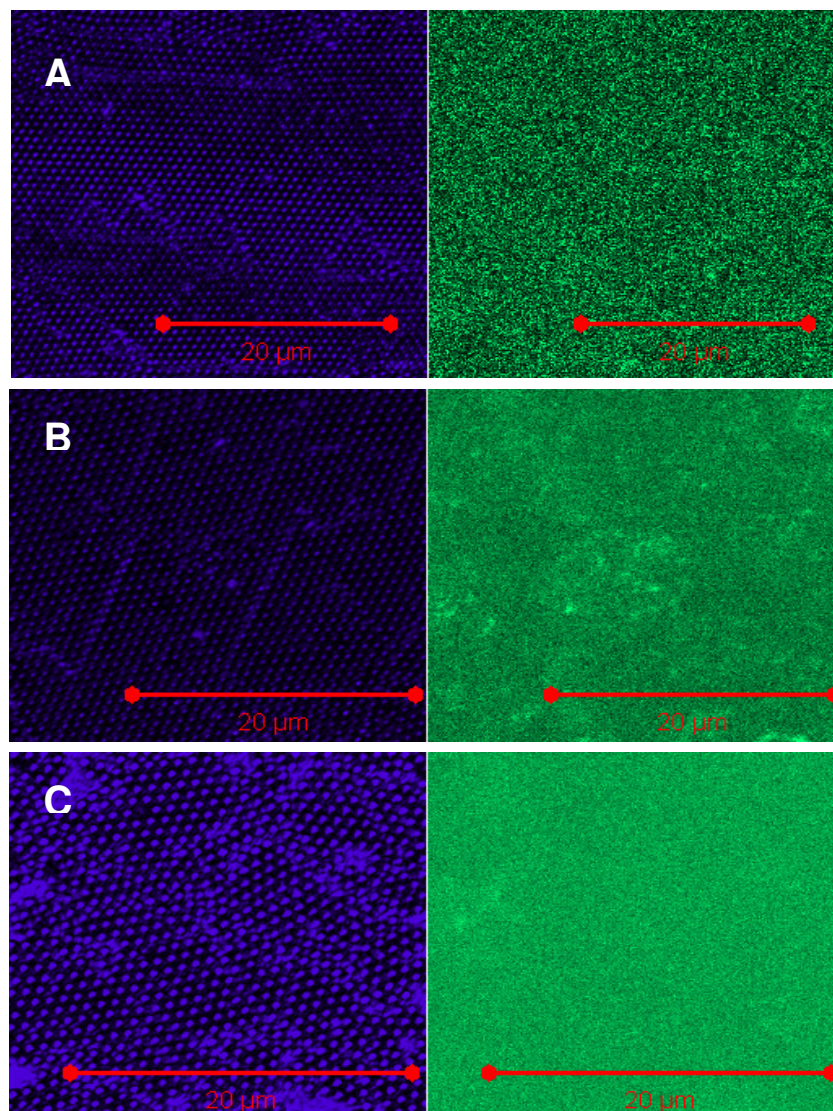
Fig. 5.12: Confocal microscope images of spanned lipid bilayers on top of selectively modified 820 nm diameter arrays (a) 11-mercapto undocanoic acid (B) Polyethylene glycol (PEG) (C) alkane thiol (C_9SH). The green colour images show the fluorescence channel and the blue colour images show the reflectance from gold nanocavity arrays. The excitation wavelength was 488 nm. The fluorescence and reflectance images collected from the same spot of the sample simultaneously using two channels.

It was expected that, the lipid bilayers would span uniformly over largest area when the substrate is hydrophilic. These three different molecules change the surface properties of the substrate. Therefore, the bilayers spanned over PEG modified array is expected to show large area of lipid bilayers without defects. Clearly, the difference between the

fluorescence channel images for selectively modified arrays was negligible for spanning of lipid arrays, which indicates minimum influence of surface modification on spanning. As discussed in Chapter 3, the surface area of the interior walls of the array was six times greater than the area of the top surface of 820 nm diameter arrays. In the case of prefilled arrays, the interior surface area is inaccessible and therefore, the formation of spanned lipid bilayers is considered as a two dimensional plane on top of gold nanocavity arrays. In that two dimensional area, around 80 % is aqueous phase because it is filled with buffer and the rest of the area is gold. This might be the reason for less impact of selective modification of the top surface on spanning of lipid bilayers across the array. In summary, the selective modification with different molecules did not make much difference in spanning of lipid bilayers across prefilled gold nanocavities. However, this selective modification with different molecules can act as a support for transmembrane proteins, which can avoid the direct contact of transmembrane protein with the metal surface. The spanning lipid bilayers on top of gold nanocavity arrays were stable in aqueous phase but collapsing of the bilayers occurs when the slide dries out even after the selective modification of top surface. Further experiments were conducted without selective modification of the arrays in the following sections.

5.3.3.1 Mobility of lipid in spanning lipids

The contrast between the fluorescence images of assembly formed on prefilled and dried substrates suggested that lipid bilayers form a continuous film on the former by spanning the fluid filled aperture but a lipid layer coats at the internal pore surface of the array in the latter case. If these interpretations are the case, we might expect a difference in lipid mobility in each instance. It was expected that if the bilayer is in direct contact with gold nanocavity array, the lateral mobility of the lipids might be considerably lower than where the lipid is suspended above the fluid filled array. Therefore, fluorescence recovery after photobleaching (FRAP) was undertaken to measure lateral mobility of lipid and to identify if there was any difference in this mobility between lipid assembled on dry or prefilled cavities. FRAP is a widely used method of studying lateral mobility of lipid bilayers it involves the irreversible photo-bleaching of fluorophore in a probe region by introducing a pulse of very intense light and then measuring the fluorescence recovery of the bleached area.[44,45,46] The recovery of fluorescence occurs due to the diffusion of molecules from the unbleached area to the bleached region. The analysis of the rate of recovery of fluorescence after photo bleaching can provide quantitative information about the diffusion rate of the lipid molecules.

Here, the lateral mobility of lipid bilayers on the prefilled cavity and dried nanocavity were studied using fluorescence recovery after photo bleaching of the DAF membrane probe. Fluorescence images of the photobleach and recovery of the lipid treated prefilled gold cavity are shown in Figure 5.13 A, B, C and Figure 5.13 D shows the fluorescence recovery curve with the best fit of this curve to Equation 5.2 (R^2 = 0.99). This equation is applicable to two dimensional diffusion of molecules to a circular bleached spot from a plane or a line source.[47] In this experiment, the spot size was 2 µm. The following equation fits the experimental recovery of the photo-bleached dye:

$$I(t,r) = I_0 - \frac{M}{(4\pi Dt)^{d/2}} \cdot e^{\frac{-r^2}{4Dt}} = I_0 - A(t) \cdot e^{\frac{-r^2}{4Dt}} \tag{5.2}$$

where I and I_0 are the fluorescence intensity after and before bleaching respectively. M is the fluorescence intensity corresponding to the bleached fluorophore; D is the diffusion coefficient; and r is the radial coordinate in nanometres. From this fit, a diffusion coefficient of 0.80 ± 0.07 $\mu m^2.s^{-1}$ was obtained for the spanning bilayers on top of the prefilled array. This value is comparable to literature values for diffusion of lipids in

planar membranes ($D \approx$ 0.1-1 $\mu m^2.s^{-1}$). For example, Hook and co-workers reported a diffusion coefficient of 0.99 ± 0.03 $\mu m^2.s^{-1}$ for supported rhodamine labelled DHPE lipids on SiOx encapsulated gold holes.[27] Figure 5.14 shows the fluorescence recovery curve after photobleaching of DAF on liposome treated dried gold nanocavity array. The bleach showed very slow recovery by comparison with spanned lipid bilayers and fitting to the Equation 5.2 yield a diffusion coefficient of 0.04 ± 0.01 $\mu m^2.s^{-1}$. Therefore, the mobility of lipid bilayers on the dried gold nanocavity array is over an order of magnitude lower than the spanned bilayers on top of prefilled arrays.
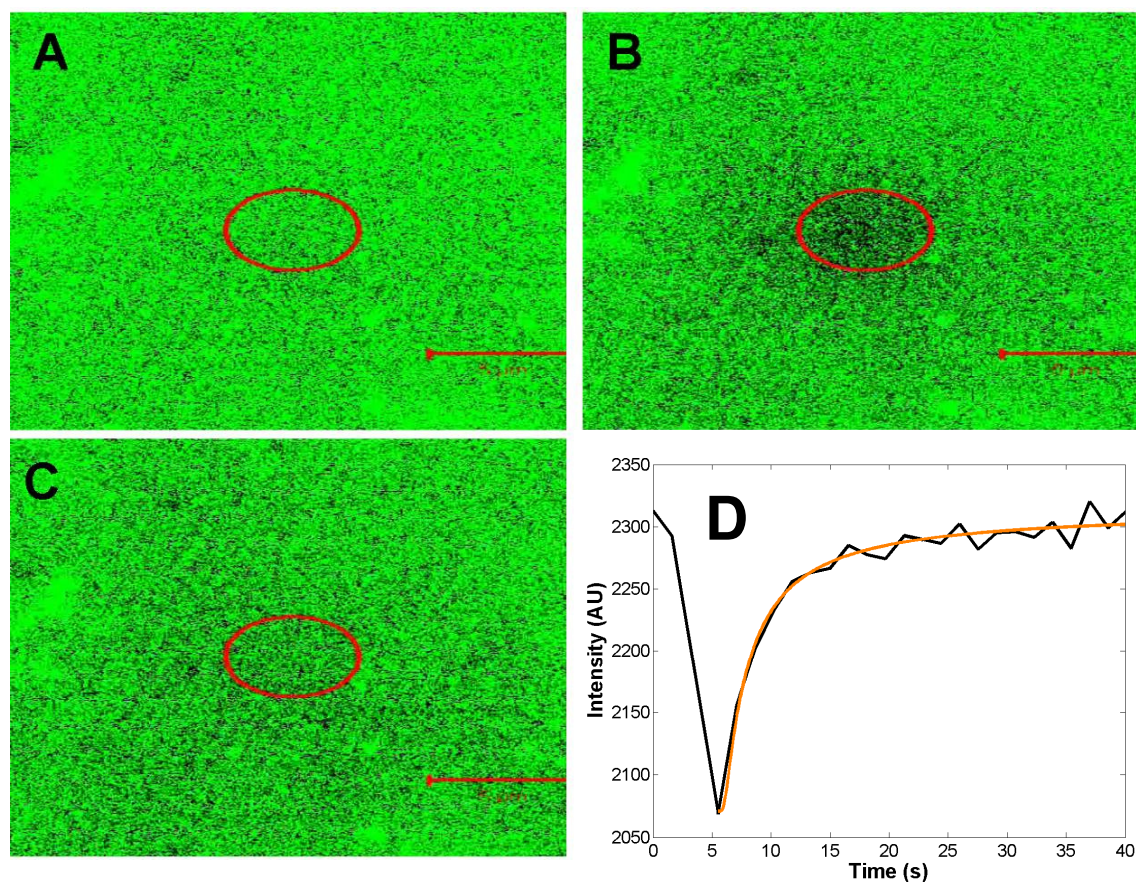

Fig.5.13:   Fluorescence images were taken during FRAP experiment: (A) before bleaching the fluorophore, (B) after bleaching and (C) after the fluorescence recovery. The red circle indicates the bleached area. (D) depicts the fluorescence recovery curve where the red line is the best fit of Equation 5.2 ($R^2 = 0.99$).

The lower diffusion coefficient for lipid treated dry arrays suggests that the lipid forms an interfacial layer on the surface of the array. The other possibility for reduced diffusivity might be due to the high curvature of spherical cavity walls. Steinem and co-workers have formed lipid bilayers across porous alumina and silicon substrate using a painting method. They used 1,2-diphytanoyl-*sn*-glycero-3-phosphocholine (DPhPC) lipid mixed

with Texas red labelled DHPE (1,2-dihexadecanoyl-*sn*-glycero-3-phosphoethanolamine) for FRAP studies. From which they have reported a diffusion coefficient of 10.9±0.7 $\mu m^2.s^{-1}$ for lipid bilayers formed across 7 μm silicon pores. However, in our study the spanned lipid bilayers across prefilled 820 nm diameter gold nanocavity arrays show a D ≈ 0.80±0.7 $\mu m^2.s^{-1}$ and this discrimination in the diffusion coefficient is probably due to the large surface of gold at the rim for smaller 820 nm arrays than porous silicon substrate.
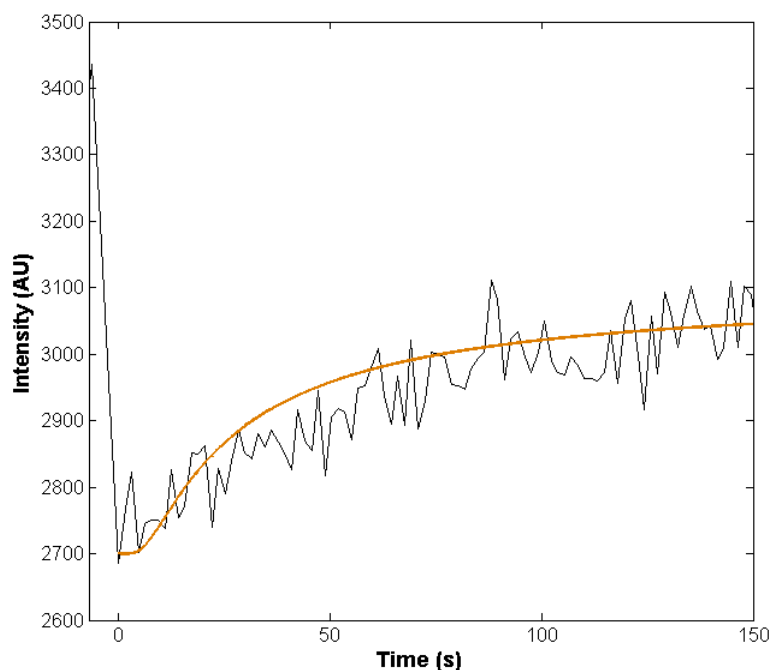

Fig. 5.14: Fluorescence recovery curve after photobleaching of dried gold nanocavity arrays after treated with DAF incorporated liposome. The black curve is the experimental data and the red line is the best fit of Equation 5.2 ($R^2 = 0.89$)

Another key observation is that the fluorescence recovery curve (Figure 5.13 D) for spanned lipid bilayers formed on top of prefilled arrays shows 100 % recovery of the fluorescence signal, which suggests that the spanned lipid bilayers were highly mobile on top of filled arrays. Whereas, the fluorescence recovery curve for lipid bilayers assembled on dried gold nanocavity arrays shows that only 50 % of the lipids were mobile. This difference in mobility of the lipid bilayers on dried and prefilled arrays indicates that lipid bilayers spanned on top of buffer filled arrays and in the case of dried arrays the lipids are in direct contact with gold surface. The 50 % mobile fraction of the dried arrays suggests that the lipid bilayers are collapsed into the cavity and bilayers formed on the interior cavity walls. In summary, the FRAP measurements indicates that

231

the lipid bilayers are in direct contact with cavity surface when the dried arrays treated with liposome solution and in the case prefilled arrays consistent with the continuous fluorescence, the lipid bilayers appeared to be spanned across the apertures once filled with PBS buffer as shown in Scheme 5.3.
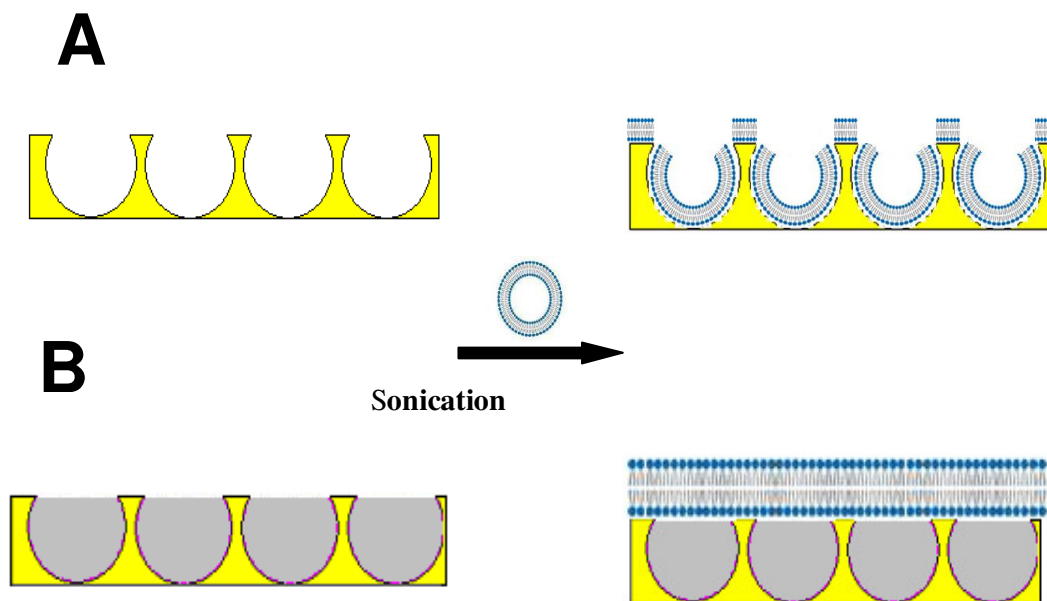
Scheme 5.3. Schematic representation of (A, left) dried nanocavity (A, right) after sonication of nanocavity with liposome. (B, left) buffer filled nanocavity and (B, right) buffer prefilled gold nanocavity array after sonication with liposome.

5.3.4 Contact angle measurements
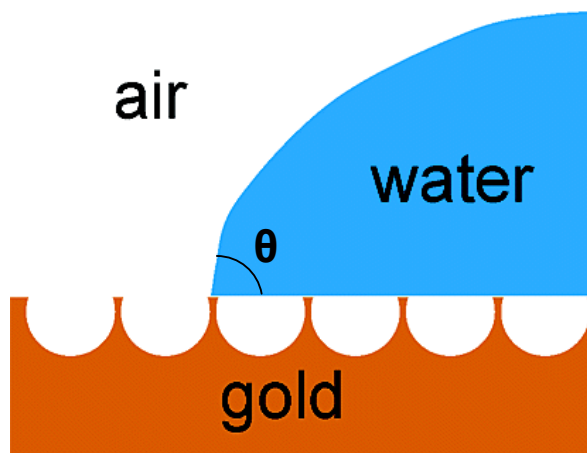
Scheme 5.4: Schematic representation of contact angle measurement for gold nanocavity arrays. *Taken from Abdelsalam et al., Langmuir, 2005, 21, 1753.*[48]

Contact angle measurements are widely used to study the surface properties particularly the hydrophilicity or hydrophobicity and wettability of solid substrates. The contact angle experiments measures the angle at the three-phase boundary (air, solvent and substrate) of a substrate. The three phase boundary is shown in Scheme 5.4. Several reports have shown that the hydrophilicity of nanocavity array substrates of this type depend on the surface structures and dimensionality.[48] For example, Baumberg and co-workers have shown that the contact angle of gold nanocavity arrays can be changed from 70° to 130° by changing the thickness of the gold nanocavity arrays.[48] The changes in the wettability of these substrates were attributed to the contact of water with air trapped inside heterogeneous substrate.

Fluorescence measurements of the lipid treated dry and prefilled gold nanocavity arrays reveal that spanning of lipid bilayer occurred on top of buffer filled arrays which results in creation of a homogeneous surface on top of prefilled gold nanocavity arrays. However, in the case of dried arrays the lipid was assembled at the interior walls of the arrays results the formation of a heterogeneous surface. In order to understand the role of surface wettability on this observation contact angle measurements were carried out for both lipid treated buffer prefilled and dry cavity arrays. It is expected that a difference in contact angle will occur between the lipid treated dried and prefilled arrays due to the

heterogeneity of the surface. Figure 5.15 shows contact angle measurements for dried and prefilled gold nanocavity arrays before and after treatment with liposome. In control experiment (Figure 5.15 A and C), the contact angle for the buffer prefilled cavity array
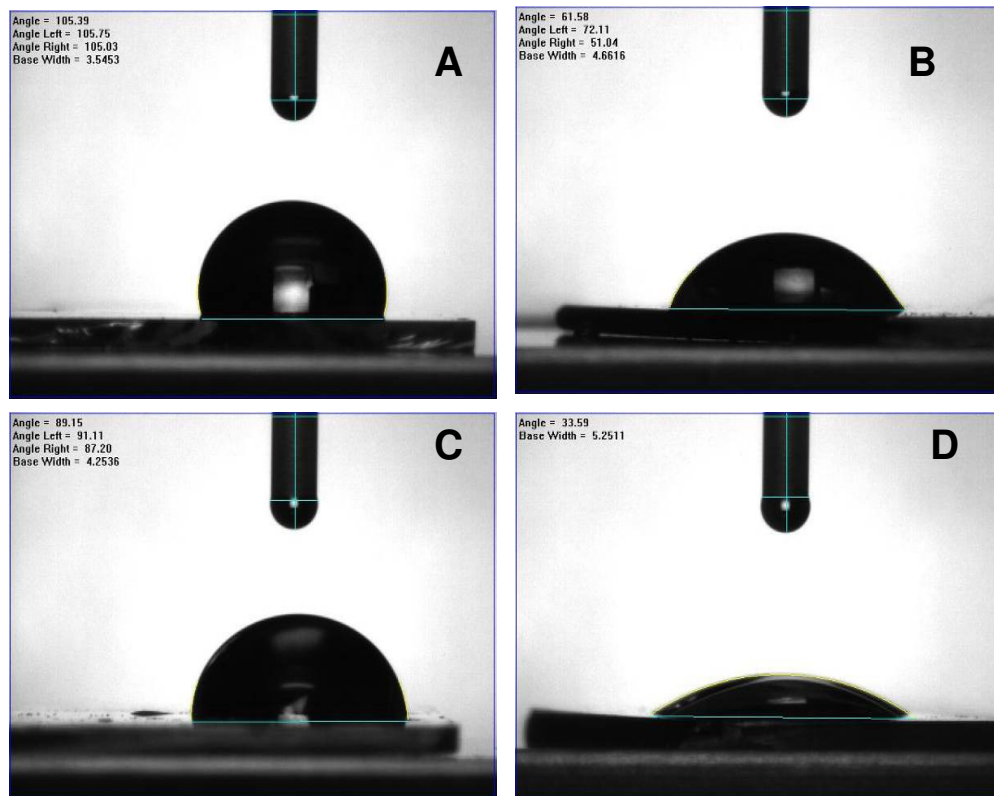

Fig. 5.15: Contact angle measurements for (a) Dry cavity (b) lipid treated dry cavity (c) buffer filled cavity (d) lipid treated prefilled array.

was approximately 89±9°, while for the dry cavity array a value of approximately 105±11° was obtained. As discussed in Chapter 2, Section 2.3.1, evidence from filling experiments suggests that the dried arrays have air trapped within their voids; therefore, half an hour sonication was required for filling the arrays with solvents. Here, the contact angle measurements show that the dried gold nanocavity arrays are more hydrophobic than the prefilled arrays that are attributed to the presence of air trapped in the voids of the array. The difference in contact angle measurements for both prefilled and dried gold nanocavity arrays indicate that encapsulation of solvent inside the cavity can change the surface properties of the arrays. The contact angle for the liposome treated prefilled gold nanocavity array was 33±4° whereas liposome treated dried array shows a contact angle of 61±5°. The contact angle for prefilled gold nanocavity arrays was reduced from 89±6°

to 33±4° when treated with liposome, which shows that the hydrophilicity of the buffer prefilled cavity array is much greater after treating with lipids. Similarly, the contact angle for dried gold nanocavity array is decreased from 105±7° to 61±5° when the array is treated with lipid bilayers. This contact angle measurement confirms modification of the surface by lipid layer on both dried and prefilled arrays. The difference in contact angles for the lipid treated dried and prefilled arrays consistent with fluorescence results and confirms a different assembly of lipid layers on each substrates. The more hydrophilic nature of the lipid treated prefilled array is consistent with the formation of a homogenous hydrophilic layer across the entire top of the prefilled array as expected for the formation of spanning lipid layer. In contrast, the lipid treated dried gold nanocavity array is less hydrophilic than lipid treated prefilled arrays suggesting the formation of lipid bilayers inside the walls of the array after collapsing the liposomes inside the cavity. These contact angle measurements strongly suggest the formation of bilayers at the nanocavity interface as shown in Scheme 5.3.

5.3.5 Characterisation of spanning bilayer by Atomic force microscopy (AFM)

Fluorescence images of liposome treated prefilled and dried arrays are consistent with a model of spanning and collapsed bilayers across the array respectively. FRAP experiments confirmed the mobility of the bilayer on top of prefilled array and much lower mobility on the lipid treated dried arrays. In order to visualize and confirm the formation of spanned bilayers across the prefilled arrays and collapsing lipid layers inside the dried arrays, atomic force microscope measurements were carried out using a Veeco bioscope AFM in tapping mode. Figure 5.16 shows both height and friction images of buffer prefilled cavities before and after treated with liposome solution. All images were collected with the same AFM tip under identical loading force and feedback parameters. During scanning of the sample, friction forces can be induced due to the interaction between the tip and the sample. This friction mode can differentiate between hard and soft sections in the sample. Bilayers formed across the gold nanocavity arrays are expected to be more deformable than the hard gold surface. The AFM measurements were carried out in contact with buffer due to the instability of bilayers when in contact with air. Cross-sections of the height images (insets of Fig. 5.16 A and C) show that the depth probed by the AFM tip after treatment with liposome is reduced from ~400 nm to ~250 nm. Correspondingly, the overall standard deviation of height (R_q) is reduced from 119 nm to 70.8 nm after the treatment of the prefilled array with lipids. As shown in both the height and friction images, the suspended lipid bilayer also broadens features and decreases their range. The range of torsional flexure of the AFM tip provides contrast in the friction images, which is reduced from an R_q of 0.0744 V to 0.0571 V after lipid treatment. Table 5.2 shows the difference in height and friction of the prefilled gold nanocavity arrays before and after treated with lipids. The difference in height and friction in AFM images supports the formation of suspended lipid bilayers on top of prefilled gold nanocavity arrays.

	R_q (height)	R_q (friction)
Bare surface	119 nm	0.0744 V
Lipid treated surface	70.8 nm	0.0571 V

Table 5.2: Height and friction of buffer prefilled gold nanocavity arrays before and after the treatment with liposome. The measurements were conducted in wet conditions.
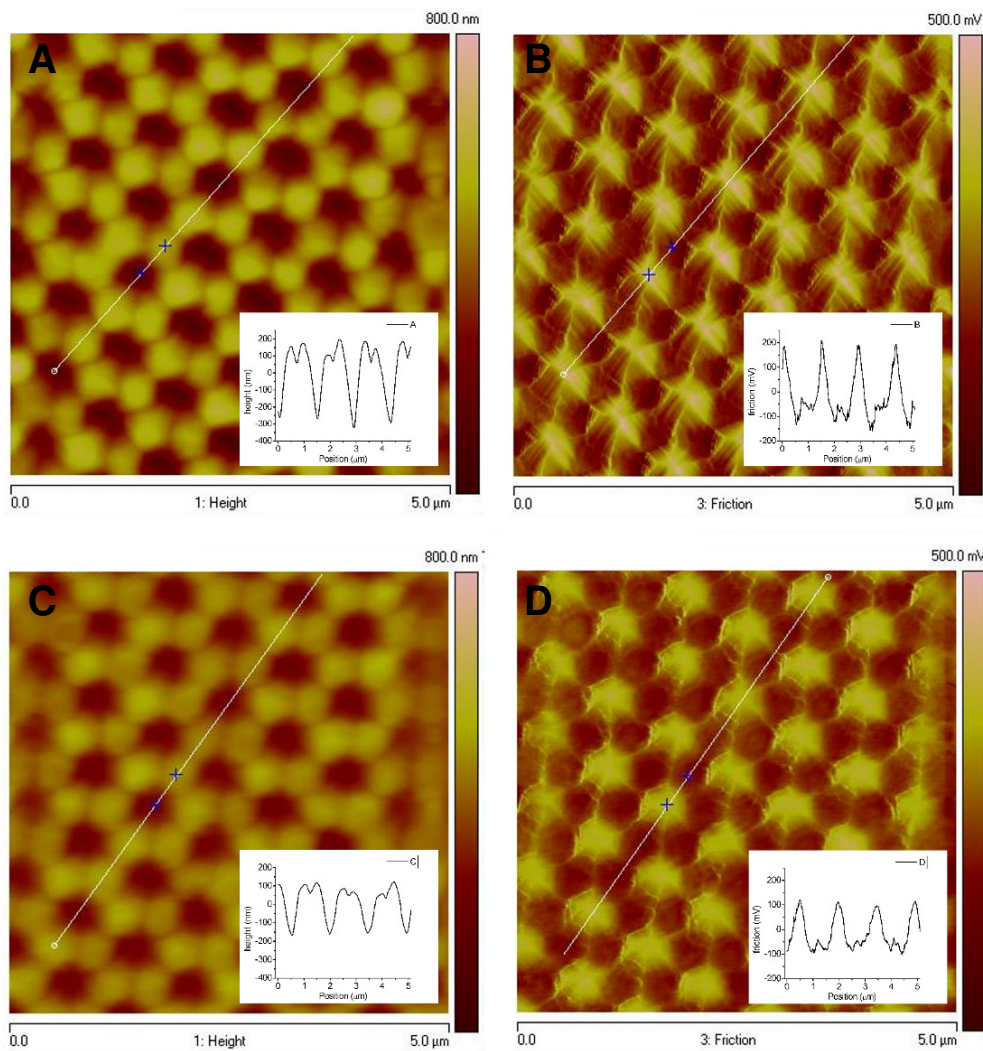

Fig.5.16: Tapping mode AFM images of prefilled arrays before and after sonication in liposome (A) Height and (B) friction images of prefilled gold nanocavities before treated with liposome solution. (C) Height and (D) friction images of spanning lipid bilayer formed on prefilled cavities. The measurements were conducted in wet conditions.

Figure 5.17 shows the height and friction images of dried gold nanocavity arrays before and after the treatment with lipids. The lipid treated dried gold nanocavity arrays appears to be smoother than the dry arrays. However, unlike the buffer prefilled cavity there is no significant difference either in friction or height profile between lipid treated arrays and bare dried arrays. The unchanged value for dried arrays might be due to the difficulties for the tip to reach the bottom of the cavity (tip-induced error). This usually arises while imaging of deep spherical nanocavities. The unchanged value for lipid treated dried arrays can also be due to the absence of deposition of lipid layers for dried arrays but this notion can be ruled out when compare with fluorescence images (Figure 5.10 D) from these arrays. The fluorescence images clearly show the presence of membrane probes inside the array. The change in the contact angle also support the results obtained from fluorescence measurements. In conclusion, the AFM measurements confirm the formation of spanning lipid bilayers on top of prefilled arrays. However, the identification of regions with defects in the spanning layer could not achieved by AFM measurements. The confirmation of bilayer formation in dried gold nanocavity arrays was inconclusive with AFM measurements.
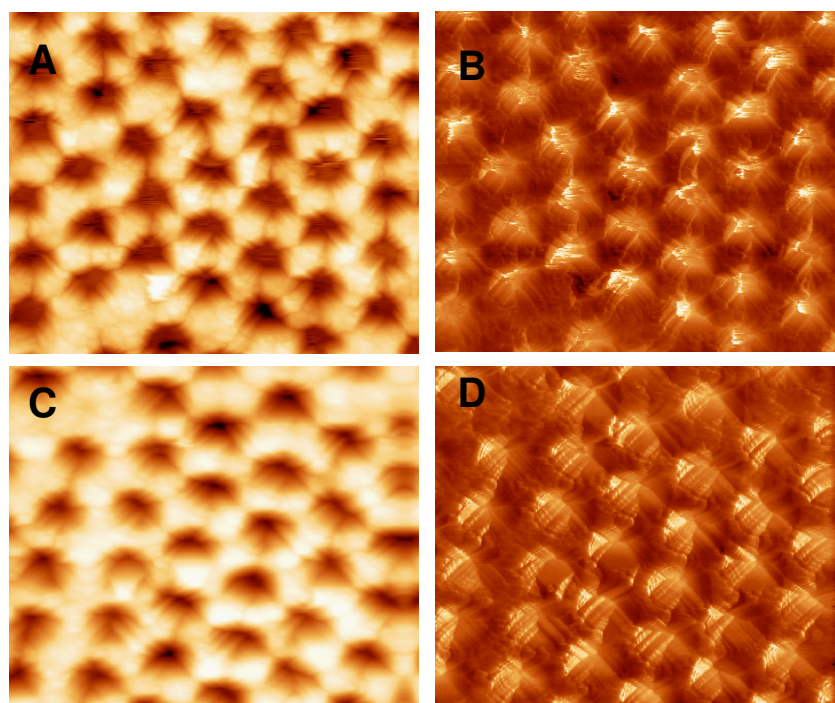

Fig.5.17: Tapping mode AFM images of dried gold nanocavities before and after treating with lipids. (A) Height and (B) friction images of dried gold nanocavities before treated with liposome solution. (C) Height and (D) friction images after treated with liposome. The measurements were conducted in wet conditions.

5.3.6 Electrochemical characterization

The formation of a defect-free lipid bilayer on a conductive substrate is expected to result in electrical insulation of the electrode. Capacitances in the range of 0.7-1.1 $\mu F/cm^2$ for lipid bilayers immobilized on planar gold substrates have been reported previously.[49,50] Stienem and co-workers have prepared spanned bilayers by means of the vesicle fusion technique, on a porous alumina substrate over which gold was deposited at the top surface of the porous alumina. The gold surface was functionalized with cholesterylpolyethylenoxy thiol by incubating the slide in 0.1 mM n-propanol solution for 12 hours. Then the liposomes with mixture of lipids were spread on the functionalized porous alumina substrate. The lipid bilayers formed on top of these substrates show a capacitance in the range of 0.7-1.1 $\mu F/cm^2$.

The capacitance of the membrane can be expressed by Equation 5.3,

$$C = \varepsilon_0 \varepsilon_r \frac{A}{D}$$

5.3

where, C is the capacitance, D is the thickness of the bilayer, A is the area of the electrode and ε_0 and ε_r are the permittivity of free space and the dielectric permittivity respectively. In order to investigate the spanning and collapsing of lipid bilayers formed on dried and pre-filled gold nanocavity arrays, capacitance measurements were conducted. Figure 5.18 shows the capacitance of buffer prefilled and dry cavity arrays measured before and after vesicle rupture on to their surface. The capacitance of the gold nanocavity array is shown as a black line and the capacitance of lipid treated dry and buffer prefilled arrays are shown in red and green respectively. Before vesicle rupture, the capacitance of gold nanocavity arrays shows a significant dependence on applied potential. However, significant differences in capacitance behaviour are evident between the dry and buffer prefilled cavity arrays after vesicle rupture. The capacitance of the bilayer formed at the dry cavity arrays is lower (6 $\mu F/cm^2$) than that for the buffer prefilled arrays (20 $\mu F/cm^2$). The variation in the capacitance of lipid treated dried and prefilled gold nanocavity arrays reveal that the lipid bilayers assemble in different ways depending on the preparation of the cavity.

239
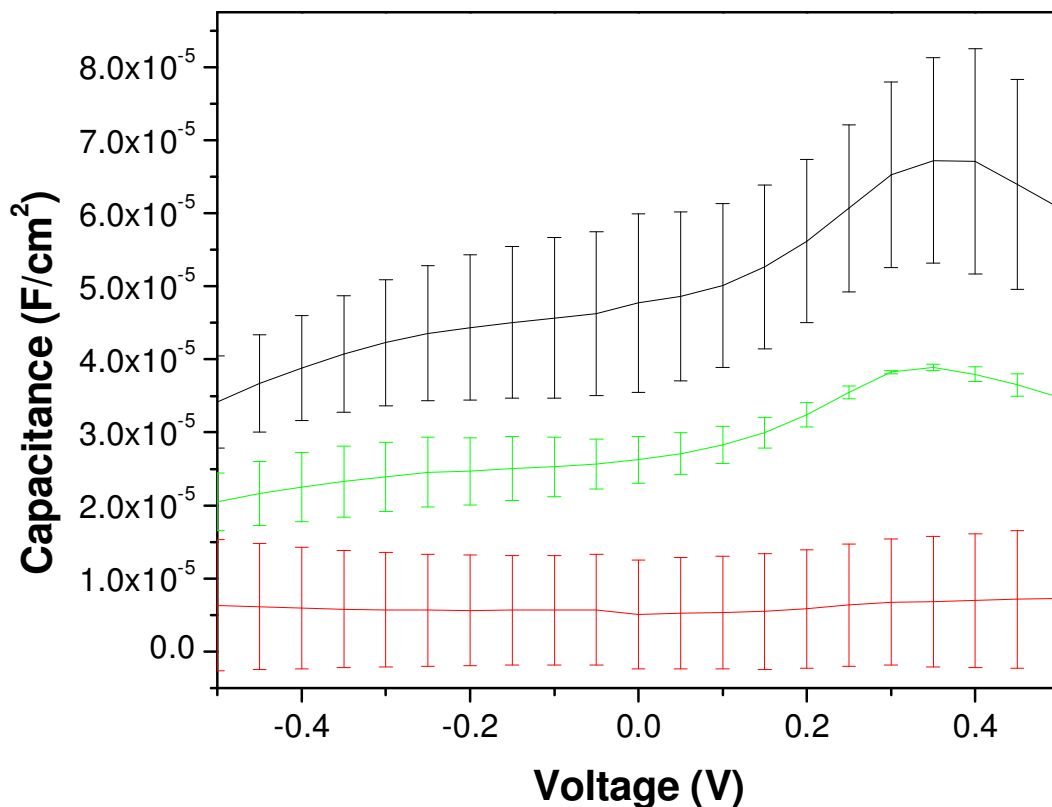
Fig. 5.18: Capacitance measurements of (—) buffer prefilled gold nanocavity array, (—), bilayer formed on top of buffer prefilled gold nanocavity array and (—) bilayer formed inside the dry nanocavity array. The error bars were calculated from three measurements. The 0.1 M PBS buffer with pH 7.4 was used as electrolyte.

Although the overall capacitance is lower for the buffer prefilled cavity arrays, they show a dependence on potential that is similar to that seen on arrays prior to modification with lipid membranes. In contrast, the capacitance of the dry cavity after bilayer shows much less potential dependence, which indicates the presence of an insulating layer at the electrode surface. Nonetheless, the capacitance is higher ($\sim$ 6 μF/cm^2) in comparison to previous reports (2.4 μF/cm^2), which is attributed tentatively to defects such as domain boundaries and discontinuities within bilayers.[51,52] The differences in capacitance between lipid-coated dry and prefilled arrays is attributed to the lipid-surface geometries shown in Scheme 5.3. In the case of the dry cavity arrays, the lipids can assemble on the internal cavity walls and this yields a low capacitance which is potential independent, as observed in Figure 5.18. However, in the case of buffer prefilled cavity arrays the liposomes rupture outside the cavities because of hydrophilicity of surface and spread to

form spanning lipid membranes along the aqueous plane. Consequently, a potential dependant capacitance remains because a significant amount of aqueous buffer is trapped inside the cavities. However, the capacitance of these arrays is lower than that observed for arrays without lipid. Capacitance measurements for the bilayer on top of prefilled and dried gold nanocavities are consistent with the formation of bilayers as suggested in scheme 5.3. Several groups have reported the membrane capacitance in the range from 0.7 to 1.1 $\mu F/cm^2$ for the lipid bilayers immobilized on planar semiconductor and gold surfaces.[53,54]

5.3.7 Fluorescence resonance energy transfer (FRET)

In order to study the interaction of molecules at the membrane with molecules inside the cavity, FRET measurements were carried out after filling the array with acceptor and incorporating donor in the membrane. Fluorescence (or Förster) resonance energy transfer (FRET) is a photophysical phenomenon which has been widely applied in biomedical applications and imaging.[38] FRET involves the non-radiative transfer of energy from the excited state of a donor to a ground-state acceptor resulting in emission from acceptor. Scheme 5.4 shows a simple scheme describing FRET. A fluorescent molecule, D, absorbs light and is excited to a higher electronic level. Then, the excited molecule transfers this energy to another fluorescent molecule, A, through a dipole-dipole interaction.[55]

$$\mathbf{D} \to {}^{\text{photon excitation}} \to \mathbf{D^*} + \mathbf{A} \to {}^{\text{energy transfer}} \to \mathbf{D} + \mathbf{A^*} \to {}^{\text{(fluorescence)}} \to \mathbf{A}$$
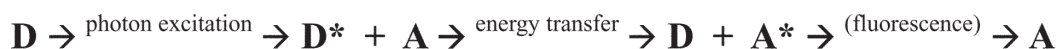
Scheme 5.4: Mechanism for FRET. A fluorescent molecule, D excites to higher electronic levels (D*) after absorption. Then, the energy is transferred to another neighbouring molecule A and that molecule excited to higher electronic level. The molecule A* returns back to ground state by emission of photon.

The rate of energy transfer (k_T) between D-A pair separated by a distance r is given by,

$$k_T = \frac{1}{\tau_D} \left[\frac{R_0}{r} \right]^6 \tag{5.4}$$

where, τ_D is the lifetime of the donor in the absence of acceptor and R_0 is the Förster distance. The Förster distance is the distance at which half of the donor molecules transfer energy to the acceptor and the other half decay by usual radiative and non-radiative pathways. R_0 is proportional to several factors as described by Equation 5.5:

$$R_0 = K(\kappa^2 n^{-4} \phi_D J[\lambda])^{1/6} \tag{5.5}$$

where, K is a numerical constant which depends on the units used for the other terms in equation and κ^2 refers to the relative orientation of the transition dipoles of the donor and acceptor. For randomly oriented donor and acceptor, it is assumed to have a value of 2/3. 'n' is the refractive index of the solvent and Φ_D is the quantum yield of the donor. $J[\lambda]$ is the overlap integral describing the degree of overlap between the donor emission and acceptor absorption spectra. The physical meaning of overlap integral for a FRET pair is illustrated in Figure 5.19. The efficiency of energy transfer between the donor and

acceptor depends on the 6th power of the distance between them and the Förster distance as shown in Equation 5.6.[56]

$$E = \frac{R_0^6}{R_0^6 + r^6}$$

5.6
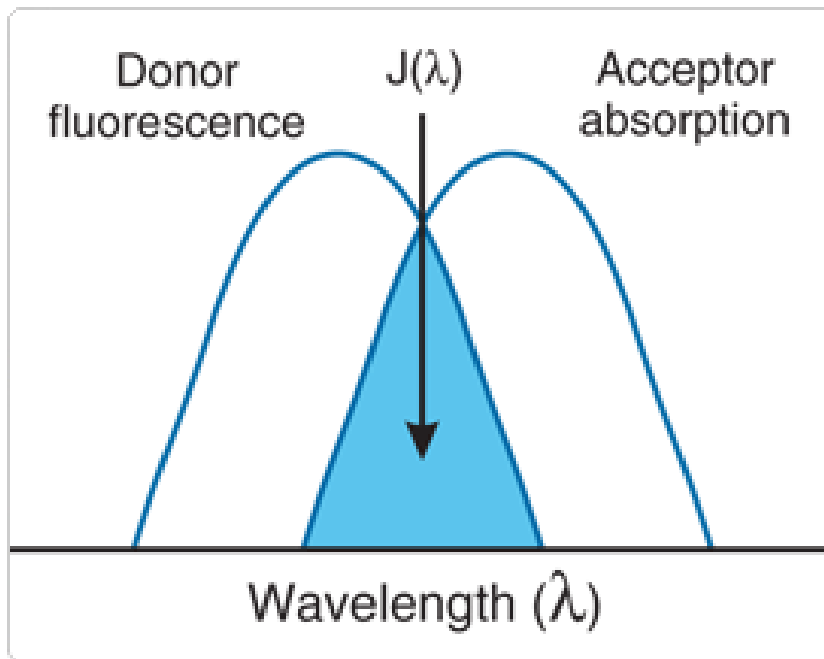
Fig. 5.19: Absorption of the donor and emission of the acceptor. The shaded area represents the spectral overlap. *Taken from Miller et al. Analyst, 2005, 130, 265.*[55]

The Förster distance depends on the overlap integral and therefore varies from one FRET pair to other, but typically it is in the range of 5-8 nm. Fluorescein and rhodamine are a well-established FRET pair due to their excellent overlap of the absorption spectrum of rhodamine (530 nm) with the emission spectrum of DAF (520 nm) as shown in Figure 5.20.[57] The Förster distance for the fluorescein and rhodamine pair is 56 Å for randomly oriented species and efficient energy transfer is expected when the molecules are closer than this distance.[58] The length scale of a single lipid bilayer is expected to be 5 nm which is compatible to the Förster distance for rhodamine-fluorescein pair. Therefore, this pair was selected for the study of interaction of molecules inside the cavity and molecules in the spanning lipid layer. One of the key motivations for this study was to use it to confirm that only a single bilayer is formed at the array. FRET measurements have been used to determine the existence of membrane domains and to determine the distance between membrane probes in the lipid membrane.[59,60] As discussed in Chapter 2, the gold nanocavity arrays can be filled with the desired solvent by sonication. Moreover,

the lipid bilayers can be spanned on top of pre-filled gold nanocavity arrays. By combining both of these methods, the interaction of the molecule in the spanned membrane on top of the arrays with the molecules inside the cavity could be used to assess the length scale of the layer formed. The FRET pair was assembled in to the assembly in two ways. In the first experiment, the membrane probe is incorporated within the liposome and then spanned across the rhodamine filled array and in the second experiment, liposome spanned across the rhodamine filled cavity then the array was exposed to DAF solution. The former experiment confirms suspension rather than collapsing of the bilayer and the latter one confirms single bilayer formation on top of prefilled array.
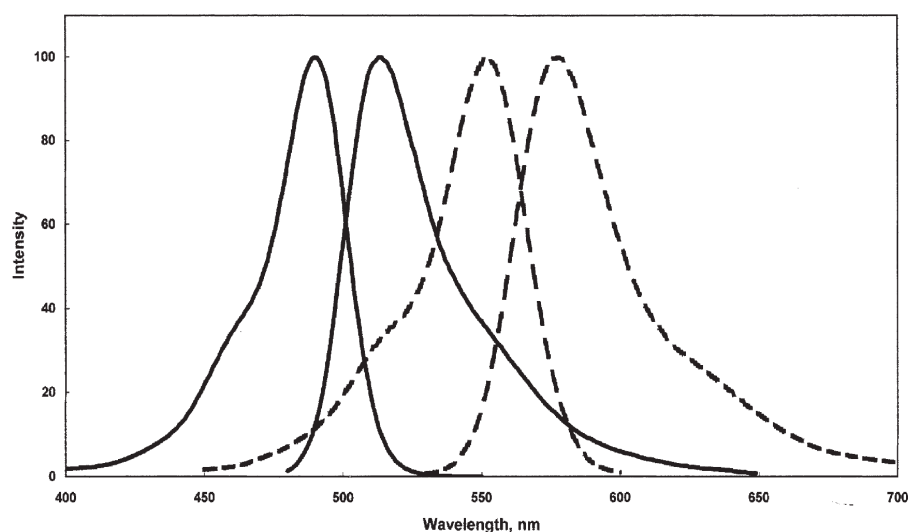
Fig. 5.20: Excitation and emission spectra of fluorescein (—) and rhodamine (----). *Taken from Miller et al. Analyst, 2005, 130, 265.*[55]
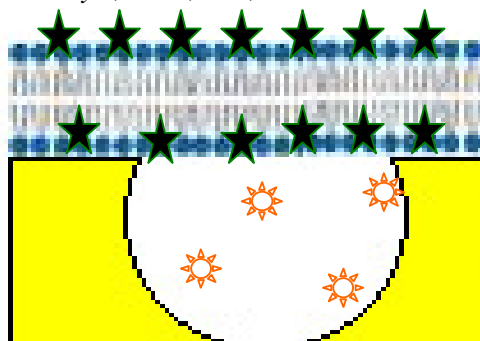
Scheme 5.5: Schematic representation of FRET pair in first approach to assembly lipid bilayers on top of gold nanocavity arrays. The orange star indicates the location of rhodamine inside the array and the green star indicates the presence of 5-dodecanoylaminofluorescein (DAF) in the spanned lipid (DMPC) bilayers.

The acceptor, rhodamine was dissolved in water and incorporated into the cavities by 30 minute sonication. Then, the rhodamine filled gold arrays were sonicated in DAF incorporated liposome solution. Scheme 5.5 shows the principle of the experiment on spanning lipid layers on rhodamine filled array. The acceptor molecules, rhodamine, are in solution and therefore they are randomly distributed inside the gold cavity array while the donor molecules are expected to be localized on the top of the cavity in the spanning lipid bilayer.

The FRET measurements were carried out using a confocal fluorescence microscope in which the fluorescence from the donor and acceptor were separated using different channels and filters. The donor, DAF molecules were excited using the 488 nm line from an argon ion laser. In the absence of the acceptor as described in Section 5.3.3, a homogenous fluorescence is observed from the DAF within the spanning lipid bilayer when the lipids lie across the top of buffer filled gold nanocavity arrays (identical to Figure 5.11 D). The absorption spectrum of rhodamine shows only 10 % absorption at 488 nm excitation compared with 520 nm. Therefore, control measurements were carried out by examining rhodamine filled cavity without DAF under 488 nm excitation. Figure 5.21 (C) and (D) show the reflectance and fluorescence images from the rhodamine filled cavity under 488 nm excitation without DAF. The emission from the rhodamine filled cavities was collected using a 560 long pass filter. Under these conditions, no fluorescent signal was detectable from the rhodamine filled cavities in the absence of DAF in the membrane at the top of rhodamine filled cavity. When the cavities are filled with the acceptor (rhodamine), energy transfer is observed between DAF at the membrane reflected in intense rhodamine emission from the underlying cavity. Figure 5.21 (A) shows the fluorescence image acquired between 515-560 nm ($\lambda_{max} \approx 520$ nm) which shows that the intensity of DAF emission is reduced in a hexagonal pattern that matches the pattern of the underlying gold cavities. Simultaneous observation of the rhodamine emission is monitored using a 560 long pass filter ($\lambda_{max} \approx 570$ nm) into the second channel. Significantly, emission intensity is now observed from the rhodamine filled cavity, as shown in Figure 5.21 (B). The observation of energy transfer between the donor molecules in the plane of the membrane and the solvated accepter molecules in the

gold cavities further confirms that the cavities are fluid filled and that the membrane is suspended across the pore opening.
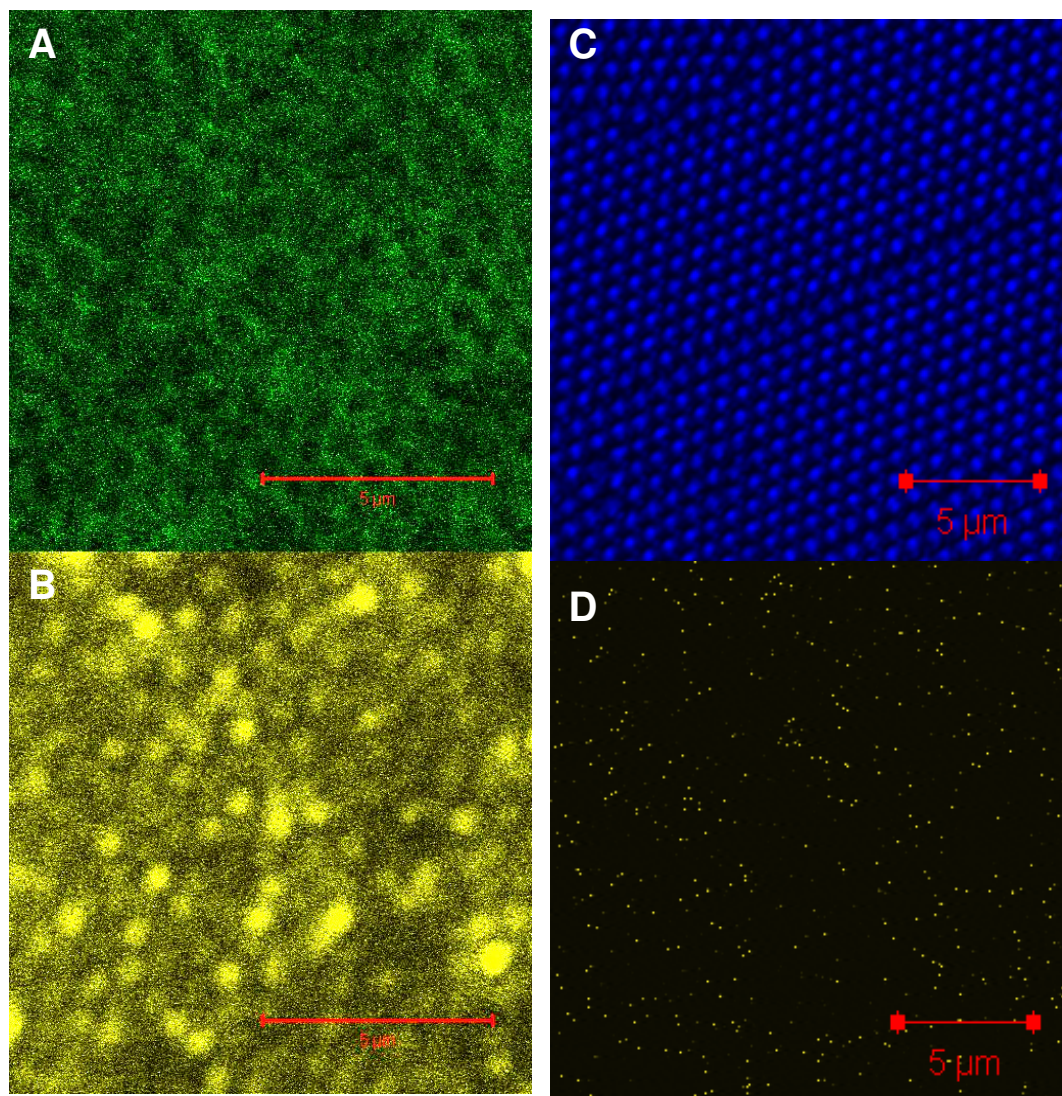

Fig. 5.21: Confocal fluorescence microscopy images of Fluorescence resonance energy transfer between DAF (in the membrane) and rhodamine (in solution inside the cavity). The gold nanocavity arrays are filled with rhodamine and DAF is incorporated into the spanning lipid bilayer formed on top of the filled array. The excitation wavelength was 488 nm. (A) Fluorescence from DAF is collected in channel 1 using a 515-560 band pass filter. (B) Fluorescence from rhodamine is simultaneously collected using a 560 long pass filter in channel 2. Figure (C) and (D) shows control measurements at 488 nm excitation for a rhodamine filled array. (C) The reflectance collected from rhodamine filled gold nanocavity arrays (D) fluorescence from rhodamine filled cavity at 488 nm excitation.

In order to confirm that only a single bilayer had formed at the top surface, we exploited the distance dependence of FRET. Here, FRET measurements were carried out after incorporating membrane probe only at the top leaflet of the lipid bilayer. This was

246

achieved by allowing the membrane probe to self-assemble into the lipid bilayer after the pre-formation of spanning lipid bilayers. The spanning lipid bilayers were formed after treating the aqueous filled array with membrane probe-free liposome as described. The rate of inter leaflet transfer in a lipid bilayer is slow, taking more than 24 hrs.[38] Therefore, the incorporation of DAF is expected to be observed only at the top leaflet of the membrane and the experiments were performed within 10 minutes of incorporation. The schematic representation of the experiment is shown in Scheme 5.6. Time series measurements were carried using confocal fluorescence microscopy in order to study the incorporation of membrane probe in the spanned lipid bilayer. The incorporation of membrane probe in the membrane was occurred within seconds. The fluorescence from rhodamine is observed within few seconds after the injection of membrane probe solution in between the cover glass and the spanned bilayer.

Scheme 5.6: Schematic representation of FRET in lipid bilayers on top of gold nanocavity arrays. The orange star indicates the location of rhodamine inside the array and the green star indicates the presence of 5-dodecanoylaminofluorescein (DAF) in the top leaflet of the spanned lipid bilayer.

Generally, FRET measurements have been conducted using macromolecules such as proteins, in which a single acceptor is attached to each donor at different ends of the molecule. Lakowicz et al. have shown that the FRET measurements require high concentrations of acceptor molecules if the donors and acceptors are unlinked.[38] The concentration of the acceptor molecule determines the proximity of the acceptor and donor molecule. The energy transfer efficiency can be determined by changing the concentration of the acceptor molecule. The schematic representation of the concentration dependent FRET is shown in Scheme 5.7. The orange stars show the acceptor, rhodamine and the green stars show the donor membrane probe, DAF. In this experiment, the gold nanocavity arrays are filled by sonication with different concentrations (1.8 mM, 100 µM, 10 µM and 1.9 µM) of rhodamine solution and the concentration of the donor molecules were kept constant in the membrane. Then, the

changes in the fluorescence intensity of both DAF and rhodamine were recorded with these different concentrations of rhodamine. Figure 5.22 reflects the fluorescence resonance energy transfer between the rhodamine inside the cavity and DAF membrane probe in the lipid bilayer on top of the arrays as greater signal intensity is observed for higher concentration of rhodamine inside the cavity. Previous reports have shown that the rhodamine also has very low percentage of absorption (<10 %) at 488 nm excitation.[55] Therefore, the changes in signal intensity can be either due to the varying concentrations of rhodamine inside the cavity which results in different energy transfer or due to the excitation of more rhodamine molecules at 473 nm excitation when the concentration is high. As a control experiment, the gold nanocavity arrays were filled with different concentrations of rhodamine then, lipid bilayers without DAF were assembled across the rhodamine filled array. The emission intensity was then recorded at 473 nm excitation for three different concentrations of rhodamine inside the array. In the control experiments, around a 70 % decrease in emission intensity was observed for 1.8 mM and 100 µM rhodamine filled array at 473 nm excitation. In a concentration dependent FRET experiment, a 6 % decrease in emission intensity is observed as shown in Figure 5.22. Therefore, the greater emission intensity in the FRET experiments can be attributed mainly to energy transfer between the DAF and rhodamine. A small contribution from emission intensity due to the direct excitation cannot be ruled out completely but cannot account for all intensity observed. Overall, the concentration dependent study supports the spanning of single lipid bilayers on top of pre-filled gold nanocavity arrays.
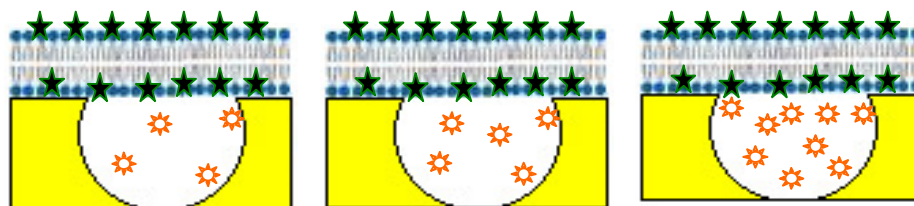
Scheme 5.7: Schematic representation of concentration dependent FRET experiment. The green stars represent membrane probe, DAF and the orange stars represent rhodamine molecules inside the cavity. The concentration of rhodamine molecules inside the array increased from left to right. Blue circle represents the polar part of the lipid.
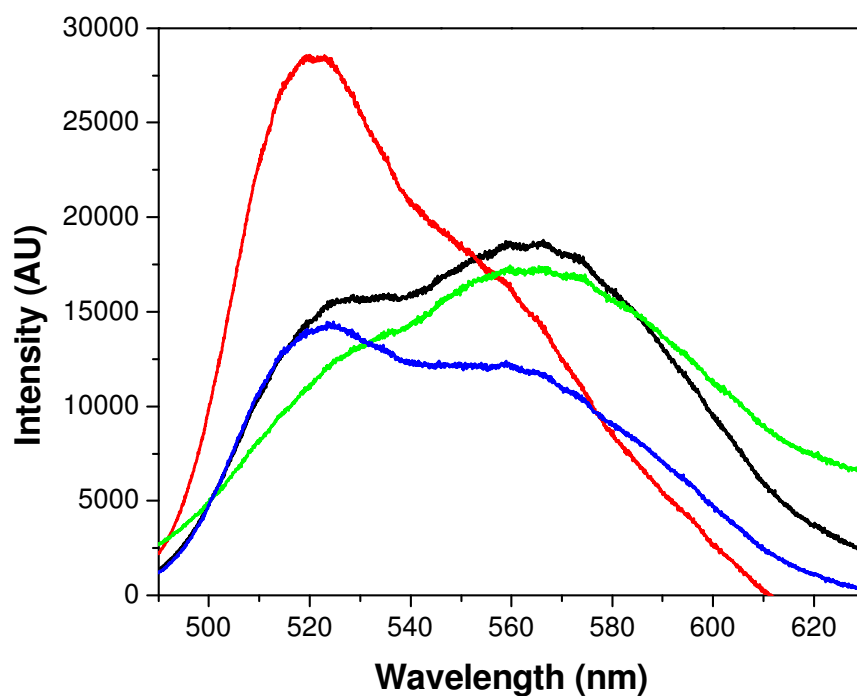
Fig.5.22: Concentration dependent FRET measurements between Rhodamine and DAF at 473 nm excitation wavelength. Gold nanocavity arrays were filled with rhodamine and then the filled array is sonicated in DAF incorporated liposome solution. The concentration of the rhodamine inside the cavities were (—) 1.8 mM (—) 100 μM (—) 10 μM (—) 1.9 μM.

5.3.8 Introduction and study of a Transmembrane protein into spanning lipid bilayer
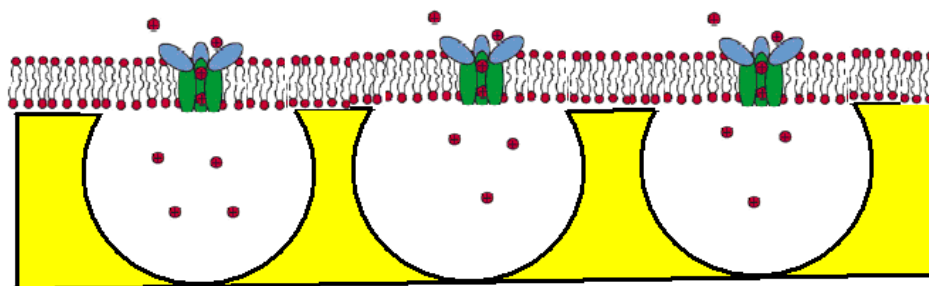
Scheme 5.8: Schematic representation of spanned lipid membranes containing ion-channels on top of water filled gold nanocavity arrays. The red circle represents monovalent ions and the flower like structure represents Gramicidin.

Ion channels are transmembrane proteins which maintain the ion balance across cell membranes. Ion-channel proteins are widely used to study the properties of artificial lipid bilayers. Most of the transmembrane proteins have to be reconstituted into bilayers using proteoliposome fusion. However, gramicidin can spontaneously self-orient into a lipid bilayer. Gramicidin forms channels in lipid bilayers with a diameter of 4 Å.[14] Scheme 5.8 shows a schematic representation of the orientation within a bilayer and indicates the ion transport properties of the ion-channel. Gramicidin channels are selective for monovalent cations. The mechanism of insertion of gramicidin in lipid bilayers depends on the polarity of the solvent. Previous reports have shown that, when the gramicidin is dissolved in ethanol it forms intertwined dimers which absorb to the membrane-solution interface,[61] and then insert into the membrane to unfold and span to the bilayer.

To investigate the ability of the spanned lipid bilayers developed here to support a transmembrane protein and to detect monovalent cations, capacitance measurements were carried out using channel forming gramicidin protein introduced to the arrays. In this experiment, the nanocavity arrays were prefilled first with de-ionized water and then spanned bilayers were formed across the array as described in Section 5.2.2. PBS buffer with pH 7.4 (0.1 M) was used as electrolyte to introduce an ion gradient between inside and outside of the bilayer. The capacitance of the spanned bilayers is therefore expected

to increase due to the ion flux if an ion channel is formed. Previous reports have shown that after the addition of gramicidin into an electrolyte, the ion channel forming rate is low and after 17 minutes the membranes were broken and reformed which resulted a 100 fold greater increase in the channel formation.[61] Therefore, in this ion gradient experiment it was expected that the capacitance might increase approximately after 20 minutes following addition of gramicidin. Figure 5.24 shows the changes in the capacitance at the spanned bilayers on the cavity arrays after gramicidin addition in an ion gradient experiment. The gramicidin protein (50 µl solution of 5 mg/ml) dissolved in ethanol was added to the electrolyte after 180 s. If the protein incorporates into the spanned lipid bilayer an increase in capacitance is expected due to flow of ions from buffer (electrolyte) to water (inside the voids). Correspondingly, the capacitance is increased by 0.4 ± 0.05 µF/cm^2, on the addition of gramicidin. According to Equation 5.3, the increase in capacitance is attributed to a higher dielectric permittivity arising due to the flow of cations from the electrolyte (PBS buffer) to the voids (water) through the channels across the lipid bilayer. To determine the effect of solvent, 50 µl of ethanol was added to the electrolyte after 700 s. The capacitance is increased by 0.15 ± 0.08 µF/cm^2 with the injection of ethanol. The ion channel forming experiment was repeated more than ten times and the measurement shown in Figure 5.23 is an example. The changes in the capacitance were recorded for more than one hour but the identical behaviour is observed even after long time. The reproducibility of this experiment was only 50 % and the remained experiments have shown different behaviour including single channel formation. Therefore, in future more work has to be carried out to confirm the channel formation and the changes in the capacitance. This preliminary study for the potential application of the spanned lipid bilayers across gold nanocavity arrays suggests that this platform can perform as sensor to detect monovalent ions.
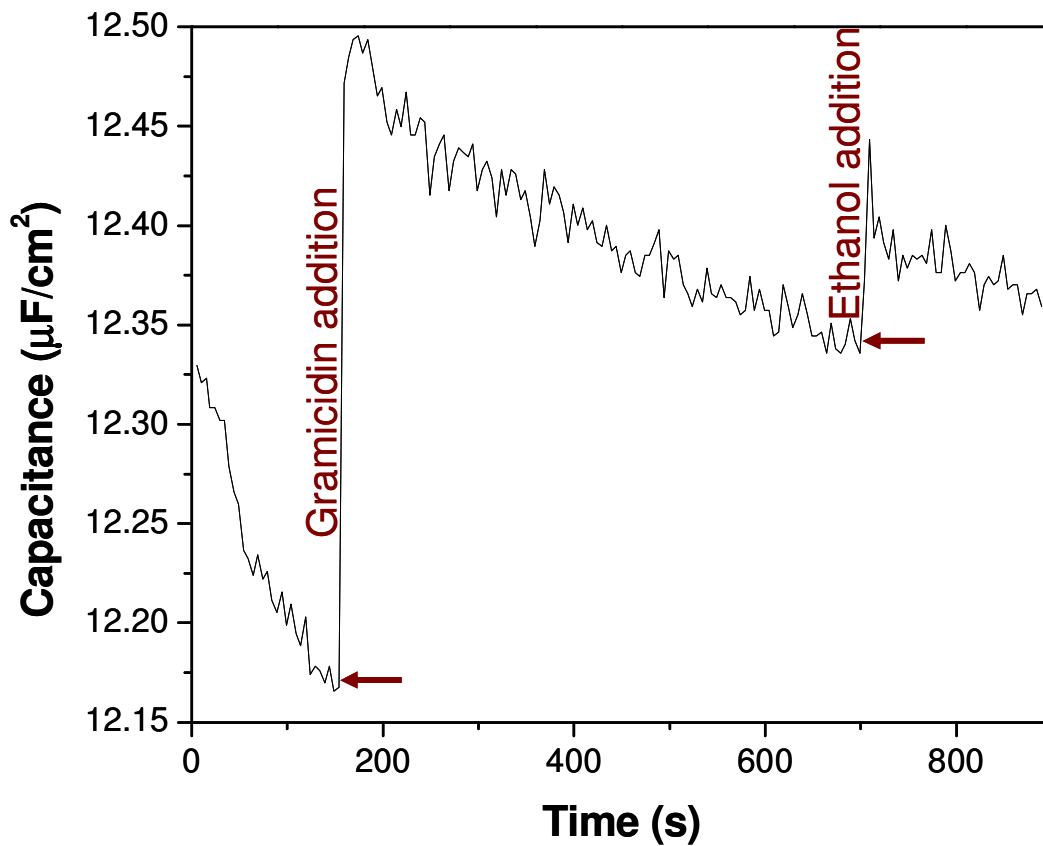
Fig. 5.23: Capacitance measurements of spanned lipid bilayers formed across 820 nm diameter water filled gold nanocavity arrays during gramicidin addition. The red arrows show the addition of gramicidin (180 s) and ethanol (700 s) to the electrolyte. The PBS buffer (0.1 M) with pH 7.4 was used as electrolyte.

5.4 Conclusions

This chapter addressed the assembly of lipid bilayers across buffer prefilled gold nanocavity arrays and compared the effect of assembly of lipid at dried gold nanocavity arrays by vesicle rupture technique. The changes in the photophysical properties of three different membrane probes were investigated after incorporating the probes in liposomes to select the most useful probe for this experiment. The excitation and emission properties of the membrane probes remain unchanged in the buffer and in liposomes suggests that the location of chromophore is in the polar region of the lipid layer. The lifetime of the membrane probes in the lipid membrane is different due to the restricted rotation of the molecules in the membrane.

The behaviour of lipid bilayers assembled on prefilled and dried arrays was distinguished using confocal fluorescence microscopy. The lipid treated dried arrays show strong evidence for localization of the bilayer at the nanocavity walls whereas the lipid treated prefilled arrays show a homogenous fluorescence on top of the array which strongly suggests that the assembly of lipid bilayer is in different manner on dried and the prefilled arrays. The changes in the lateral mobility of the membrane probes on top of dried and prefilled gold cavity arrays were studied using fluorescence recovery after photobleaching technique. The diffusion coefficient of the membrane probe, DAF, in spanned lipid bilayer was determined as 0.8 ± 0.07 $\mu m^2.s^{-1}$. The mobility of the lipid bilayers formed on dried arrays appears to be reduced by approximately an order of magnitude compared to the spanned lipid bilayers.

The assembly of lipid bilayers on both dried and prefilled arrays was characterized by capacitance measurements. The capacitance of the spanned lipid bilayers is 20 $\mu F/cm^2$ reduced to 6 $\mu F/cm^2$ for the lipid bilayers assembled on dried arrays. The spanning of lipid bilayers on top of the gold nanocavity arrays is confirmed using fluorescence resonance energy transfer technique. An energy transfer between DAF in the spanning bilayer membrane and rhodamine in the underlying solution was observed demonstrating the interaction of molecules in the bilayer and molecules inside the array. FRAP and FRET experiments also strongly suggest the presence of spanning lipid bilayers.

The changes in the capacitance value in an ion gradient experiment reveal that the monovalent ions in the solution can be detected using a transmembrane protein Gramicidin. In conclusion, the pattern of lipid bilayers on dried and buffer filled arrays are completely different. All measurements to investigate the arrangement of lipid bilayers point out that the bilayers are collapsed at the interior cavity walls for dried arrays whereas; the lipid bilayers are spanned across the cavity walls on top of filled arrays.

The main advantage of spanning the lipid bilayer on top of gold nanocavity is the proximity of both sides of the membrane bilayer to aqueous environments, as demonstrated by the FRET experiments. In addition, the composition of the solution inside the cavities can be varied by choosing appropriate solvent. A further advantage is the possibility of plasmonic enhancement from these nanocavities, which may aid sensitivity in applying these materials to study the assembled protein.

5.5 References

[1]   Nel, A. E.; Madler, L.; Velegol, D.; Xia, T.; Hoek, E. M. V.; Somasundaran, P.; Klaessig, F.; Castranova, V.; Thompson, M. *Nature Mater.*, **2009**, *8*, 543.

[2]   Hauck, T. S.; Ghazani, A. A.; Chan, W. C. W. *Small*, **2008**, *4*, 153.

[3]   Brian, A. A.; McConnell, H. M. *P. Natl. Acad. Sci.-Biol.,* **1984,** *81*, 6159.

[4]   Bockmann, R. A.; Hac, A.; Heimburg, T.; Grubmuller, H. *Biophys. J.,* **2003,** *85*, 1647.

[5]   Seu, K. J.; Pandey, A. P.; Haque, F.; Proctor, E. A.; Ribbe, A. E.; Hovis, J. S. *Biophys. J.*, **2007,** *92*, 2445.

[6]   Salafsky, J.; Groves, J. T.; Boxer, S. G. *Biochemistry,* **1996,** *35*, 14773.

[7]   McConnell, H. M.; Watts, T. H.; Weis, R. M.; Brian, A. A. *Biochim. Biophys. Acta,* **1986,** 864, 95.

[8]   Sim E. *Membrane biochemistry*, Chapman and Hall, London, New York, **1982**.

[9]   Tanford, C. *Science* **1978**, *200*, 1012.

[10]   Singer, S. J.; Nicolson, G. L. *Science* **1972**, *175*, 720.

[11]   Gaines, G. L. *Thin Solid Films* **1983**, *99*, R9-R13.

[12]   Simon, A.; Girard-Egrot, A.; Sauter, F.; Pudda, C.; D'Hahan, N. P.; Blum, L.; Chatelain, F.; Fuchs, A. *J. Colloid Interf. Sci.,* **2007**, *308*, 337.

[13]   Mueller, P.; Rudin, D. O.; Tien, H. T.; Wescott, W. C. *Nature,* **1962**, *194*, 979.

[14]   Steinem, C.; Janshoff, A.; Ulrich, W. P.; Sieber, M.; Galla, H. J. *BBA-Biomembranes* **1996,** *1279*, 169.

[15]   Wiegand, G.; Arribas-Layton, N.; Hillebrandt, H.; Sackmann, E.; Wagner, P. *J. Phys. Chem. B,* **2002,** *106*, 4245.

[16]   Yu, Q. M.; Golden, G. *Langmuir,* **2007,** *23*, 8659.

[17]   Sackmann, E. *Science,* **1996,** *271*, 43.

[18]   Purrucker, O.; Fortig, A.; Jordan, R.; Tanaka, M. *Chemphyschem.,* **2004**, *5*, 327.

[19]   Goennenwein, S.; Tanaka, M.; Hu, B.; Moroder, L.; Sackmann, E. *Biophys. J.,* **2003**, *85*, 646.

[20]   Reimhult, E.; Kumar, K. *Trends Biotechnol., 2008, 26*, 82.

[21]   Tanaka, M.; Sackmann, E. *Nature, 2005, 437*, 656.

[22]   Janshoff, A.; Steinem, C. *Anal. Bioanal. Chem., 2006, 385*, 433.

[23]   Tiefenauer, L. X.; Studer, A. *Biointerphases, 2008, 3*, FA74.

[24]   Hennesthal, C.; Drexler, J.; Steinem, C. *Chemphyschem., 2002, 3*, 885.

[25]   Schmitt, E. K.; Nurnabi, M.; Bushby, R. J.; Steinem, C. *Soft Matter, 2008*, *4*, 250.

[26]   Schmitt, E. K.; Weichbrodt, C.; Steinem, C. *Soft Matter, 2009*, *5*, 3347.

[27]   Jonsson, M. P.; Jonsson, P.; Dahlin, A. B.; Hook, F. *Nano Lett., 2007,* 7, 3462.

[28]   Bartlett, P. N.; Baumberg, J. J.; Coyle, S.; Abdelsalam, M. E. *Faraday Discuss.,*
       2004, 125, 117.

[29]   Mallon, C.T.; Jose B.; Forster, R.J.; Keyes, T.E., *Chem. Commun., 2010*, *46*, 106.

[30]   Lukomska, J.; Gryczynski, I.; Malicka, J.; Makowiec, S.; Lakowicz, J. R.;
       Gryczynski, Z. *Biochem. Bioph. Res. Co., 2005*, *328*, 78.

[31]   Lakowicz, J. R.; Malicka, J.; Huang, J.; Gryczynski, Z.; Gryczynski, I.
       Biopolymers, 2004, *74*, 467.

[32]   Malicka, J.; Gryczynski, I.; Lakowicz, J. R. *Biopolymers, 2004*, *74*, 263.

[33]   Lakowicz, J. R. *Topics in fluorescence spectroscopy*, Springer, Plenum Press,
       New York, **1991**.

[34]   Kalb, E.; Paltauf, F.; Hermetter, A. *Biophys. J., 1989*, *56*, 1245.

[35]   Streuli, C. H.; Grant, M. E.; Erb, E.-M.; Engel, J., *Extracellular Matrix Protocols*,
       Humana Press, Totowa, N. J., **2000**, 139, 71.

[36]   Mason W. T, *Fluorescent and luminescent probes for biological activity*,
       Academic Press, London, **1993**.

[37]   Li, L.; Szmacinski, H.; Lakowicz, J. R. *Anal. Biochem., 1997*, *244*, 80.

[38]   Lakowicz, J. R. *Principles of Fluorescence spectroscopy,* New York, Springer,
       2006.

[39]   Cosgrave, L.; Devocelle, M.; Forster, R. J.; Keyes, T. E. *Chem. Commu.*, **2010**,
       46, 103.

[40] Mueller, P.; Rudin, D. O.; Tien, H. T.; Wescott, W. C. *Nature,* **1962**, *194*, 979.

[41] Drachev, L. A.; Jasaitis, A. A.; Kaulen, A. D.; Kondrash.A.; Liberman, E. A.; Nemecek, I. B.; Ostroumo.S., Semenov, A. Y.; Skulache.V. *Nature,* **1974**, *249*, 321.

[42] Pagano, R. E.; Ruysscha, J.; Miller, I. R. *J. Membrane Biol.,* **1972**, *10*, 11.

[43] Lohner, K.; Konovalov, O. V.; Samoilenko, I. I.; Myagkov, I. V.; Troitzky, V. I.; Berzina, T. I. *Thin Solid Films,* **1996**, *288*, 262.

[44] Ladha, S.; Mackie, A. R.; Harvey, L. J.; Clark, D. C.; Lea, E. J. A.; Brullemans, M.; Duclohier, H. *Biophys. J.,* **1996**, *71*, 1364.

[45] Lalchev, Z. I.; Mackie, A. R. *Colloid Surface B,* **1999**, *15*, 147.

[46] Mackie, A.; Harvey, L.; Ladha, S.; Clark, D.; Brullemans, M.; Lea, E.; Duclohier, H. *Biophys. J.,* **1994**, *66*, A399.

[47] Seiffert, S.; Oppermann, W. *J. Microsc.-Oxford,* **2005,** *220*, 20.

[48] Abdelsalam, M. E.; Bartlett, P. N.; Kelf, T.; Baumberg, J. *Langmuir,* **2005**, *21*, 1753.

[49] Schmitt, E. K.; Weichbrodt, C.; Steinem, C. *Soft Matter,* **2009**, *5*, 3347.

[50] Schmitt, E. K.; Nurnabi, M.; Bushby, R. J.; Steinem, C. *Soft Matter,* **2008**, *4*, 250.

[51] Drexler, J.; Steinem, C. *J. Phys. Chem. B,* **2003,** *107*, 11245.

[52] Gao, H.; Feng, J.; Luo, G. A.; Ottova, A. L.; Tien, H. T. *Electroanal.,* **2001,** *13*, 49.

[53] Stora, T.; Lakey, J. H.; Vogel, H. *Angew. Chem. Int. Edit.,* **1999**, *38*, 389.

[54] Cheng, Y. L.; Bushby, R. J.; Evans, S. D.; Knowles, P. F.; Miles, R. E.; Ogier, S. D. *Langmuir,* **2001**, *17*, 1240.

[55] Miller, J. N. *Analyst,* **2005**, *130*, 265.

[56] Kenworthy, A. K.; Edidin, M. *J. Cell Biol.,* **1998,** *142*, 883.

[57] Merzlyakov, M.; Li, E.; Casas, R.; Hristova, K., *Langmuir,* **2006,** *22*, 6986.

[58] You, M.; Li, E.; Wimley, W. C.; Hristova, K. *Anal. Biochem.,* **2005,** *340*, 154.

[59] Silvius, J. R.; Nabi, I. R. *Mol. Membr. Biol.,* **2006,** *23*, 5.

[60]   Posokhov, Y. O.; Merzlyakov, M.; Hristova, K.; Ladokhin, A. S. *Anal. Biochem.* **2008**, *380*, 134.

[61]   O'Connell, A. M.; Koeppe, R. E.; Andersen, O. S. *Science,* **1990**, *250*, 1256.

Chapter 6

Conclusions and Future work

This thesis focussed on the development of a biomimetic plasmonic platform to enable incorporation of transmembrane proteins. A truly biomimetic environment to study transmembrane protein requires aqueous phase at both interfaces of the membrane to permit study the ion transport properties of ion channels or to accommodate the cytoplasmic tail of the transmembrane protein such as integrin. Therefore, highly reproducible nano-scale arrays with ordered voids were fabricated using nanosphere lithography in which the voids can act as an aqueous chamber. Gold nanocavity arrays were fabricated on conductive substrates such as FDTO and smooth gold on silicon using templated electrochemical deposition. Chapter 2 focussed on the influence of gold nanocavity arrays on the photophysical properties of ruthenium dye bound to the surface and free dye inside the cavity were investigated. Gold nanocavity arrays required 30 minutes sonication to fill the array with solvents. The gold nanocavity arrays on FDTO exhibit greater enhancement in emission intensity from ruthenium dye filled arrays. The enhancement in emission intensity from gold nanocavity arrays was compared with cobalt nanocavity arrays. An order of magnitude enhancement in emission intensity is observed from dye filled gold nanocavity arrays compared to dye filled cobalt arrays. The monolayers of surface active ruthenium dye shows greater enhancement in Raman signal intensity at the resonance wavelength of the dye. Future work could include the study of enhancement of organic fluorophore filled arrays which could further lead to development of sensitive sensors to study dye labelled proteins.

The gold nanocavity arrays on FDTO show greatest enhancement in both Raman and emission signal intensity. The location of the enhancement from gold nanocavity arrays was investigated using a two step adsorption processes. Chapter 3 described the selective modification of top surface and interior walls of the gold nanocavity arrays. In the first step, the probe is adsorbed on the top surface of the array before dissolving the polystyrene spheres. Then, the signal intensity from the edge modified array is compared with the signal intensity from the interior walls of the array. The

dye is selectively adsorbed at the interior walls of the array after blocking the top surface of the array with alkane thiol. The study reveals that the top surface of the gold nanocavity arrays ($t_N=0.8\pm0.04$) provide greater enhancement in both emission and Raman signal intensity. The greatest enhancement is observed for 240 nm diameter arrays compared to 430, 600 and 820 nm diameter arrays at $t_N=0.8\pm0.04$. Future work could involve the study of lifetime measurements from ruthenium dye adsorbed selectively on top surface and interior walls of the arrays.

Chapter 4 describes the thermal stability of three different diameters, 240, 430 and 820 nm, gold nanocavity arrays. The distortion of the top surface of the arrays appears to occur at 300 °C. The melting of the gold nanocavity arrays are observed at 500 °C, which results the formation of homogeneous, smoother arrays. The greatest enhancement in emission intensity is observed from the monolayers of ruthenium dye adsorbed on 500 °C annealed gold nanocavity arrays. Therefore, this platform can be useful in sensing metal enhanced hybridization assays. However, the Raman signal intensity of the arrays decreased as function of temperature. Therefore, it is crucial to coat some layers such as alumina on top of it to use this platform in non-ideal conditions. Future work could involve the study of enhancement in emission intensity from annealed arrays using different organic dyes which could be useful for the development highly sensitive, reusable fluorescence based sensors.

Chapter 5 describes the preparation of the spanning lipid bilayers across the buffer filled gold nanocavity arrays to use it as a biomimetic platform. The formation of lipid bilayers on dried and pre-filled gold nanocavity arrays were investigated using confocal fluorescence microscopy. The formation of spanning lipid bilayers on top of pre-filled arrays was studied using capacitance measurements. The interaction of molecule in the bilayer with the molecules inside the array was investigated using FRET measurements. The ion gradient measurements were carried out to study the ion transport properties of the gramicidin in the spanned lipid bilayers. The changes in the capacitance after the injection of gramicidin are monitored using electrochemical measurements which confirm the spanning of lipid bilayers across filled gold nanocavity arrays. This design can be used as a sensor to detect monovalent ions. Future work involves the application of this platform for nucleic acid hybridization assays and to study the dynamics of transmembrane proteins such

as integrin. In future, dynamics of transmembrane proteins such as integrin could be studied on this biomimetic platform using the vesicle fusion method. Changes in the stability and mobility of lipid bilayers after selective modification of the top surface of the arrays is not studied in this work which can be addressed in future using confocal fluorescence microscopy. More detailed studies of ion-channel forming proteins on spanning lipid bilayer can be studied using capacitance measurements which will be useful for the development of highly sensitive sensors.

In conclusion, the gold nanocavity arrays shows great enhancement in both emission and Raman signal intensity. The 240 nm diameter arrays at 785 nm excitation, gives best enhancement in Raman signal intensity compared large diameter arrays at $t_N=0.8\pm0.04$. Therefore, this array can be useful as an effective SERS platform for sensor applications. However, the greater enhancement in signal intensity is observed for arrays annealed at 500 ℃, therefore, annealed arrays would be the best platform for luminescence enhancement measurements. The spanning of lipid bilayers across prefilled gold nanocavity arrays was achieved by vesicle fusion technique. Therefore, this platform can provide a biomimetic surface for transmembrane proteins.

APPENDIX A

**Synthesis of Ru(dpp)₂(amidophen-16-(acetylthio)-hexadecanyl)(PF₆)₂**

Synthesis of 5-amido-1,10-phenanthroline-(16-acetylthio-hexadecanyl):

220 mg (1.132 mmol) of NH₂phen and 340 mg (1.029 mmol) of 16-(acetylthio)-hexadecanoic acid were dissolved in 15 ml anhydrous DMF and stirred for 30 minutes. 2 equivalents (0.5695 g, 2.058 mmol) DMTMM was added to the reaction which was then stirred for 18 hr. When the reaction was completed the solution was added to 100 ml H_2O and the resulting precipitate was collected by vacuum filtration and washed with plenty of water and diethyl ether. The crude solid was sonicated in 50 ml acetone and the undissolved material was removed by vacuum filtration. This was carried out multiple times on the precipitate until the product was found to be sufficiently pure. 0.1213 g was recovered (21.1 % yield). Purity was confirmed by NMR analysis. ^{1}H NMR in deuterated DMSO. 10.12 (1H, s, NH), 9.12 (1H, dd, C-H), 9.03 (1H, dd, C-H), 8.60 (1H, dd, C-H), 8.44 (1H, dd, C-H), 8.17 (1H, s, C-H), 7.83 (1H, dd, C-H), 7.74 (1H, dd, C-H), 2.80 (2H, t, CH_2), ~2.5 obscured by solvent peak (2H, t, CH_2), 2.3 (3H, s, CH_3), 1.69 (2H, quintet, CH_2), 1.47 (2H, quintet, CH_2), 1.4-1.2 (22H, m, eleven CH_2).

Synthesis of Ru(dpp)₂(amidophen-16-(acetylthio)-hexadecanyl)(PF₆)₂:

55.1 mg (1.084×10^{-4} mol) amidophenanthroline-16-(acetylthio)-hexadecanyl and 94.6 mg Ru(dpp)₂Cl₂ were dissolved in 50 ml 80 : 20 EtOH : H_2O. This solution was refluxed for 16 hr and then the reaction mixture was rotary evaporated down to about 15 ml. Ammonium hexafluorophosphate was used to precipitate the product as a PF₆ salt. The orange product was collected by vacuum filtration and washed with water and diethyl ether. 0.1475 g was recovered (87 % yield). Purity was confirmed by NMR analysis. GC-MS: 1418 (M^+, -145). ^{1}H NMR in deuterated DMSO. 10.45 (1H, s, N-H), 8.91 (1H, d, C-H), 8.78 (1H, d, C-H), 8.68 (1H, s, C-H), 8.35 (1H, d, C-H), 8.32 (1H, d, C-H), 8.26 (5H, m, C-H), 8.20 (2H, m, C-H), 8.14 (1H, t, C-H), 7.90 (1H, m, C-H), 7.82 (3H, m, C-H), 7.8 (2H, m, C-H), 7.7-7.5 (20H, m, C-H), 2.78 (2H, t, CH_2), 2.67 (2H, t, CH_2), 2.29 (3H, s, CH_3), 1.70 (2H, quintet, CH_2), 1.46 (2H, quintet, CH_2), 1.44 (22H, quintet, CH_2).

Synthesis of $[Ru(bpy)_2(pic\text{-}C_{16})]^{2+}$
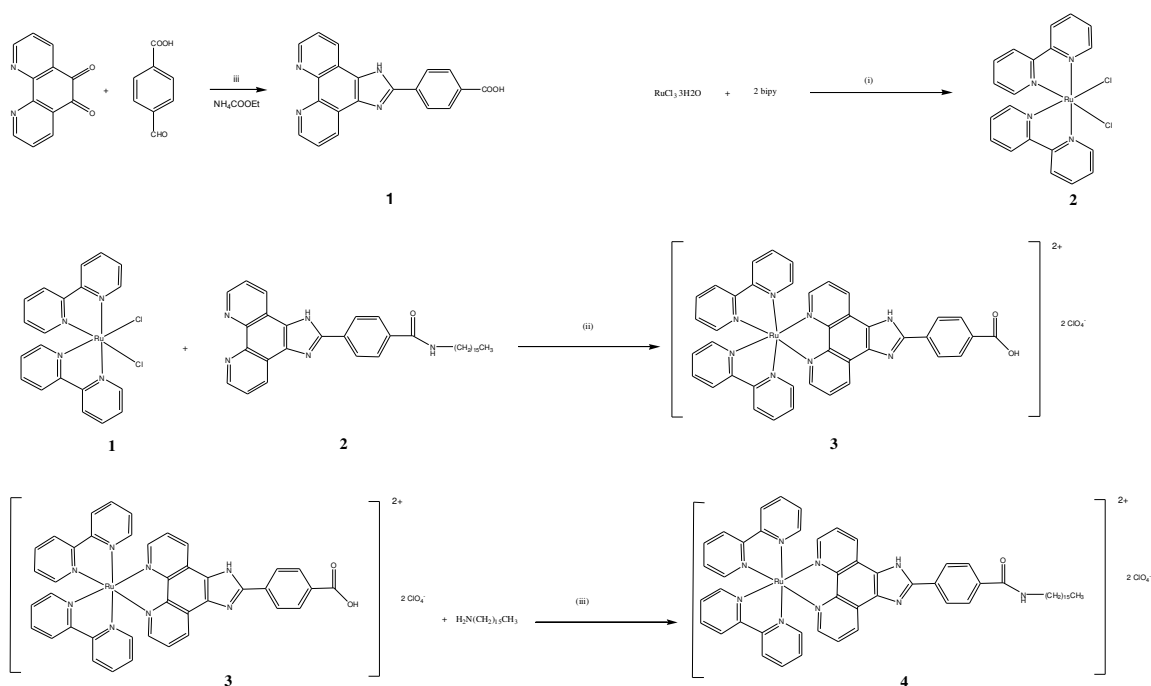
Scheme: Synthesis of $[Ru(bpy)_2(pic\text{-}C_{16})]^{2+}$ complex.

Ruthenium trischloride, 4-carboxybenzaldehyde, 1,10-phenanthroline-5,6-dione, ammonium acetate and lithium perchlorate were used directly as provided by Sigma Aldrich. The ligand $PICH_2$ and complex $[Ru(bipy)_2PICH_2]^{2+}$ were prepared according to procedures previously reported in literature.[1,2] One to one equivalents of 4-carboxybenzaldehyde and 1,10-phenanthroline-5,6-dione were condensed in the presence of an excess of ammonium acetate in refluxing acetic acid. The reaction of condensation afforded $PICH_2$ (Scheme 1) in 70% yield as yellow solid. The complex $[Ru(bipy)_2(PICH_2)]^{2+}$ was synthesised by refluxing $[Ru(bpy)_2Cl_2]$ and $PICH_2$ in ethanol overnight (Scheme 2). The ethanol was removed under reduced pressure and the complex was precipitated by addition of small aliquots of a saturated aqueous solution of lithium perchlorate.

2-(4-Carboxyphenyl)imidazo[4,5-f][1,10]phenanthroline [PICH$_2$] (**Compound 1**) : ^{1}H-NMR (400 MHz, DMSO-d_6) δ/ppm: 14.0 (1H, s), 13.1 (1H, s, br), 9.1 (2H, m), 9.0 (2H, m), 8.44 (2H, d, J=4.0Hz), 8.20 (2H, d, J=4.0Hz), 7.85(2H, m).

[Ru(bpy)$_2$Cl$_2$] (**Compound 2**): ^{1}H-NMR (400 MHz, DMSO-d_6) δ/ppm: 9.97 (2H, d, J=4.03 Hz), 8.49 (2H, d, J=4.0 Hz), 8.07(2H, t, J= 7.7 Hz), 7.77 (2H, t, J=6.6 Hz), 7.68 (2H, t, J=7.7Hz), 7.1 (2H, t, J=6.6 Hz).

[Ru(bipy)$_2$(PICH$_2$)]2ClO$_4$ (**Compound 3**): ^{1}H-NMR (400 MHz, DMSO-d_6) δ/ppm: 9.12 (2H, d, *J*=8.20 Hz), 8.89 (2H, d, J= 8.45 Hz), 8.85 (2H, d, J=8.40 Hz), 8.46 (2H, d, *J*=8.52 Hz), 8.22 (2H, t, J=8.21 Hz), 8.10 (4H, m), 7.88 (6H, m) ,7.60 (4H, m), 7.37 (3H, t, J=7.67 Hz).

Synthesis of [Ru(bpy)$_2$(pic-C$_{16}$)]$^{2+}$ (Compound 4):

[Ru(bipy)$_2$(PICH$_2$)]2ClO$_4$ (140 mg ,0.15 mmol) and hexadecane-1-amine (72 mg, 0.30 mmol) were dissolved in 10 ml of dry *N,N*-dimethylformamide. After 10 minutes of stirring, DMTMM[3] (300 mg, 1 μmol) was added and the reaction was stirred for ten hours at room temperature, in dark. Addition of small aliquots of sodium perchlorate saturated aqueous solution led to precipitation of the crude product as an orange powder, which was collected and washed with small amounts of cold water. The product was isolated as pure ruthenium complex after being purified on neutral aluminium oxide by gel-chromatography (eluent: dichloromethane/methanol 90:10) and recrystallized in the minimum amount of methanol. The pure product was collected by filtration and finally dried in air. Yield: 55%. ^{1}H-NMR (DMSO-d6, 400 MHz) δ/ppm: 9.07 (d, 2H, J=8.6Hz), 8.66 (d, 2H, J=8.0 Hz), 8.61 (d, 2H, J=8.0 Hz), 8.32 (d, 2H, J=8.0 Hz), 8.0-7.88 (m, 6H), 7.86 (d, 2H, J=5.5 Hz), 7.72 (dt, 2H, J1=5.0 Hz, J2=2.7Hz), 7.59 (d, 2H, J=5.7Hz), 7.45 (t, 2H, J=6.3 Hz), 7.22 (t, 2H, J=6.5 Hz), 3.31 (t, 2H, J=7.26 Hz), 1.57 (t, 2H, J=5.9 Hz), 1.36-1.09 (m, 29H), 0.76 (t, 3H, J=5.9Hz).

References

[1] Steck, E. A.; Day, A. R. *J. Am. Chem. Soc. 65,* **1943**, 452.

[2] Forster, R. J.; Pellegrin, Y.; Keyes, T. E. *Electrochem. Commun.* **2007,** *8* 1899.

[3] Kunishima, M.; Kawachi, C.; Morita, J.; Terao, K.; Iwasaki, F.; Tani, S. *Tetrahedron* **1999,** *55*, 13159.

APPENDIX B